UNIVERSITY OF CAPE TOWN
IYUNIVESITHI YASEKAPA • UNIVERSITEIT VAN KAAPSTAD

The effect of bend radius on the impulse transfer characteristics of V-hulls

This work is submitted in partial fulfilment of the requirements
of the degree of Master of Science in Engineering
specialising in Mechanical Engineering

Author:
Vinay Ramaswami Shekhar

Supervisor:
Prof. Genevieve Langdon

November 3, 2015

Blast Impact and Survivability Research Unit
Department of Mechanical Engineering
Faculty of Engineering and The Built Environment
University of Cape Town

This page has been intentionally left blank.

Declaration

1. I know that plagiarism is wrong. Plagiarism is to use another's work and pretend that it is one's own.
2. I have used the IEEE convention for citation and referencing. Each significant contribution to, and quotation in, this report from work(s) of other people has been attributed, and has been cited and referenced.
3. This report is my own work.
4. I have not allowed, and will not allow anyone to copy my work with the intention of passing it off as his or her own work.

Signature Vinay R. Shekhar

Vinay R. Shekhar (SHKVIN001)

This page has been intentionally left blank.

Abstract

This work is based primarily on the effects of V-tip bend radii on the impulse transfer to V-plates subjected to localised blast loading.

Three rigid V-plates with V-angles of 60°, 90° and 120° were designed and fabricated from steel plates. Blast tests with PE4 charges ranging from 19 g to 58 g at a stand-off distance (SOD) of 34 mm were performed. The geometric scaling was based on the dimensions of the TM-57 landmine and the Casspir APC MK II.

In the numerical model, the optimum element length for the air mesh was obtained by performing a mesh convergence study on the Arbitrary Lagrangian-Eulerian (ALE) mesh, and validated using the impulse values measured from a 58 g detonation onto a 120° V-plate as it resulted in the highest impulse. Element lengths of 1.5, 2.0 and 3.0 mm were investigated. Element lengths of 1.5 and 2.0 mm both produced accurate results, though the run-time for an element length of 2.0 mm was significantly lower. A validation study compared the numerically predicted impulses with those of the experiments and the results were found to be within an acceptable percentage variation. Hence a 2.0 mm element length was chosen for the Arbitrary Lagrangian-Eulerian mesh.

The initial computational cost of the simulations was found to be relatively high. In an attempt to reduce these costs, tests were performed which looked at modelling the various components with rigid material models. The deflection of the clamp frames due to the pressure loading of the blast wave was found to be insignificant and thus the clamp frame was modelled as rigid. It was found that there was no significant variation in the impulse transferred when the V-plates were modelled as a rigid or deformable material but there was a significant reduction in the run-time. Thus the V-plates were also modelled with a rigid material.

The first set of simulations investigated the effect of the bend radius on the impulse transferred for three V-angles (that is 60°, 90° and 120°). In general, for all V-angles, it was found that impulse increased as bend radius increased. For the 90° and 120° V-plates, the impulse transferred was observed to plateau for bend radii greater than 160 mm. The increase in impulse transferred was attributed to the increased

plate areas subjected to the maximum pressures as well as the reduced rates of pressure dissipation for the larger bend radii. There was no significant variation in the pressure distributions for larger bend radii (> 160 mm) which explained the plateau observed in impulse transferred. For both the 90° and 120° V-plates a dip in impulse was observed for bend radii between 0 and 20 mm. This was determined to be due to reduced peak pressures and an increase in gas flow for bend radii in this range.

When two different clamp frame designs were compared it was found that the predicted impulses and force-time histories were virtually identical. The last set of simulations investigated the effects of fixing the height of the explosive relative to the clamp frame and increasing the bend radius of the V-plates. These tests showed that the variation in the impulse was small and that the peak pressure dropped while duration of loading increased with increasing bend radii (and stand-off distance).

From this study it was found that, in general, as the bend radius increased the impulse increased and that the 60° V-plates showed the greatest sensitivity to bend radius effects. The 90° and 120° V-plates showed little to no increase in impulse for bend radii greater than 160 mm. It was observed that the clamp frame design had no significant effect on the impulse transferred. At lower bend radii (< 100 mm), both the V-angle and the bend radius influenced the impulse transferred. For bend radii between 100 and 160 mm, increasing the bend radius increased the impulse transferred, while changing the V-angle had little to no effect.

Acknowledgements

I would like to extend my sincere thanks to the people who have contributed towards the completion of this work.

Firstly I would like express my gratitude to my research supervisor, Prof. G.S. Langdon for her suggestions on how best to scope out this work and the excellent advice on how to analyse and present results. I really appreciate how patient and understanding she was when I got flustered trying to get results and was not making progress with the research.

Computations were performed using facilities provided by the University of Cape Town's ICTS High Performance Computing team: `http://hpc.uct.ac.za`. I would like to acknowledge the resources provided by the HPC centre that enabled the simulations to be performed. In particular I would like to thank Andrew Lewis from the University of Cape Town's ICTS High Performance Computing team for helping setup my account and for giving me advice on the setting up of script files and the running of simulations on the HPC servers. I would also like to thank the NRF for providing funding for this research.

The advice provided by Richard Curry on the optimisation of my simulations and the design of the rigid V-plates was greatly appreciated. I would also like to thank Victor Balden, for his advice on the simplification of the numerical model and for suggesting the use of the HPC centre at UCT for running my simulations.

I'd also like to thank all the remaining BISRU staff for providing a ton of advice during the seminars on ways to improve this work. A special thank you to all the BISRU post-graduates for making the lab a fun, sometimes weird, but most definitely an interesting and friendly environment to work in. I am in particular grateful to my friends Gideon Volschenk and Dale Warncke for some crucial LS-DYNA help.

Lastly I'd like to thank my parents for all the support that they have given me throughout the course of this research.

This page has been intentionally left blank.

Table of Contents

List of Tables

List of Figures

List of Listings

This page has been intentionally left blank.

Glossary

ϵ_0 Strain rate.

γ The ratio of the specific heats $\left(\text{that is } \frac{C_p}{C_v}\right)$.

μ Defined as $\frac{\rho}{\rho_0} - 1$.

ν Poisson's ratio.

ω The Grüneisen parameter.

ω_d Damped frequency (in $\mathrm{rad\,s^{-1}}$).

ω_n Natural frequency (in $\mathrm{rad\,s^{-1}}$).

ρ Current density (in $\mathrm{kg\,m^{-3}}$).

ρ_0 Reference density (in $\mathrm{kg\,m^{-3}}$).

σ Stress (in MPa).

C Viscous damping coefficient (in $\mathrm{N\,s\,m^{-1}}$).

C_p Specific heat at constant pressure.

D Detonation velocity (in $\mathrm{m\,s^{-1}}$).

E Young's Modulus.

E_0 Internal energy per unit reference volume.

$I_{experimental}$ Experimentally measured impulse (in $\mathrm{N\,s}$).

$I_{numerical}$ Numerically predicted impulse (in $\mathrm{N\,s}$).

M_p Mass of the pendulum (in kg).

$NCPU$ The number of CPUs used.

P_{CJ} Chapman-Jouguet pressure.

p Pressure (in MPa).

T Natural period (in s).

T_M Melting temperature.

U Shock velocity (in $\mathrm{m\,s^{-1}}$).

u Particle velocity (in $\mathrm{m\,s^{-1}}$).

$\ddot{X}$ Acceleration (in $\mathrm{m\,s^{-2}}$).

$\dot{X}$ Velocity (in $\mathrm{m\,s^{-1}}$).

Acronyms

ALE Arbitrary Lagrangian-Eulerian.

ANFO Ammonium Nitrate Fuel Oil.

APC Armoured Personnel Carrier.

AP-mine Anti-Personnel mine.

AT-mine Anti-Tank mine.

BISRU Blast Impact and Survivability Research Unit.

CAD Computer-Aided Design.

DOB Depth of Burial.

DRU Defence Research Unit.

EOS Equation of State.

FEM Finite Element Method.

FSI Fluid-Structure Interaction.

HPC High Performance Computing.

IED Improvised Explosive Device.

JWL Jones-Wilkins-Lee.

MMALE Multi-Material Arbitrary Lagrangian-Eulerian.

MRAP Mine-Resistant Ambush Protected vehicle.

NRF National Research Foundation.

PE4 Plastic Explosive No. 4.

RDX Cyclotrimethylenetrinitramine.

SDOF Single Degree-Of-Freedom.

SHPB Split-Hopkinson Pressure Bar.

SOD Stand-Off Distance.

SPH Smooth Particle Hydrodynamics.

TNT Trinitrotoluene.

WWI World War I.

WWII World War II.

Chapter 1

Introduction

The performance of V-plates when subjected to blast loading is of interest in the design and optimisation of military vehicle hulls. This chapter aims to provide a background into the research on which this report is based. The objectives of the research are then stated and finally an outline of the report is provided.

1.1 Background and motivation

The idea behind a landmine has existed since the 16th century and the first Anti-Tank mines (AT-mines) were developed and used in World War I (WWI) and World War II (WWII) to counteract the threat of assault tanks [1]. In order to neutralise the threat of these mines, a number of devices such as mine flails and rollers were fitted to the front of armoured vehicles and used to detonate the mines [1]. The problem with these devices was that they suffered damage when the mine detonated which limited their reusability, hence mine ploughs were developed to pick up and move the mines safely off the road [1]. During the wars in Rhodesia in the 1970s, landmine detonations started becoming more common, which stimulated the development of landmine protected armoured personnel carriers (APC) [1].

Armoured vehicles have been used by the military in one form or another for almost one thousand years. One of the first notable uses of these vehicles was in 1125 in China [2]. Major development of armoured vehicles for personnel transport only started at the end of WWI when, in 1918, tanks were converted to carry troops by the British Army [2]. Most armoured cars were based on standard production cars onto which steel plate was attached [2]. During the Cold War the FV 432 (from Britain) and M113 (from America), shown in Figure 1.1, were developed and used as APCs [2]. The FV 432 APC and the M113 APC had been designed to protect their occupants against potential nuclear, biological and chemical attacks by the Soviet Union during the Cold War and hence their hulls were not designed to protect the occupants against landmine explosions [2].

(a) British FV 432 APC [3] (b) M113 APC [4]

Figure 1.1: Photographs of two Armoured Personnel Carriers designed and developed during the Cold War [3, 4]

The first use of a V-hull in a landmine protected APC can be attributed to the SKPF/VKPF M/42 APC, shown in Figure 1.2, which was developed by Sweden during WWII [1]. The advantage of the V-shaped hull is that it deflects the blast wave around the passenger compartment. The next V-hulled APC was the Camel which was developed by the South African Defence Research Unit (DRU) and had a sharp internal V-angle of 43° [1]. This sharp V-angle meant that these vehicles had a high centre of gravity and hence a tendency to topple over. Since then further development has been performed on the use of V-shaped hulls for APCs.

Figure 1.2: Photograph of an SKPF/VKPF M/42 APC developed by Sweden during WWII [5]

The early V-hulled vehicles were designed around a standard chassis and suspension arrangement [1]. The use of a monocoque chassis meant that many of the exposed suspension components were moved inside the V-hull and so were better protected from a landmine blast [1]. The early iterations of monocoque chassis landmine protected vehicles (such as the Hippo Mark I) were unreliable and difficult to handle [1]. The Hippo was eventually developed into the Casspir in 1979 (Shown in Figure 1.3), which had addressed the major negative aspects of the Hippo, such as power and handling [1]. This was achieved by using a larger V-angle, thus reducing the centre of gravity of the vehicle. Additionally, the armour for the vehicle was manufactured by welding plates together [1].

Figure 1.3: Photograph of a Casspir APC developed by the DRU

More than a hundred experiments have been performed using scaled V-plates at the Blast Impact and Survivability Research Unit (BISRU). These tests investigated the effects of the included angle of the V-plates on the impulse transfer and mid-point deflection characteristics of the steel V-plates, with the V-tip radius fixed at 2 mm. The early tests found that the plates with a smaller included angle performed the best in terms of impulse transfer [6]. Additionally, welded V-plates were tested as an alternate manufacturing technique and were found to be significantly weaker than the equivalent folded plate [6]. To reduce the centre of gravity of the APC, plates where the V-tip was cut-off were tested as shown in Figure 1.4. It was found removing the V-tip reduced the ability of the V-plate to deflect the blast wave [7]. When composite V-plates were investigated it was found that it was not possible to manufacture them with the small V-tip radius (previously used for the steel V-plates) so larger radii between 25 and 54 mm were used [8].

From past work [6–9] it was decided that it would be useful to determine the effects of the V-tip radius on the impulse transfer characteristics of V-plates, as this is a manufacturing process variable when folding is used to produce a V-shaped hull.

Figure 1.4: Schematics of the V-plates with reduced height [7]

1.2 Objectives

This research involved the development of a numerical model for V-plates subjected to blast loading. This model could then be used to investigate the effects of a number of geometric parameters on the impulse transfer characteristics of these V-plates. The objectives of the research are listed below:

1. To develop a computational model that can accurately predict the transmitted impulse of V-plates subjected to localised blast loading.

2. Determine the influence of the V-tip radius on the impulse transfer characteristics of V-plates with varying included angles.

3. Investigate the effects of two clamp frame designs on the impulse transfer and pressure distributions on V-plates with different V-angles.

4. Determine the effects of fixing the position of the explosive charge relative to the clamp frame while increasing the bend radius of the V-plates on the impulse transfer and pressure-time characteristics of the V-plates.

5. Determine loading distributions in regions of the plate located further away from the detonation point and how V-angle and bend radius influences this. Use these pressure distributions to determine whether the reasons for the reduced impulses predicted by Pickering [6] and Warncke [9] was due to the reduced size of the air mesh used.

1.3 Report outline

Following this introduction, a review of the relevant literature is provided in Chapter 2. A brief history of landmines and the development of armoured personnel carriers APC is provided, which is followed by the development and use of V-hulls for these vehicles. This includes an explanation of the benefits and shortfalls of the use of a V-hull versus a flat hull. The previous work on V-plates is described. Finally some of the theory of explosives, blast testing and numerical modelling techniques are detailed.

In Chapter 3 details of the experiments are given. The design of the rigid V-plates is shown, followed by a description of the experimental setup (including the setup of the explosive PE4 charge and the detonator.) The explosive and geometric scaling, and blast test results are then presented.

The first step in the development of the numerical blast model is to perform a convergence study of the air mesh (ALE) in order to choose the optimum mesh density. This is reported in Chapter 4 and uses the results of Chapter 3 to validate the chosen mesh size. Chapter 5 details the process used to optimise the rest of the numerical model to reduce the computational time of each simulation.

Once the optimal numerical model was obtained it could be used to investigate the objectives. An analysis of the development of the pressure and velocity fields for V-plates of varying bend radii and V-angle is provided in Chapter 6. In Chapter 7 the results and analysis of the numerical simulations performed based on the three sets of simulations that were investigated are provided.

In Chapter 8, the main conclusions that could be drawn from the research are stated, while recommendations for future testing and research are provided in Chapter 9.

This page has been intentionally left blank.

Chapter 2

Literature review

This literature review starts with a brief history of landmines and Armoured Personnel Carriers (APC), and the effect of landmines on the design of APCs. Some blast loading theory is then provided, which leads into the discussion of previous experimental work in blast loading. The numerical side of the research is then considered by looking at instances of blast loading in numerical packages. Finally, previous numerical simulations of the blast loading of V-plates in various numerical packages are reviewed.

2.1 Landmines, IEDs and armoured vehicles

Landmines can be described as explosive devices that are triggered by an intended target (either people or vehicles) [10]. They can be buried in the ground or fixed to objects above the ground [11] and have been in existence since the 16th century [1]. In the early days, soldiers tunnelled under enemy positions and detonated explosives [1]. The first pressure-sensitive landmines were designed by Immanuel Nobel and were first used in the Crimean War [12]. This design was copied and used by a Confederate general during the American Civil War, when an artillery shell was buried and triggered with a trip wire [13]. The use of landmines increased significantly during WWII.

A landmine typically comprises an explosive contained within a casing which is made of metal, plastic or wood [11]. Landmines can be categorised into Anti-Tank mines (AT-mines) which are designed to immobilise a tank by blowing its tracks off [10] and Anti-Personnel mines (AP-mines) which are targeted at people and are further categorised based on how they injure their targets [11]. Landmines cause injury and death primarily due to the blast overpressure [14]. Additional effects include large scale plastic deformation of the vehicle hull and fragmentation resulting from the tearing vehicle components [14]. AT-mines are larger than AP-mines [10] and were developed to counteract the threat of assault tanks during WWI [1]. AT-mines usually contain between 2 and 9 kg of explosives, compared to 10 g and 250 g of explosives in an

AP-mine [15]. AT-mines also require a detonator which has a larger mass (*i.e.* between 100 g and 300 g) when compared to AP-mines (*i.e.* between 5 g and 50 g) [15]. Figure 2.1 shows examples of an AT-mine and an AP-mine.

(a) A Russian TM-46 Anti-Tank mine (b) An American M14 Anti-Personnel mine

Figure 2.1: Photographs showing Anti-Tank and Anti-Personnel landmines

During World War II (WWII) it is estimated that more than 300 million AT-mines were used [11]. It is also estimated that there are currently 84 million landmines in 64 countries around the world [15], and that landmines cause the death of 24000 people every year, with most of these people being civilians [12]. In more recent conflicts in Iraq and Afghanistan, Improvised Explosive Devices (IEDs) have become a prevalent threat [16]. An IED can be described as an exploding mine, which is often placed at the side of a road and can be triggered in a number of different ways [17]. They are low-technology homemade devices that use commercial or homemade explosives [18, 19]. It is reported that IEDs have resulted in the death of over 2000 soldiers in Iraq since 2001 [18].

AT-mines were used extensively in the 1970s during the Rhodesian Bush War [1] and there are an estimated 1.5 million mines still present in Zimbabwe [20]. The two mines that were most commonly used were the TM-46 and TM-57 Anti-Tank mine [21]. This prompted the development of landmine protected Armoured Personnel Carrier (APC) [1].

Armoured vehicles have been used in conflicts long before the invention of the internal combustion engine [2]. The earliest notable use of an armoured vehicle can be traced to China in the year 1125 [2]. Once the internal combustion engine was invented at the end of the 19th century, armoured vehicle development took-off. At the end of World War I (WWI) in 1917, the British Army commissioned an armoured vehicle based on an assault tank that would be capable of transporting a large number of troops or supplies [2]. This was the first major development of the APC. The function of the APC is to transport troops onto the battlefield. On average the personnel compartment of an APC is capable of holding six to nine troops [22]. Before World War II (WWII), the British made the greatest strides in the development of armoured

vehicles [23], while the USA did very little armoured vehicle development between 1919 and 1930 [2]. Most armoured cars used during WWII were manufactured by attaching steel plates onto the chassis of standard production cars [2]. An example of such an armoured car is shown in Figure 2.2.

Figure 2.2: Photograph of a British Standard Beaverette armoured car [24]

The Cold War saw the development of what is now considered to be a modern APC in the form of the FV 432 (from Britain) and the M59 and M113 (from America) [23] as shown in Figure 1.1. It was anticipated that the Soviet Union would launch a nuclear, biological or chemical attack and hence the APCs developed by Britain and the USA, such as the FV 432 APC and the M113 APC, were designed to withstand such an attack. The M113 became the most used APC in the world [22], though due to the fact that it had a weak floor, many personnel were killed or injured due to AT-mines during the Vietnam War [2].

Landmine clearing devices are a method of protecting troops from landmines. During WWII various devices were developed to clear landmines, including mine flails, rollers and mine ploughs [1]. Examples of these devices are shown in Figure 2.3. The problem with most landmine clearing devices is that they suffer damage when the mines detonate, which limits the rate at which mine fields can be cleared. Modern improvements in technology have led to new developments in landmine detection, including electromagnetic induction (which is suitable for mines containing metal) and ground penetrating radar (which works even if the mines are plastic) [25].

(a) U.S. Army M1A1 Abrams tank with mine plough

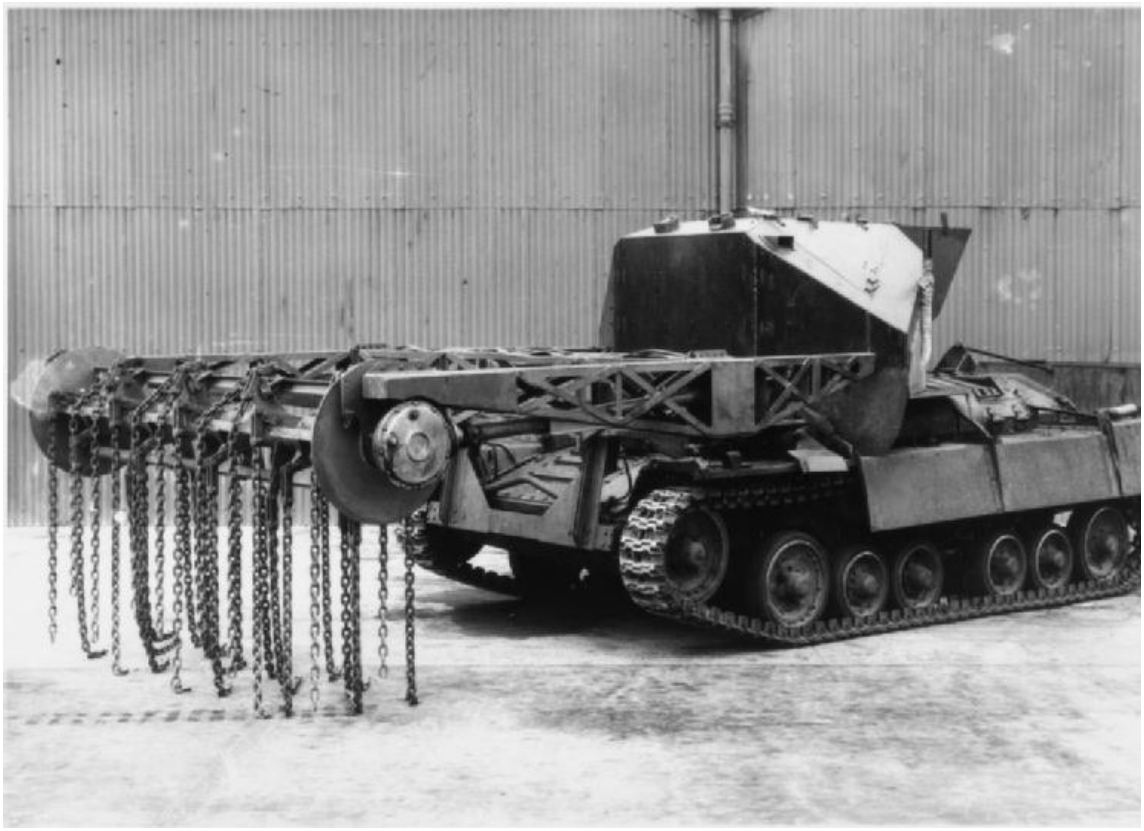

(b) Experimental flail mounted on a Valentine tank

Figure 2.3: Examples of the mine clearing devices

Mine-Resistant Ambush Protected vehicles (MRAPs) use a V-hull and armour plating to protect its occupants against landmines and IEDs and provide significantly better protection for military personnel than conventional high mobility, multi-wheeled vehicles (HMMWVs) [26] such as the one depicted in Figure 2.4. The USA only started major development of MRAPs in 2006, due to the threat of Improvised Explosive Devices (IEDs) [26].

Figure 2.4: Photograph of a Greek Army M1114GR HMMWV

Shneck [14] summarised the development of mine resistant vehicles into four categories:

- Generation 1 - Improvised kits manufactured in the field by soldiers
- Generation 2 - Kits designed and manufactured for field installation
- Generation 3 - Vehicles using a standard chassis, onto which a mine resistant hull was mounted
- Generation 4 - Vehicles using a monocoque chassis which incorporated the mine resistant hull

The first example of a generation 3 vehicle was the SKPF/VKPF M/42 APC, a landmine protected APC developed by the Swedish with a V-shaped hull [1]. The V-shaped hull provided protection by deflecting the blast wave outwards and away from the passenger compartment.

The next V-hulled APC was developed during the Rhodesian Bush War by the South African Defence Research Unit (DRU). The DRU built the Camel (later called the Hyena), which was based on the Ford F-250 chassis and was powered by a 6 cylinder water cooled Ford engine [1]. These vehicles had a sharp V-angle of 43° and hence had tendency to topple over due to the raised centre of gravity. This sharp V-angle also meant that there was insufficient space within the cabin for troops and equipment [1]. A similar vehicle was developed by Rhodesia, the Rhino, based on a Land Rover Defender chassis and a Land Rover engine, but with a shallower V-angle of 90° [1].

The early V-hulled vehicles can be categorised as Generation 3 mine protected vehicles with a standard chassis and suspension arrangement, usually take from a production off-road vehicle. The advantage of this setup is that the costs of manufacturing are reduced, while the mine resistant capabilities of the V-hull are retained. The disadvantage is that the mass of the vehicle is greatly increased, which significantly hinders the performance of the vehicle [14].

The first APC which used a monocoque V-hull was the MRV-1, developed by the South African DRU in 1972. The Leopard was based on a similar design and the first prototype was developed in 1974 [1].The Leopard was manufactured from a Volkswagen Kombi chassis and engine. Figure 2.5 shows a Leopard APC.

Figure 2.5: Photograph of the Leopard landmine resisting or 'anti-landmine' vehicle [27]

The use of a monocoque chassis classified these vehicles as Generation 4 mine resistant vehicles. These vehicles usually had excellent mine resistance and performance [14], although they were significantly more expensive to build, due to the custom nature of the design. Another advantage of the monocoque design was that critical suspension components were better protected from a landmine blast, since they could be moved into the V-hull [1]. Early iterations of such vehicles (such as the Hippo Mark I) were found to be unreliable and difficult to handle [1]. The Casspir (shown in Figure 2.6) was developed in 1979 to overcome the negative performance characteristics of the Hippo [1]. The Casspir had a V-angle of approximately 95° as shown in Figure 2.7, which was larger than the Hippo, meaning that the centre of gravity was reduced which improved the performance of the vehicle [1].

Figure 2.6: Photograph of a Casspir at the South African Police Museum, Pretoria. [28]

Figure 2.7: Photograph of a back of a Casspir showing the V-angle

While the Casspir APC continues to remain in service, there has been further development of landmine protected APCs. In the 1980s the Ingwe APC was developed by Sandrock-Austral, while the Wolf was developed by the DRU. Much like the Casspir, the Ingwe and the Wolf had V-shaped hulls which were manufactured from armoured steel. The Wolf was also heavier and more powerful than the Casspir [1]. In the 1990s, the Mamba APC was developed in South Africa and replaced the Buffel APC. It had a chassis based on a Unimog and utilised an armoured steel V-hull. It was both lighter and less powerful than the Casspir and the Wolf and was also capable of carrying fewer personnel [23]. More recent landmine protected APCs include the Scout and Marauder. These vehicles have benefited from improvements in their engines and armour plating. Hence their power output was greater, resulting in a greater torque, higher top speeds and a longer range.

2.2 Explosives and blast loading

An explosion can be defined as a rapid release of energy which generates a pressure wave of finite amplitude and duration [29, 30]. While an explosion can be caused by different types of events, such as the failure of a pressure vessel or the muzzle blast from a gun, most are the result of chemical or nuclear explosive materials [29]. Explosive materials are substances that when subjected to a suitable trigger are rapidly converted into gas products, developing large amounts of heat at high pressures [31, 32].

The first time explosives were used was in China in 220 BC, when alchemists accidentally created black powder [32]. In the 1600s the use of black powder increased when the Europeans used it for mining [31–33]. Explosives can be split into four categories, namely high explosives, low explosives (propellants), blasting agents and binary explosives [31].

Black powder is a low explosive, because when ignited it burns rather than detonating like high explosives [33]. It contains a fuel, which is a mixture of charcoal and sulphur and an oxidiser, which is potassium nitrate [32]. Low explosives are used as propellants in ammunition as they allow the projectile to gain a high velocity without destroying the barrel of the gun [31].

All modern explosives are classified as high explosives. High explosives can be further split into primary and secondary explosives. Primary explosives detonate when they are exposed to heat or shock and have the ability to transfer the detonation to other explosives which are more stable (*i.e.* secondary explosives). They are also generally more expensive and hence are only used in small amounts to initiate larger explosions [31, 32]. Examples of primary explosives include lead azide and mercury fulminate [33].

Secondary explosives can be further sub-categorised into military and industrial explosives. Military explosives include Trinitrotoluene (TNT) and Cyclotrimethylenetrinitramine or RDX, while Ammonium Nitrate Fuel Oil (ANFO) is an example of an industrial explosive [32, 33].

When detonated, secondary explosives breakdown rapidly into more stable components, such as water vapour and nitrogen gas, releasing a large amount of heat. The detonation velocities of secondary explosives are in the range of $1500\,\mathrm{m\,s^{-1}}$ to $9000\,\mathrm{m\,s^{-1}}$ and result in the generation of a shock wave [32].

A shock wave is defined as the discontinuous separation of the portion of a material that is stationary and the portion that is moving [33, 34]. The initial particle velocity, internal energy, density and pressure jump suddenly as it crosses the shock front and can be obtained from the Rankine-Hugoniot equations, which can be derived from the conservation of mass, momentum and energy [33, 34]. These derivations result in Equations (2.1) to (2.3) [34], where the subscript 0 represents the unshocked state and the subscript 1 represents the shocked state.

$$\frac{\rho_1}{\rho_0} = \frac{U - u_0}{U - u_1} \tag{2.1}$$

$$p_1 - p_0 = \rho_0(u_1 - u_0)(U - u_0) \tag{2.2}$$

$$E_1 - E_0 = \frac{1}{2}(u_1^2 - u_0^2) \tag{2.3}$$

Combustion is the fast and highly exothermic oxidation reaction of any substance. For explosives, it is defined as an exothermic, rapid-oxidising reaction which produces high temperature gaseous products [32]. When explosives combust they can either deflagrate or detonate depending on the speed at which the decomposition reaction occurs, and in general, propellants deflagrate and explosives detonate [31, 34].

Deflagration is defined as the ignition of combustible material when subjected to a flame, spark, shock or high temperature. This results in the burning of the material at subsonic speeds, producing solid and gas products at low, sustained pressures [31, 32]. The rate of deflagration increases with an increase in the degree of confinement, pressure and temperature. The pressure increases if the gaseous products cannot escape during the deflagration process, which in turn increases the rate of deflagration [32]. If the rate of deflagration increases to a value in the range from $1000\,\mathrm{m\,s^{-1}}$ to $1800\,\mathrm{m\,s^{-1}}$, it is classified as a low order detonation, and if the rate reaches $5000\,\mathrm{m\,s^{-1}}$, it is classified as a high order detonation [32].

Detonation occurs when the explosive material decomposes through the propagation of a shock wave at a velocity which is an order of magnitude higher than that of the deflagration process at a speed greater than the speed of sound [31, 32]. The process can be initiated via the same means as the deflagration process or from the detonation of a primary explosive. In the detonation process the explosive material is converted into gas products at very high temperatures and pressures [31].

2.3 Response of flat panels to localised blast loading from cylindrical charges

A number of studies have been conducted which investigated the blast loading of flat plates. In particular this survey will consider a couple of studies that focused on flat plates subjected to localised blast loading from cylindrical charges.

Jacob *et al.* [35] reported results from tests on cold rolled, quadrangular mild steel plates, subjected to blast loading from cylindrical PE4 charges. Plates of thickness 1.6 mm, 2.0 mm, 3.0 mm and 4.0 mm were tested, while the charge heights used ranged from 1.8 mm to 14 mm and the charge diameters ranged from 24 mm to 64 mm. The stand-off distance (SOD) was fixed at 12 mm by using a polystyrene pad to separate the explosive from the plate as shown in Figure 2.8 [35]. The experiments were performed using the ballistic pendulum at the BISRU labs. Jacob *et al.* [35] performed three sets of tests, looking at the impulse transferred to the pendulum, the modes of failure and the mid-point deflection of the plates, The first set considered the effect of charge height and plate thickness, the second set investigated the effect of charge diameter and plate thickness and the third set explored the effect of changing the length to width ratios of the plates [35].

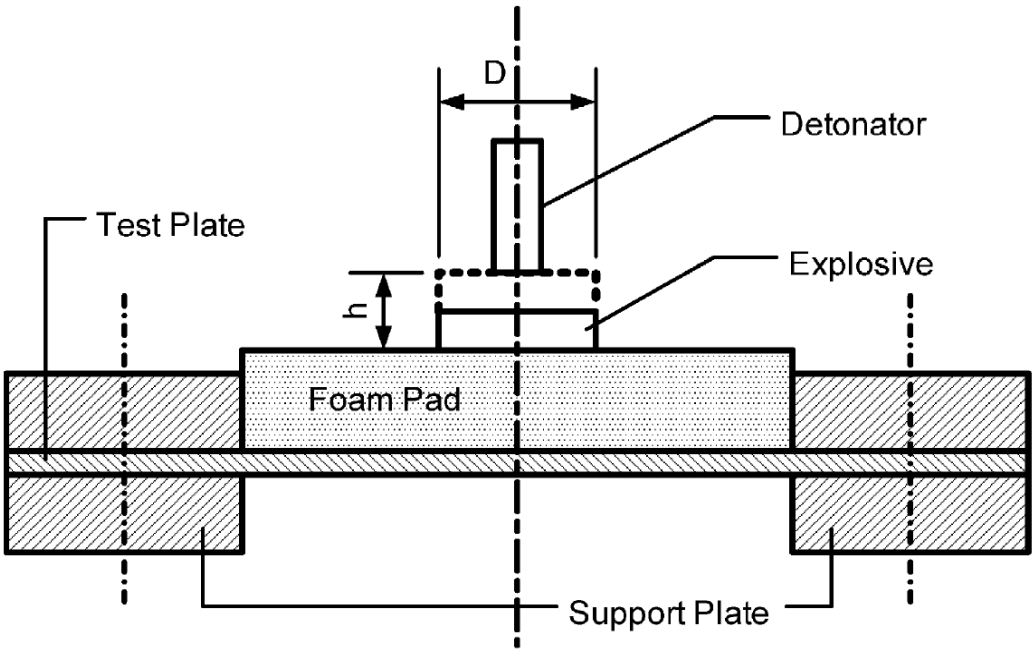

Figure 2.8: Side profile of the explosive and plate arrangement used by Jacob *et al.* [35]

Jacob *et al.* [35] observed large plastic deformations in all the tests performed in the form of a dome, although this was less pronounced on the 4 mm plates. The mid-point deflection was observed to increase with an increase in impulse and thinning was seen for the 1.6 mm, 2.0 mm

and 3.0 mm thick plates at higher impulses. As the impulse increased further, the thinner plates showed partial tearing, while the 4.0 mm plates showed only tearing [35].

In the first set of tests, Jacob *et al.* [35] found that, as expected, increasing the charge height (and as a result the charge mass) for a constant charge diameter increased the impulse. Plate deflection was found to be closely related to the thickness of the plate, with an increase in deflection with a decrease in plate thickness. It was also observed that changing the shape of the exposed area (*i.e.* either square or rectangular) did not influence the plate deformation. For the second set of tests, the charge diameter was varied for a constant charge height. Since the charge mass increases with an increase in charge diameter, it was expected that the impulse would increase as well. Once again an increase in plate thickness resulted in a decrease in mid-point deflection. The third set of tests considered the effects of a constant charge diameter to plate width ratio of 0.2. It was found that as the plate width increased the mid-point deflection increases as the plates were less stiff. Finally linear relationships were observed for impulse versus charge height, impulse versus charge diameter and impulse versus the height to diameter ratio of the charges [35].

Langdon *et al.* [36] investigated the blast response of quadrangular plates which were stiffened with four different types of stiffeners. The configurations considered used single, double, cross or double-cross arrangements of stiffeners as shown in Figure 2.9. Like the testing performed by Jacob *et al.* [35], the stand-off distance between the cylindrical PE4 explosive charge and the plate was 12 mm and the charge diameter was fixed at 36 mm [36].

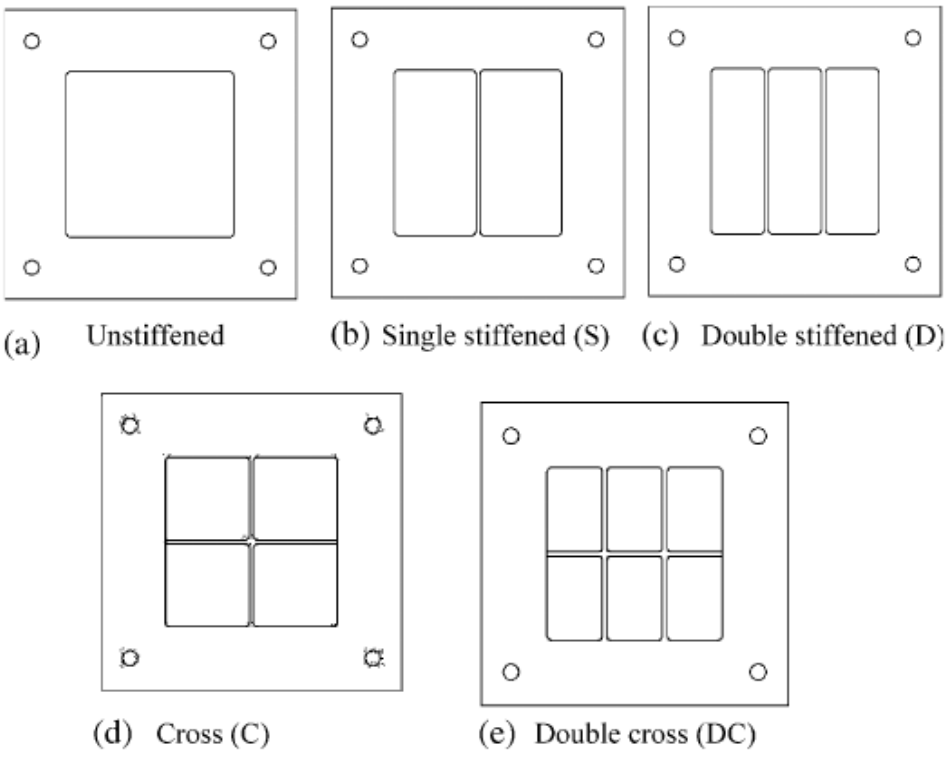

Figure 2.9: Profiles of the plate configurations tested by Langdon *et al.* [36]

The unstiffened plates, showed similar modes of failure to those observed by Jacob *et al.* [35], with the presence of large plastic deformation in the form of a circular dome, with thinning at the centre of the plate for higher impulses [36]. The plates with a single stiffener showed a significant reduction in central deflection but tearing occurred at lower impulses along the stiffener edges. The deformation of the double stiffened plates had mid-point deflections that were similar to the unstiffened plates. At higher impulses these plates displayed tearing failure along the stiffened edges, eventually resulting in petalling at the highest impulses [36]. The cross stiffened plates displayed deformation similar to the single stiffened plates, except that rather than two peaks, four peaks were produced. Like the single stiffener, the cross stiffener reduced the central deflection significantly. At higher impulses tearing was observed which initiated at the centre and progressed outwards along the stiffener edges. The last configuration used the double-cross stiffener, which showed deformation profiles that were a combination of those observed for the single and double stiffeners. The central deflection was similar to the single stiffener plates, with the double stiffeners deflecting outwards. A similar trend as the other stiffened plates was observed as the impulse increased, with thinning and tearing observed along the stiffener edges, followed by petalling at the highest impulse. In general the introduction of a stiffener reduced the deflection but resulted in tearing occurring at lower impulses [36].

Zakrisson *et al.* [37] performed numerical and experimental studies on square plates of size 600 mm × 600 mm, with a circular exposed area of diameter 500 mm. The plates were subjected to near field explosions from cylindrical charges with a length to diameter ratio of 1:3 and a stand-off distance (SOD) of 250 mm. The explosive used was the Swedish army's plastic explosive Sprängdeg m/46, which is made of 86% PETN and 14% mineral oil [37].

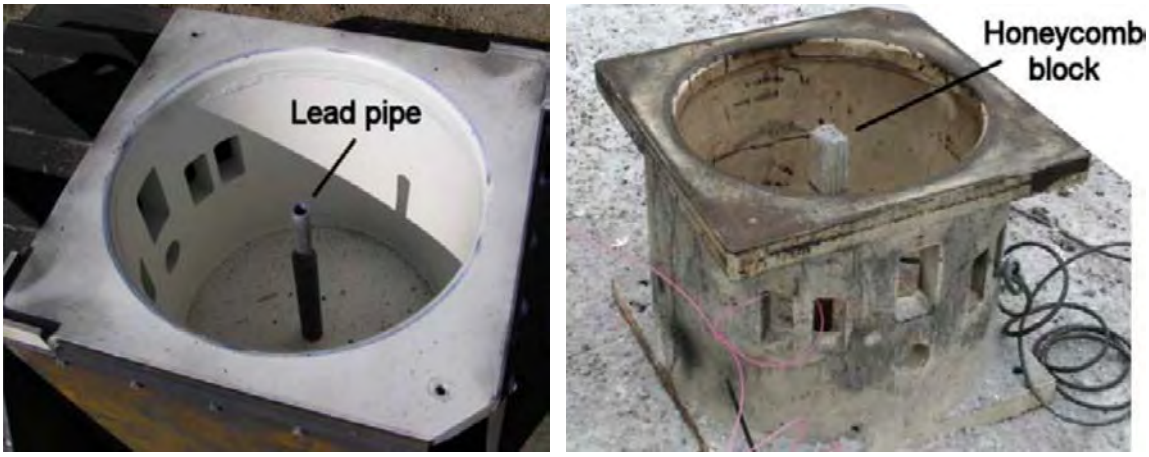

(a) Test setup using a lead pipe (b) Test setup using an aluminium honeycomb block

Figure 2.10: Photographs of two experimental setups with different deflection measuring devices used by Zakrisson *et al.* [38]

Zakrisson *et al.* [37] found that measuring the transient deflection using high speed cameras or other electronic measurements required an large amount of post processing and hence used a lead pipe to measure the transient mid-point deflection of the plate in the first set of experiments

performed. Zakrisson *et al.* [37] determined that the inertia of the lead pipe resulted in an overestimation of the maximum mid-point deflection and hence used an aluminium honeycomb block to measure the deflection. Both deflection devices are shown in Figure 2.10.

The measured deflections were compared with the results obtained using three blast modelling techniques, namely 2D Euler, 3D Euler and CONWEP. This was done to determine how well the three techniques modelled the experiments [37]. The simulations which used either a 2D or 3D Eulerian mesh to model the blast loading showed good correlation with the experiments for the deformation and velocity, while those that used the empirical CONWEP blast function significantly underpredicted the plate deformation and the plate velocity. The impulse for the Eulerian simulations used the FSI force to calculate the impulse and the predicted values were found to be within 1.0 to 1.6% of the experimental results [38].

Jacob *et al.* [39] investigated experimentally the effect of stand-off distance (SOD) on the blast response of 1.9 mm thick mild steel plates with an exposed area of radius 53 mm. The stand-off distance was varied from 13 mm to 300 mm using mild steel blast tubes to set the SOD. The explosives used were cylindrical PE4 charges with 34 mm diameters and masses from 4 g to 15 g. Figure 2.11 shows the arrangement used for the experiments.

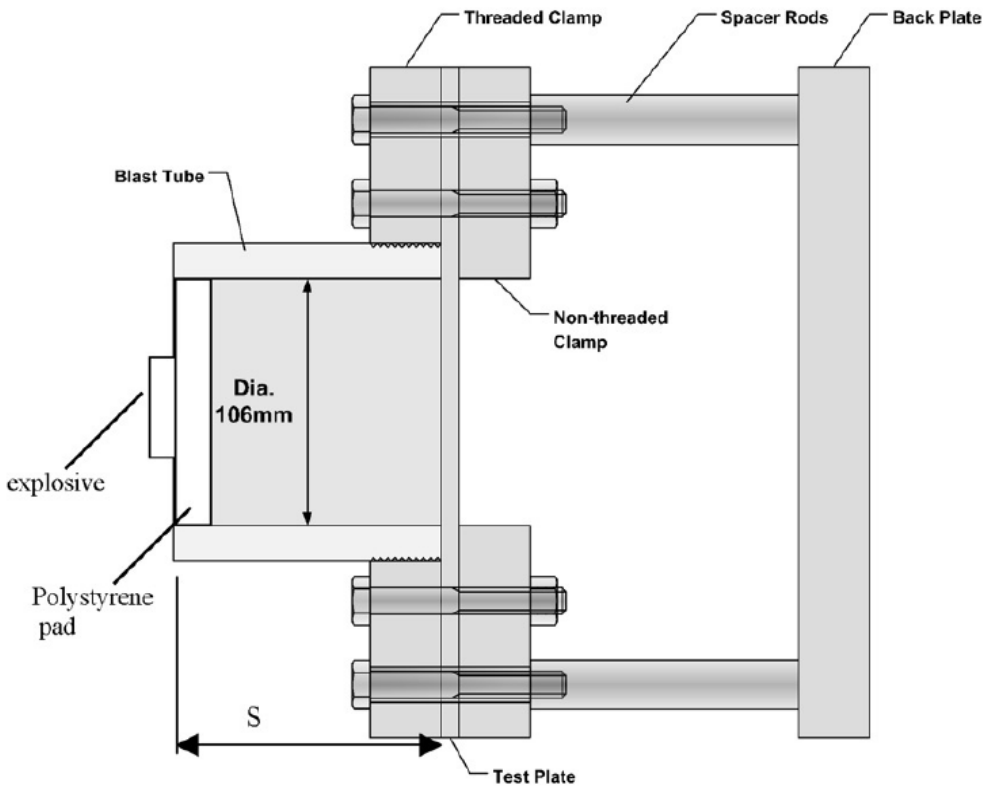

Figure 2.11: Schematic of the explosive and plate arrangement used by Jacob *et al.* [39]

Most of the plates tested displayed large plastic deformation with an increase in mid-point deflection with an increase in impulse. As the stand-off distance increased the change in mid-point deflection for an increase in impulse was less significant. The effects of impulse on mid-point deflection was found to be greatest for stand-off distances between 13 mm and 50 mm. For the larger charge masses (15 g to 17 g) some of the plates also showed partial tearing at the boundary. At stand-off distances greater than 100 mm the deformation profile was a uniform dome, while at lower stand-off distances the deformation profile was in the form of a smaller dome at the centre along with the larger domed profile [39].

2.4 Experimental testing of V-plates

2.4.1 Testing of steel V-plates

Pickering [6] investigated the effects of internal V-angle on the performance of small-scale V-plates subjected to localised explosive loading. Folded and welded V-plates were both tested, to investigate the effects of the manufacturing techniques on the V-plate response. A fixed internal bend radius of 2 mm was used for the folded V-plates to ensure that the V-tip radius did not affect the performance of the V-plates. The V-angles investigated for the folded V-plates were 60°, 90°, 120°, 150° and 180° (*i.e.* A flat plate) while the welded V-plates had a V-angle of 120°. All the plates tested were manufactured from DOMEX-700 MC and were 2 mm thick. Figure 2.12 shows 3D CAD renderings of the V-plates tested by Pickering [6].

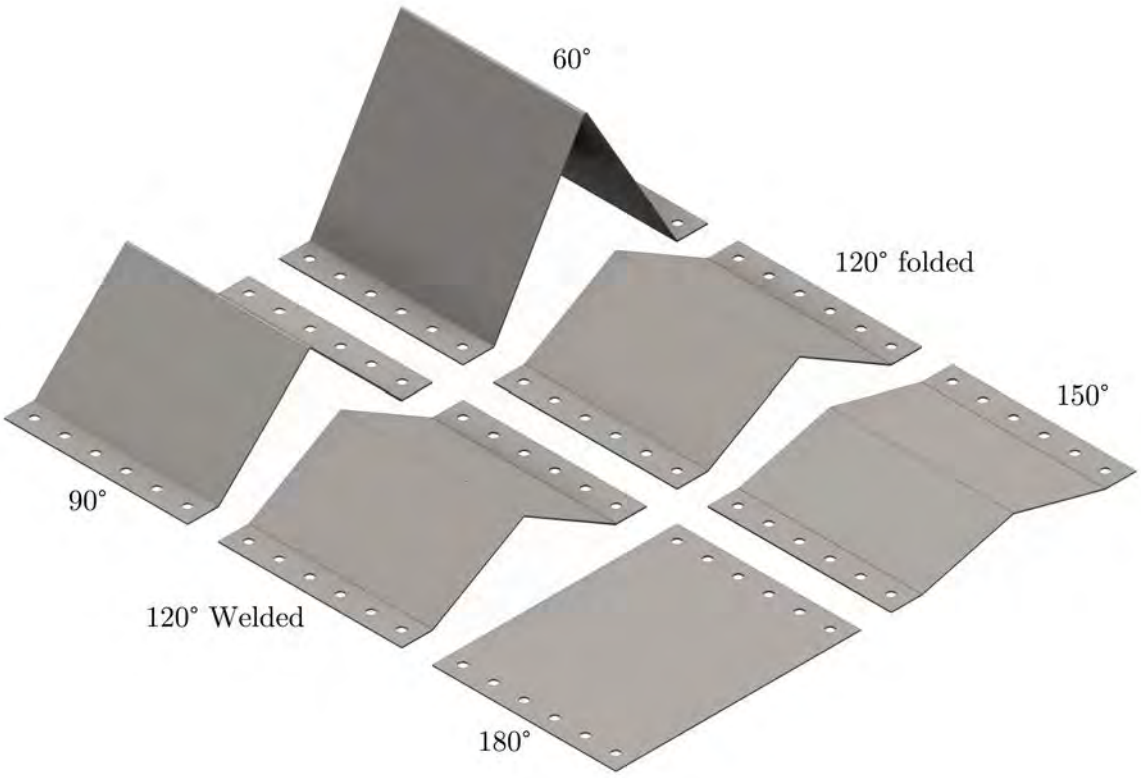

Figure 2.12: CAD renderings of the V-plates tested by Pickering [6]

The explosive used was Plastic Explosive No. 4 (PE4) and the diameter and mass of the charge was scaled based on the TM-57 Anti-Tank mine [40] using Hopkinson-Cranz blast scaling [41]. The width of the V-plates and the Stand-Off Distance (SOD) were scaled down from the width and ground clearance of the Casspir APC MK II [23]. Using these scaling relations, a SOD of 50 mm was obtained. It was noted that the Casspir was designed to withstand a blast of 14 kg of TNT, which corresponded to a charge of 19 g. For the 120° V-plates, Pickering [6] investigated a

range of stand-off distances between 18 and 50 mm. It was found that a SOD of 50 mm resulted in negligible deflections, so a SOD of 34 mm was used for the majority of the tests.

For the range of stand-off distances investigated, Pickering [6] observed that as the stand-off distance increased, the mid-point deflection decreased but the impulse transferred was not affected. It was also found that impulse and mid-point deflection increased as the charge mass increased for a fixed V-angle. The impulse transferred to the pendulum increased as the V-angle increased, and that smaller V-angles resulted in smaller mid-point deflections [42].

While it was observed that the smaller V-angles resulted in smaller impulses and deflections, it was also noted that the centre of gravity of a possible landmine protected vehicle was raised. The V-hull on early APCs such as the Camel, had a sharp V-angle of 43° which reduced space within the cabin for personnel and equipment as well as affecting manoeuvrability of the vehicle [1].

Pickering [6] found that the welded V-plates were significantly worse than the folded V-plates. This was due to the weld bead being of a lower strength than the DOMEX-700 MC, as well as due to imperfections in the welds. Hence from the study it was concluded that the 120° folded V-plate offered the best compromise between impulse transfer and the increase in ride height.

Since it was found that the best performing V-plates resulted in a vehicle with a high centre of gravity, it was determined that it would be useful to investigate if the V-plate designs could be modified to reduce the total height. Hence, Naidoo [7] investigated the performance of shallow V-plates subjected to localised blast loading. The height of the V-plates was reduced by manufacturing them with a flat middle area, defined by a cut-off ratio [43]. The cut-off ratio is defined at the percentage of the height of the original V-hull that is replaced with a flat plate. Naidoo [7] investigated cut-off ratios of 25, 50, 75 and 100% (which represents a flat plate), with V-angles of 60°, 90° and 120° as shown in Figure 2.13.

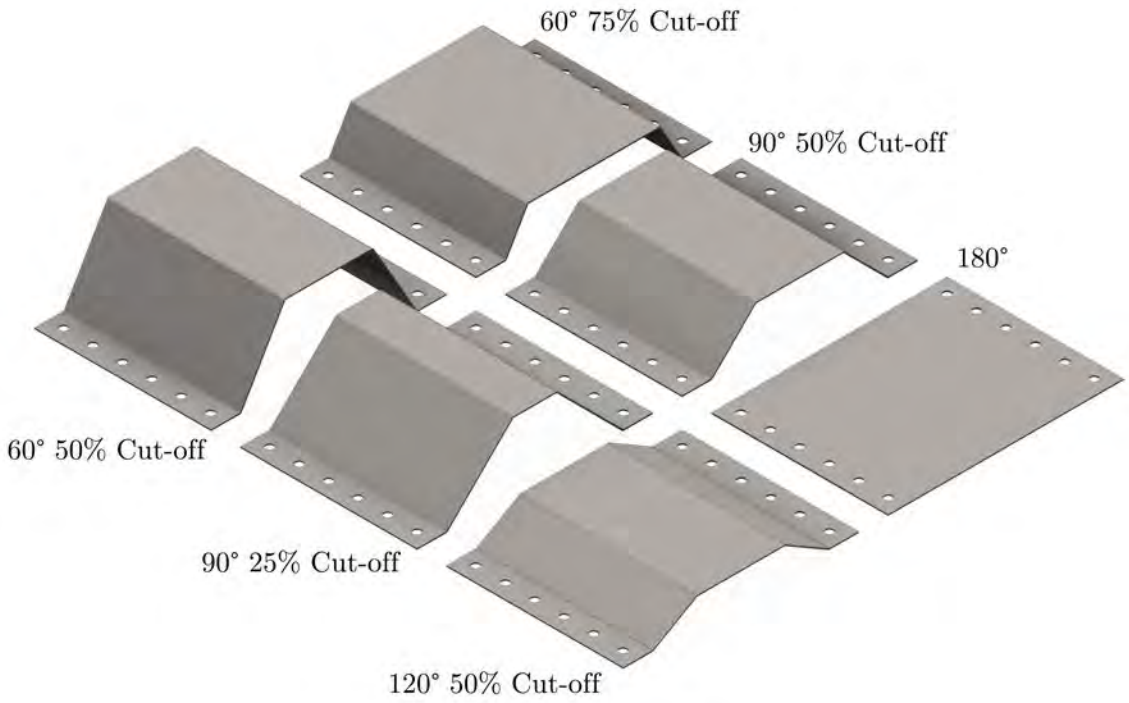

Figure 2.13: 3D CAD models of the shallow V-plates tested by Naidoo [7]

To allow for comparisons to be drawn with previous studies, the V-plates were manufactured from 2 mm thick, DOMEX-700 MC steel plates. The shallow V-plates performed poorly compared to the equivalent V-plates. This was observed with an increase in the impulse transferred and deflection as the cut-off ratio increased. Hence it was determined that removing the sharp tip of the V-plates had a detrimental effect on the impulse deflection characteristics of V-plates and moreover this method of reducing the total height of the V-plates was not suitable [7].

In order to retain the sharp V-tip, but still reduce the total height, Warncke [9] investigated the blast response of modified V-plates subjected to localised blast loading. The V-plates were modified by reducing the total height of the V-plates at the end closer to the clamp frame. Similarly to the test performed by Naidoo [7], cut-off ratios of 25, 50, 75 and 100% were investigated but with a V in the mid section and a flat area near the boundary. A selection of the V-plates tested are shown in Figure 2.14, while Figure 2.15, shows the height reduction that results from increasing the cut-off ratio.

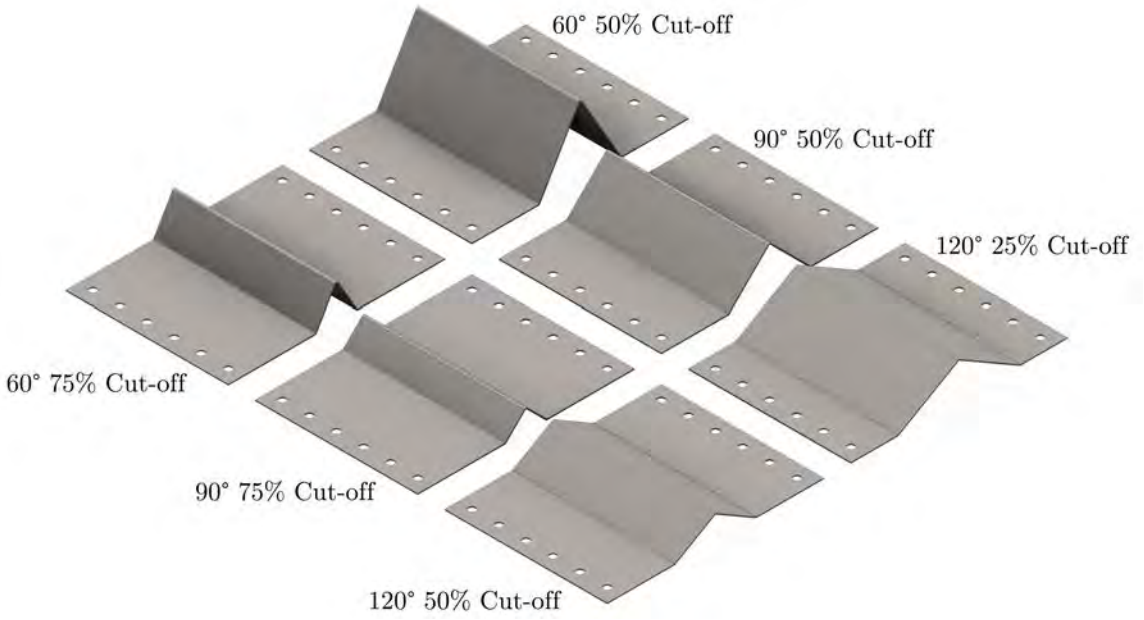

Figure 2.14: 3D CAD renderings of the shallow V-plates tested by Warncke [9]

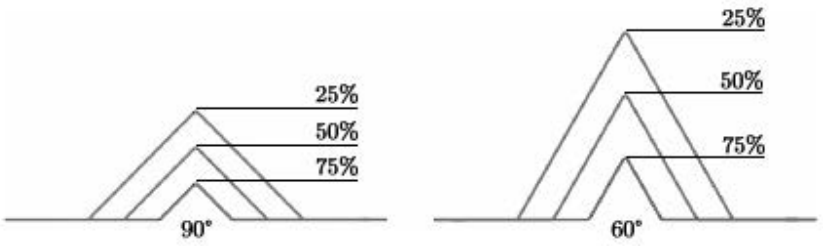

Figure 2.15: Schematic showing the height reduction of the V-plates tested by Warncke [9]

To allow for comparisons with the results of Pickering [6], the geometry of the V-plates, explosive charges, the stand-off distance and the plate material were identical to those used by Pickering [6]. It was observed that an increase in the cut-off ratio resulted in an increase in the impulse transferred to the ballistic pendulum [9], though this effect was less significant than that observed in the plates tested by Naidoo [7]. Additionally it was found that these plates experienced additional deflection in the clamped region due to the reduced stiffness in those areas. Hence it was concluded that this technique was a suitable method for the reduction of the total height of the V-plates, provided the flat regions at the base of the V-plate could be stiffened.

Another study involving V-plates subjected to buried charge explosions was performed by Anderson [44]. The plates tested had V-angles of 90°, 120° and 180°. The V-plates were manufactured by cutting the flat plates and welding the two halves together. The structure was then strengthened with three bracing plates as shown in Figure 2.16. The mass of the flat steel plates was 300 kg, while the V-plates were slightly heavier (3%) due to the bracing. A 625 g high explosive charge was used with a length to diameter ratio of 1/3. The stand-off distance used was 200 mm for the flat plates and 250 mm for the V-plates, while the depth of burial was 50 mm [45].

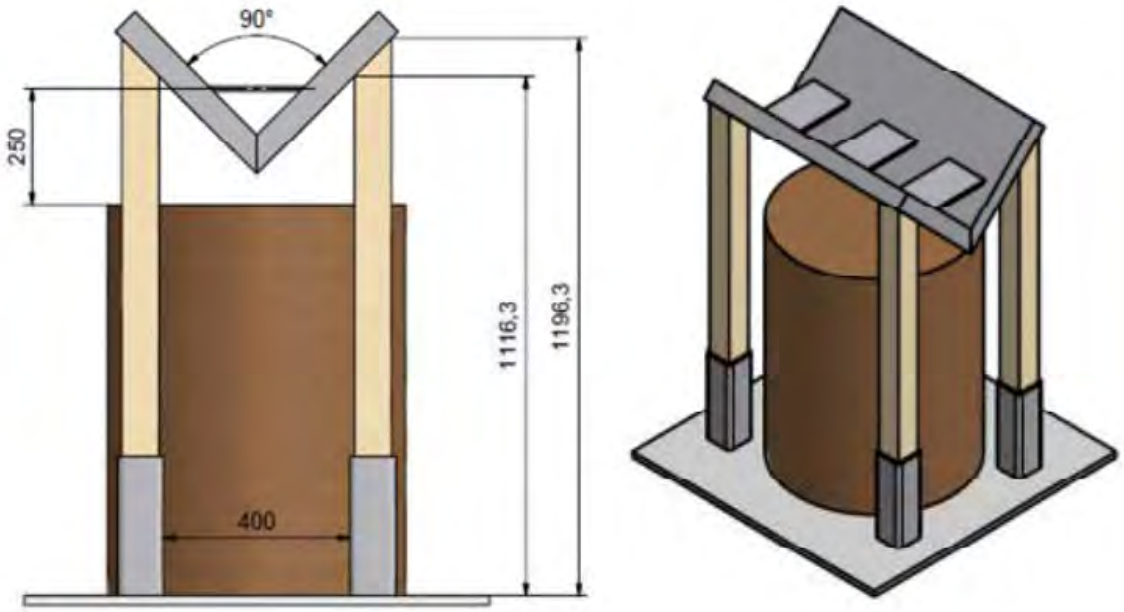

Figure 2.16: Schematic of a 90° V-plate tested by Anderson [44], showing the bracing plates

The velocity of the plates resulting from the blast pressure wave was inferred from two cable-pull potentiometers and an accelerometer placed at the centre of the plates. From these values the momentum (impulse) transferred to the plate was calculated. From the study it was found that, for flat plates, an increase in the sand density resulted in an increase in the momentum transferred to the plate. It was also found that when the stand-off distance was increased the momentum transferred decreased. Finally it was found that when the V-angle was increased the momentum transfer reduced by 40% for the 120° V-plates and 60% for the 90° V-plates [45].

2.4.2 Testing of composite V-plates

Early development of landmine protected APCs with V-shaped hulls, such as the Camel and Rhino [1], utilised a steel V-hull that was attached to the chassis of a production off-road vehicle (such as the Land Rover Defender or Ford F-250). While the steel V-hull provided excellent protection against a landmine explosion it also increased the mass of the vehicle. To ensure that these vehicles had adequate performance capabilities, larger, more powerful engines were required. Another method of improving performance is to reduce weight. This can be achieved by utilising composite materials in the structure of the APC.

Follett [46] investigated the response of steel and composite V-panels to blast loading. V-angles of 90°, 95°, 101°, and 107° were tested. Unlike the studies in references [6, 7, 9, 44], a PE4 charge mass of 240 g and larger stand-off distances (480 mm and 590 mm) were used. The PE4 charge was buried in either dry or wet sand, with a 50 mm depth of burial (DOB). The bend radius of the V-plates was not specified in the results.

It was found that composite panels experienced fibre failure, matrix failure and delamination on the outer surface, while delamination was visible on the inner surface of the panels. The delamination on the inner face was attributed to a compressive wave passing through the material when the pressure wave reached the outer face [46]. It was also found that the composite panels suffered smaller permanent deformations than the steel V-plates, and it was concluded that the composite V-panels were a better choice for V-hull design. It should be noted that the impulse transferred to the test arrangement was not presented in the study. Follet [46] noted that the clamp frame experienced plastic deformation due to the repeated blast loading, and the force transfer to the rest of the structure was not considered.

Hobson [8] investigated the response of composite V-panels to localised blast loading. The objective of the study was to determine if composite panels would provide better blast resistance than steel V-plates. The geometry of the charge and the stand-off distance were chosen to be identical to those used by Pickering [6]. Previous studies [6, 7, 9] had used the clamp frame design shown in Figure 2.17(a). Hobson [8] determined that there would be a high likelihood of the composite panels shearing along the clamped boundaries and used a new clamp frame as shown in Figure 2.17(b), which would reduce the chances of the panels shearing when they were tested.

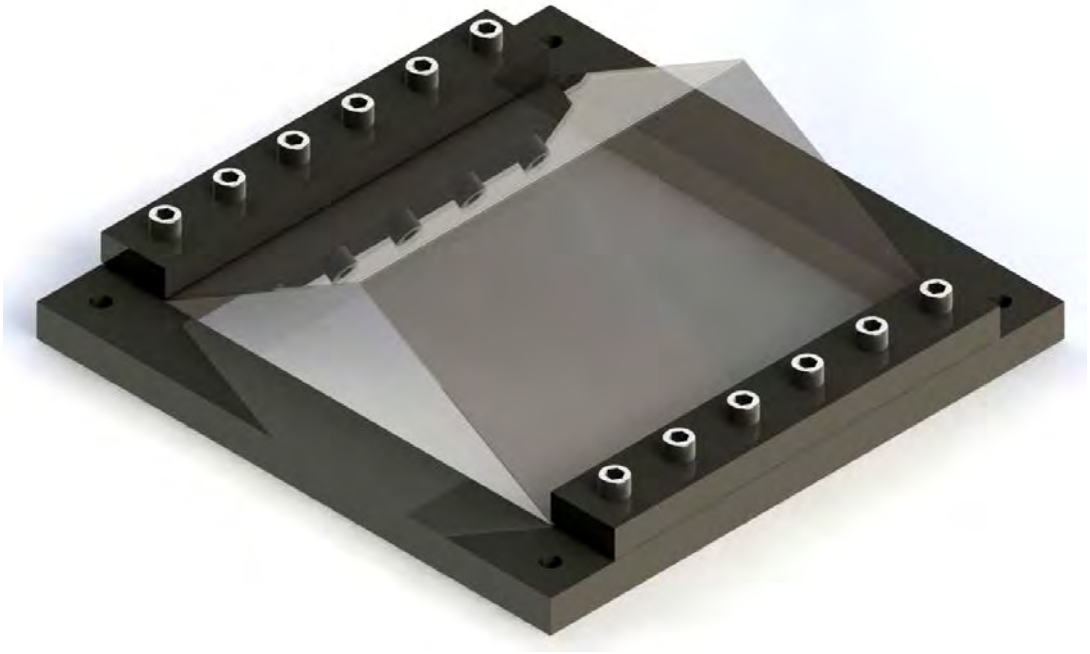

(a) Clamp frame used by Pickering [6],Naidoo [7] and Warncke [9]

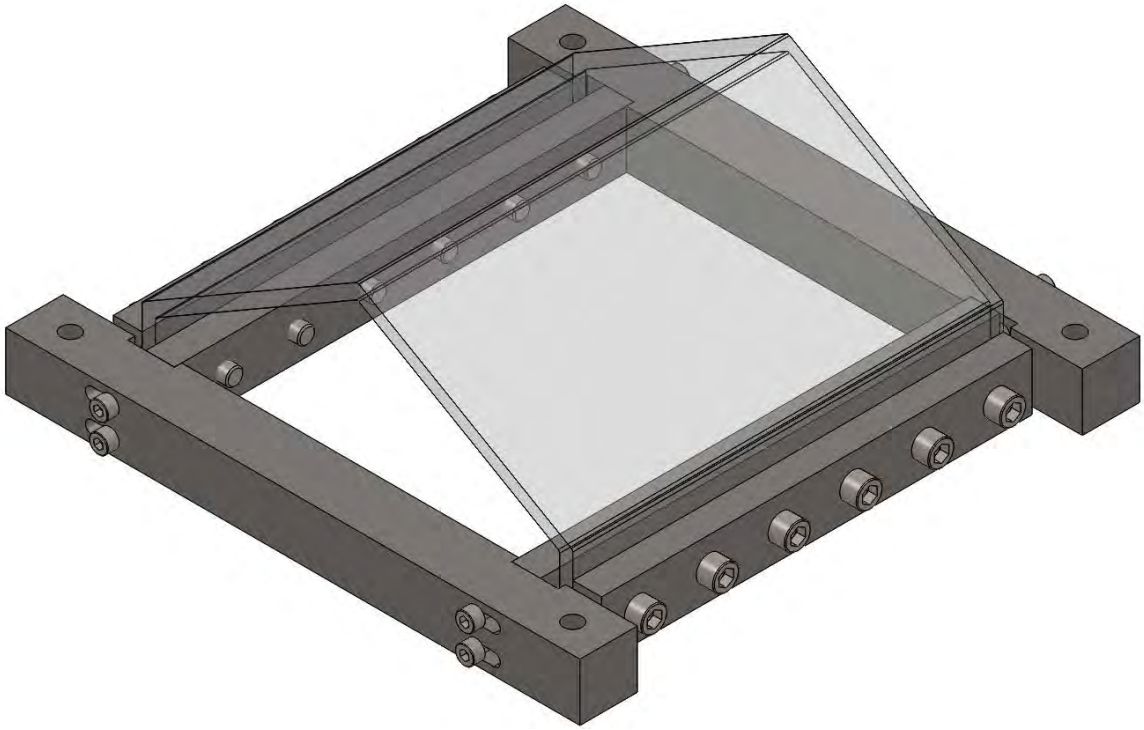

(b) Clamp frame designed for testing composite V-panels [8]

Figure 2.17: 3D CAD renderings of the two clamp frame designs used

The composite panels were manufactured with V-angles of 60°, 90° and 120° and the thickness of the composite V-panels was chosen so that the mass would be identical to the steel V-plates. The steel V-plates were manufactured with a sharp V-tip radius of 4.0 mm, hence it was decided that the composite panels should use the same V-tip radius [8] as shown in Figure 2.18. In the early stages of the manufacturing process it was identified that the chosen V-tip radius was unfeasible as the resin was collecting at the V-tip. Thus the bend radius of the mould was increased from 4 mm to 25 mm. The resulting V-panels had V-tip radii that varied from 25 mm to 51 mm due to imperfections in the moulds and inconsistencies in the manufacturing [8].

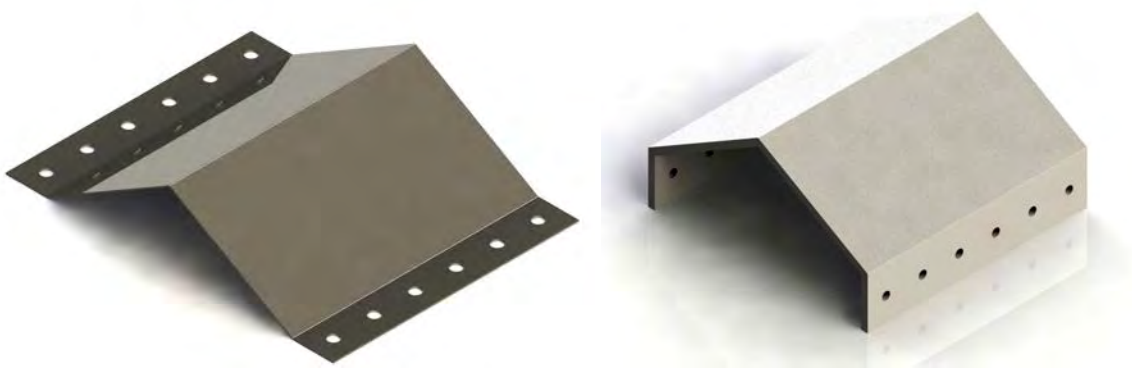

(a) Old design for a 120° V-plate (b) New design for a 120° V-plate

Figure 2.18: 3D CAD models of the V-plates tested by Pickering [6] and Hobson [8]

When impulse transfer was used as a measure of performance, it was observed that the 120° composite and steel V-panels had identical impulse transfer characteristics [8]. However the 60° composite V-panels transferred a greater portion of the impulse to the pendulum. Similar to the experiments reported by Follet [46], Hobson [8] found that the deflections of the composite panels were smaller than that of the steel panels although the composite panels tested showed more damage than that observed by Follet [46]. The panels exhibited delamination, fibre failure and matrix failure on the outer face, while some also suffered from fibre failure on the inner surface [8]. This suggested that these composite panels were not suitable for use in the V-hull of APCs as any personnel or vehicle components located on the inside of the V-hull would be damaged by shrapnel from the torn fibres [8].

From the results it was not possible to determine if the variation in V-tip radii influenced the impulse transfer [8], as the range of bend radii tested was small and was inconsistent. Furthermore, Hobson [8] observed that the impulses obtained for the steel V-plates were lower than those recorded by Pickering [6]. Since the only difference between the two sets of tests was the clamp frame arrangement, it was concluded that the variation in the impulse transferred was due to the clamp frame [8].

2.5 Numerical blast modelling in LS-DYNA

While it may be ideal to perform experimental blast testing, this is not always possible due to availability of testing facilities and the costs associated with manufacturing and testing of each panel. Hence it becomes necessary to use numerical simulations to investigate the blast response of various structures. Additionally it can be easier to optimise specific parameters (such as the material used or the geometry) using a numerical model.

Tabatabaei *et al.* [47] presented a comparison of three methods of modelling a blast load in LS-DYNA. The first technique utilised the CONWEP blast function to model the blast loading, which is a purely Lagrangian approach. The second method used the Multi-Material Arbitrary Lagrangian-Eulerian (MMALE) solver in LS-DYNA, while the third technique involved the coupling of the CONWEP blast function with the MMALE solver [47].

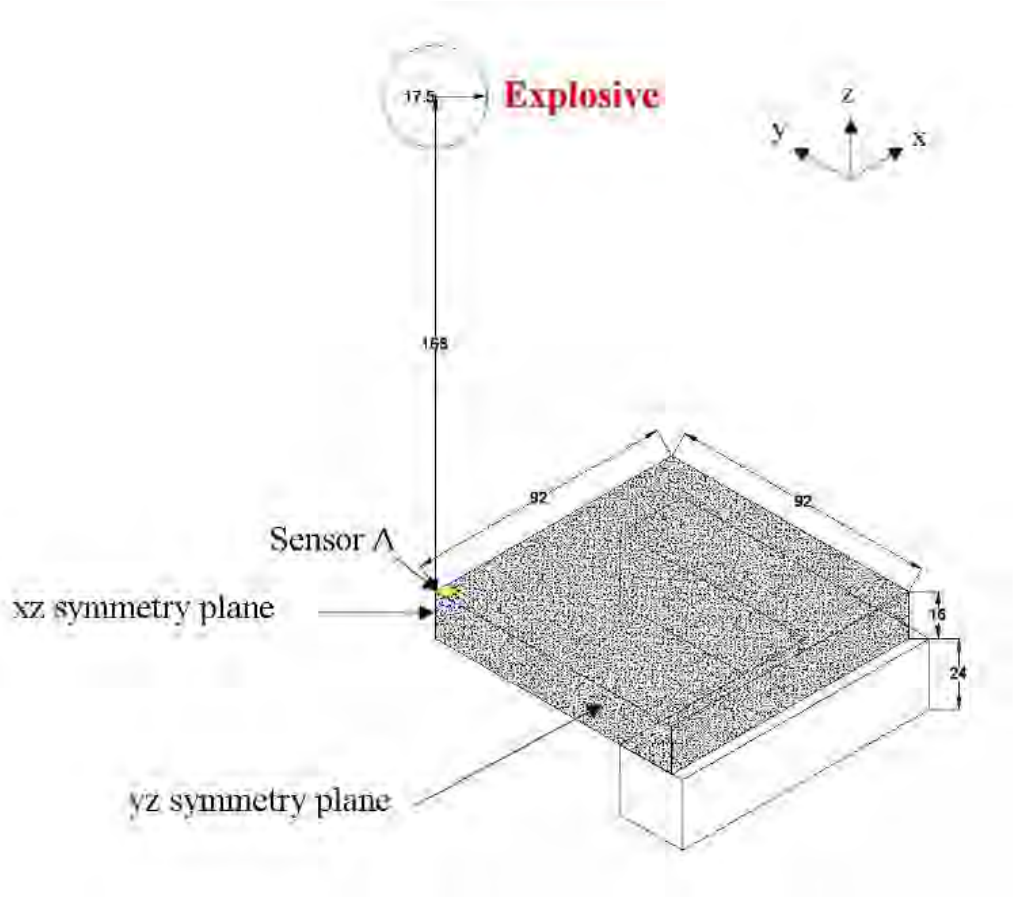

Figure 2.19: 3D schematic of the explosive and plate arrangement used by Tabatabaei [47] (dimensions in cm)

The experiment that was simulated was based on a test that was previously performed, which used a 36 kg cylindrical TNT charge set 1.68 m away from a 1.84 m by 1.84 m square steel reinforced concrete target. Two pressure transducers located at stand-off distances of 7.42 m and 1.68 m measured the incident and reflected pressures. Figure 2.19 show the basic geometry used

in the numerical models. All three models used quarter symmetry and the concrete block was meshed with Lagrangian solid elements. The concrete material model used was the continuous surface cap model (CSCM) while the steel reinforcement was modelled using a piecewise linear plasticity model for steel [47].

The CONWEP blast function was implemented using the LOAD_BLAST_ENHANCED card in LS-DYNA. The ALE simulation used the initial volume fraction card to determine the portion of the air that contained the explosive charge. The explosive charge was modelled using a high explosive burn material model for TNT with a JWL Equation of State. The air was modelled using a null material model and a linear polynomial EOS. In the coupled approach the air mesh was reduced to the region just around the concrete target and the explosive was not modelled. Instead a single element obtained information about the blast wave from the blast equations and transferred it into the ALE mesh. These pressures could then propagate through the air mesh and impinge on the concrete target [47].

The simulation using the CONWEP blast function took the least amount of time to run while the complete ALE simulation took the longest time to run. The CONWEP blast simulation was the only one of the three simulations to capture the pressure from the far field pressure transducer due to the much greater computational costs of the two other techniques. The CONWEP blast simulation underpredicted the peak pressure and overpredicted the impulse at the far field pressure sensor. For the pressure sensor that was closer to the plate, the CONWEP blast simulation also underpredicted the peak pressure. The peak pressures of the full ALE simulation and the coupled simulation were similar to each other, while the coupled simulation had a lower run time [47]. This suggests that the coupled simulation would be an appropriate technique for modelling blast loading, provided the stand-off distance is sufficiently large.

In an attempt to improve the protection of APCs, Williams *et al.* [48] used the CONWEP blast model in LS-DYNA to simulate the explosive loading of flat plates. An ALE model was not used due to the high computational costs associated with the modelling technique. The numerical model was validated using experiments performed on square aluminium and steel targets subjected to blast loading from 6 kg cylindrical C4 buried charges. The simplicity of the CONWEP blast model meant that the sand was not modelled and thus effects such as soil moisture content, depth of burial and soil type were not captured by the model [48].

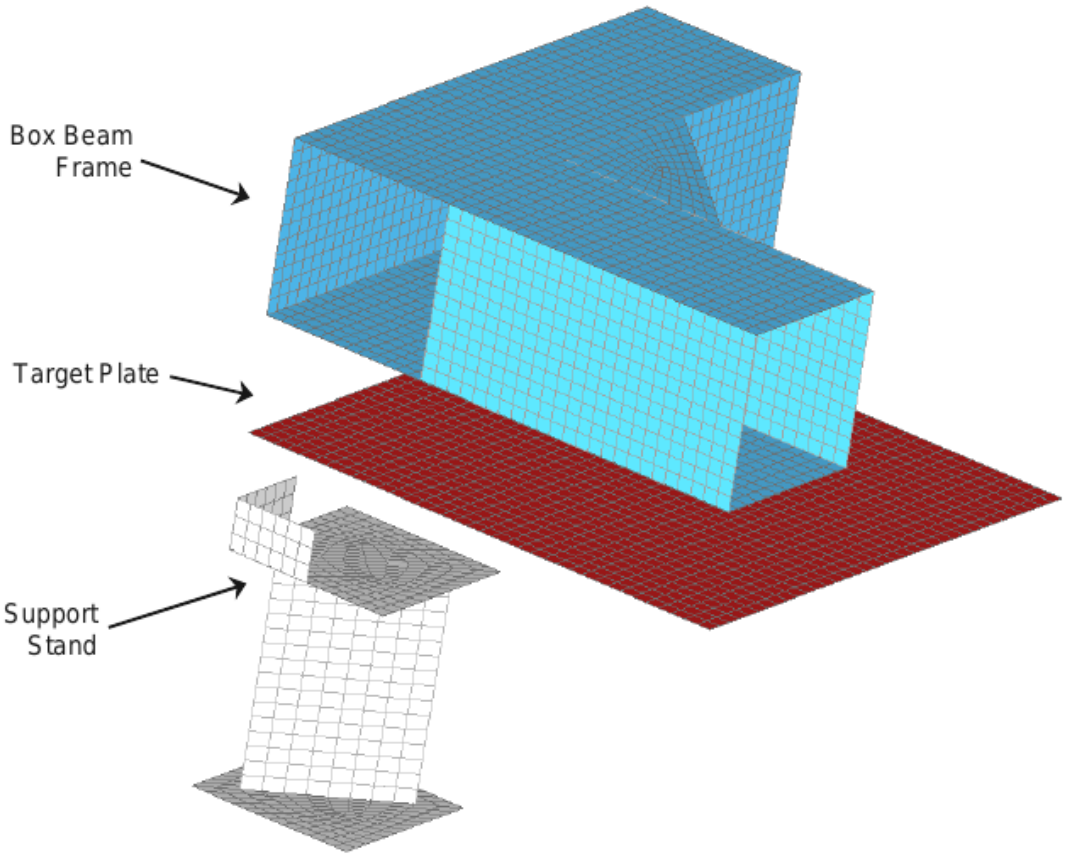

Figure 2.20: 3D schematic of the numerical model used by Williams [48]

The experiments performed used 1.83 m by 1.83 m targets made from 5083-H131 aluminium armour and rolled homogeneous armoured steel. The target plates were supported on four support stands placed 400.6 mm above the ground, with the C4 charge buried at a depth of 50 mm. Additional mass of 10 620 kg was placed on top of the frame to represent the mass of the vehicle. Strain gauges and piezo-pins were used to measure the deformation of the plates. Figure 2.20 shows the meshed finite element model of the target plate, frame and support stand. A quarter symmetry model was used to reduce computational time. Lumped mass was added to the top of the frame to simulate the additional mass on the top of the test rig. The model used shell elements with plastic kinematic material models with different values for the different material used [48].

The results of the study found that for the aluminium plates the model predicted a deformation of 115 mm, while the measured deformation was 298 mm. When the quantity of explosive used in the model was increased, the results more closely matched the experiments. This was due to the fact the effects of the soil were not captured by the model. Hence it was suggested that the CONWEP blast model is suitable for modelling simple blast loading scenarios, but more complicated models involving soil and fragmentation should utilise an ALE model [48].

Ozinsky [49] and Volschenk [50] both used 2D axisymmetric models to investigate the blast loading of structures. Ozinsky [49] investigated the response of stainless steel tubes to internal blast loading from spherical PE4 charges, while Volschenk [50] investigated the response of layered flat plates made of DOMEX-550 MC and DOMEX-700 MC steel. Multi-Material Arbitrary Lagrangian-Eulerian (MMALE) models were used in both sets of simulations, with the explosive modelled using a high explosive burn material model and a JWL EOS. The air was modelled using a null material model and an ideal gas EOS [49, 50]. Ozinsky [49] used elements with a length of 1.0 mm for the ALE mesh and 0.25 mm for the cylindrical tube. The Lagrangian targets were modelled using Johnson-Cook material models and Gruneisen Equations of State (EOS). The experimental and numerical setup used by Ozinsky [49] is shown in Figure 2.21. Pressure tracers were placed at the end of the tube and along the length of the plates. The pressure histories from the tracers were then integrated, multiplied by the associated area and added together to give the total impulse transferred to the ballistic pendulum [49, 50].

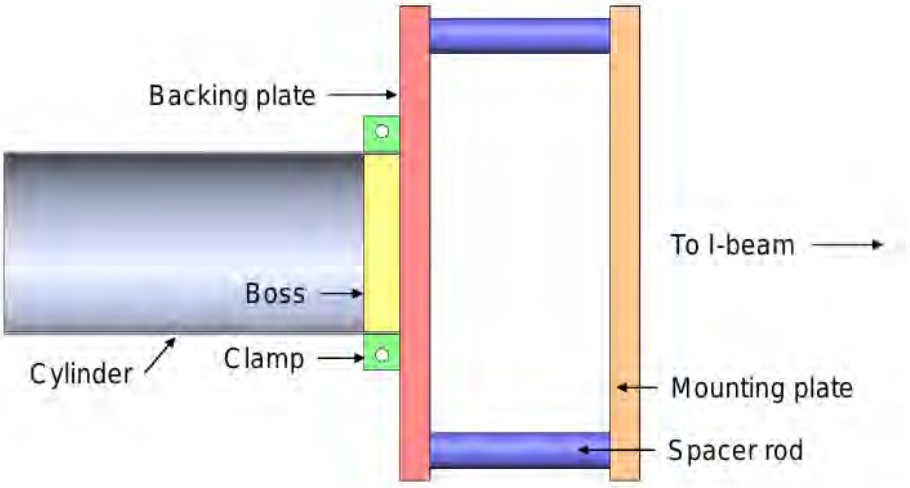

(a) Experimental setup

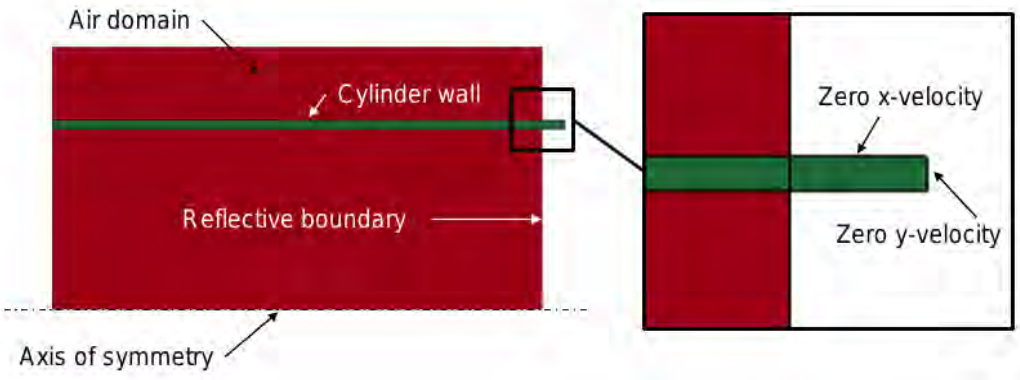

(b) Numerical model

Figure 2.21: Experimental setup and numerical model used by Ozinsky [49] to model the blast loading of cylindrical tubes

Volschenk [50] found that the numerical model accurately predicted the experimental deflection of the layered plates for some of the charge masses and configurations tested. In general it was determined that the pressure predicted by the explosive detonation had been too low for most of the simulations and hence the numerical model underpredicted the impulse transfer [50]. The numerical model developed by Ozinsky [49] showed good correlation with the experiments in terms of deformation for most charge masses. At higher charge masses the model tended to underpredict the deformation of the tubes. For all tests performed, the numerically predicted impulse showed good correlation with the experimentally measured values [49].

Geretto [51] used LS-DYNA to investigate the effects of degrees of confinement on the impulse and deflection of square plates subjected to blast loading in air. Three configurations were investigated, namely unconfined, fully vented and fully confined [51]. Both experimental tests and numerical simulations were conducted and the simulations were performed using LS-DYNA. All the simulations were performed using a quarter symmetry model as shown in Figure 2.22 using an Arbitrary Lagrangian-Eulerian (ALE) formulation to model the explosive detonation, the air and the fluid-structure interaction (FSI) [51]. The advantage of an ALE formulation is that the solid parts for the Lagrangian plate and clamp frames can be included in the Eulerian mesh.

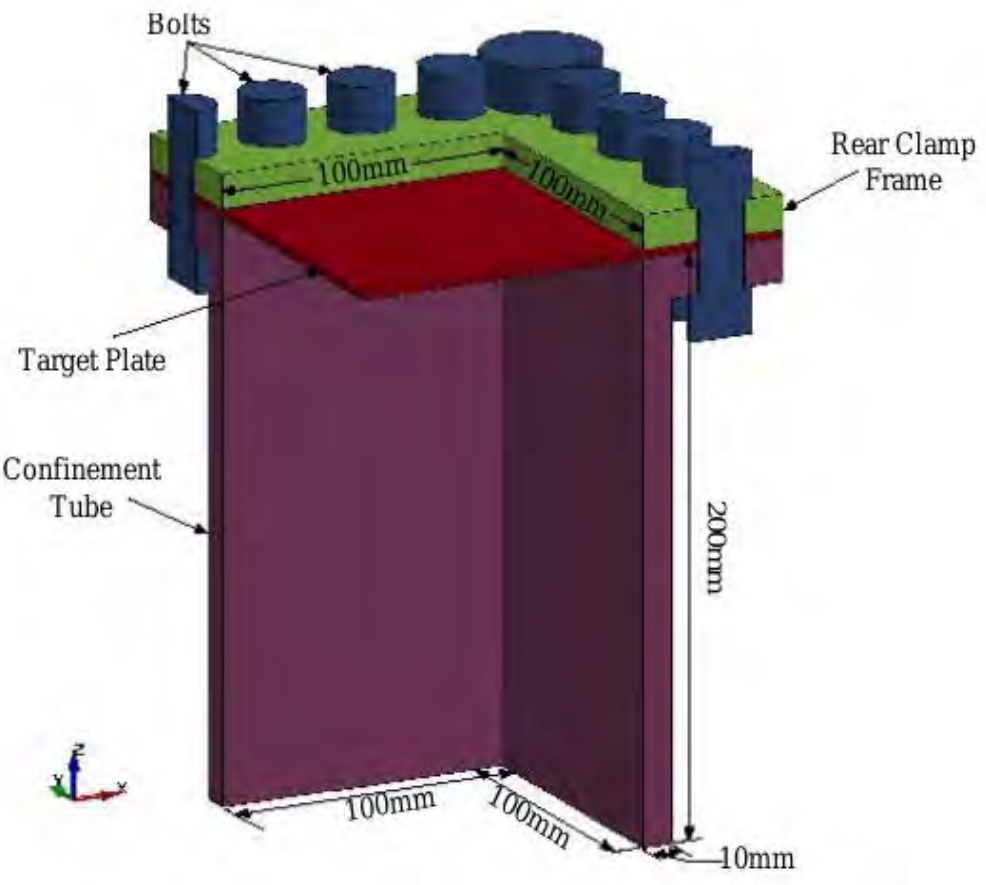

Figure 2.22: 3D view of the numerical model for the fully vented case used by Geretto [51]

The target plates were meshed with four noded uniform Belytschko-Tsay shell elements while the clamp frames were modelled using solid elements. The air mesh was modelled using uniform solid ALE elements. The experiments performed used a spherical explosive charge, hence an identical charge was used in the simulations. A null material model and a linear polynomial Equation of State (EOS) were used to model the air, while a high explosive burn material model and a Jones-Wilkins-Lee (JWL) EOS were used to model the explosive. By performing two sets of mesh convergence studies Geretto [51] found that the optimum mesh length was 1.0 mm for the target plates and 2.0 mm for the air block. The blast simulation was modelled through three phases. These were the pre-loading of the bolts, the blast loading and the unloading. In order to reduce computational time, the air mesh was switched off during the unloading and pre-loading phases. A 3D view of the model used by Geretto for the fully vented case is shown in Figure 2.22. Both the transient and final mid-point deflections and deformation profiles obtained from the simulations were found to be very similar to the results obtained from the experiments, although the numerical model was found to slightly underpredict the peak pressures [51].

In general an MMALE simulation is more computationally costly than a CONWEP blast simulation. This is due to the inclusion of the air and explosive in the MMALE model. The MMALE simulations do show better correlation with experimental tests if the models are correctly setup, while the CONWEP simulations tend to underpredict both impulse and deformation.

2.6 Numerical simulations of the blast loading of V-plates

2.6.1 Modelling the loading and V-plate response following explosive detonation in ANSYS AUTODYN

Showichen [52] used ANSYS AUTODYN to simulate the performance of armoured vehicle hulls to a landmine explosion. Three hull configurations were investigated: a flat single floor, flat double floor and V-hull bottom (with a V-angle of 160°). Two of these configurations are shown in Figure 2.23. Due to difficulties in finding the thicknesses of the floors used on armoured vehicles, three values were tested (*i.e.* 10, 20 and 30 mm). The simulations used a 10 kg hemispherical TNT charge, with a stand-off distance between 300 and 600 mm which corresponds to the mass of the largest AT-mines and the variation in ground clearance of most MRAPs respectively. A rolled homogeneous armoured steel was used for the plates, with a Johnson-Cook material model [52].

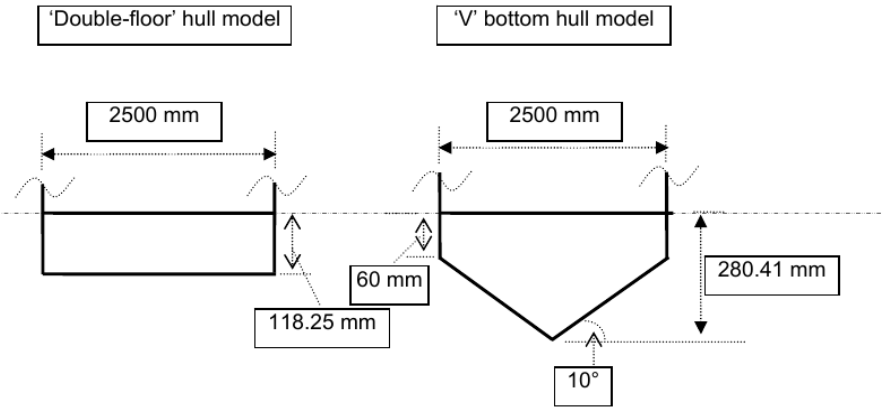

Figure 2.23: Side profiles of the double hull and V-hull arrangements investigated by Showichen [52]

The explosive detonation was simulated using a 2D axisymmetric model in order to reduce the computational time. The pressure profile was mapped into a 3D quarter symmetry model which included the various plate models. The edges of the plates were fully constrained and flow out boundary conditions were used on the outer faces of the air block [52].

The results showed that the V-hulls experienced the smallest deformations but higher accelerations, when compared to the other two configurations. The higher accelerations were determined to be due to the outer hull impacting the inner hull, and hence it was also concluded that if this impact could be prevented the accelerations of a double floor hull and V-shaped hull would be lower than that of a single flat hull of equivalent mass. Hence it was found to be more beneficial to add a second hull and introduce an air gap between the two hulls, rather than increasing the thickness of a single hull [52].

Pickering [6] also used AUTODYN to simulate the localised blast loading of steel V-plates. A quarter symmetry model was used, while the geometry of the V-plates and explosives was based on the experiments performed previously (See Section 2.4). A Johnson-Cook material model for DOMEX-700 MC steel was used for the plates. Similarly to the work performed by Showichen [52], A 2D axisymmetric model was used to model the detonation to reduce the computational costs of each simulation. The blast wave was then mapped from 2D to the 3D quarter symmetry model. Another simplification that was made to the model was to use a smaller air block with dimensions of 100 mm x 100 mm for the simulations. Finally the clamped region of the plate was modelled with an encastre boundary condition [42]. Figure 2.24 shows the numerical model used by Pickering [6].

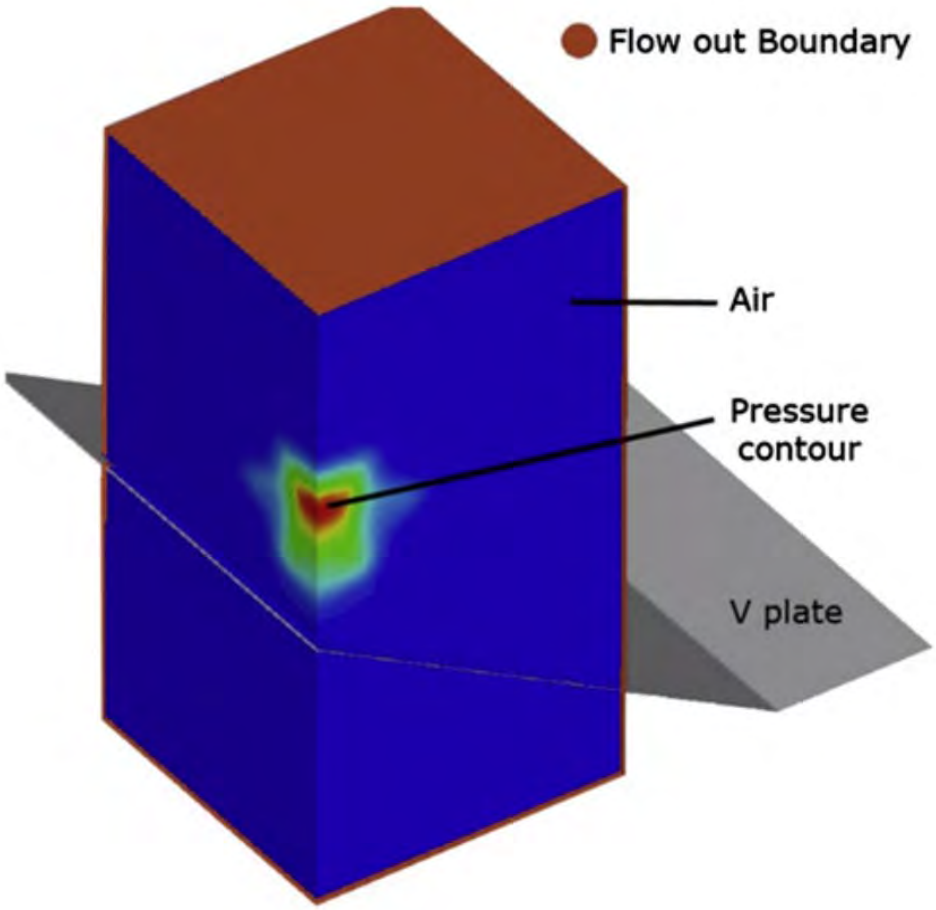

Figure 2.24: 3D view of the numerical model used by Pickering [6]

The mid-point deflections were recorded for each of the simulations. These values were validated by comparing them with the results of the experiments. It was observed that only one third of the numerically predicted deflections matched with the experiments, while in general the numerical model under-predicted the mid-point deflection of the V-plates. These variations were attributed to the material properties used for DOMEX-700 MC and the asymmetric nature of the loading during the experiments [42].

Follett [46] modelled the blast loading of composite V-plates using ANSYS AUTODYN. Unlike Pickering [6], the explosive charge was buried in sand and hence the both air and sand were modelled. Once again, a 2D axisymmetric model was used to model the detonation of the explosive in the sand. For the flat plates tested, the entire simulations were modelled using a 2D axisymmetric environment. A 3D quarter symmetry model was used for the V-plates, while the pressure wave was mapped from 2D to 3D. The V-plates were modelled with shell elements and the composite material was modelled as 40 layers that were 0.5 mm thick, while the steel material was modelled as a single layer that was 5 mm thick [46].

The displacements predicted by the V-plate simulations were found to be significantly lower than those measured in the experiments [46]. The flat plates showed better correlation with the experiments though the predicted deflections were generally lower than the experimental values. Follet [46] did not report on the impulse transfer characteristics of the V-plates as these were not measured in the experiments.

2.6.2 Modelling of V-plate response to blast loading in ABAQUS

ABAQUS was used by Paykani *et al.* [53] to model the blast loading of V-plates. The V-plates had a V-angle of 120° and were modelled using solid elements with a mesh biased towards the centre (where most of the deformation was expected to occur). The V-plates were modelled using 53332 linear tetrahedral elements, with six elements through the thickness, while the cores were modelled using 31616 linear hexahedral elements [53]. A Johnson-Cook material model for DOMEX-700 MC steel was used, with material parameters identical to those used by Chung Kim Yuen *et al.* [42]. The V-plates tested were created as a sandwich type structure with multiple layers. An example of the V-structure is shown in Figure 2.25. Steel was used for the outer layer (labelled "1" in Figure 2.25) (which was exposed to the pressure loading of the blast wave), while aluminium was used for the innermost layer in all the simulations (labelled "4" in Figure 2.25) (furthest from the blast wave). The two inner layers (labelled "2" and "3" in Figure 2.25) were some form of energy absorbing material (such as aluminium foam, balsa wood or a honeycomb).

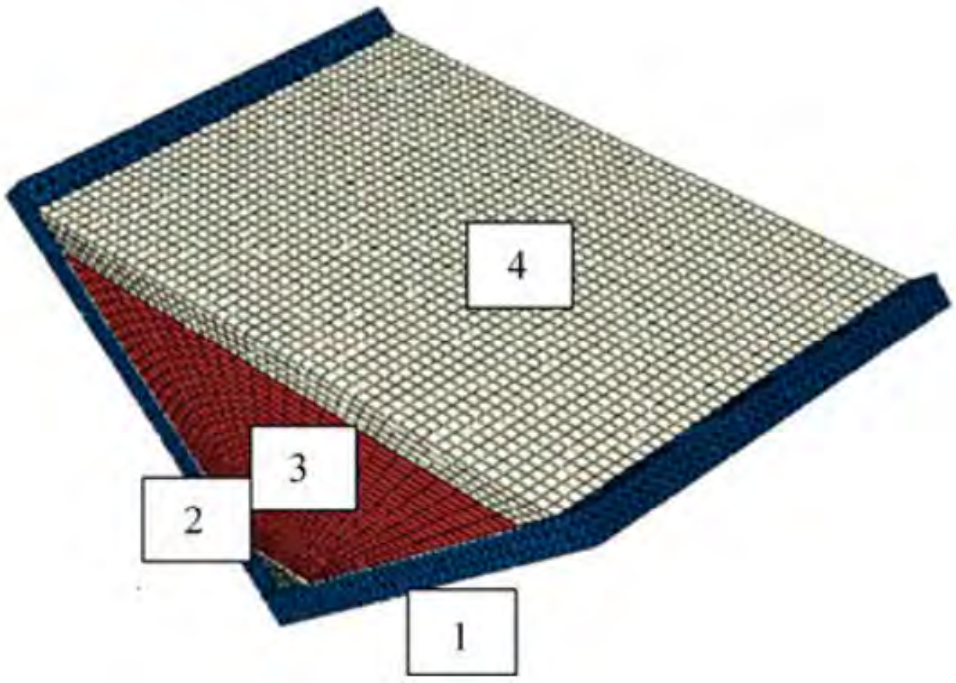

Figure 2.25: 3D schematic of the meshed V-structure used by Paykani [53] and Saeimi-Sadigh [54]

Unlike the previous work performed in AUTODYN, the explosive and detonation were not modelled. Rather the blast wave was modelled as an impulsive load, with a peak pressure of 5436 MPa [53]. This approach did not require an Eulerian mesh, which reduced computational cost. However the reflected pressure waves were not captured by this model, meaning that the model may have under-predicted the deflections.

The analysis was performed by comparing the permanent deformations, stresses and strains for each configuration. It was determined that including the energy absorbing layers resulted in

lower deformations and lower stresses in the outer steel plate. Finally it was found that while balsa wood and the honeycomb had no significant effect on the performance of the V-hull, the aluminium foam was able to improve the blast mitigation characteristics of the V-plates [53].

Saeimi-Sadigh *et al.* [54] continued the work conducted by Paykani *et al.* [53], by investigating the effects of changing the thickness of the V-plate (used for the outer layer) on the deformation characteristics of the V-shaped structure. V-plates with thicknesses of 1, 1.5 and 2 mm were tested. The testing arrangement used was identical to that used by Paykani [53]. The best energy absorbing material from the previous study was found to be aluminium foam, hence it was used for this study. As expected, the study found that as the thickness of the V-plates was increased, the deformation of the plates decreased.

2.6.3 Modelling of V-plate response to explosions in CTH

Anderson [44] modelled the experiments presented in Section 2.4 using the multi-material Eulerian wave-code CTH. Initial simulations were performed for the flat plates with a 2D axisymmetric model as shown in Figure 2.26. Following this 3D simulations using half symmetry were performed for the V-plates and finally 3D simulations were also performed for the flat plates. By performing a convergence study, Anderson [44] determined that an element length of 10 mm was suitable for the Eulerian mesh for both the 2D and 3D simulations.

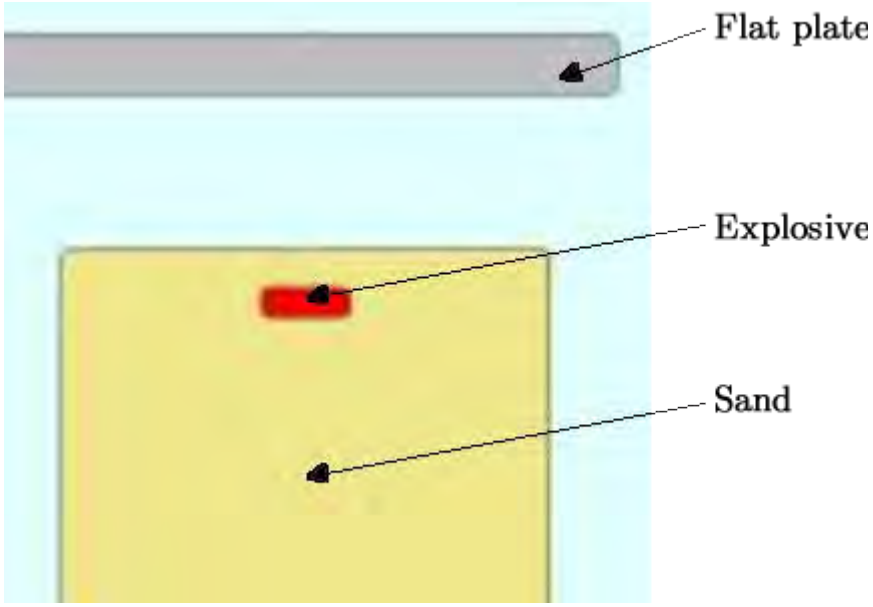

Figure 2.26: 2D axisymmetric numerical model of a flat plate used by Anderson [44]

Anderson [44] found that the simulations using flat plates showed good correlation with the experiments. The impulses were observed to be slightly greater than the experimental values. The simulations over-predicted the momentum transferred for the 90° V-plates and 120° V-plates, by 61% and 43% respectively, although the trends for the V-plate simulations were similar to those observed in the experiments. Hence it was concluded that the model developed was suitable for testing flat plates, and would be conservative for V-hull design and hence would result in heavier V-hulls [45].

2.6.4 Modelling of blast loading and response of V-plates in LS-DYNA

Warncke [9] used LS-DYNA to model the localised blast loading of V-plates. The simulations were based on experiments that had been performed (described in Section 2.4), hence the same geometries of the V-plates and the explosive charges was used. The blast loading was modelled using an Arbitrary Lagrangian-Eulerian (ALE) formulation. The steel V-plates were modelled with a Johnson-Cook material model for the DOMEX-700 MC [9]. The parameters used for this material model were identical to those used by Pickering [6]. The air was modelled as an ideal gas, with a linear polynomial Equation of State (EOS). The explosive was modelled using the properties of PE4, with a High Explosive Burn material model (available in the LS-DYNA material library) and a Jones-Wilkins-Lee (JWL) EOS.

The experiments were modelled using quarter symmetry, while the V-plates were fully constrained along the clamped boundary. Shell elements with an uniform element length of 1 mm were used for the V-plates, while the air block was modelled using solid ALE elements with a length of 2 mm. The numerical model used is shown in Figure 2.27. Unlike the previous work performed in AUTODYN [6, 46, 52], a 3D model was used for the entire simulation including the detonation.

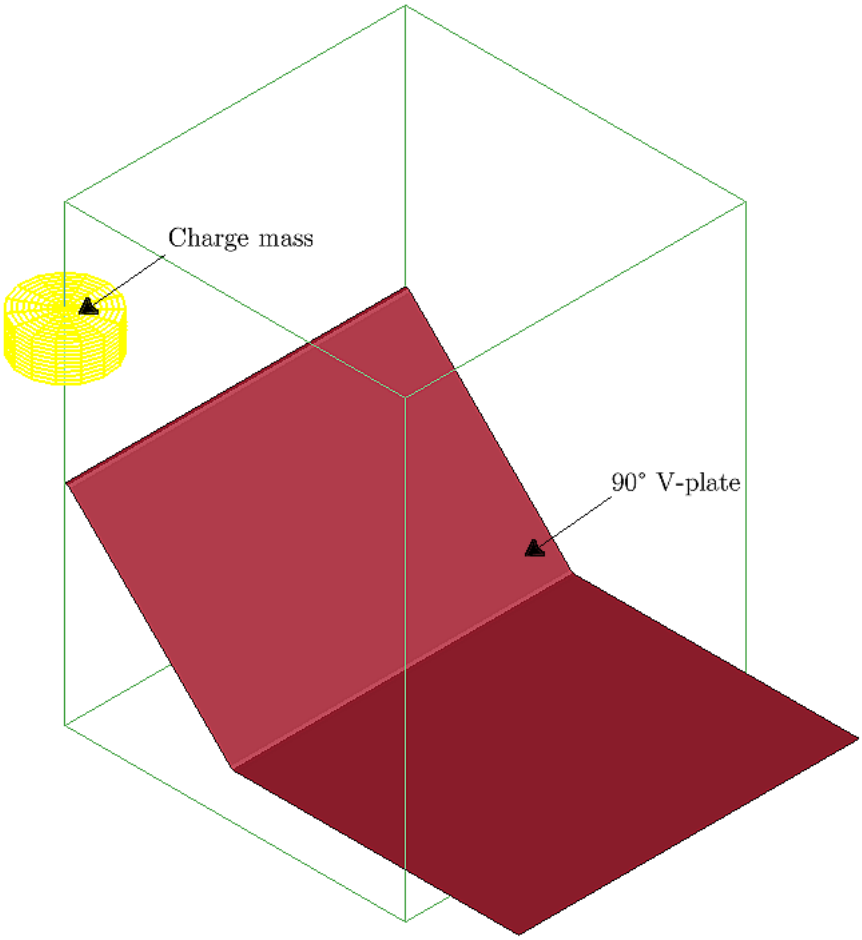

Figure 2.27: 3D view of the numerical model used by Warncke [9]

Warncke [9] found that the numerical model was able to predict the deflections with reasonable accuracy. In general, the predicted deflections were within 2 mm (one plate thickness) of the experimental deflections, though the predicted impulses were approximately 40% lower for all the numerical simulations that were performed, when compared to the experiments. The significantly lower impulses were attributed to a simplified clamping model and the smaller air mesh not covering the whole plate surface [9].

Barsotti *et al.* [55] used both Smooth Particle Hydrodynamics (SPH) and an Arbitrary Lagrangian-Eulerian (ALE) formulation to simulate the experiments performed by Anderson [44]. The ALE simulations used quarter symmetry, as shown in Figure 2.28, and the mesh was biased in the region of detonation. The tube, ground plate and target plate were modelled as Lagrangian parts, while the air, soil and explosive were modelled as Eulerian parts using the initial volume fraction geometry card in LS-DYNA. The soil was modelled using the soil material model in LS-DYNA, while the explosive was modelled using the High Explosive Burn material model and JWL EOS. A piecewise liner plasticity material model was used for the tube and a rigid material model with the properties of mild steel were used for the target plate [55].

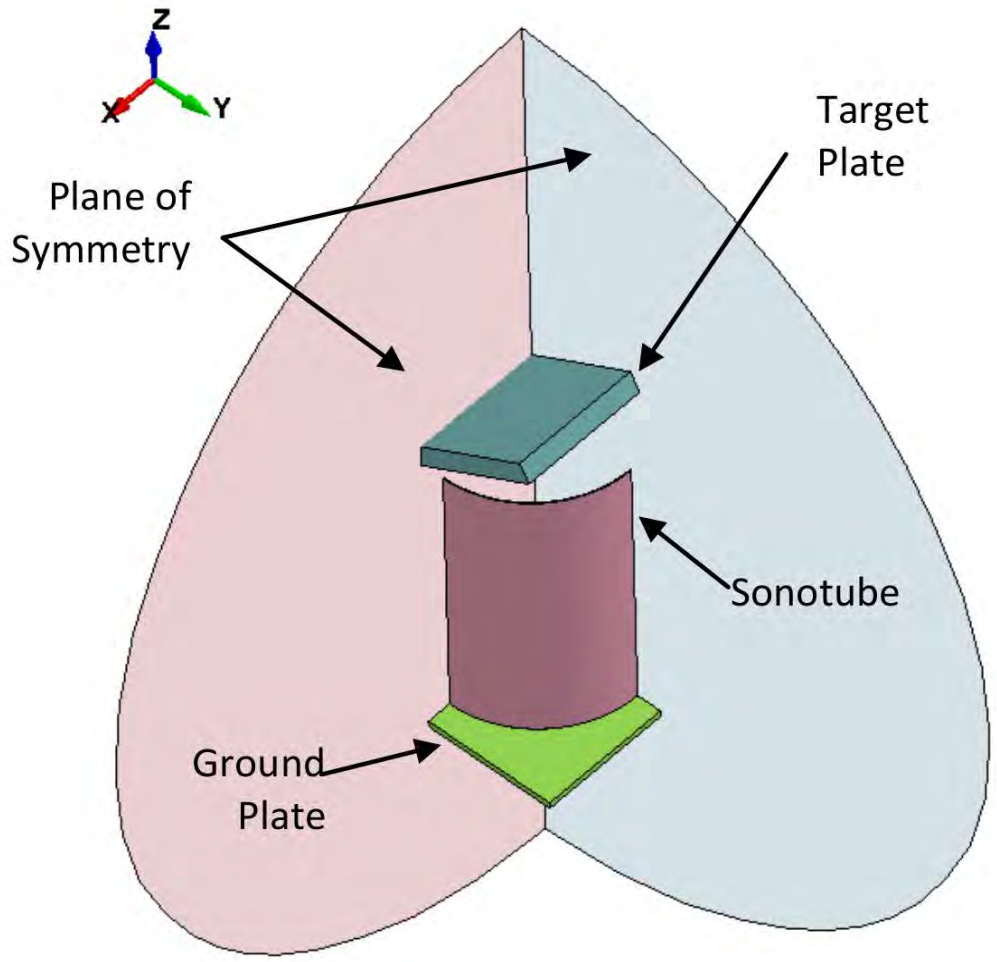

Figure 2.28: 3D quarter symmetry schematic of the ALE model used by Barsotti [55]

The time step used for the detonation process was limited to 10% of the calculated time step to ensure that the detonation process was correctly captured. It was then increased to 67% of the calculated time step for the explosive-plate interaction phase [55]. The momentum calculated from the simulations was compared with the results of the simulations performed using the CTH Eulerian wave code by Anderson [44]. It was found that the ALE simulations underpredicted the momentum, although the predicted momentum was closer to experimental values, than the simulations performed using the CTH Eulerian wavecode. The lower impulse values were attributed to material leakage in the coupling of the Lagrangian and Eulerian parts and losses during the advection cycles of the Eulerian calculations [55].

Following the ALE simulations, SPH simulations of the experiments were also performed. SPH particles were used to model the soil and the explosive, while the plate was modelled as a Lagrangian solid as shown in Figure 2.29. To avoid difficulties associated with boundary conditions, no symmetry was used for the SPH simulations. The tube was not modelled as it was found to have no significant effect on the simulations performed with the ALE model. The material models used for the soil, explosive and target plate were identical to those used in the ALE model. The time steps used for the detonation and plate interaction phases were also identical to the ALE simulations [55].

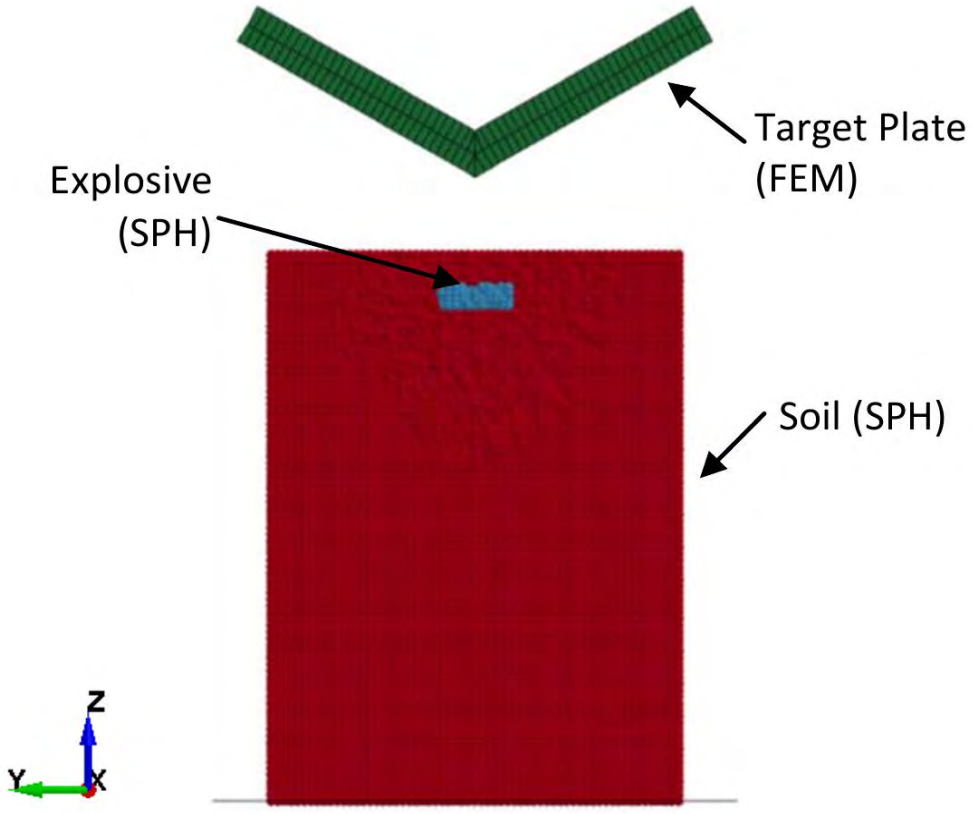

Figure 2.29: Side view of the SPH model used by Barsotti [55], showing the explosive, soil and target plate

Unlike the ALE simulations, the SPH simulations overpredicted the impulse transferred for both the 90° and 120° V-plates, by 18% and 14% respectively. The predicted values were also closer to the experimental values than both the simulations performed by Anderson [45] using the CTH wavecode and the LS-DYNA ALE simulations [55].

2.6.5 Summary of V-plate simulations

Simulations of the response of V-plates were performed in various commercial codes including ABAQUS, ANSYS AUTODYN and LS-DYNA. In ABAQUS, the blast wave was treated as a pressure load and applied to the V-structures via a load curve. In AUTODYN, the detonations were modelled using 2D axisymmetry and then the pressure waves were mapped into 3D before interacting with the plates. In LS-DYNA, MMALE models were used to model the air and explosive, while the plates were modelled with shell elements. Both AUTODYN and LS-DYNA models were capable of capturing reflected pressure effects.

Chapter 3

Rigid V-plate experiments

This chapter provides details of the experiments performed on rigid V-plates, the rigid V-plate design, the test procedures and results. The term rigid V-plate is used herein to refer to thick V-plates which will undergo insignificant deformation during blast loading.

3.1 Rigid V-plate design

The rigid V-plates were designed to prevent deformation when subjected to blast loading. The aim of the experiments was to provide impulse values to validate the numerical simulations.

Three plates were manufactured with internal angles of 60°, 90° and 120° and were designed based on the geometry of the panels tested by Hobson [8]. Each rigid V-plate was welded from 6 individual parts, a base plate (which was bolted onto the ballistic pendulum via four mounting holes), two side pieces (which represented the clamped region), two angled plates and a supporting brace. A three-dimensional CAD drawing of the 120° rigid V-plate is shown in Figure 3.1, while Figure 3.2 shows a photograph of the manufactured V-plates. A 0 mm V-tip radius (that is, a sharp tip) was specified to reduce the machining time.

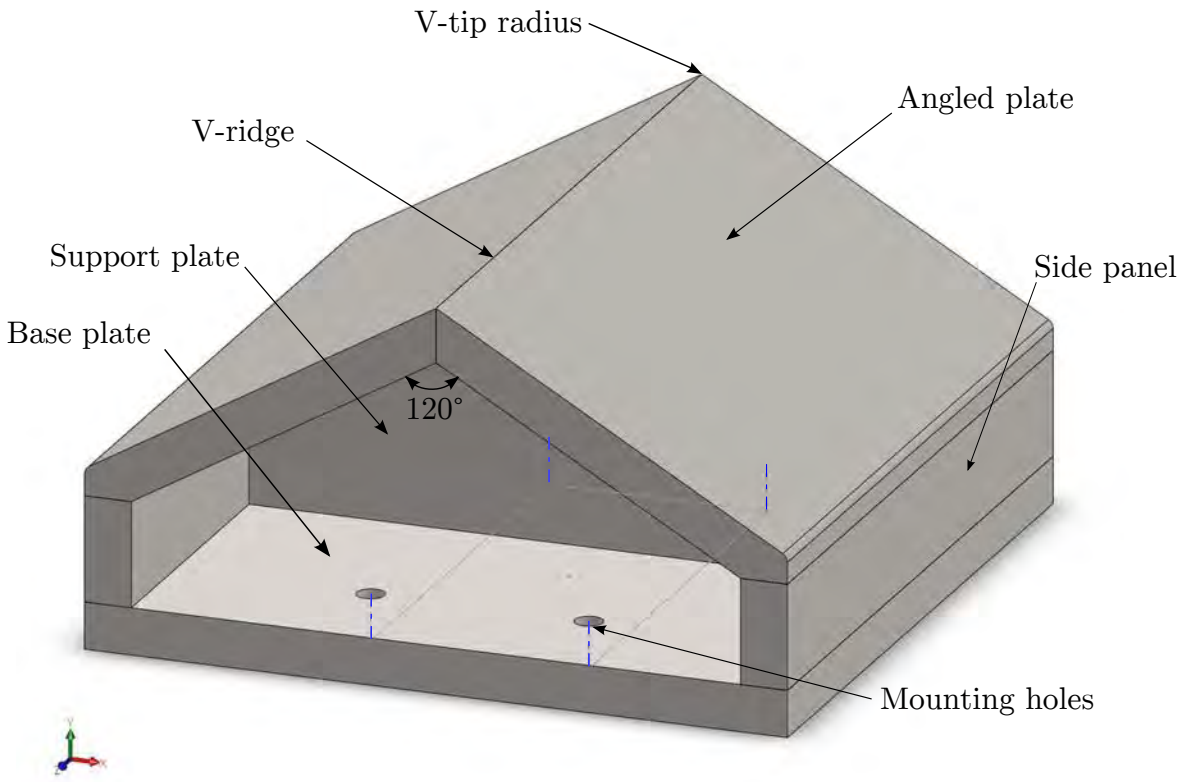

Figure 3.1: Three-dimensional CAD view of the 120° rigid V-plate

(a) 60° (b) 90° (b) 120°

Figure 3.2: Photographs of the manufactured V-plates

3.2 Experimental setup

The experiments were performed using the blast chamber and ballistic pendulum at BISRU. Test panels are usually attached to the pendulum using a clamp frame, spacer bolts and a back plate, as shown in Figure 3.3. The rigid V-plates were designed with a built in back plate and hence were bolted directly onto the pendulum, as shown in Figure 3.4, meaning that the usual clamp frame, spacer bolts and back plate arrangement were not required. The pendulum was balanced using counterbalance masses to minimise the rotation of the pendulum as it swings.

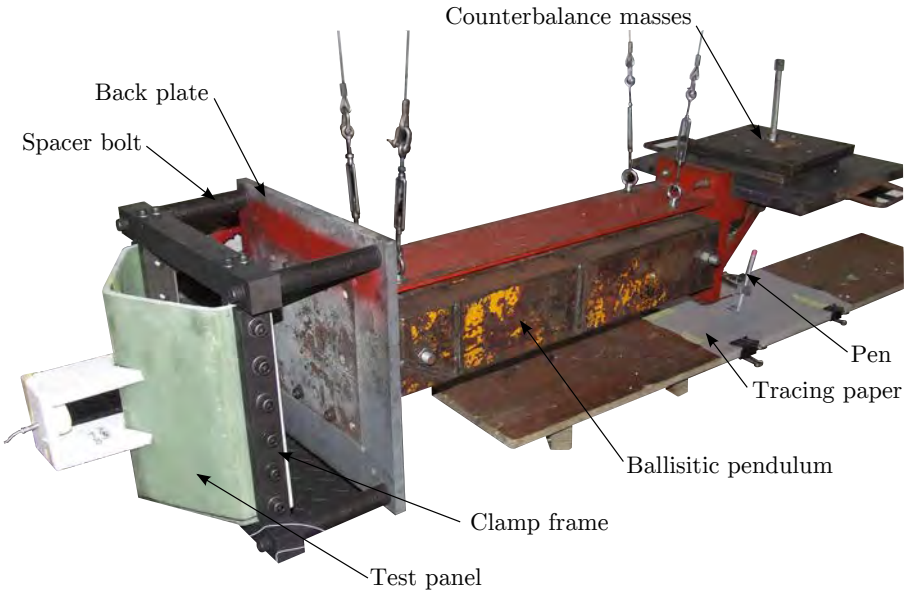

Figure 3.3: Photograph of the typical blast test setup [8]

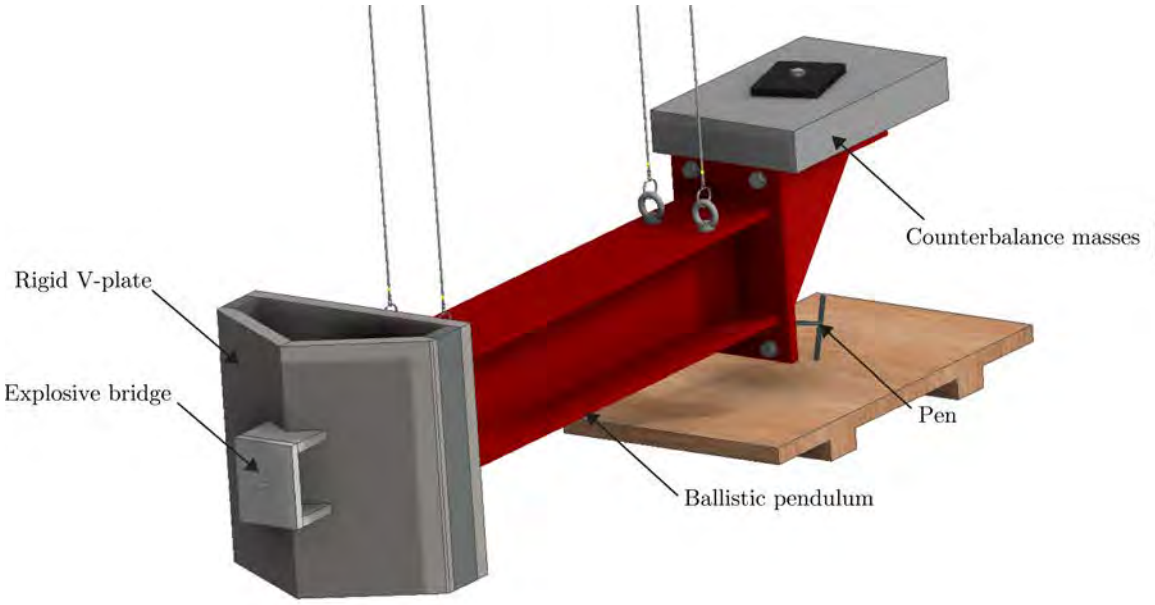

Figure 3.4: CAD model of the test setup used for the rigid V-plates

The blast loading was created by detonating discs of the plastic explosive PE4 situated at the midpoint of the V-ridge at a SOD of 34 mm. A polystyrene bridge was cut to a height equalling the sum of the required standoff and the height of the cylindrical PE4 charge mass as shown in Figure 3.5. The PE4 charge was placed on the inside of the bridge and attached to the V-plate. The detonator was then pushed approximately 1 mm into the cylinder of explosive material.

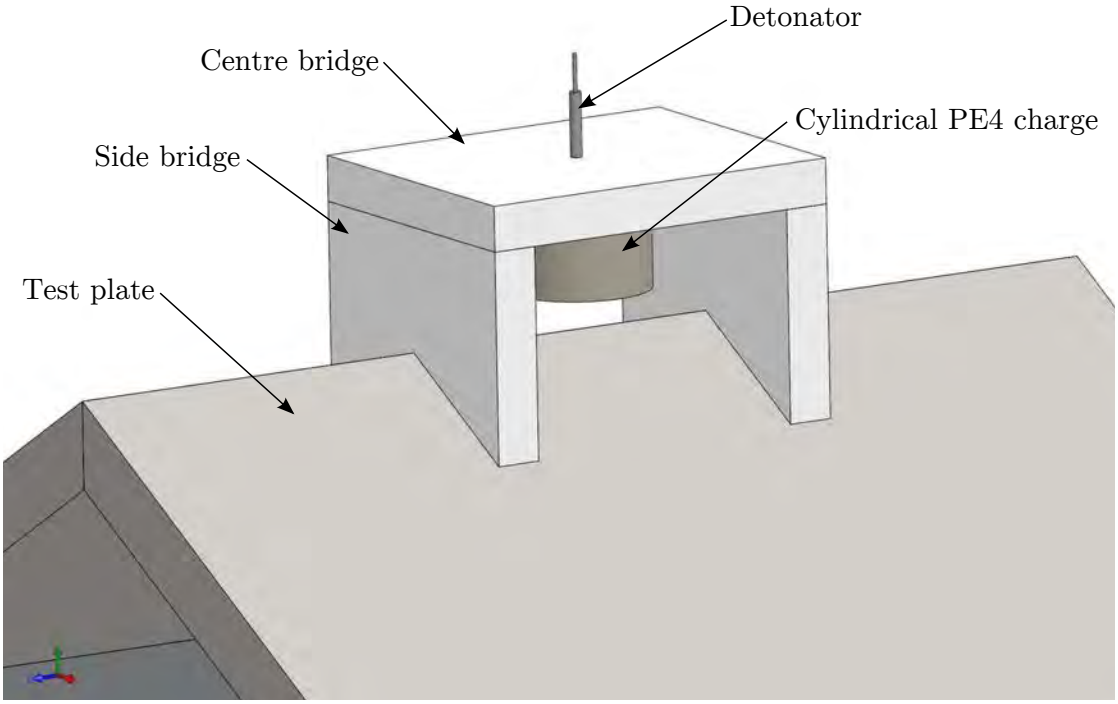

Figure 3.5: Three-dimensional CAD view of the polystyrene bridge, explosive and detonator

The impulse transferred to the pendulum was calculated using the maximum swing of the pendulum, captured in both the forward and backward directions on a piece of tracing paper via a pen mounted to the rear of the pendulum as shown in Figure 3.3. The detailed derivation of the equations used to calculate the impulse transfer are based on SDOF vibration and are in Appendix B.

3.2.1 Scaling of plate and charge sizes

The geometry of the V-plates was scaled down from the geometry of a Casspir APC MK II [23]. The ratio of the width of the Casspir hull to the width of the V-plate was found to be 1:8.16, hence the same scaling needed to be applied to the explosive charge and the stand-off distance. The PE4 charge was scaled down from the diameter of a TM-57 Anti-Tank mine of 312 mm [40]. This scaling yielded a charge diameter of 38 mm. The stand-off distance was scaled based on the ground clearance of the Casspir (410 mm) which would produce an experimental stand-off distance of 50 mm. Pickering [6] found that a 50 mm SOD produced negligible deflections and used a lower SOD of 34 mm. Pickering [6] and Hobson [8] used charge masses of 19, 29, 40, 45 and 58 g for their tests. The same charge masses and a 34 mm stand-off distance were used herein.

3.3 Blast test results

The impulses obtained during the air blast experiments are shown in Table 3.1. A graph of impulse versus charge mass for tests on the three V-angled plates is shown in Figure 3.6. It is evident from Figure 3.6 that the impulse increased with increasing internal angle and with increasing charge mass, as expected. The experimental results and test parameters that were used to determine the impulse values can be found in Appendix C. These results were used in Chapters 4 and 5 for the numerical simulations.

Table 3.1: Results of the impulse transferred in N s from the experiments performed on the rigid V-plates

	V-angle (°)		
Charge mass (g)	**60**	**90**	**120**
19	12.31	16.64	18.19
29	15.88		24.07
40	21.47	23.78	30.70
45	20.91		30.49
58	21.30	28.90	32.32

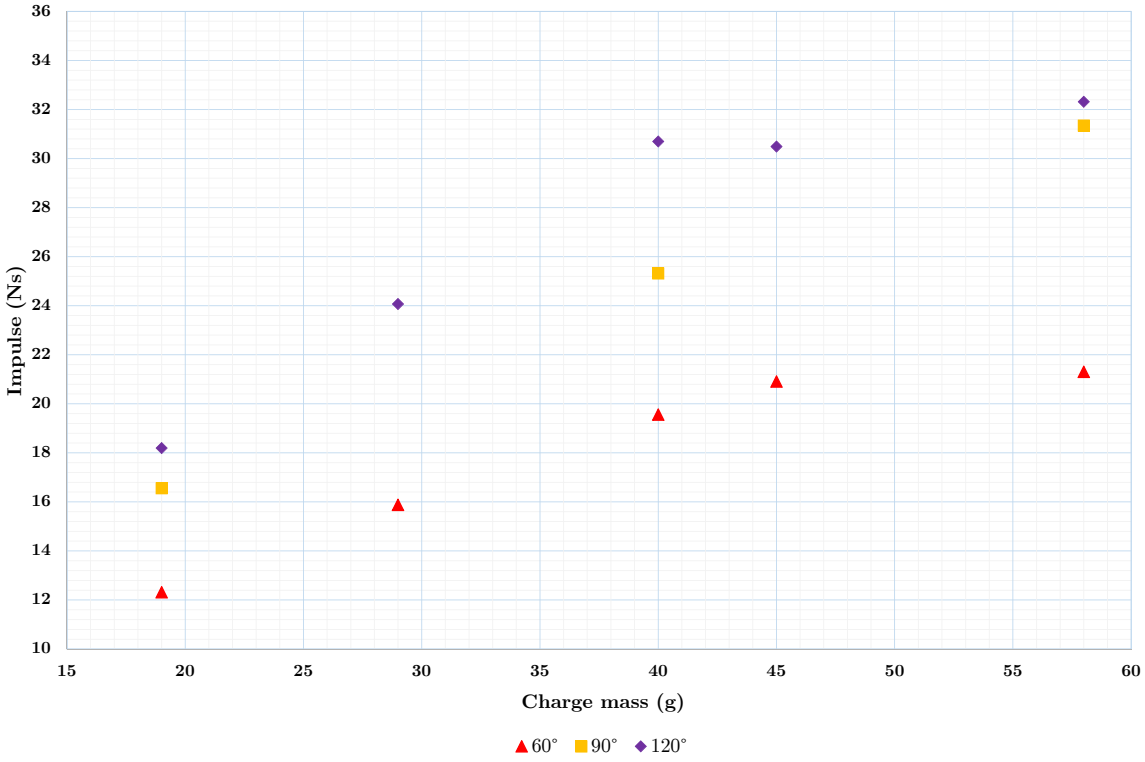

Figure 3.6: Graph of impulse versus charge mass for the three rigid V-plates tested

Chapter 4

Modelling blast loading and impulse transfer

LS-DYNA was used herein to model the blast loading and impulse transfer from a PE4 charge, using the experimental arrangement described in Chapter 3. This chapter details the process followed in developing the Eulerian mesh for the numerical model. The minimum termination time required for the simulations was investigated, to ensure that the loading phase was modelled completely while also minimising the simulation run time. The mesh convergence study is reported to determine the optimum element length for the air mesh. A mesh validation is reported for the chosen element size using the experimental results reported in Chapter 3.

4.1 Model description used for the convergence study

The initial quarter symmetry model had the same geometry as the rigid V-plate tests reported in Chapter 3, and is shown by the red region in Figure 4.1. The V-plates were modelled using shell elements and a rigid material model with the Young's modulus, Poisson's ratio and density of steel (that is, $E = 210\,\text{GPa}$, $\nu = 0.33$ and $\rho = 7870\,\text{kg}\,\text{m}^{-3}$). The element size chosen for the V-plates was 2.0 mm. It was found that there was no significant reduction in the computational time obtained by increasing the element length used for the plate mesh, hence 2.0 mm was chosen as it resulted in very low leakage forces. The plate was fully constrained as it was not expected to deform during the loading phase.

The air block is shown in Figure 4.1 by the box bounding the red portion of the V-plate. The cylindrical PE4 explosive charge was also modelled with quarter symmetry as shown by the green region in Figure 4.2. The detonation point was set to be 1 mm from the top of the PE4 explosive disc and is shown with a blue star in Figure 4.2.

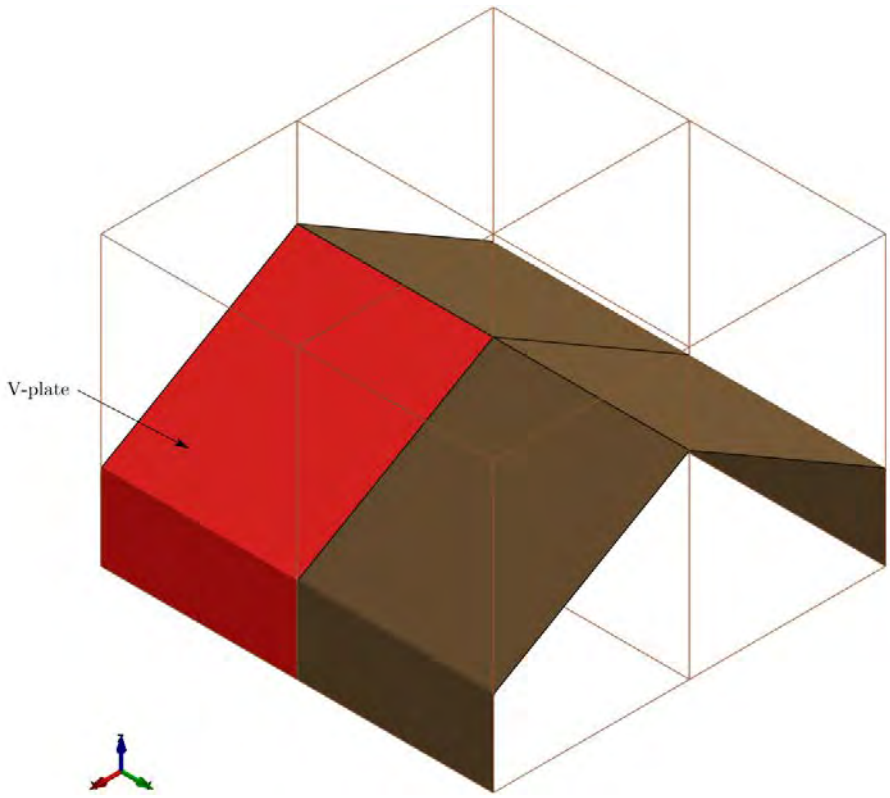

Figure 4.1: Numerical model used for initial simulations, showing a 120° V-plate

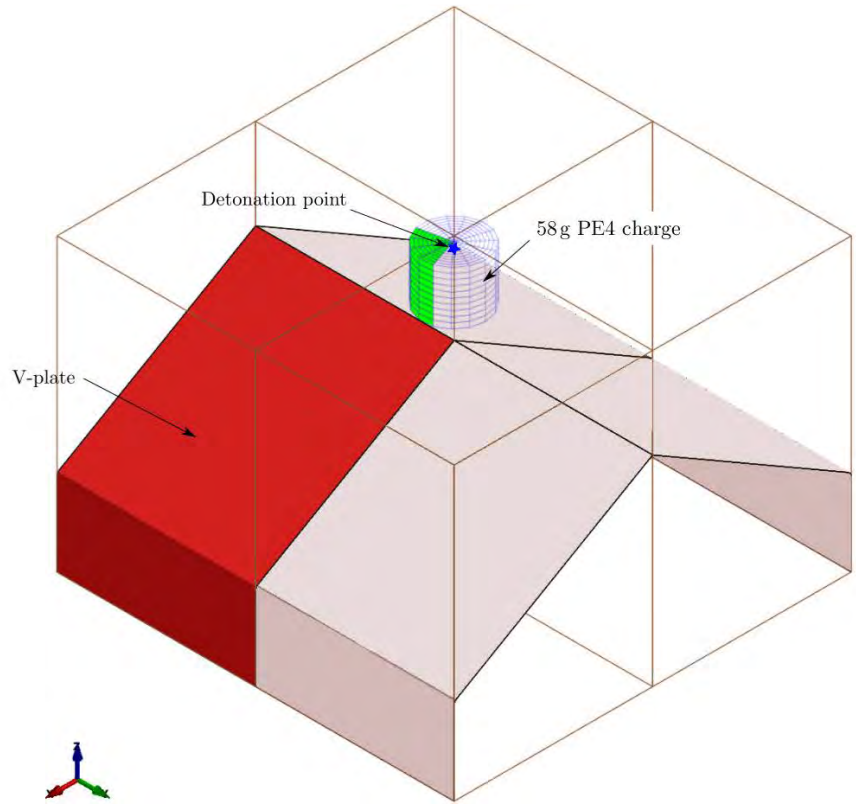

Figure 4.2: Numerical model used for initial simulations, showing a 120° V-plate and a 58 g PE4 explosive disc

4.2 Minimum required termination time

In order to minimise the simulation time, but still ensure that all the impulse transfer was captured, the required duration was determined. A 60° V-plate was simulated, since the explosive material would have the greatest distance to cover along the plate, with a 58 g charge which was the largest charge that was tested (which meant the largest amount of explosive material). A long termination time of 0.6 ms was used, and the pressure histories at the different locations of the plate were examined.

To determine a suitable termination time, it was necessary to identify the time at which the pressure across the plate had equalised. Four tracer points were located at the extremities of the quarter symmetry plate as shown in Figure 4.3.

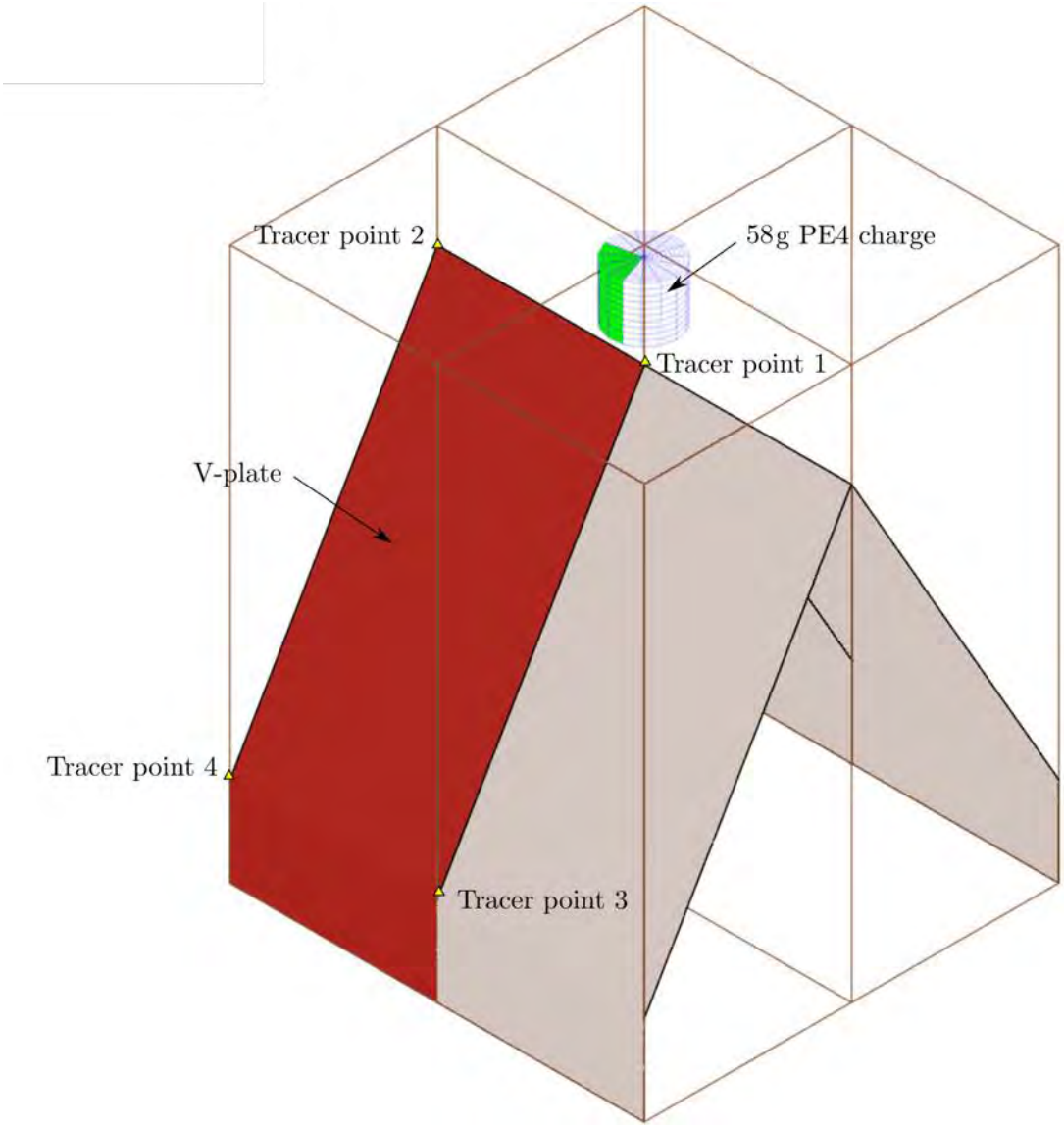

Figure 4.3: Schematic showing the rigid V-plate geometry, the four tracer points and the 58 g PE4 explosive disc

Figure 4.4 shows the pressure histories for tracer points 1 to 4. The maximum pressure was captured by tracer point 1 as it was closest to the charge location. The peak pressure recorded at tracer point 1 was two orders of magnitude higher than that observed at the other three tracer locations. It was still necessary to record the pressure across the entire plate as it would contribute to the total impulse transferred and the load at the more distant locations may have different transient characteristics. A zoomed in view of the pressure histories was plotted in Figure 4.5. From Figure 4.5 it was noted that the pressure equalised by 0.4 ms. Hence for all simulations that were performed a termination time of 0.4 ms was used.

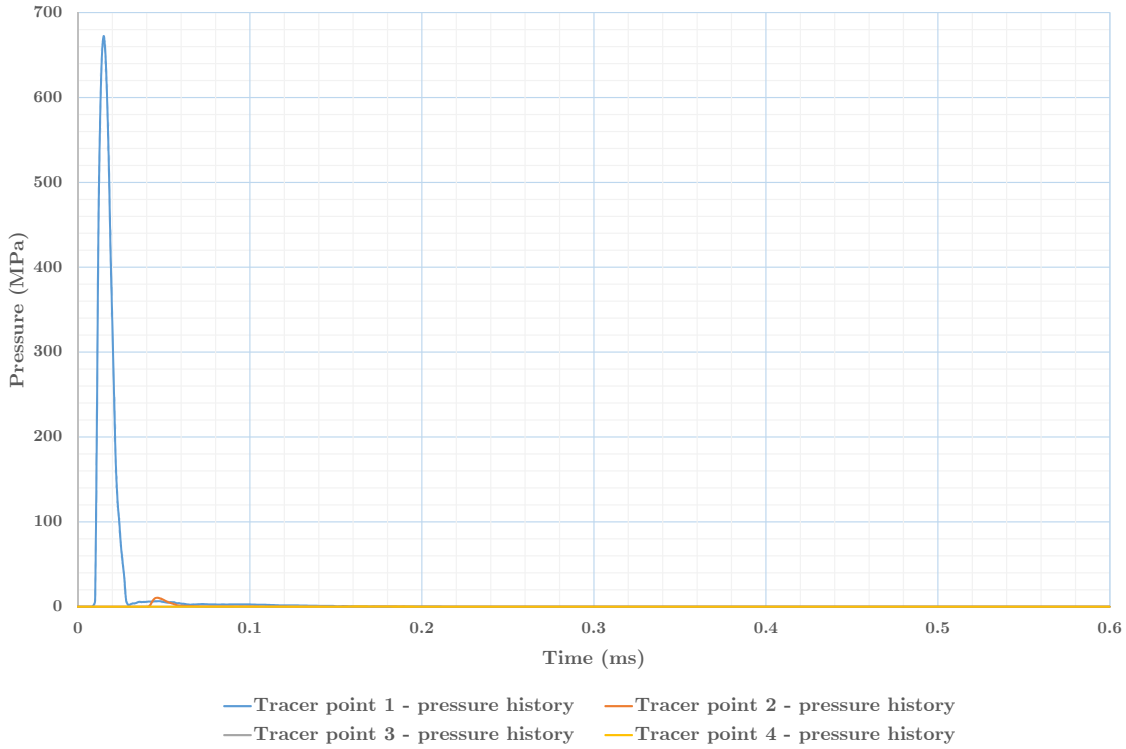

Figure 4.4: Graph of the simulated pressure histories for the four tracer points following a 58 g PE4 detonation

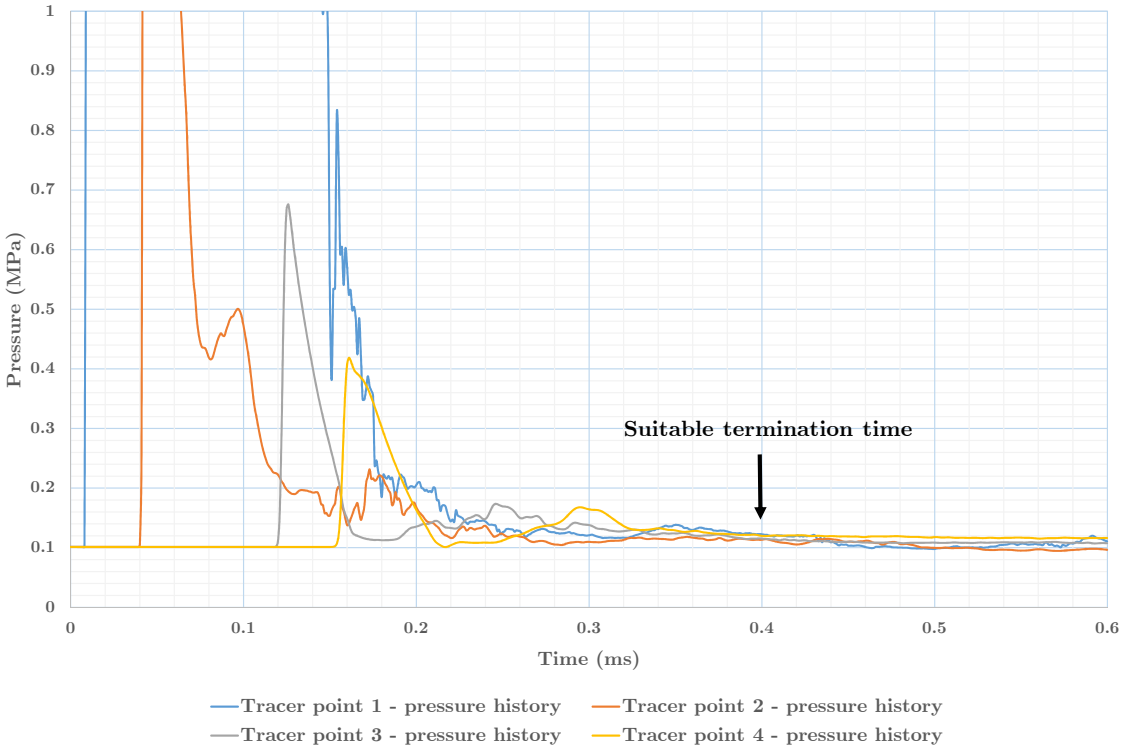

Figure 4.5: Graph of the simulated pressure histories for the four tracer points following a 58 g PE4 detonation, zoomed in to the 0-1 MPa range

4.3 Eulerian mesh convergence study

The optimum mesh size required was found by varying the element length of the ALE mesh and comparing the predicted impulse with the experimentally measured values. The total run-time for each simulation was also considered. The impulse was obtained from the fluid-structure interaction (FSI) force history outputs. The two forces used were the Z-force and Z-force leakage values. These force history curves were integrated with respect to time and then added together. The result was multiplied by four, to account for quarter symmetry. The maximum value was then taken to be the impulse transferred. Each of the simulations performed were run using 8 CPU's and 650 million words of memory.

Three element lengths were investigated for the Eulerian mesh: 1.5, 2.0 and 3.0 mm. It was not possible to use an element length of 1.0 mm as the computers available to run the simulation did not have sufficient memory. The experiment chosen for the mesh convergence study used the 120° rigid V-plate with a 58 g charge mass. This test was chosen as it resulted in the highest impulse transferred to the blast pendulum (as shown in Chapter 3). Table 4.1 shows the results of the convergence study. The measured impulse from the experiment was found to be 32.32 N s. Element lengths of 1.5 mm and 2.0 mm resulted in low percentage errors, while the simulation with an element length of 3.0 mm resulted in a large error.

Table 4.1: Table showing the effect of mesh density on impulse transfer and computational time

Mesh density (mm)	NCPU	Impulse (Ns)	Percentage error	Run time (hr)
1.5	8	31.11	3.8	07:33:56
2	8	30.08	6.9	02:39:31
3	8	23.27	28.0	00:32:41

Figure 4.6 shows the effect of the element length used for the Eulerian mesh on the impulse transferred and the computational time. The difference in the error in the impulse predicted for 2.0 mm elements versus 1.5 mm elements is 3.3%, while the reduction in computational time is 64.9%. The element length of 2.0 mm gave efficient run times with reasonable accuracy and was used herein.

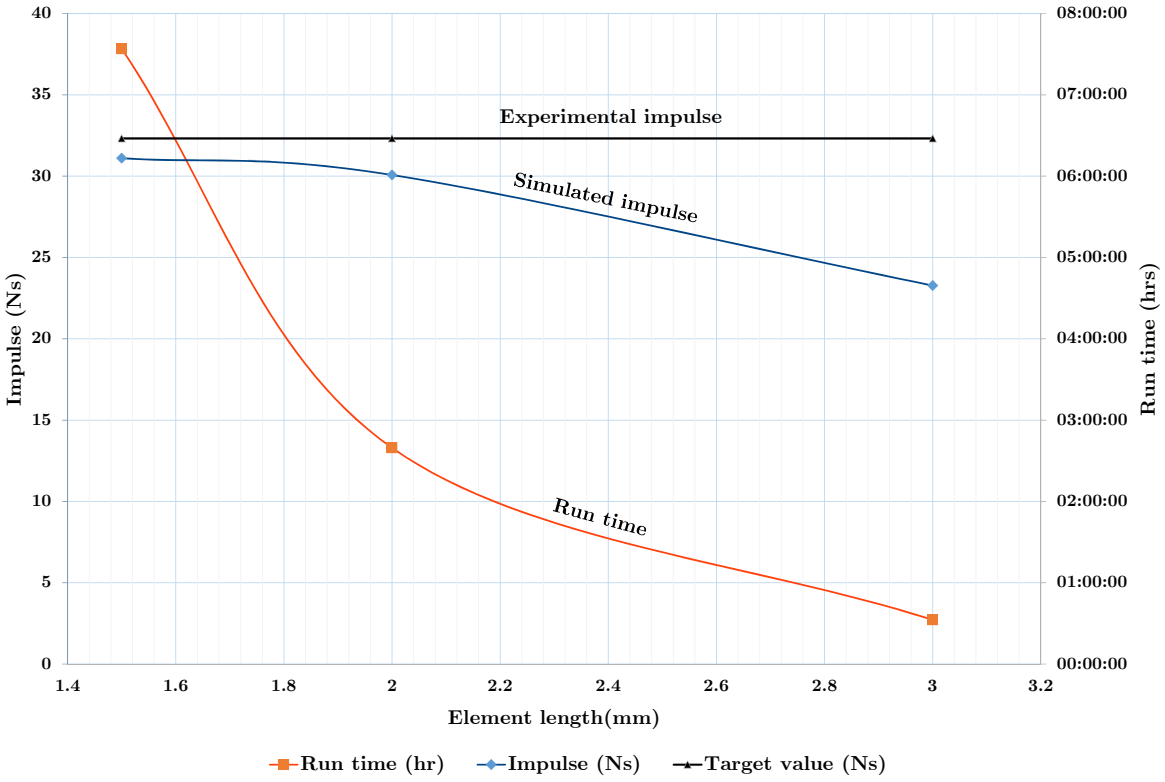

Figure 4.6: Graph showing the effect of the ALE mesh density on the impulse transferred and the computational time

4.3.1 Numerical validation

Once the optimal mesh size was determined, it was necessary to confirm that this element size would work for all the permutations of V-angle and charge mass. Table 4.2 shows the impulse values obtained from the numerical and experimental tests and the percentage difference between the results calculated using Equation (4.1). It is noted that the error from the 58 g detonation onto the 120° V-plate (described in the preceding section) was larger than the average absolute error of 4.08%, and that the largest variation was 2.5 N s.

Table 4.2: Table showing the comparison between the measured experimental and numerical impulse values in N s for the rigid V-plates

	Charge mass (g)	**19**	**29**	**40**	**45**	**58**
60°	**Experimental**	12.31	15.88	19.56	20.91	21.30
	Numerical	13.04	16.42	18.89	21.07	22.54
	Percentage error	5.91%	3.37%	3.43%	0.77%	5.82%
90°	**Experimental**	16.64		23.78		28.90
	Numerical	16.55	18.59	25.31	27.48	31.35
	Percentage error	0.53%		6.44%		8.47%
120°	**Experimental**	18.19	24.07	30.70	30.49	32.32
	Numerical	18.80	24.92	29.69	30.84	30.08
	Percentage error	3.33%	3.53%	3.28%	1.16%	6.94%

$$\%Error = \frac{|I_{experimental} - I_{numerical}|}{I_{experimental}} * 100 \tag{4.1}$$

Figures 4.7 to 4.9 show the experimental and numerical impulse values. Error bars corresponding to a 10% uncertainty in the experimental results were also plotted. A 10% error corresponds to between a 1.2 and 3.2 N s variation in the experimental results (which is a variation of 5 mm in the measured values of ΔL and ΔR). This uncertainty can be attributed to the motion of the pen when recording the horizontal displacement of the ballistic pendulum. It is evident from Figures 4.7 to 4.9 that all the values obtained from the numerical simulations lay within this range. Hence it was concluded that the chosen mesh size of 2.0 mm for the Eulerian mesh was acceptable. This mesh length was used for all subsequent numerical simulations.

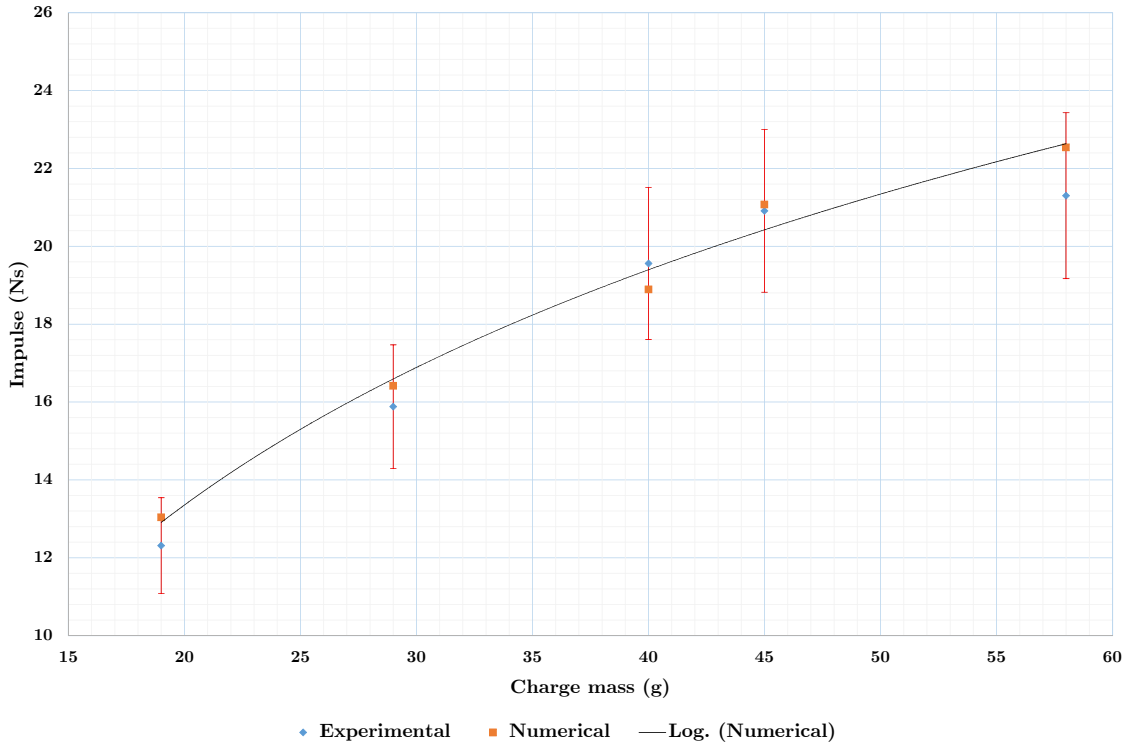

Figure 4.7: Graph showing the comparison between the experimental and numerical tests for the 60° rigid V-plates

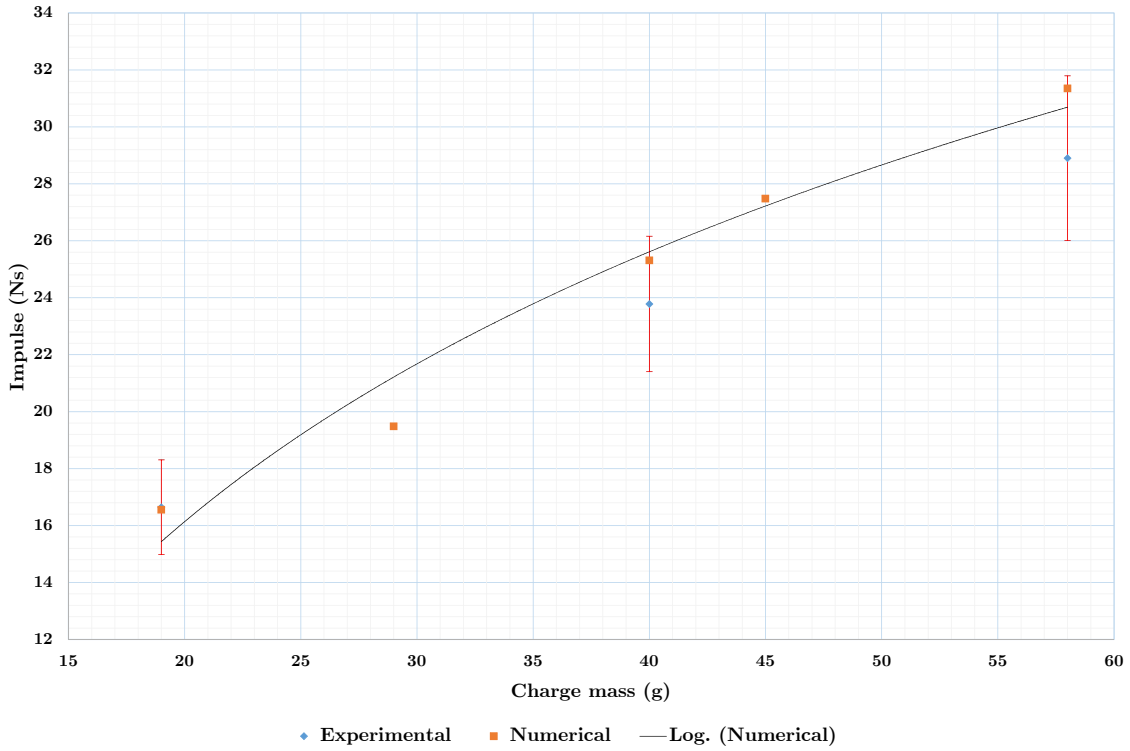

Figure 4.8: Graph showing the comparison between the experimental and numerical tests for the 90° rigid V-plates

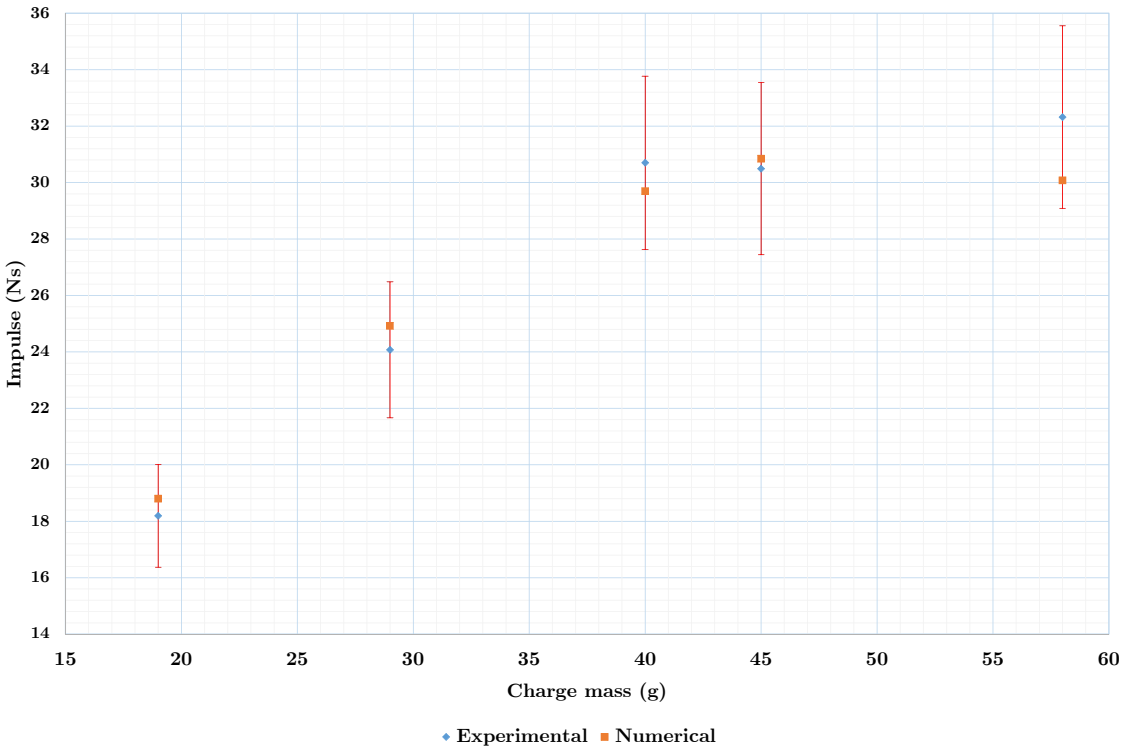

Figure 4.9: Graph showing the comparison between the experimental and numerical tests for the 120° rigid V-plates

This page has been intentionally left blank.

Chapter 5

Numerical model development

This chapter details the steps taken to reduce the computational costs of the numerical simulations by simplifying the model. A basic model description is provided, followed by the results of numerical tests performed to test various simplifications (by either removing unnecessary components in the model or changing the material models used). The final model (including some simplifications) is then described.

5.1 Basic model description

Figure 5.1 shows the numerical models used for the blast simulations in this chapter. The two models, both quarter symmetry, had different clamp frame designs based on past experiments. Figure 5.1(a) and Figure 5.1(b) show the components that were modelled (That is the V-plate, clamp frames and bolts). The components were modelled using the techniques described in Appendix A. The PE4 explosive discs are also shown, with the actual explosive modelled represented by the green portion of the blue cylinders. The air mesh is represented as the box that bounds the entire model.

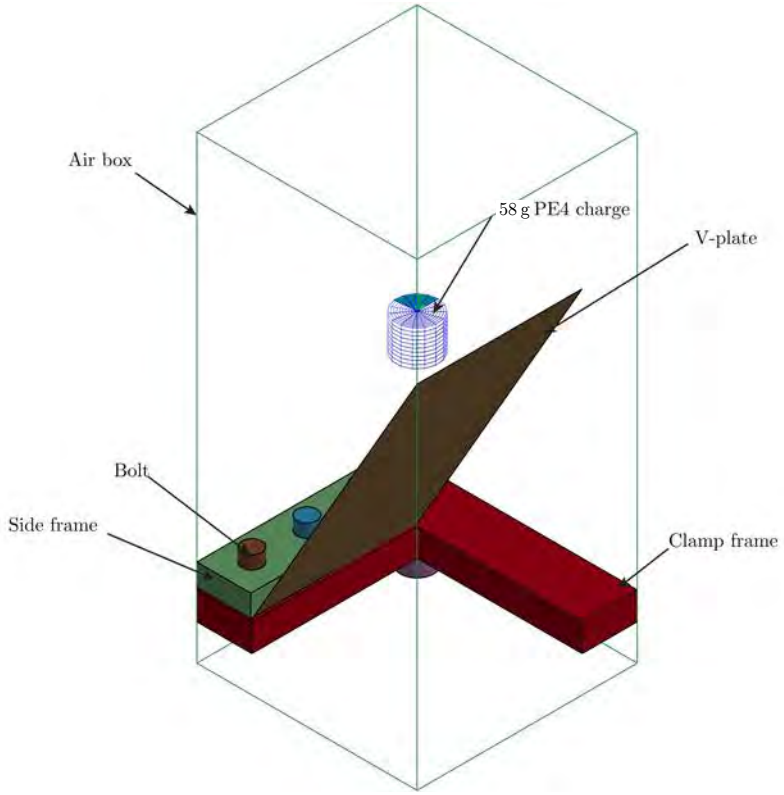

(a) Old clamp frame design, with 60° V-plate (test arrangement used by Pickering [6])

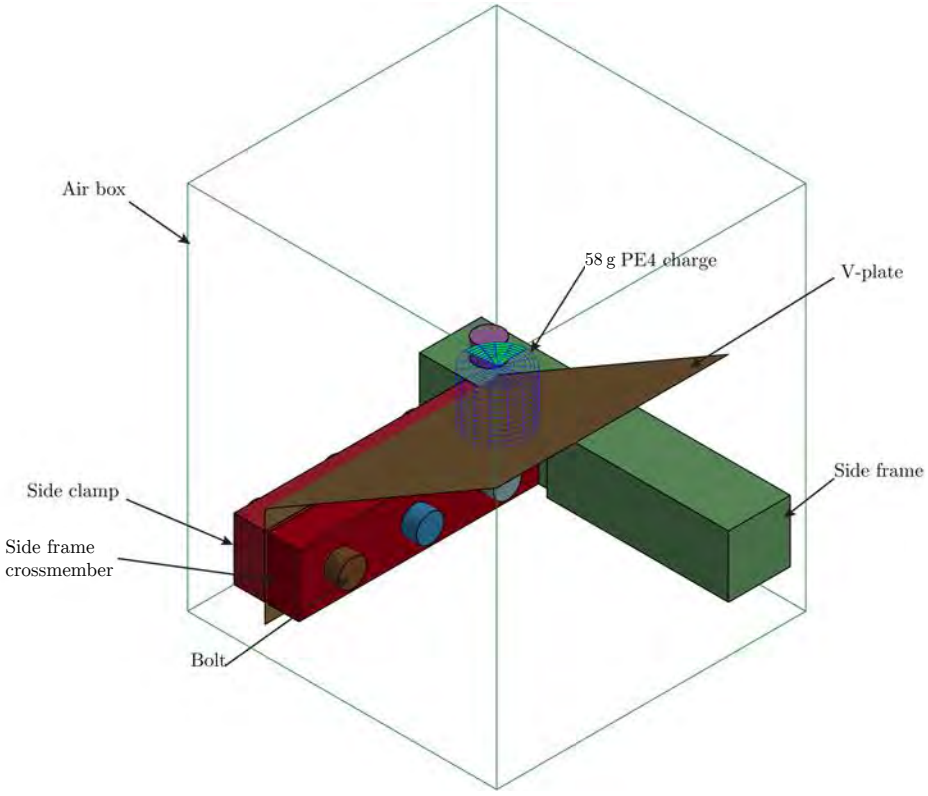

(b) New clamp frame design, with 120° V-plate (test arrangement used by Hobson [8])

Figure 5.1: Numerical models, showing V-plates and 58 g PE4 explosive discs with the air meshes shown as bounding boxes

5.1.1 V-plate model

The V-plates were modelled using shell elements with a uniform element length of 1.0 mm to ensure that the regions with holes could be meshed uniformly. The V-plates were manufactured from DOMEX-700 MC steel in work by Pickering [6], Naidoo [7], Warncke [9] and Hobson [8]. The material models used were a Johnson-Cook material model and a rigid material model. The general properties for DOMEX-700 MC steel are presented in Table 5.1. The Johnson-Cook material model parameters were obtained from the work of Volschenk [50] and are shown in Table 5.2.

Table 5.1: General properties for DOMEX-700 MC steel [56]

ρ (kg m^{-3})	E (GPa)	ν	C_p (J kg^{-1} K)	T_M (K)
7870	210	0.33	452	1800

Table 5.2: DOMEX-700 MC Johnson-Cook material parameters [50]

A (MPa)	B (MPa)	n	C	M	$\dot{\epsilon_0}$ (s^{-1})
756	550	0.52	0.0085	1	0.0166

5.1.2 Clamp frame geometries and material models

The clamp frame components and bolts were modelled using solid elements with a uniform element length of 1.0 mm. Rigid and elastic material models were considered for the clamp frames. The material properties used in the LS-DYNA keycards were identical to those shown in Table 5.1.

5.1.3 Air mesh description

The air boxes used were 200 mm x 200 mm blocks of varying heights. Three different heights were required for the three V-angles tested. The heights of the air block for the 60°, 90° and 120° V-plates were 417.5 mm, 317.5 mm and 240 mm respectively (for the two clamp frame designs). The air blocks had a grid size of 2.0 mm, based on the results of Chapter 4.

The material model used for the air was the null material model in LS-DYNA with the properties shown in Table 5.3. An ideal gas EOS, given by Equation (5.1) [57] was used to model the air. In LS-DYNA an ideal gas can be modelled using a linear polynomial EOS, given by Equation (5.2), where C_0, C_1, C_2, C_3, C_6 are set to zero while C_4 and C_5 are set to $\gamma - 1$ [57]. Equation (5.3) provides the definition for the parameter μ, where V is the relative volume [58].

$$p = (\gamma - 1)\frac{\rho}{\rho_0}E \tag{5.1}$$

$$p = C_0 + C_1\mu + C_2\mu^2 + C_3\mu^3 + (C_4 + C_5\mu + C_6\mu^2)E \tag{5.2}$$

$$\mu = \frac{1}{V} - 1 \tag{5.3}$$

Table 5.3: Properties for air used for the null material model in LS-DYNA [30]

ρ_0 ($\mathrm{kg\,m^{-3}}$)	E_0 ($\mathrm{kJ\,kg^{-1}}$)	γ	C4	C5
1.184	253.3	1.4	0.4	0.4

5.1.4 PE4 explosive charges

The explosive charges were modelled as cylindrical discs with a 38 mm diameter and a height varied to match the charge mass (19, 40 and 58 g). The disc heights are shown in Table 5.4. The stand-off distance was fixed at 34 mm for all the simulations, measured from the tip of the V-plate to the base of the charge. The geometry and stand-off distance were based on the TM-57 Anti-tank mine and the ride height of the Casspir APC MK II respectively, as described in Chapter 3.

Table 5.4: Heights of the PE4 discs tested for the different charge masses

Charge mass (g)	Height (mm)
19	10.46
40	22.03
58	31.94

The explosive was modelled using the Jones-Wilkins-Lee (JWL) EOS [57] given by Equation (5.4) and a high explosive burn material model in LS-DYNA [57]. The material and EOS properties for the explosive are shown in Table 5.5. The parameter ω is known as the Grüneisen coefficient and is used to describe the effects of shock waves on entropy production [33]. It should be noted that the properties used are for C4, which has similar characteristics to PE4, with the only difference being the plasticisers used. The air and explosive were modelled using techniques similar to those used in previous numerical studies in LS-DYNA involving the blast loading of structures [49–51] .

$$p = A\left(1 - \frac{\omega}{R_1 V}\right)e^{-R_1 V} + B\left(1 - \frac{\omega}{R_2 V}\right)e^{-R_2 V} + \frac{\omega E}{V} \tag{5.4}$$

Table 5.5: JWL EOS and high explosive burn material properties [59]

ρ_0 ($\mathrm{kg\,m^{-3}}$)	D ($\mathrm{m\,s^{-1}}$)	P_{CJ} (GPa)	A (GPa)	B (GPa)	R_1	R_2	ω	E_0 ($\mathrm{GJ\,m^{-2}}$)
1601	8193	28	609.77	12.95	4.5	1.4	0.25	9

5.2 Tests performed in the development of the numerical model

A comparison between elastic and rigid material models for the clamp frame was first considered. It was found from initial simulations that there was a large computational cost associated with the use of an elastic material for the bolts and clamp frames. Since a clamp frame modelled with an elastic material would deflect when loaded, it was necessary to determine if this deflection was significant. It was also useful to determine if the plate could be accurately modelled using a rigid material, to reduce the computational time of the simulations. Three configurations were tested and the impulse transferred in the different configurations was compared:

- Rigid clamp frame, Johnson-Cook material model for DOMEX-700 MC steel plate.
- Rigid clamp frame, rigid plate.
- No clamp frame (fully constrained boundary conditions set at the clamp frame region), rigid plate.

5.2.1 Clamp frame material effects

In order to determine if the clamp frames could be modelled with a rigid material, it was necessary to determine the maximum deflection of an elastic clamp frame under the pressure loading of a blast. The "old clamp" frame design was simulated, shown in Figure 5.1(b), as this clamp frame experienced greater pressure loading when compared with the new design. 60°, 90° and 120° V-plates were simulated with the bend radius set at 0 mm and 58 g PE4 charge. The model that produced the highest pressures was then used to determine the maximum predicted deflection of the clamp frame.

Figure 5.2 shows the locations of the tracer points used to determine the pressure in the different regions of the plate. Tracer points one to four were previously used to determine the required run-time for the simulations in Chapter 4. Tracer points three and four were used to determine the pressure acting on the vertical face of the clamp frame, while two more tracer points (*i.e.* five and six) were added to determine the pressure acting on the horizontal face of the clamp frame.

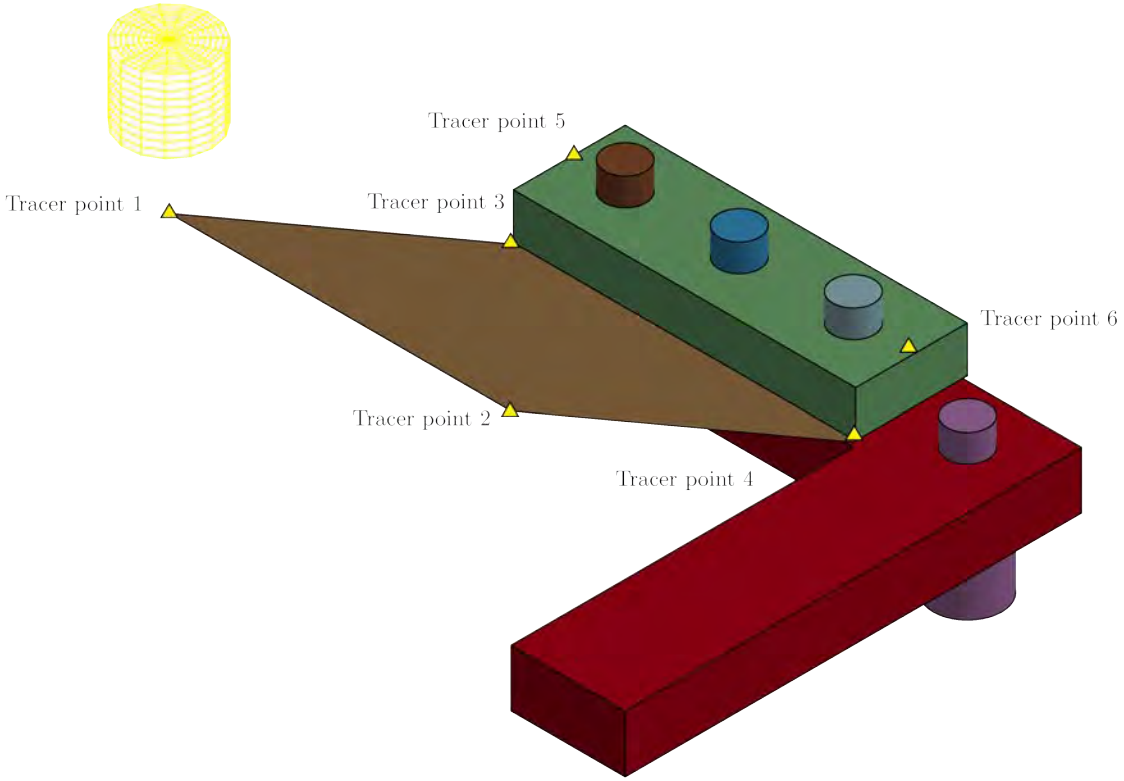

Figure 5.2: Location of the four tracers used to track the pressure across the plate as well as the additional two tracers used to determine the deflection of the clamp frame

Two configurations were considered, as shown in Figure 5.3, which were used to determine the maximum deflection. Figure 5.3(a) and (b) are the idealised pressure loading of the clamp frame in the vertical and horizontal directions respectively. Figures 5.4 and 5.5 show the pressure histories for the four tracers, for the 120° V-plate simulation. It was evident that the pressure at tracer point 4 lower than the pressure at tracer point 3 and the pressure at tracer point 5 lower than the pressure at tracer point 6. The pressure along the frame was linearly interpolated between the pressures at the two relevant tracer points, as shown in Figure 5.3. The peak pressure is observed at different times. This is expected as tracers 4 and 6 are further away from the explosive. To simplify the analysis the pressure recorded by the tracers was assumed to act at the same time, was recorded and then treated as a quasistatic load acting on the clamp frame.

The clamp frame was idealised as a simply supported structure rather than a fully restrained structure. A greater deflection would be observed for a simply supported structure, as shown in Equations (5.5) and (5.6)[60], and hence it was used for the analysis. This analysis was based on the static deflection of a beam.

$$\Delta d = \frac{L^4}{EI}\left(\frac{w}{384}\right) \tag{5.5}$$

$$\Delta d = \frac{L^4}{EI}\left(\frac{5w}{384}\right) \tag{5.6}$$

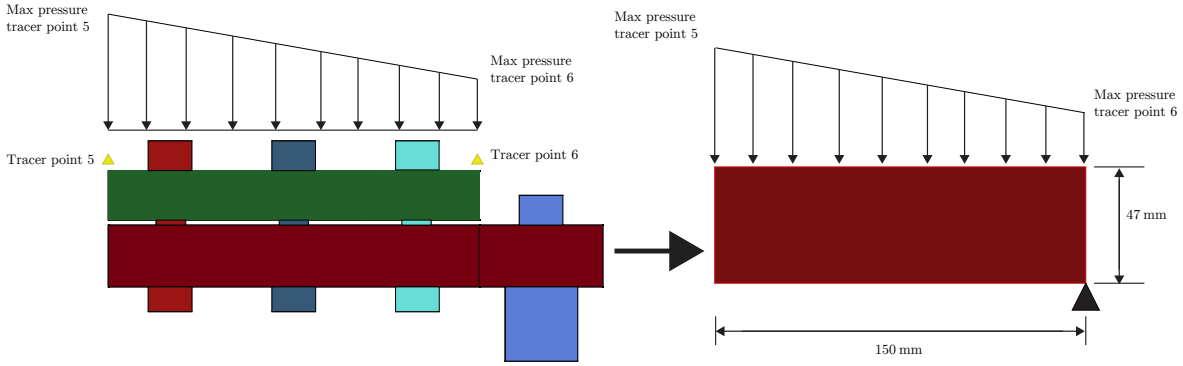

(a) Configuration 1: Used to determine the vertical deflection of the clamp frame

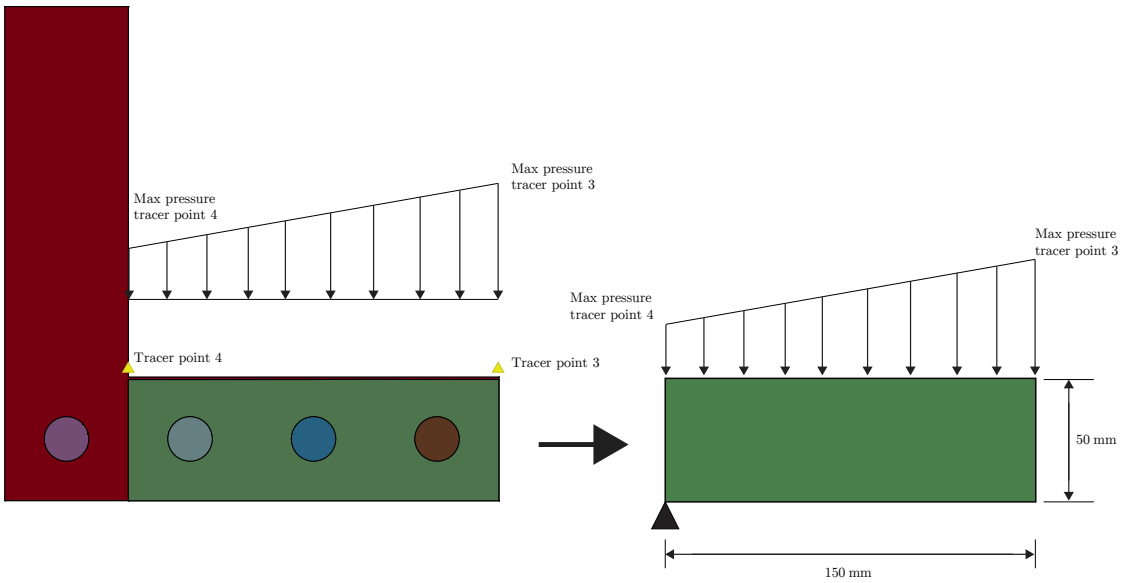

(b) Configuration 2: Used to determine the horizontal deflection of the clamp frame

Figure 5.3: The two configurations investigated to determine the maximum deflection of the clamp frame

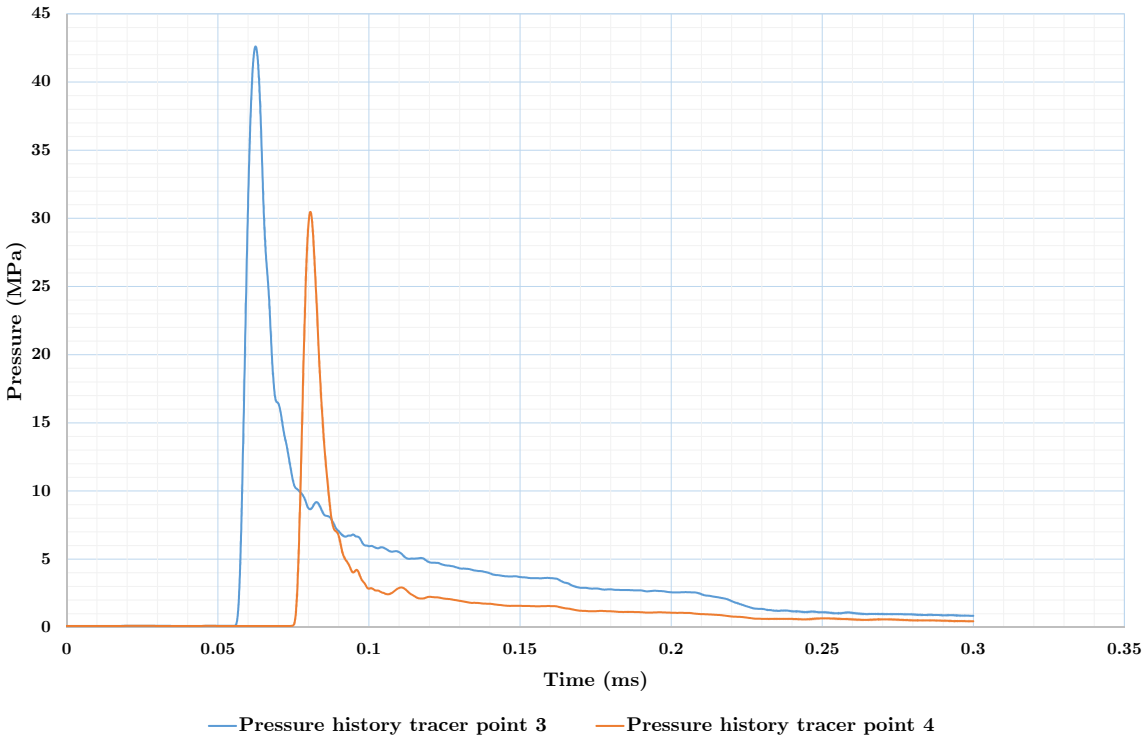

Figure 5.4: Graph showing the pressure-time histories for tracer points three and four for the 120° V-plate with a 58 g charge

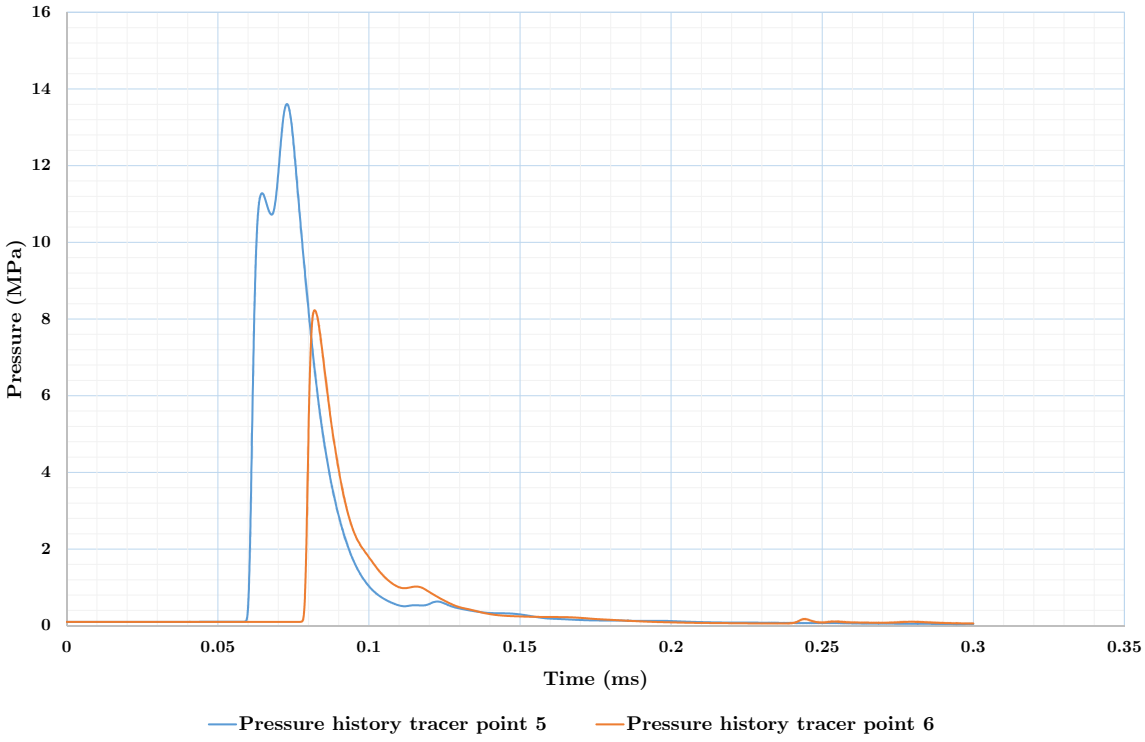

Figure 5.5: Graph showing the pressure-time histories for tracer points five and six for the 120° V-plate with a 58 g charge

Table 5.6 show the maximum pressures obtained from the four tracer points. It can be seen that the highest pressures were observed in the simulation that used the 120° V-plate. These pressures were converted into load intensities (*i.e.* force per unit length) by multiplying the values by the depth of the clamp frame in the specific direction.

Table 5.6: Table showing the maximum pressures recorded by tracers three to six for the 60, 90 and 120° V-plates

	60° plate; 58 g charge		**90° plate; 58 g charge**		**120° plate; 58 g charge**	
Tracer point	**Pressure (MPa)**	**Force/ length ($\mathbf{N\,mm^{-1}}$)**	**Pressure (MPa)**	**Force/ length ($\mathbf{N\,mm^{-1}}$)**	**Pressure (MPa)**	**Force/ length ($\mathbf{N\,mm^{-1}}$)**
3	5.30	248.88	0.95	44.47	42.60	2002.34
4	1.97	92.47	1.20	56.56	30.47	1432.16
5	10.95	547.41	11.20	559.92	13.61	680.27
6	3.75	187.49	7.22	360.97	8.23	411.42

$$\Delta d = \frac{L^4}{EI}\left(\frac{w_1 - w_2}{240} + \frac{w_2}{384}\right) \tag{5.7}$$

In Equation (5.7), w_1 and w_2 represent the maximum force/length values and L represents the length of the beam. Equation (5.7) is obtained by using the principle of superposition. This allows for deflection due to a uniformly increasing load to be added to the deflection due the uniformly distributed load. Looking at Equation (5.7) the maximum deflection would occur when w_2 was equal to zero. Furthermore in Figure 5.4, when the pressure history at tracer point 3 is at its maximum value, the pressure history at tracer point 4 is zero. A similar observation is made in Figure 5.5 for tracer points 5 and 6.

The maximum horizontal and vertical deflections of the clamp frames were calculated using Equation (5.7) and the values in Table 5.6, The force/length values from Table 5.6 were used for w_1 and w_2 was set to zero. Table 5.7 shows the deflections in the horizontal and vertical directions, where it is observed that the maximum deflection in the horizontal direction was 0.668 mm and the maximum deflection in the vertical direction was 0.256 mm (both for the 120° plates). These values are significantly lower than the dimensions of the clamp frame and are comparable to the clamping tolerances, confirming that it is acceptable to use a rigid material model for the clamp frames and bolts.

Table 5.7: Table showing the deflections in the horizontal and vertical directions for the 60, 90 and 120° V-plates

	60° plate; 58 g charge	**90° plate; 58 g charge**	**120° plate; 58 g charge**
Horizonal deflection (mm)	0.0829	0.0148	0.6668
Vertical deflection (mm)	0.2063	0.2110	0.2564

5.2.2 V-plate material effects

Three configurations were simulated and are listed in Table 5.8. Configurations 1 and 3 are shown schematically in Figure 5.6. For each configuration two V-angles were tested (*i.e.* 60° and 120°) with three charge masses (*i.e.* 19, 40 and 58 g).

Table 5.8: Table showing specifications for the simulated configurations

	Configurations		
	1	**2**	**3**
Clamp frame modelled	Yes	Yes	No
Clamp frame material	Rigid	Rigid	N/A
V-plate material	Johnson-Cook, deformable	Rigid	Rigid

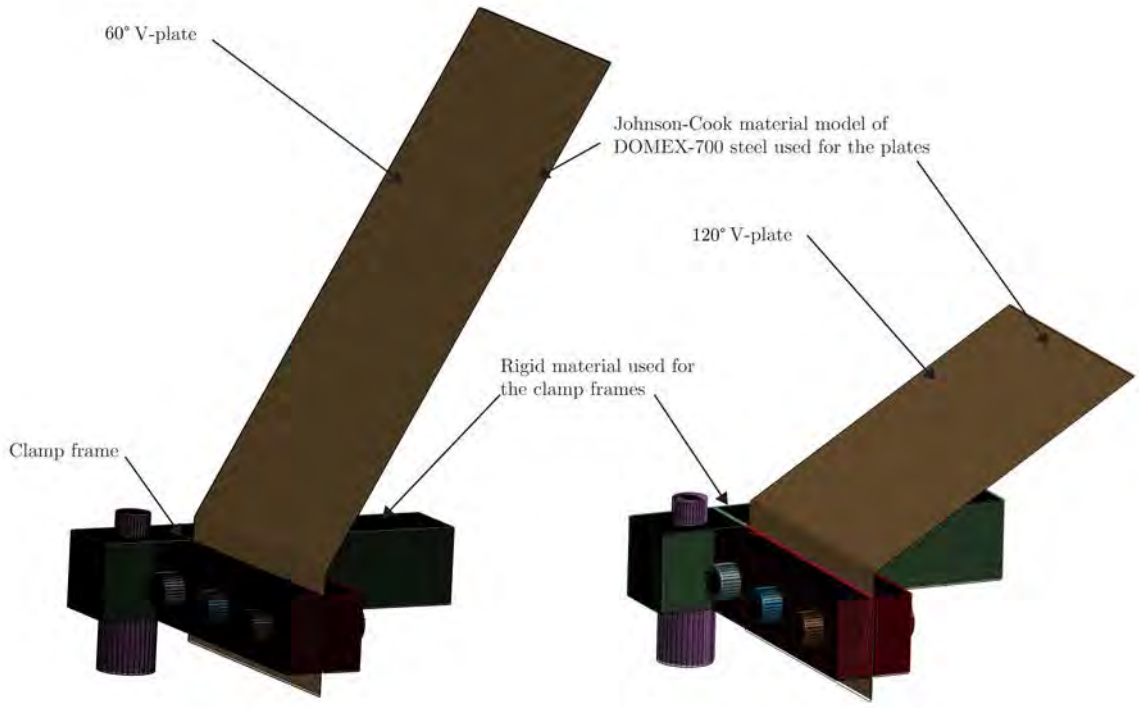

(a) Configuration 1: Rigid clamp frames

Figure 5.6: Schematics showing configurations 1 and 3

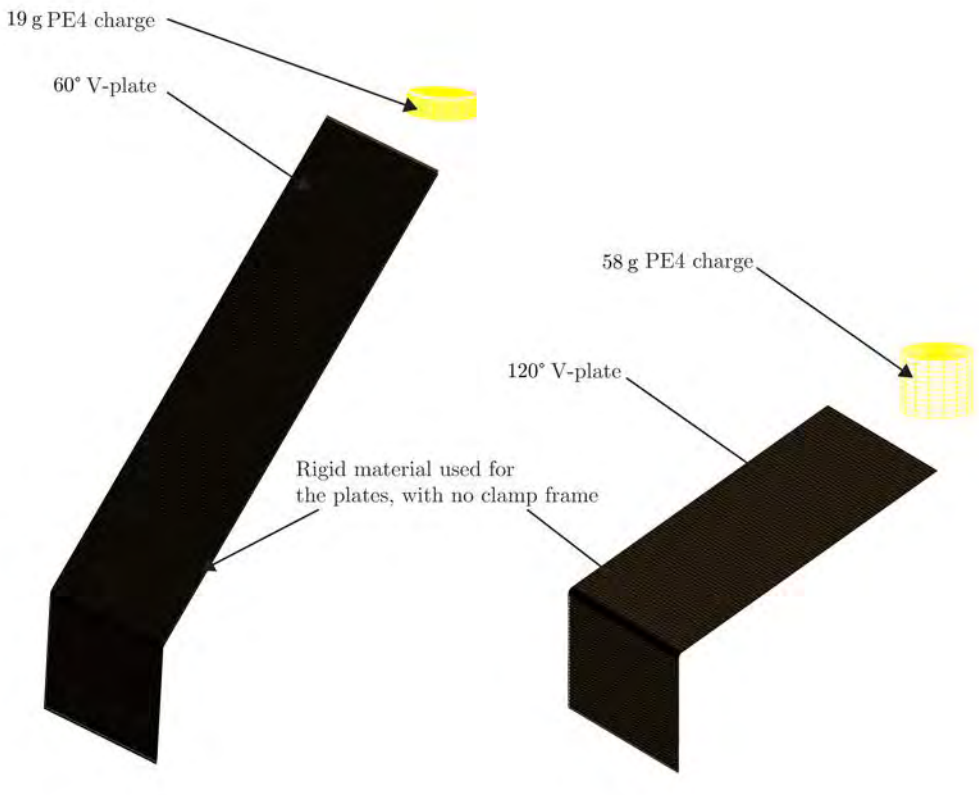

(b) Configuration 3: No clamp frame

Figure 5.6: Schematics showing configurations 1 and 3 (cont.)

Table 5.9 shows the results of the simulations, where the differences are compared to the impulse obtained using configuration 1 as the reference. From the 60° V-plate simulations it was evident that all the impulse values were within 2 N s. Furthermore it was evident that configuration 3 (that is the model with no clamp frame and a rigid plate) produces impulse values that are closer to configuration 1. This would suggest that it would be ideal to use the simplest model for all the simulations. However, Table 5.9 also shows that configuration 3 was not accurate for the 120° V-plates as the impulses were significantly lower. The impulse values for the simulations using a rigid clamp frame and a rigid V-plate (that is, configuration 2) were found to be within 2 N s for both the 60° and the 120° V-plates. These results suggest that using a rigid material model for the V-plates is suitable as the predicted impulses are close to those of the more complex simulations.

Table 5.9 also shows a comparison of the run-times of the different configurations. The rigid V-plate model in configuration 2 reduced the run-times by approximately 10 hours for the 60° V-plates (20%) and approximately 20 hours for the 120° V-plates (50%). Removing the clamp frame reduced the run-times far more (from an average of 36 hours in configuration 1 to 3.5 hours in configuration 3) but with an unacceptable loss in accuracy for the 120° V-plates.

Table 5.9: Table showing the comparison of the impulse transferred and run-time when the plate is modelled as rigid versus deformable, for a 60° and 120° V-plate with a range of charge masses

		#1		#2		#3	
		Rigid clamp frame; Johnson-Cook plate		**Rigid clamp frame; Rigid plate**		**No clamp frame; Rigid plate**	
Charge mass (g)	**V-angle**	**60°**	**120°**	**60°**	**120°**	**60°**	**120°**
19	**Impulse (N s)**	11.65	23.17	13.49	22.51	13.04	18.80
	Difference (N s)	N/A	N/A	1.84	0.66	1.39	4.37
	Run-time (h)	27.45	34.55	17.98	15.80	4.03	2.02
	Difference (h)	N/A	N/A	9.47	18.75	23.42	32.53
40	**Impulse (N s)**	19.04	33.61	20.28	35.25	18.89	29.69
	Difference (N s)	N/A	N/A	1.24	1.64	0.15	3.92
	Run-time (h)	38.40	33.98	30.12	13.28	5.07	2.38
	Difference (h)	N/A	N/A	8.28	20.70	33.33	31.60
58	**Impulse (N s)**	20.98	39.66	22.98	40.74	22.54	30.84
	Difference (N s)	N/A	N/A	2.00	1.84	1.59	8.82
	Run-time (h)	33.83	38.80	24.97	14.92	4.88	2.65
	Difference (h)	N/A	N/A	13.87	23.88	33.95	36.15

Figures 5.7 to 5.9 show the force-time histories for the different configurations tested with a 120° V-plate and a charge of 19, 40 and 58 g respectively. For each charge mass it was evident that the peak pressure for configuration 1 is lower than that for configuration 2, but the general profile and the duration are the same. The difference in the peaks can be explained by the fact that in configuration 1 the plate deforms absorbing some of the energy and reducing the peak force. Thus, it is concluded that it is acceptable to use configuration 2 for the all the simulations. It should be noted that the peak force is decreased even further for configuration 3. It is evident from Figure 5.9 that two peaks occur for configuration 1. This second peak was due to the deformation of the V-plate, though it had no effect on the total impulse transferred. This explains the similar impulses observed for configurations 1 and 2.

Figure 5.9 shows the force-time history for configuration 1 with a 58 g charge. A secondary peak is evident at 0.05 ms. This secondary peak is present, but has a much lower magnitude when the charge mass is reduced to 40 g in Figure 5.8, while the secondary peak is not observed in Figure 5.7. The larger charge masses result in an increase in the peak pressure, which results in an increase in the initial deformation of the V-plates, which inturn creates the secondary peak on the force-time history plots. While this secondary peak does change the shape of the force-time history plots, it does not result in a significant change in the total impulse.

From this analysis it was observed that the predicted impulses were reduced when the clamp frame was not included. Furthermore, the peak forces were reduced when the clamp frame was not included. Hence, while it is acceptable to model the V-plates and clamp frame as rigid, the clamp frame must be included in the model to ensure that the impulses predicted are accurate.

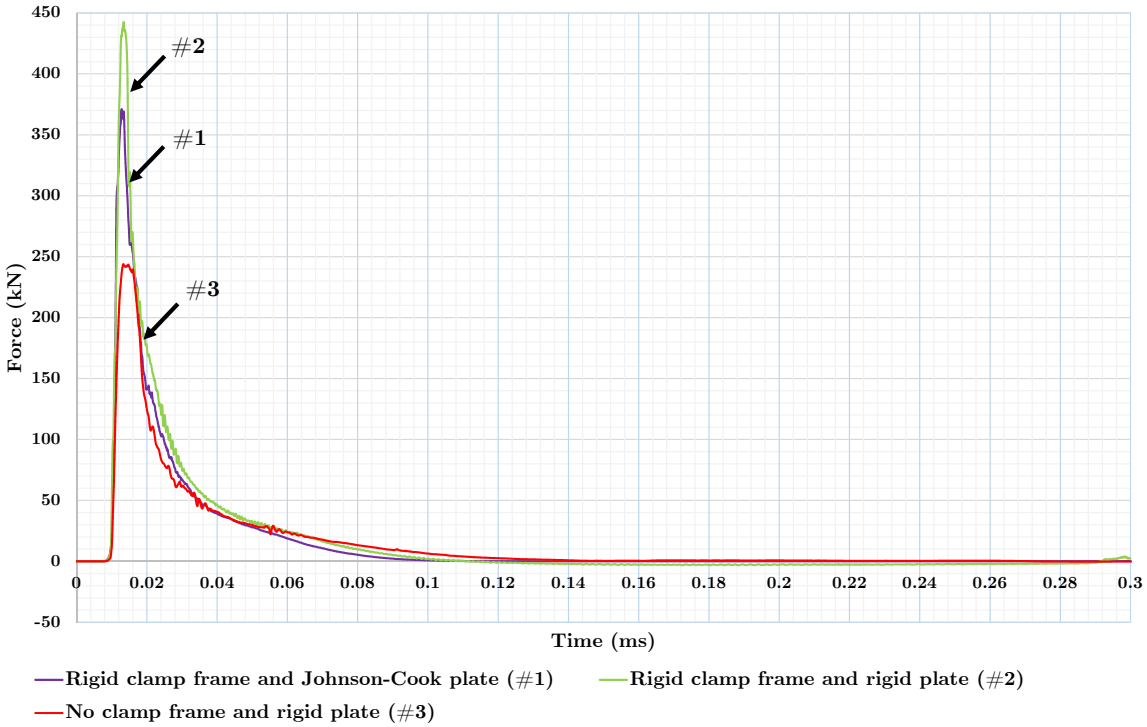

Figure 5.7: Graph showing the force-time histories for 120° V-plates with a 19 g charge for different plate materials

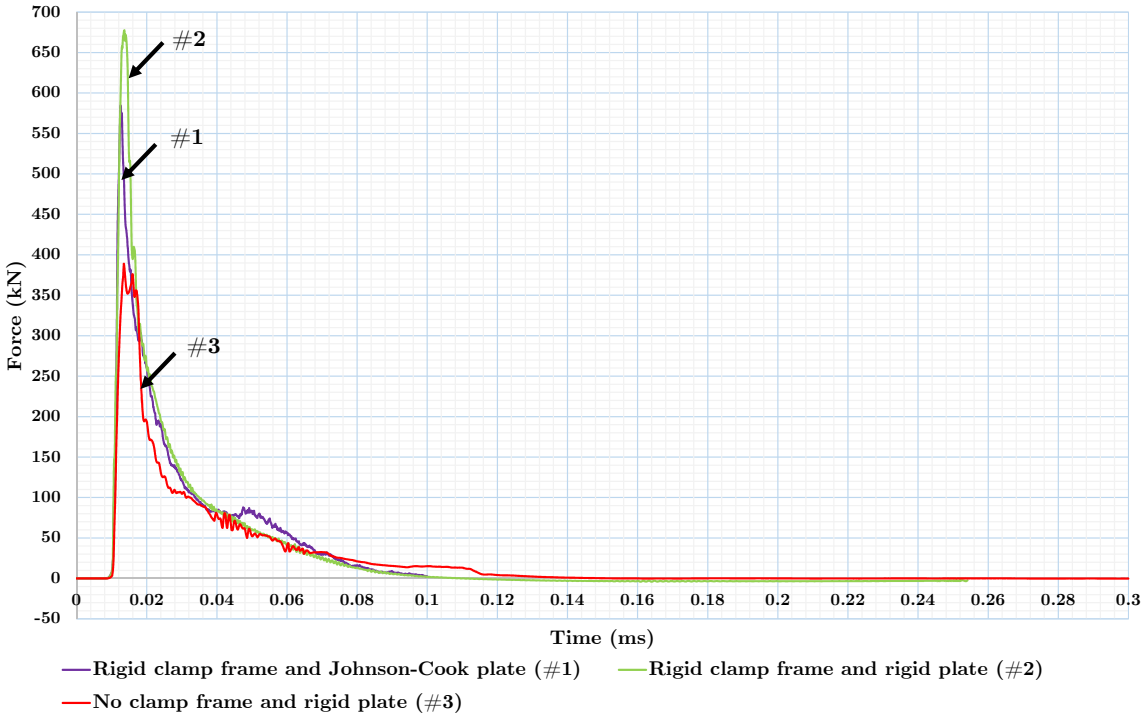

Figure 5.8: Graph showing the force-time histories for 120° V-plates with a 40 g charge for different plate materials

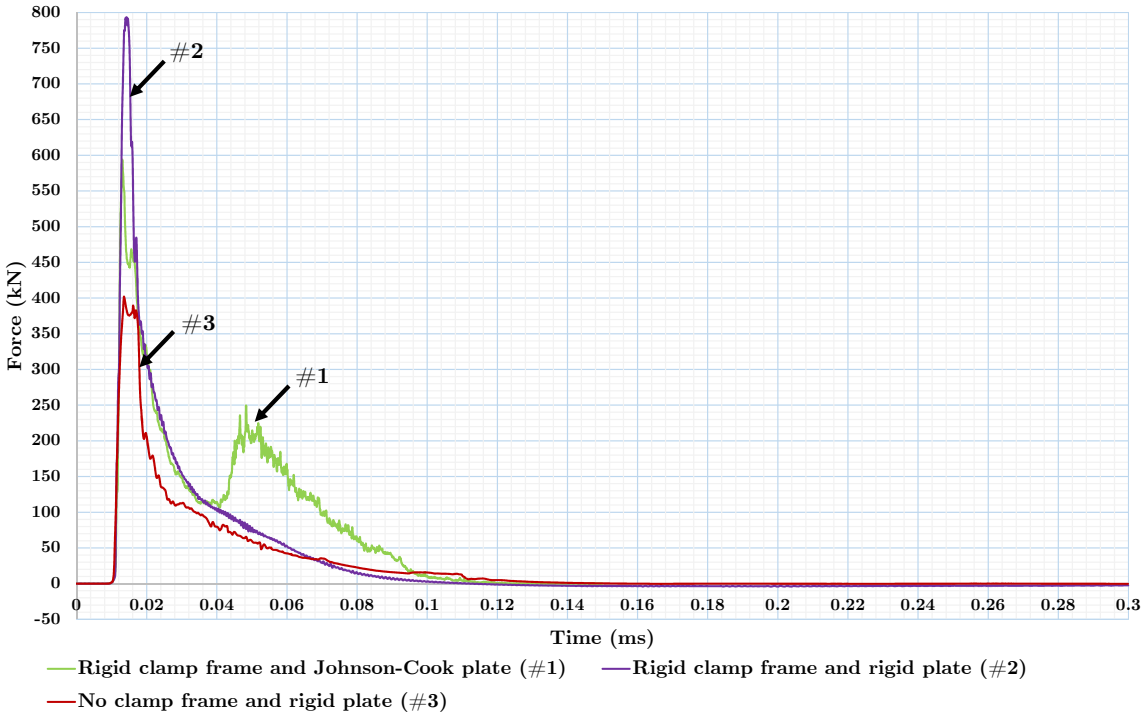

Figure 5.9: Graph showing the force-time histories for 120° V-plates with a 58 g charge for different plate materials

5.3 Summary of final model

The final model used for the remaining simulations was the model in which both the V-plates and the clamp frames were modelled with a rigid material model for steel. An element size of 1.0 mm was chosen for the V-plates and the clamp frames, while the ALE mesh used elements with a length of 2.0 mm. Three charges masses of PE4 were considered for the simulations, which were 19, 40 and 58 g. The termination time for the simulations was set at 0.4 ms, based on the simulations performed in Chapter 4.

Chapter 6

Qualitative description of explosion development and prediction on V-plates

This chapter looks at the distribution of the explosive material across the surface of V-plates with varying bend radii. The simulations that investigated the bend radius effects used the new clamp frame design shown in Figure 6.1. It was noted in Section 2.4 that Hobson [8] found that it was not possible to manufacture composite V-panels with a small bend radius and thus the manufactured panels had bend radii that varied between 25 and 54 mm. Hence when investigating bend radius effects it was decided to use the new design. Figure 6.2 shows 60, 90 and 120° V-plates with bend radii of 160 mm. For this bend radius, the effect of the V-angle is smaller than that of the curvature of the V-plate. Analysis of the explosive pressure waves and velocity vectors was performed in an attempt to better understand how an increase in the bend radius influenced the pressure distribution and impulse transfer.

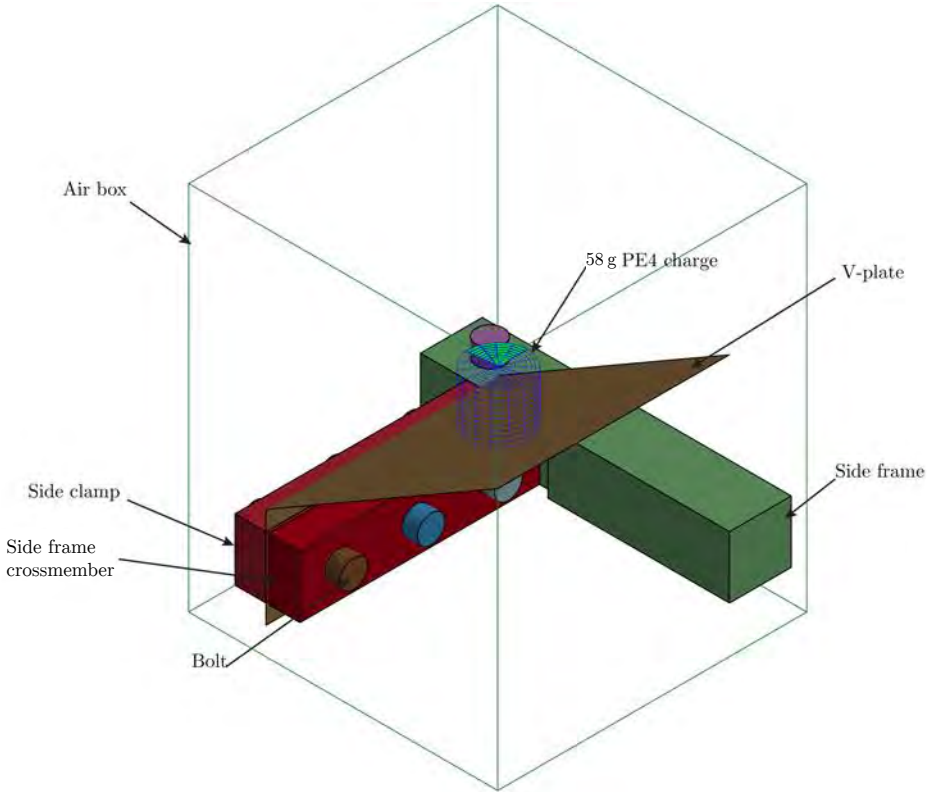

Figure 6.1: New clamp frame design, with 60° V-plate (test arrangement used by Hobson [8])

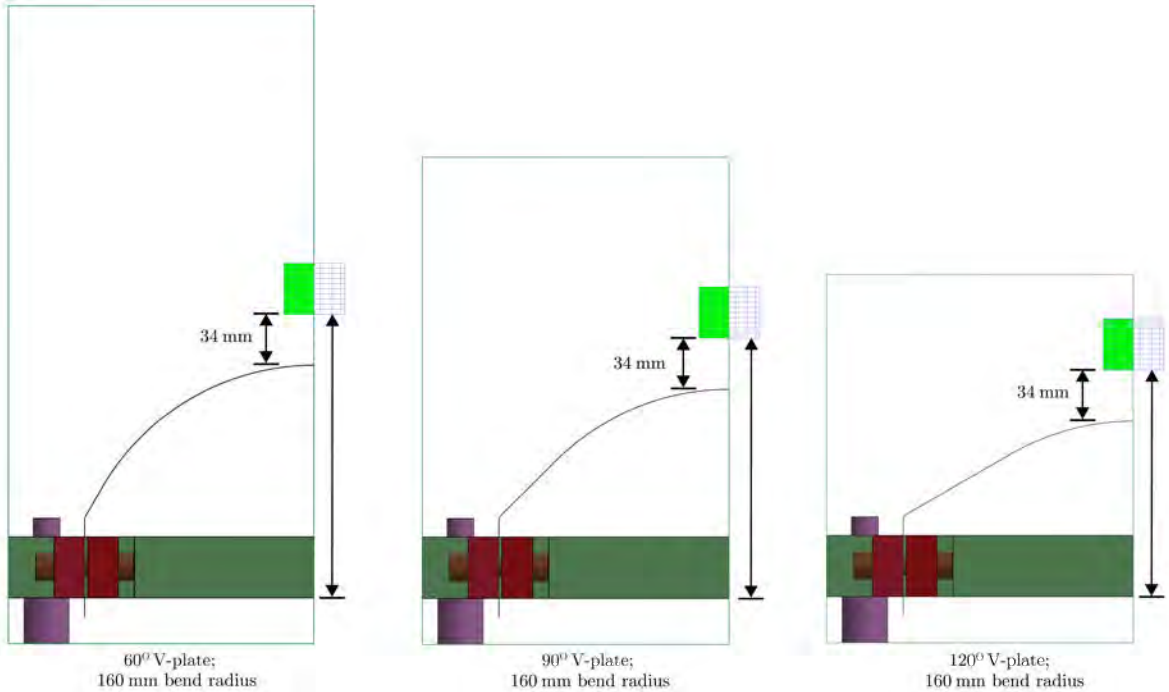

Figure 6.2: Schematics of V-plates with different V-angles, showing the significance of the curvature for large bend radii

6.1 Initial pressure wave development and explosive material development

It was useful to observe the pressure development before the pressure wave and gas products reach the V-plate. This was conducted so that the variation in the pressure waves when the explosive products impinge the plates with different bend radii could be observed. Figure 6.3(a) shows the fringe levels used for the pressure development shown in Figure 6.3. The maximum pressure was observed in Figure 6.3(c) when the pressure is 14.8 GPa at 2.5 µs, the maximum pressure then dropped to 500 MPa at 10.0 µs. Due to the detonation point being 1 mm below the top of the explosive, the pressure wave developed in a domed shape directed downwards toward the V-plate. This was first observed in Figure 6.3(c) at 2.5 µs. At 5.0 µs it was evident that the majority of the pressure was moving downwards, although some of the pressure wave was developing upwards at a lower pressure. In Figure 6.3(e) at 7.5 µs, the domed shape was still present in the downward direction and the pressure distribution was more uniform. By 10 µs the pressure has decreased significantly from the initial pressures observed at 2.5 µs.

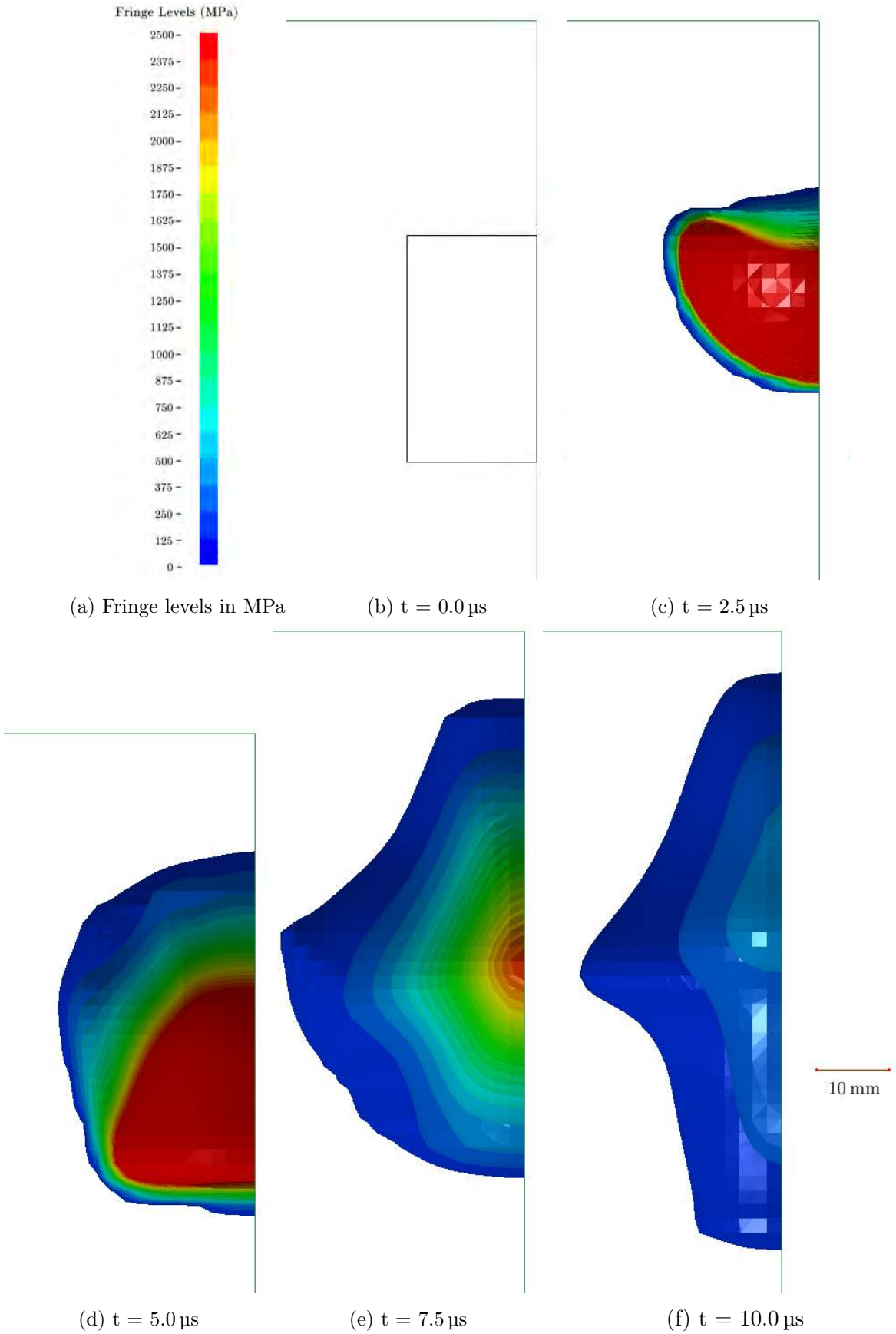

(a) Fringe levels in MPa (b) t = 0.0 µs (c) t = 2.5 µs

(d) t = 5.0 µs (e) t = 7.5 µs (f) t = 10.0 µs

Figure 6.3: Pressure development of the explosive gas products for a 58 g charge (prior to impinging the plate)

6.1.1 Explosive material development

Figures 6.5 and 6.6 show the development of the explosive materials for plates with bend radii of 0 and 160 mm, with 58 g detonations. These cases represent the minimum and maximum bend radii investigated so would show the greatest differences in the nature of the flow of the explosive products over the V-plates. The fringe levels shown in Figure 6.4 represent the volume fraction of the air which is occupied by the explosive.

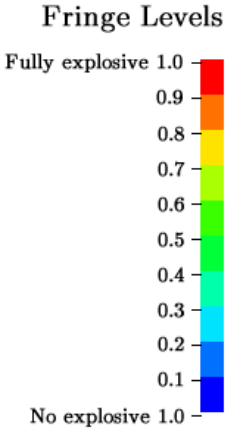

Figure 6.4: Fringe levels used for Figures 6.5 and 6.6

The explosive loading for a 0 mm bend radius is shown in Figure 6.5. Figure 6.5(a) and 6.6(a) show the shape of the PE4 explosive disc before the detonation. Figure 6.5(b) shows the explosive material at 50 µs, during the time when the plate was being loaded; a large amount of explosive material was in contact with the plate. The explosive products flowed down and around the plate (as shown in Figures 6.5(c) and (d)) and the extremities of the plate experienced a pressure loading, although this loading had a significantly lower magnitude than the loading in Figure 6.5(b). The gas products had moved away from the upper regions of the V-plate after 200 µs. The clamp frame was subjected to pressure loading as the explosive gases passed over it, shown in Figures 6.5(e) and (f). Figure 6.5(g) shows that by 300 µs the explosive gas products had moved away from the V-plate and clamp frame arrangement and were no longer loading the plate.

Figure 6.6 show the explosion development for the 160 mm bend radius. Figure 6.6(b) shows the explosive distribution at 50 µs. Similarly to the 0 mm bend radius (Figure 6.5(b)) a large amount of explosive material was in contact with the plate at this stage. Due to the large bend radius the height of the explosive charge is lowered. Since the identical air mesh to that used for the 0 mm bend radius was used, it was possible to observe the explosive materials develop in the upward direction, away from the plate. A similar trend cannot be observed in Figure 6.5 since the charge is much closer to the top of the air mesh and flows out through the top of the air mesh during the blast event. Figures 6.6(c) and (d) then show that the explosive products moved horizontally rather than travelling down the V-plate, due to the large bend radius at the V-tip,

the explosive products were deflected at a shallower angle. After 200 µs, it was evident that the gas products had moved away from the V-plate, shown by Figure 6.6. Additional figures which look at the explosive material distribution for other bend radii can be found in Appendix D, which show similar trends for the 90 and 120° V-plates.

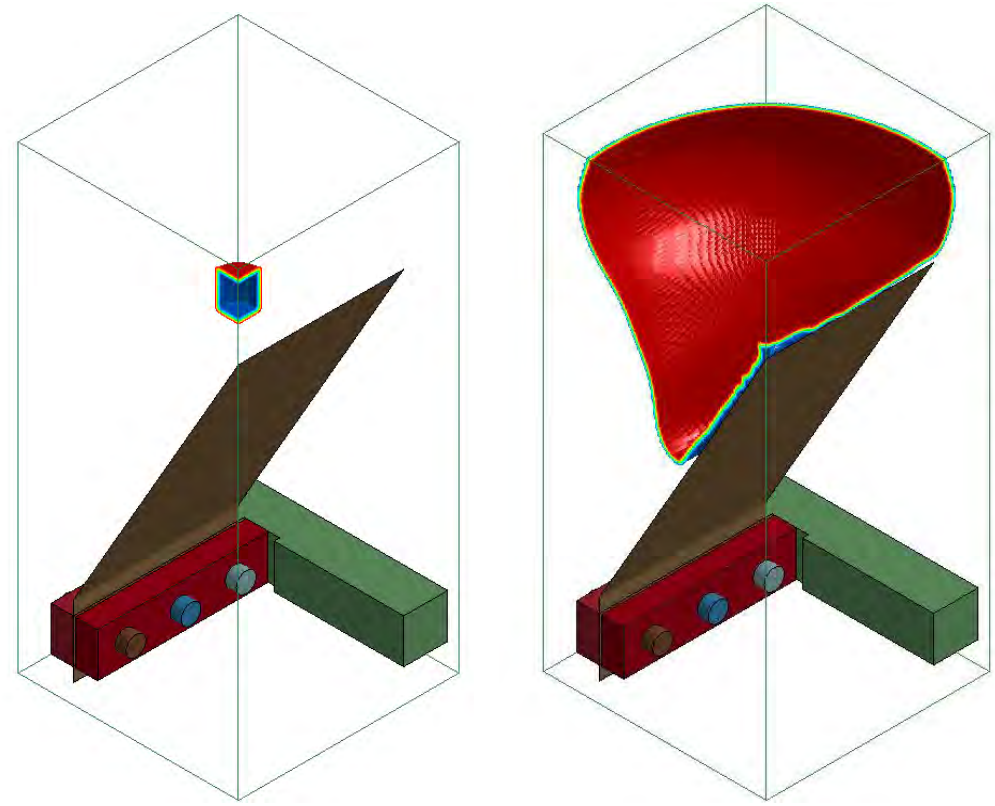

(a) t = 0 µs (b) t = 50 µs

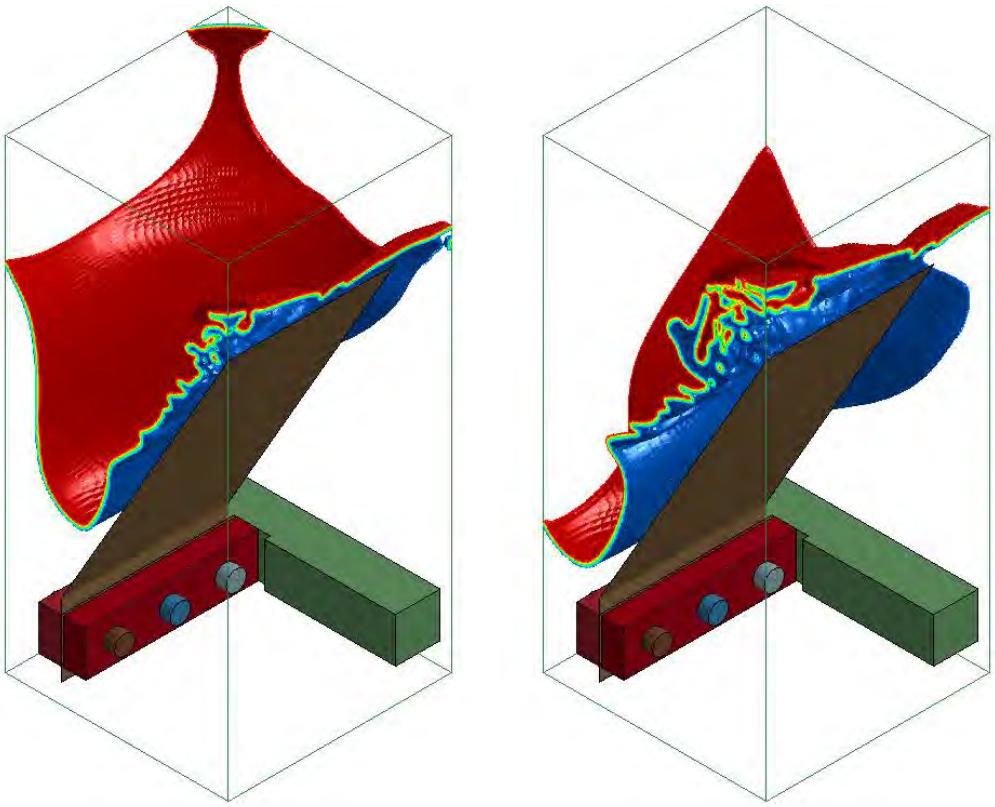

(c) t = 100 µs (d) t = 150 µs

Figure 6.5: Explosive development for a 60° V-plate with a bend radius of 0 mm and a 58 g charge from 0 to 300 µs

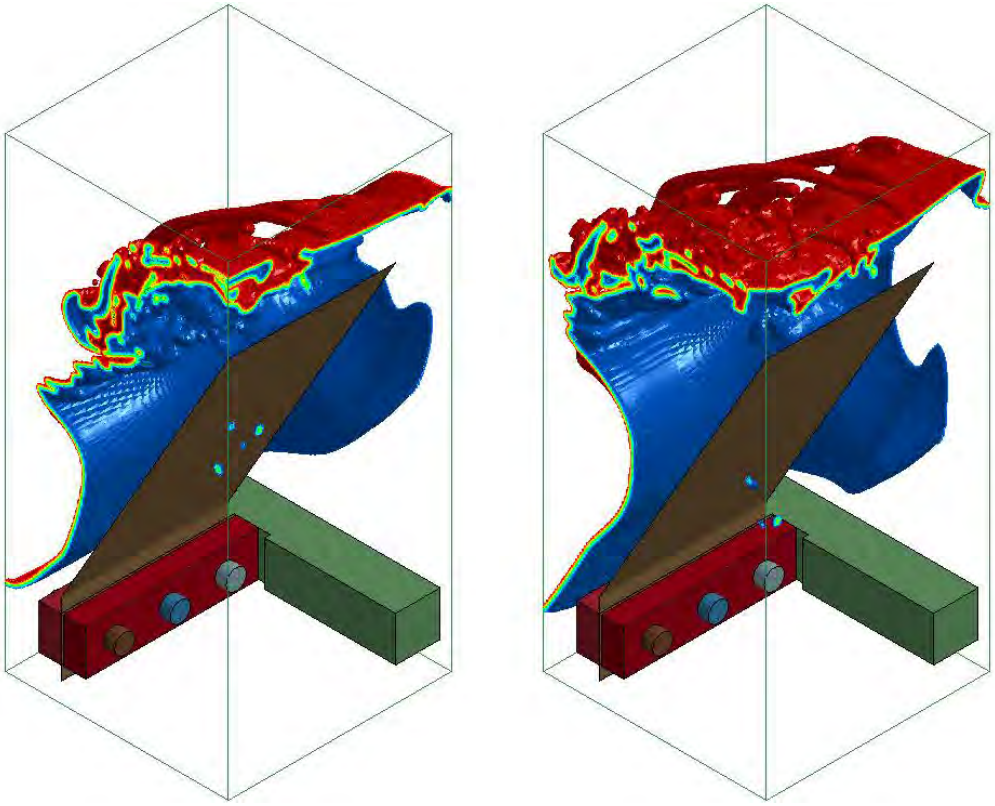

(e) t = 200 µs (f) t = 250 µs

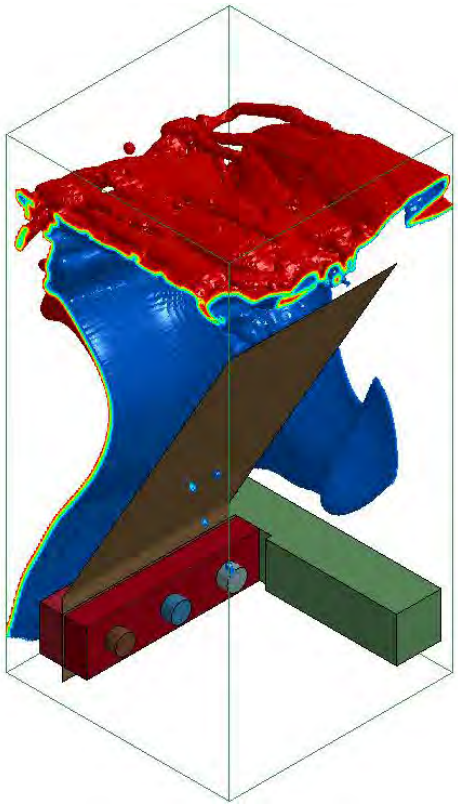

(g) t = 300 µs

Figure 6.5: Explosive development for a 60° V-plate with a bend radius of 0 mm and a 58 g charge from 0 to 300 µs

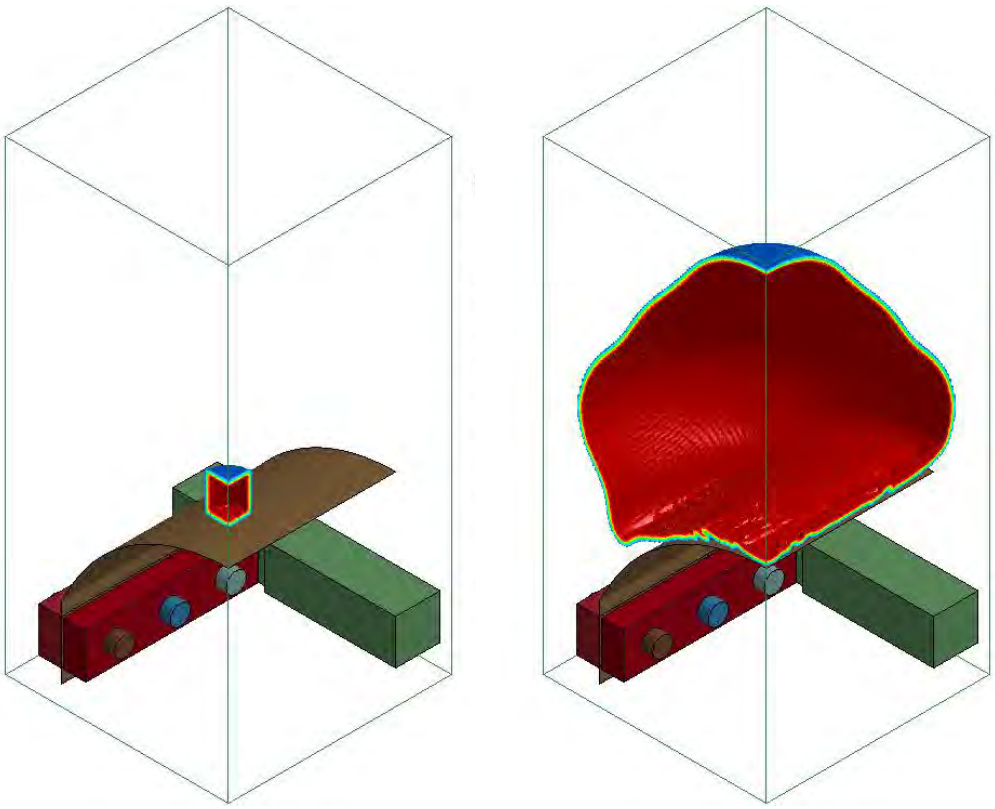

(a) t = 0 µs (b) t = 50 µs

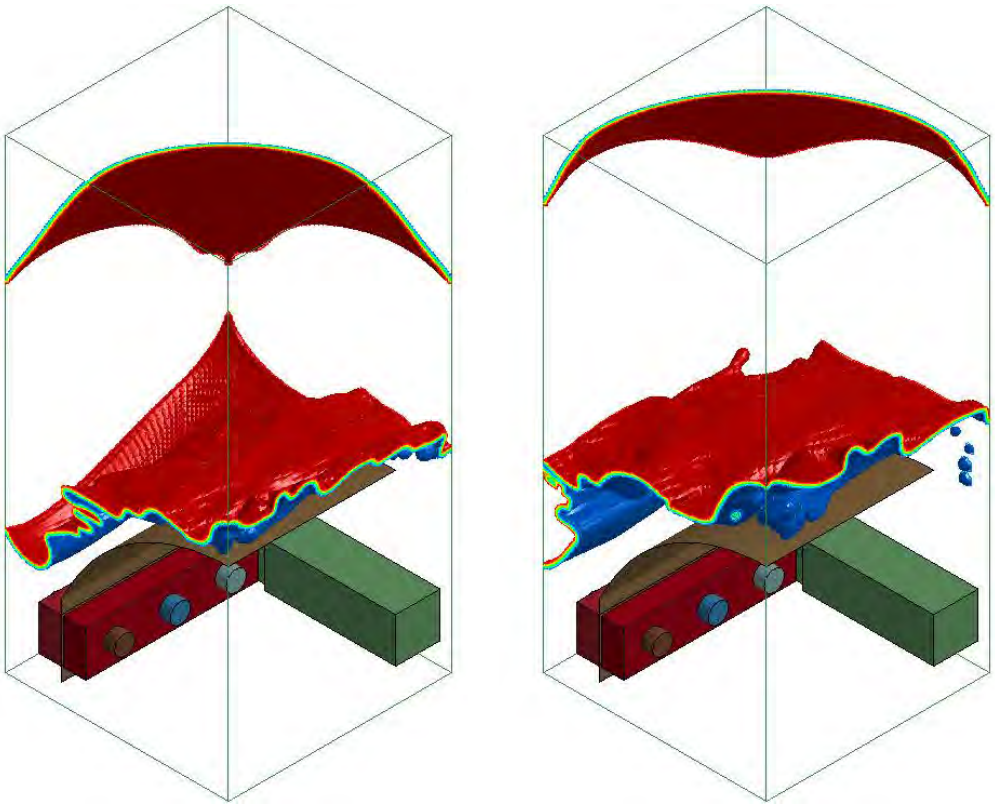

(c) t = 100 µs (d) t = 150 µs

Figure 6.6: Explosive development for a 60° V-plate with a bend radius of 160 mm and a 58 g charge from 0 to 200 µs

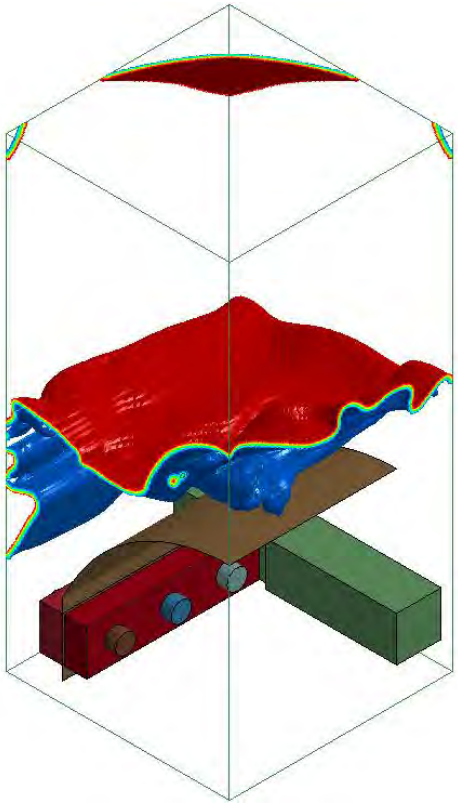

(e) t = 200 µs

Figure 6.6: Explosive development for a 60° V-plate with a bend radius of 160 mm and a 58 g charge from 0 to 200 µs

6.1.2 Cutting planes and profile views used

Figure 6.7 shows the model and two cutting planes (*i.e.* the ridge profile and the crosscut planes). These two planes are shown as they are used in the analyses of the pressure and explosive development along the V-profile and along the ridge in the subsequent subsections.

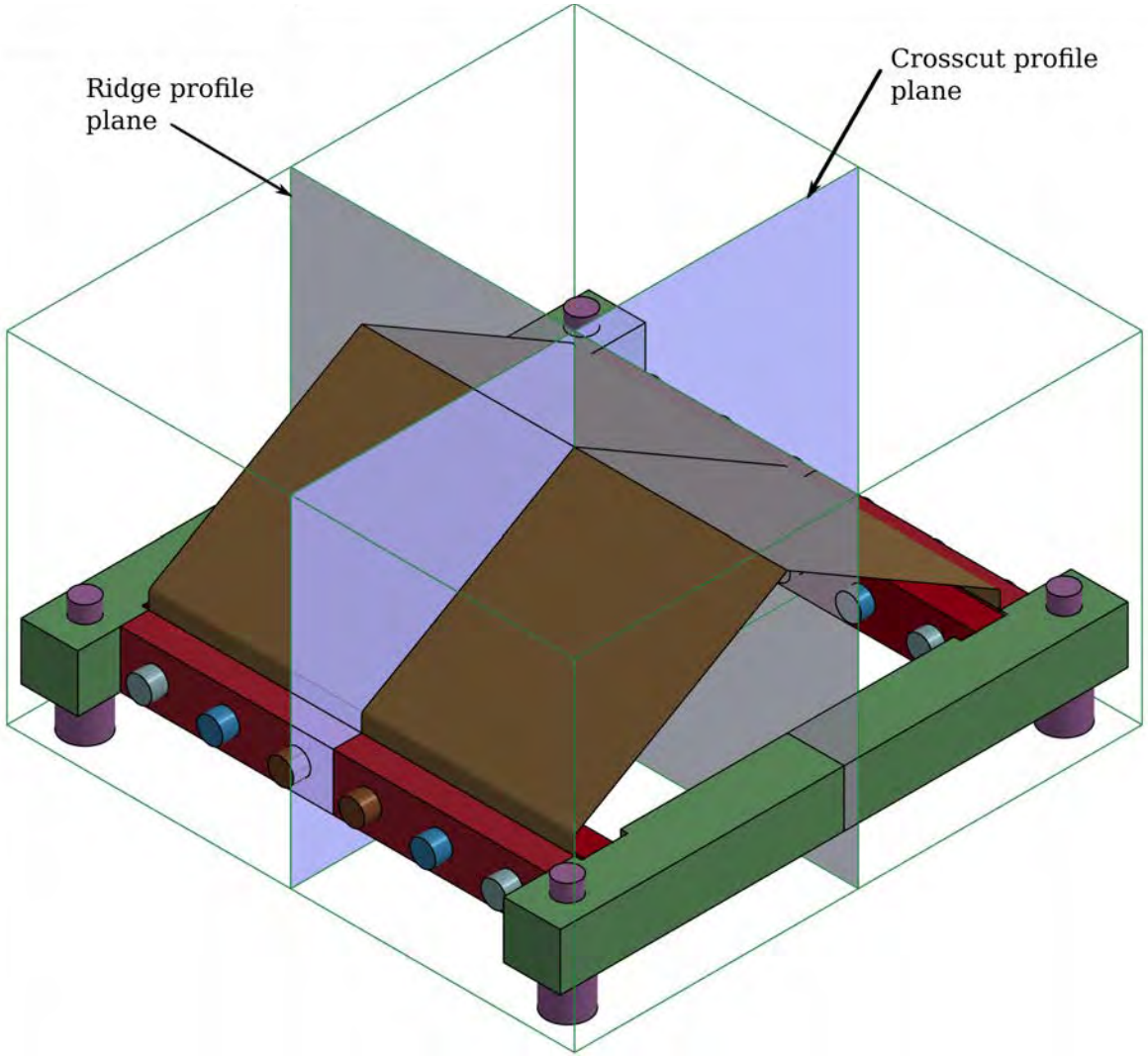

Figure 6.7: Schematic showing the ridge and crosscut profile views

6.2 60° V-plates, crosscut profile views

The pressure flow and velocity of the gas products were considered for a few different cases. Both the crosscut and ridge profile views are shown. This made it possible to determine what effect (if any) the bend radius had on the velocity of the gas products and the pressure distribution. All these simulations used 58 g detonations near plates with bend radii of 0, 30, 100 and 160 mm. These simulations were chosen as they included the minimum and maximum bend radii that could be investigated. The fringe levels were fixed for all the figures considered, with the pressure range set between 0 and 1100 MPa and the velocities were set between 0 and 7108 $\mathrm{m\,s^{-1}}$ as shown in Figure 6.8. The contour plots indicate the pressures and the arrows indicate the velocity (magnitude and direction) of the explosive products, for Figures 6.9 to 6.31.

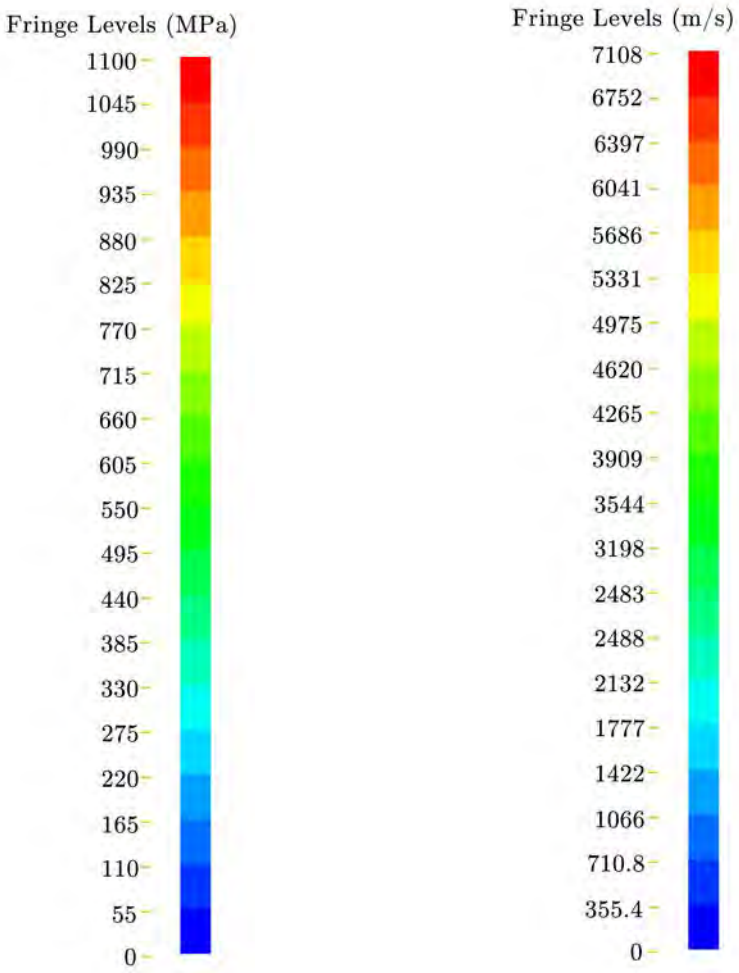

(a) Pressure fringe levels (in MPa) (b) Velocity fringe levels (in $\mathrm{m\,s^{-1}}$)

Figure 6.8: Pressure and velocity fringe levels used for all the subsequent figures of the field outputs (that is, Figures 6.9 to 6.31)

6.2.1 0 mm bend radius

Figure 6.9 shows the pressure and velocity histories along the V-profile for a plate with a 0 mm bend radius. Figures 6.9(a) and (b) show that, as expected, the maximum pressure was observed at the V-tip when the pressure wave reached the plate and started to move down. From Figures 6.9(c) and (d) it was evident that the maximum pressures were predominantly at the V-tip. By 30 µs the pressure wave had started to dissipate and the pressure levels were approaching zero in the tip region. The velocity vectors observed in Figure 6.9(d) show that the explosive products were flowing down along the V-plate and loading the rest of the V-plate. The velocity vectors at the surface of the plate were not flowing in the same directions as the rest of the distribution for times shown. Further analysis is presented in Section 6.4.

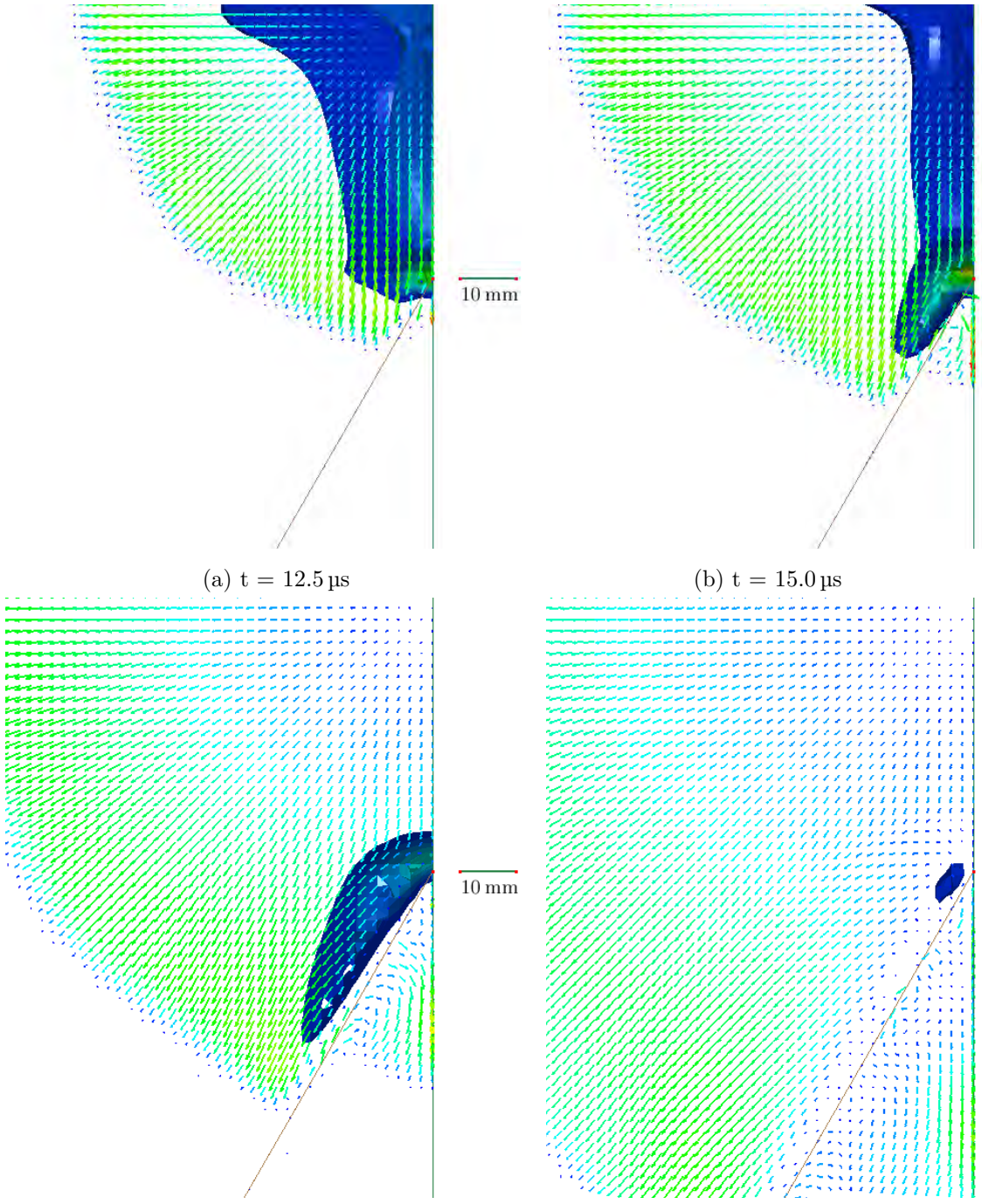

(a) t = 12.5 µs (b) t = 15.0 µs

(c) t = 20.0 µs (d) t = 30.0 µs

Figure 6.9: Crosscut profile view showing the pressure time history development and material velocity for a 60° V-plate with a bend radius of 0 mm and a 58 g charge

6.2.2 30 mm bend radius

The pressure and velocity histories along the V-profile for a plate with a 30 mm bend radius are shown in Figure 6.10. From Figures 6.10(a) and (b), it can be seen that once again the maximum pressure occurred at the V-tip, but unlike the sharp tipped V-plate shown in Figure 6.9(a), the maximum pressure acted over a larger area. Additionally, comparing Figure 6.10(d) and Figure 6.9(d), it was evident that the pressure had not completely dissipated for the plate with a 30 mm bend radius by 30 µs and was still loading the plate. At 30 µs, the velocity of the gas products flowing down the plate was similar to that observed in Figure 6.9(d), although the flow was less uniform and appeared to be flowing at a different angle to the V-angle. At 15 µs and 20 µs there appears to be more circulation (Eddy formation) for a 30 mm bend radius when compared to a 0 mm bend radius, this would be expected as the more circular profile would allow the flow to develop behind the plate. The magnitude of these Eddies reduces significantly around 30 µs and the flow behind the plate becomes more uniform.

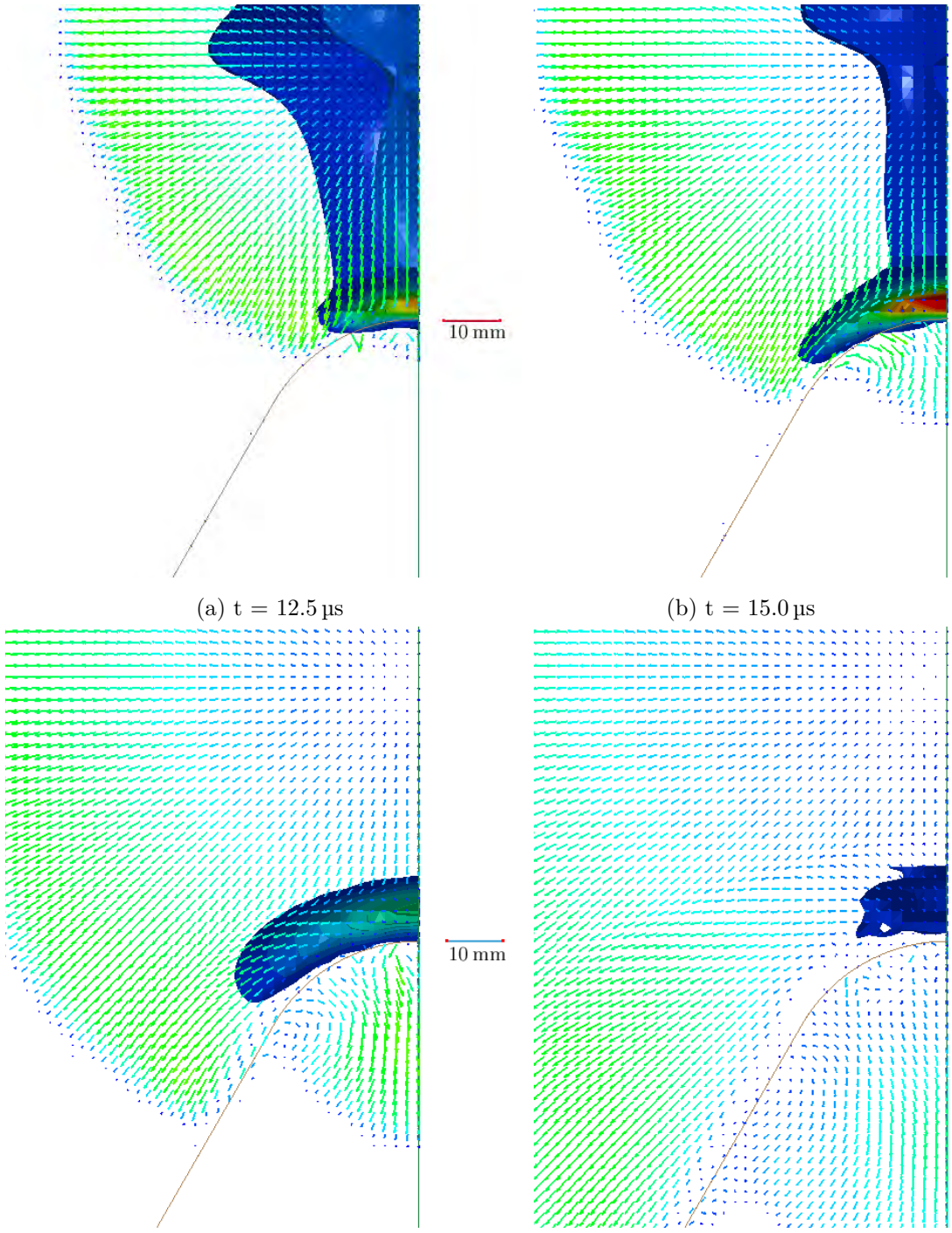

(a) t = 12.5 µs (b) t = 15.0 µs

(c) t = 20.0 µs (d) t = 30.0 µs

Figure 6.10: Crosscut profile view showing the pressure time history development and material velocity for a 60° V-plate with a bend radius of 30 mm and a 58 g charge

6.2.3 100 mm bend radius

Figure 6.11 shows the pressure and velocities histories for the crosscut profile view of a V-plate with a bend radius of 100 mm. It can be seen that the curvature effect was more significant than the V-angle at this bend radius, as the pressure wave remained only on the curved portion of the plate. When the pressures were compared with the smaller radius crosscut profiles in Figures 6.9 and 6.10, it can be seen that the maximum pressure occurred over a greater portion of the plate. By 30 µs the pressure wave was still present at the V-tip but had dissipated after 35 µs. The magnitude of the velocity observed at 30 µs was higher than that observed at lower V-tip radius plates and the flow was less uniform. Once again, Eddies with a high velocity form behind the plate at 15 µs. Unlike the V-plate with a 30 mm bend radius in Figure 6.10, the circulation behind the plate was still visible at 30 µs and only becomes more uniform by 35 µs.

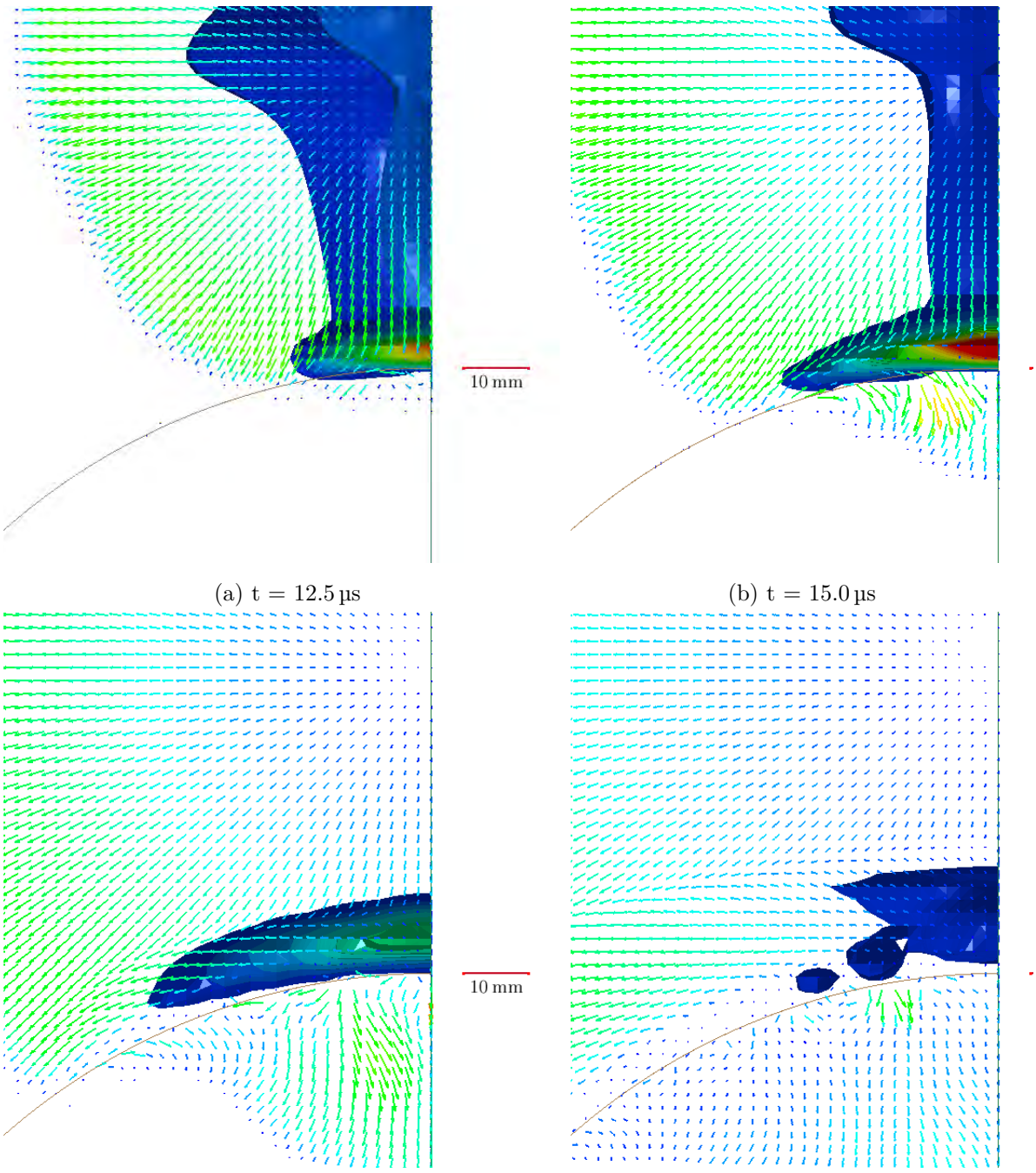

(a) t = 12.5 µs (b) t = 15.0 µs

(c) t = 20.0 µs (d) t = 30.0 µs

Figure 6.11: Crosscut profile view showing the pressure time history development and material velocity for a 60° V-plate with a bend radius of 100 mm and a 58 g charge

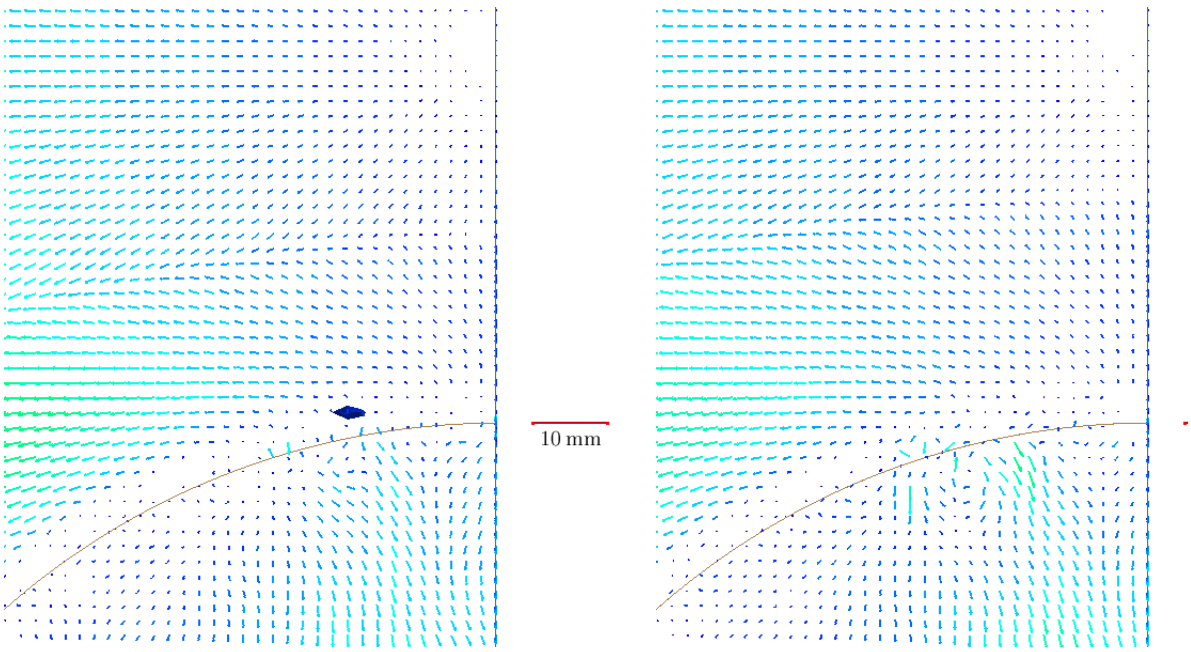

(a) t = 35.0 µs (b) t = 40.0 µs

Figure 6.11: Crosscut profile view showing the pressure time history development and material velocity for a 60° V-plate with a bend radius of 100 mm and a 58 g charge

6.2.4 160 mm bend radius

Figure 6.12 shows the pressure and velocities histories for the crosscut profile view of a V-plate with a bend radius of 160 mm. When compared to the 100 mm radius plate in Figure 6.11 it is evident that the pressure histories along the V-profile were almost identical (in terms of the pressure development and the maximum pressures). The peak pressure appears to act over a slightly larger area for the 100 mm bend radius while the magnitude of the velocity observed at 30 µs appears to be greater than that observed in Figure 6.11(d). The shape of the gas flow was very similar to the 100 mm bend radius simulation and the pressure dissipated by 35 µs. A similar formation of Eddies at the V-tip behind the V-plate was observed, though they appear to dissipate by

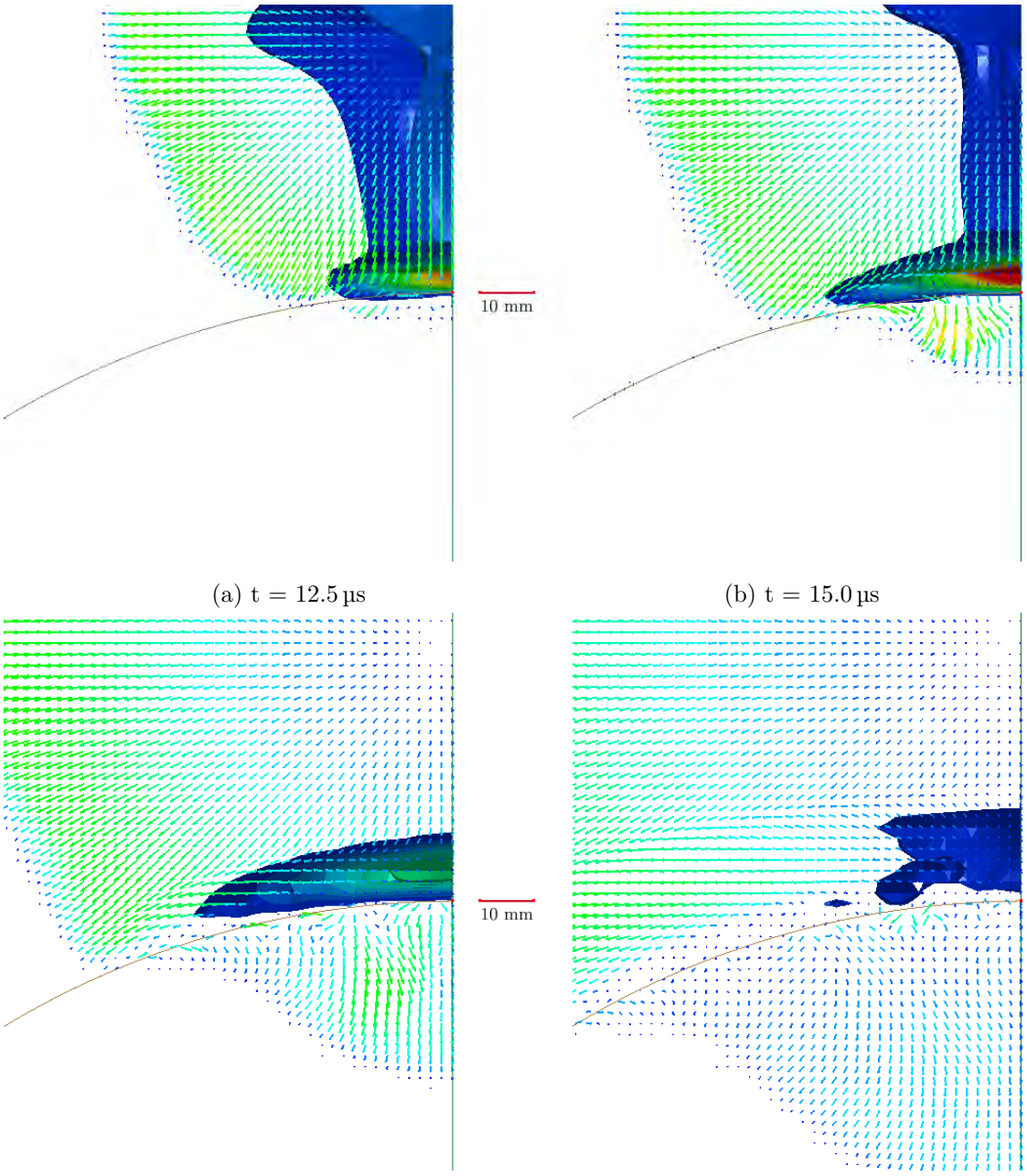

(a) t = 12.5 µs (b) t = 15.0 µs

(c) t = 20.0 µs (d) t = 30.0 µs

Figure 6.12: Crosscut profile view showing the pressure time history development and material velocity for a 60° V-plate with a bend radius of 160 mm and a 58 g charge

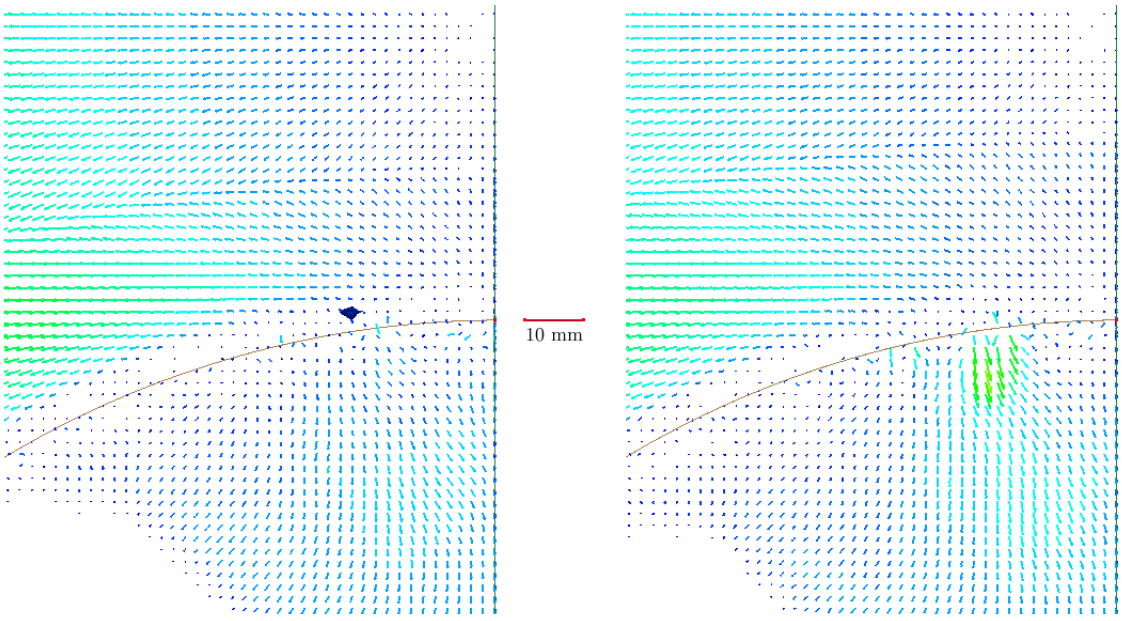

(a) t = 35.0 µs (b) t = 40.0 µs

Figure 6.12: Crosscut profile view showing the pressure time history development and material velocity for a 60° V-plate with a bend radius of 160 mm and a 58 g charge

6.3 60° V-plates, ridge profile views

6.3.1 0 mm bend radius

Comparisons were made between the pressure and velocity time history along the ridge for the minimum and maximum bend radii investigated as shown in Figures 6.13 and 6.14. Figures 6.13(a) and (b) and Figures 6.14(a) and (b) show that the maximum pressure and the pressure distribution do not vary as the bend radius was increased from 0 mm to 160 mm. This was expected as the ridge does not change between the two tests. From the crosscut analyses it was seen that at 30 µs the pressure had not dissipated for the plates with the larger bend radii. Once again this effect was seen when the ridge profiles were analysed. For a bend radius of 0 mm the gas velocity behind the V-plate appears to be much larger than the gas velocity for the 160 mm bend radius V-plate. This flow is predominantly directed downwards and can be attributed to the explosive materials impinging on the V-plate at the sharp V-tip.

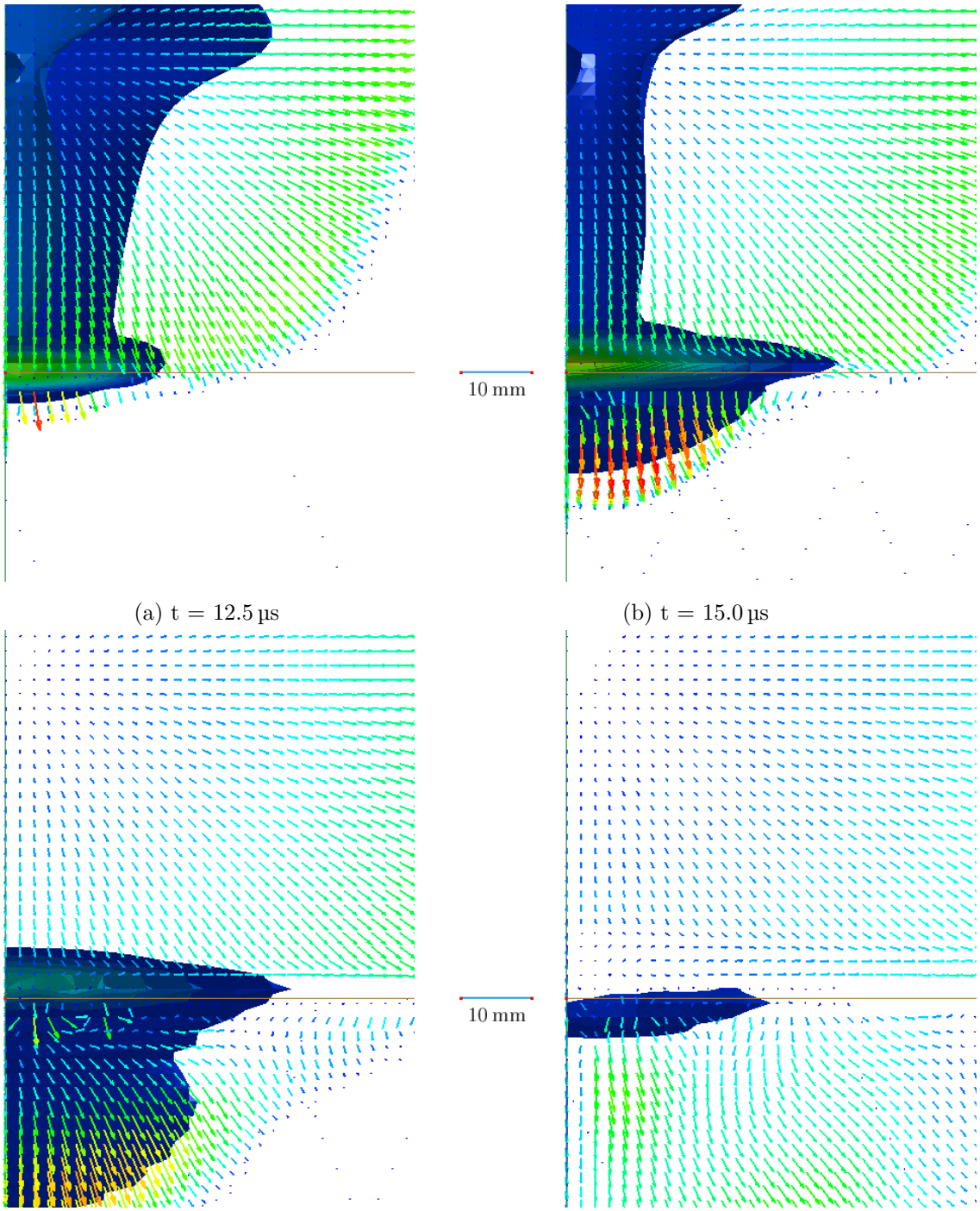

(a) t = 12.5 µs (b) t = 15.0 µs

(c) t = 20.0 µs (d) t = 30.0 µs

Figure 6.13: Ridge profile view showing the pressure time history development and material velocity for a 60° V-plate with a bend radius of 0 mm and a 58 g charge

6.3.2 160 mm bend radius

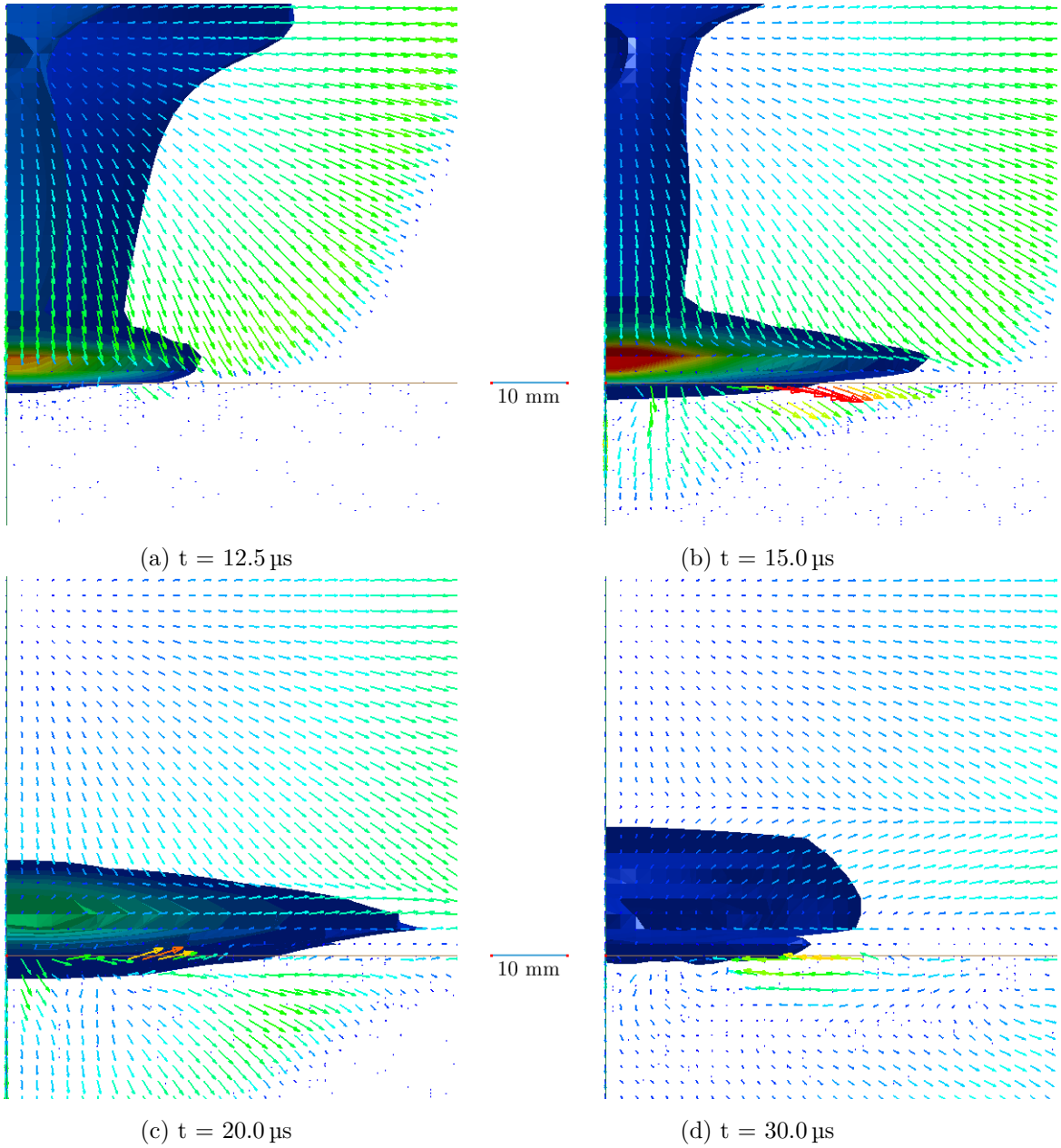

(a) t = 12.5 µs (b) t = 15.0 µs

(c) t = 20.0 µs (d) t = 30.0 µs

Figure 6.14: Ridge profile view showing the pressure time history development and material velocity for a 60° V-plate with a bend radius of 160 mm and a 58 g charge

6.4 60° V-plates, velocity vector analysis

Figures 6.15 to 6.17 show magnified views of sub-figures (b) and (d) in each of Figures 6.9, 6.10 and 6.12 respectively. This was done so that the velocity vectors along the V-profile could be investigated for the different bend radii. It can be seen from Figure 6.15 that the majority of the gas products followed the direction of the V-plate and travelled down the plate for a 0 mm bend radius. This is shown by the velocity vectors following the 60° V-angle. Figures 6.16 and 6.17 show that, as the bend radius is increased, more of the gas products moved in the lateral direction and hence did not move down the plate; this effect becomes more pronounced as the bend radius increases. As expected the gas products at the surface of the V-plate were not flowing in the same direction as the rest of the explosive products and had a lower magnitude. This was due to surface friction on the V-plate. The effect was the same for all the V-angles and bend radii and thus was dependant on the fluid flow (rather than the geometry of the V-plates).

For the 0 mm bend radius at 30 µs, the gas flow was parallel to the plate (30° to the vertical) closer to the plate. Further from the plate, the angle of the flow was larger (approximately 45° to the vertical). This is due to both the detonation and the reflection of the pressure wave off the surface V-plate.

At a bend radius of 30 mm at 30 µs the gas flow close to the plate followed a more shallow angle (approximately 45°) when compared to the 30° angle observed for the 0 mm bend radius. The flow was more lateral further away from the plate surface with an angle of approximately 65°. The 160 mm bend radius showed a similar flow pattern to the 30 mm bend radius, with largely lateral flow further away from the plate at an angle which was greater than 65°.

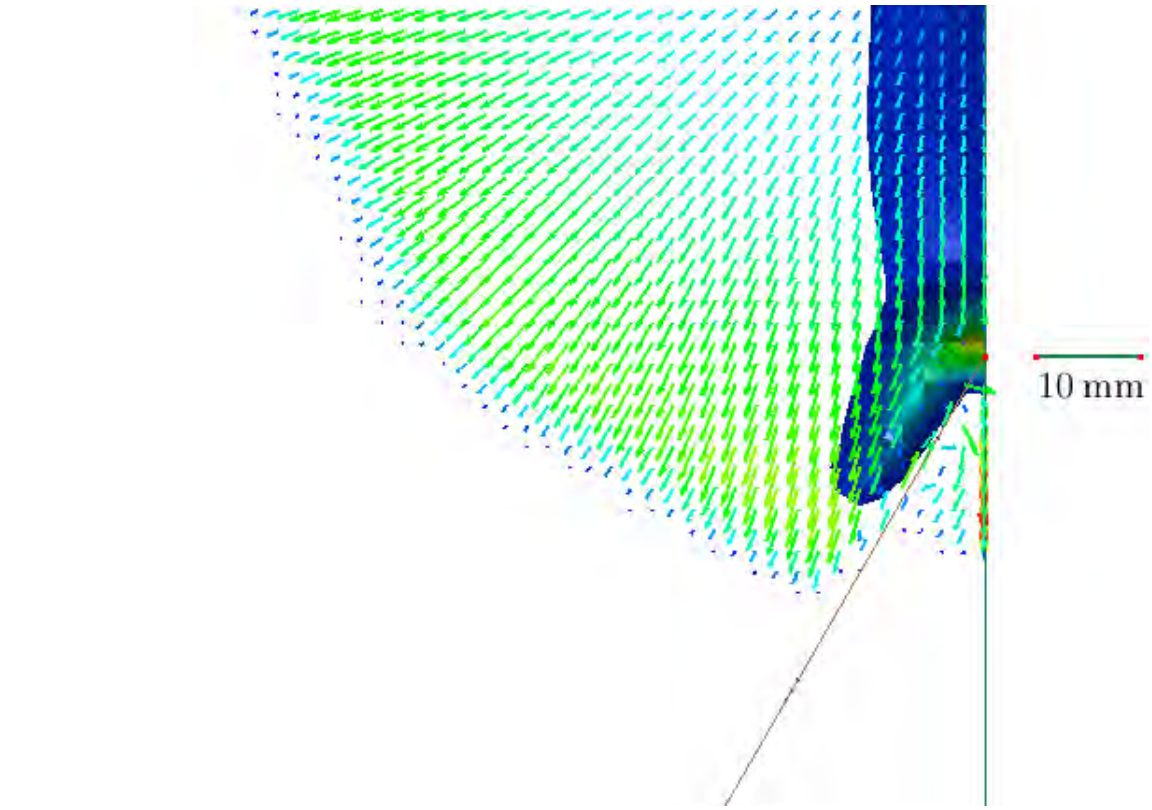

(a) t = 15 µs

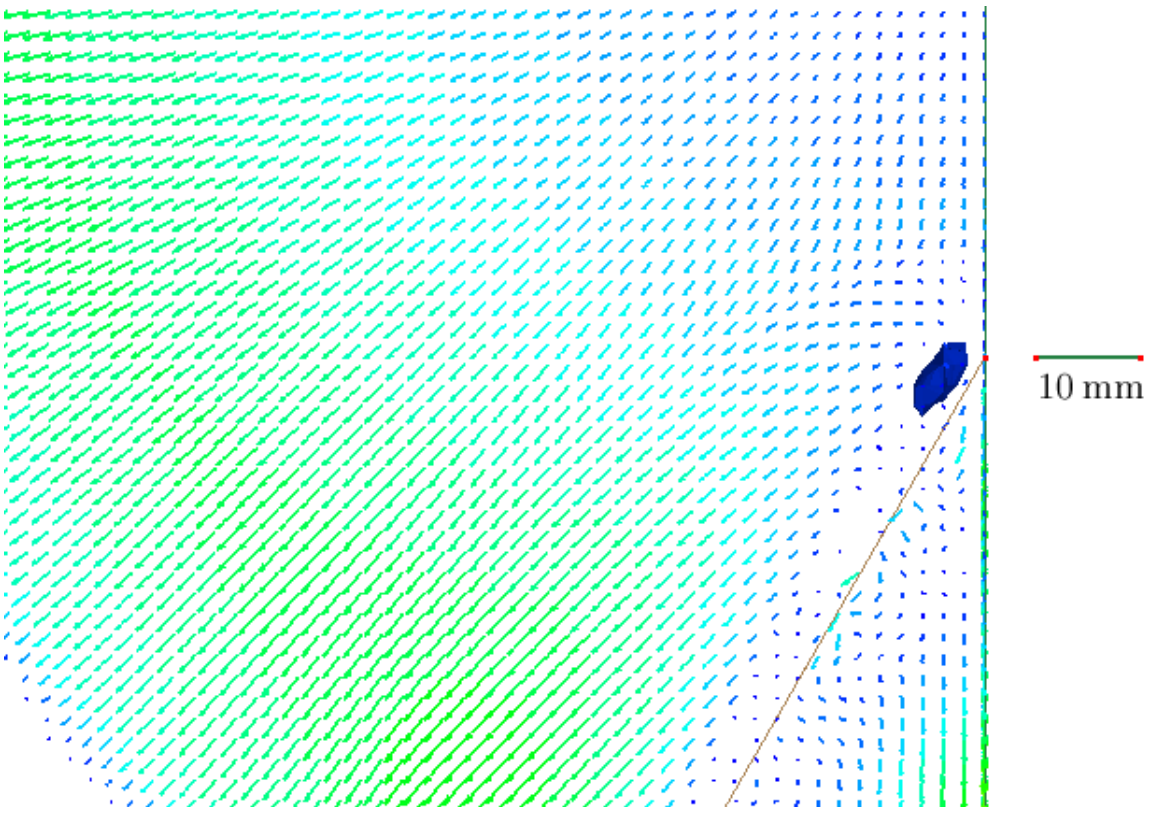

(b) t = 30 µs

Figure 6.15: Magnified view of the crosscut profile view showing the pressure time history development and material velocity for a 60° V-plate with a bend radius of 0 mm and a 58 g charge at 15 and 30 µs

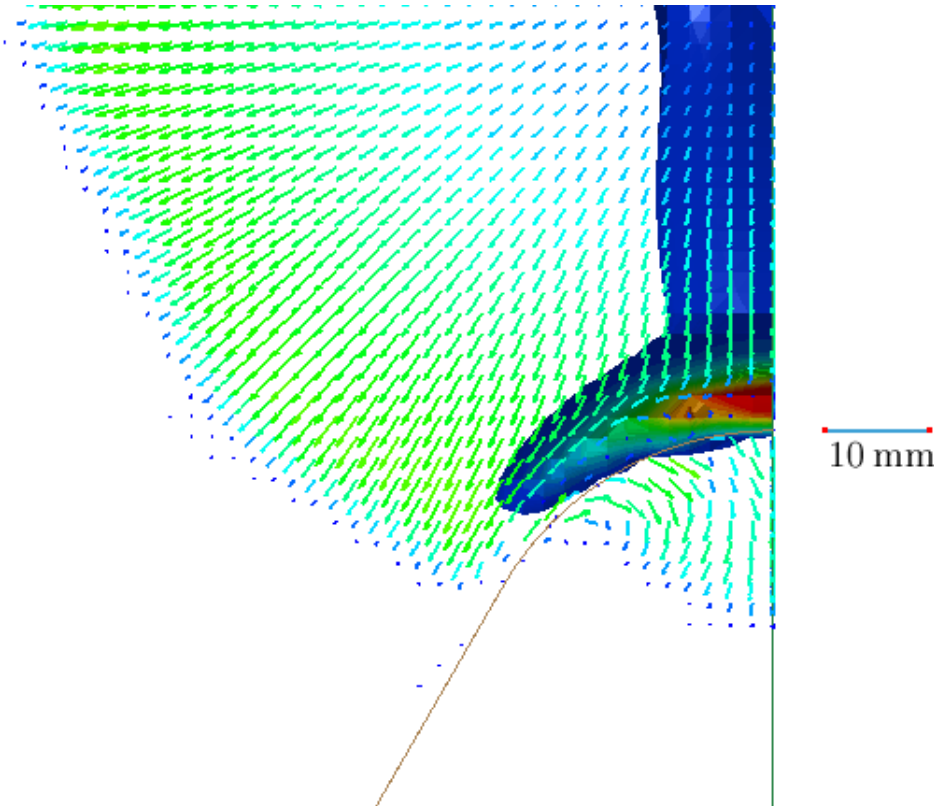

(a) t = 15 µs

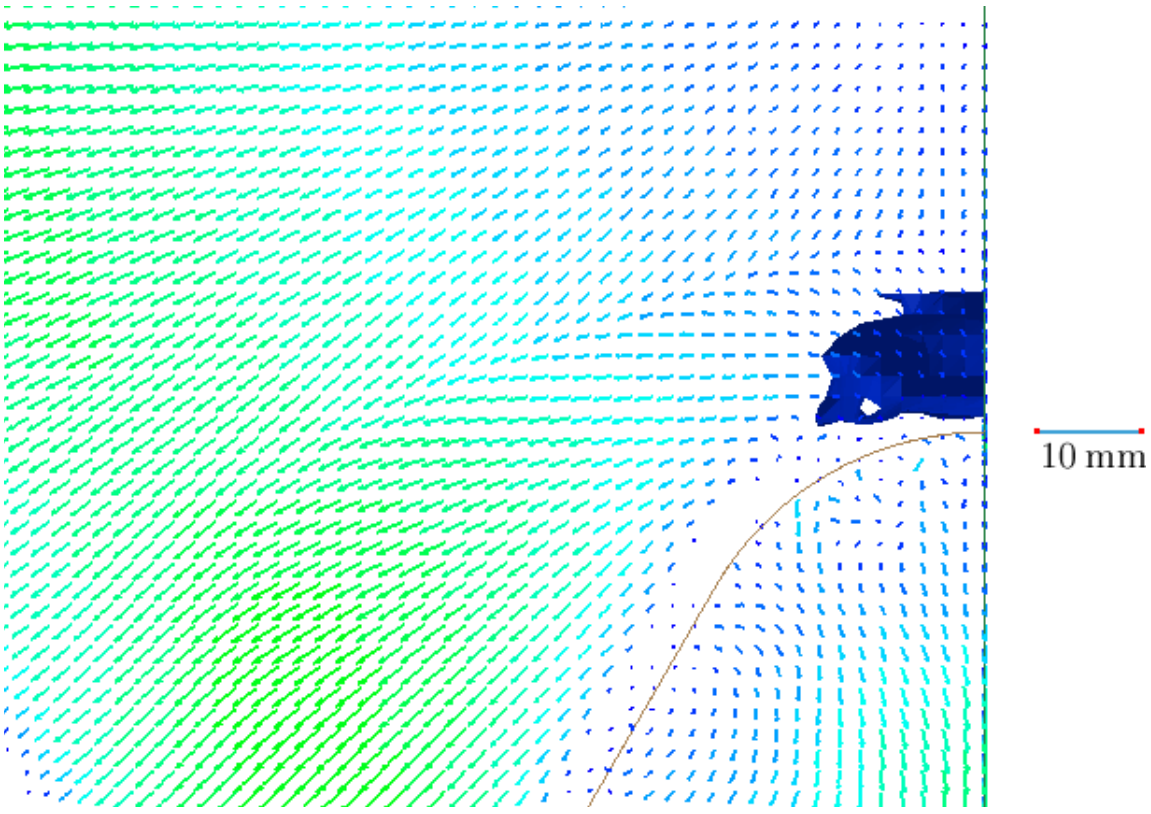

(b) t = 30 µs

Figure 6.16: Magnified view of the crosscut profile view showing the pressure time history development and material velocity for a 60° V-plate with a bend radius of 30 mm and a 58 g charge at 15 and 30 µs

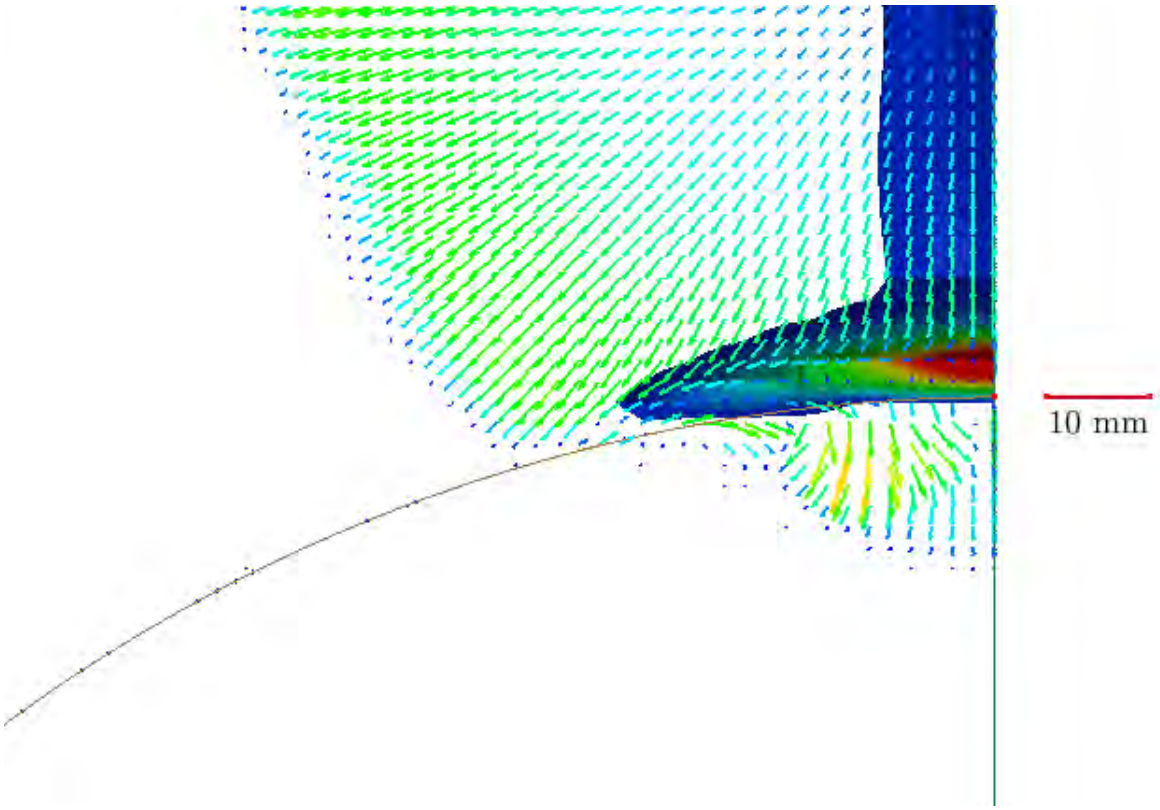

(a) t = 15 µs

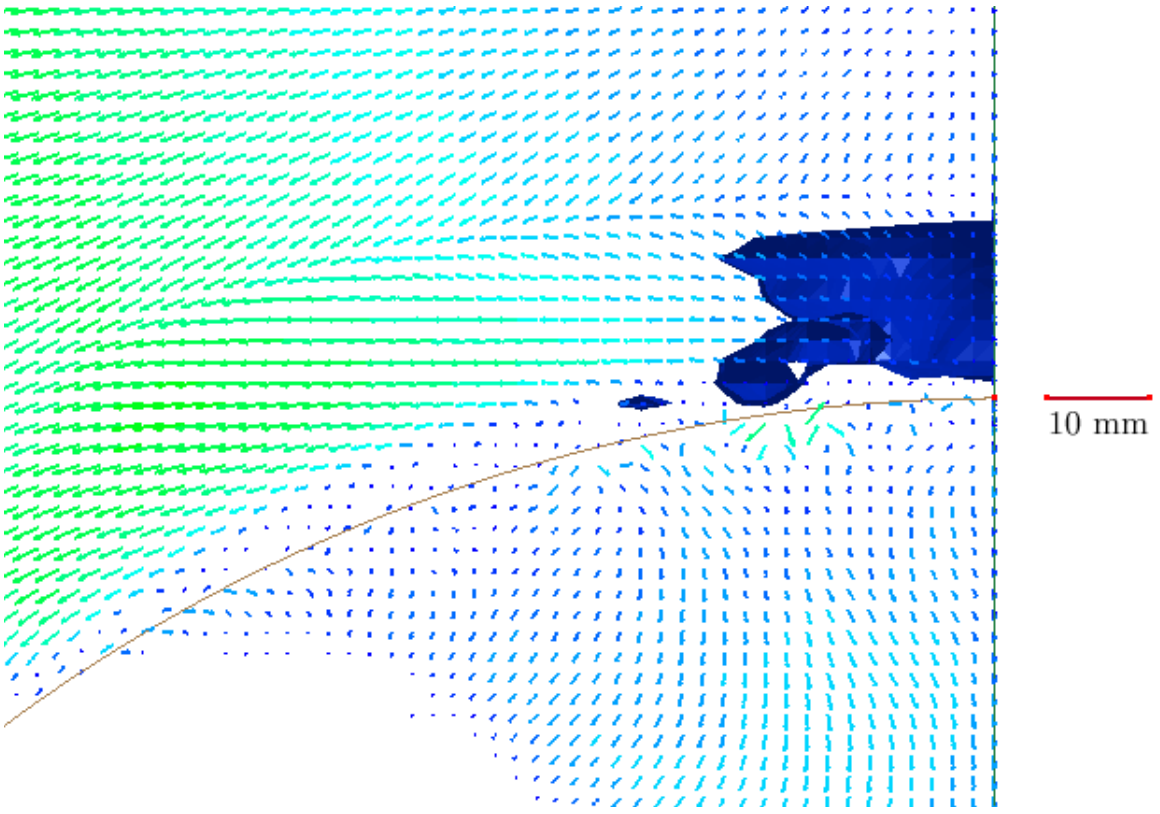

(b) t = 30 µs

Figure 6.17: Magnified view of the crosscut profile view showing the pressure time history development and material velocity for a 60° V-plate with a bend radius of 160 mm and a 58 g charge at 15 and 30 µs

6.5 90° V-plates

The effects of the bend radius on the development of explosive products in the 90° V-plate simulations were similar to those observed for the 60° V-plates in Figures 6.5 and 6.6. Figures which show the explosive material distribution for these cases can be found in Appendix D.

6.5.1 Crosscut profile views

The pressure-time and velocity-time histories of the explosive gas products were plotted for bend radii of 0, 160 and 200 mm and a 58 g charge mass and are shown in Figures 6.18 to 6.20. Figure 6.18 shows the pressure-time history of the crosscut profile view for a 90° V-plate with a 0 mm bend radius. From Figure 6.18(a) it can be seen that the maximum pressure was concentrated at the tip of the V-plate. From Figures 6.18(b) and (c) it can be seen that the pressure distribution was similar to that observed for the 60° V-plate with a 0 mm bend radius, where the pressure wave travels down the plate and decreases in magnitude. At 30 µs the pressure wave had begun to dissipate, although the effect was less significant than that seen for the 60° V-plate with a 0 mm bend radius at the same time.

Figures 6.19 and 6.20 show the pressure and velocity time-histories of the crosscut profile view for a 90° V-plate with a 160 mm and 200 mm bend radius respectively. When compared with Figure 6.18, it can be seen that the peak pressure at the top of the V was greater for the simulations with the larger bend radius, and that the peak pressure acted over a larger area. At 30 µs, the pressure wave had not dissipated from the top of the plate for the two simulations with large bend radii, when compared to the 0 mm bend radius simulation.

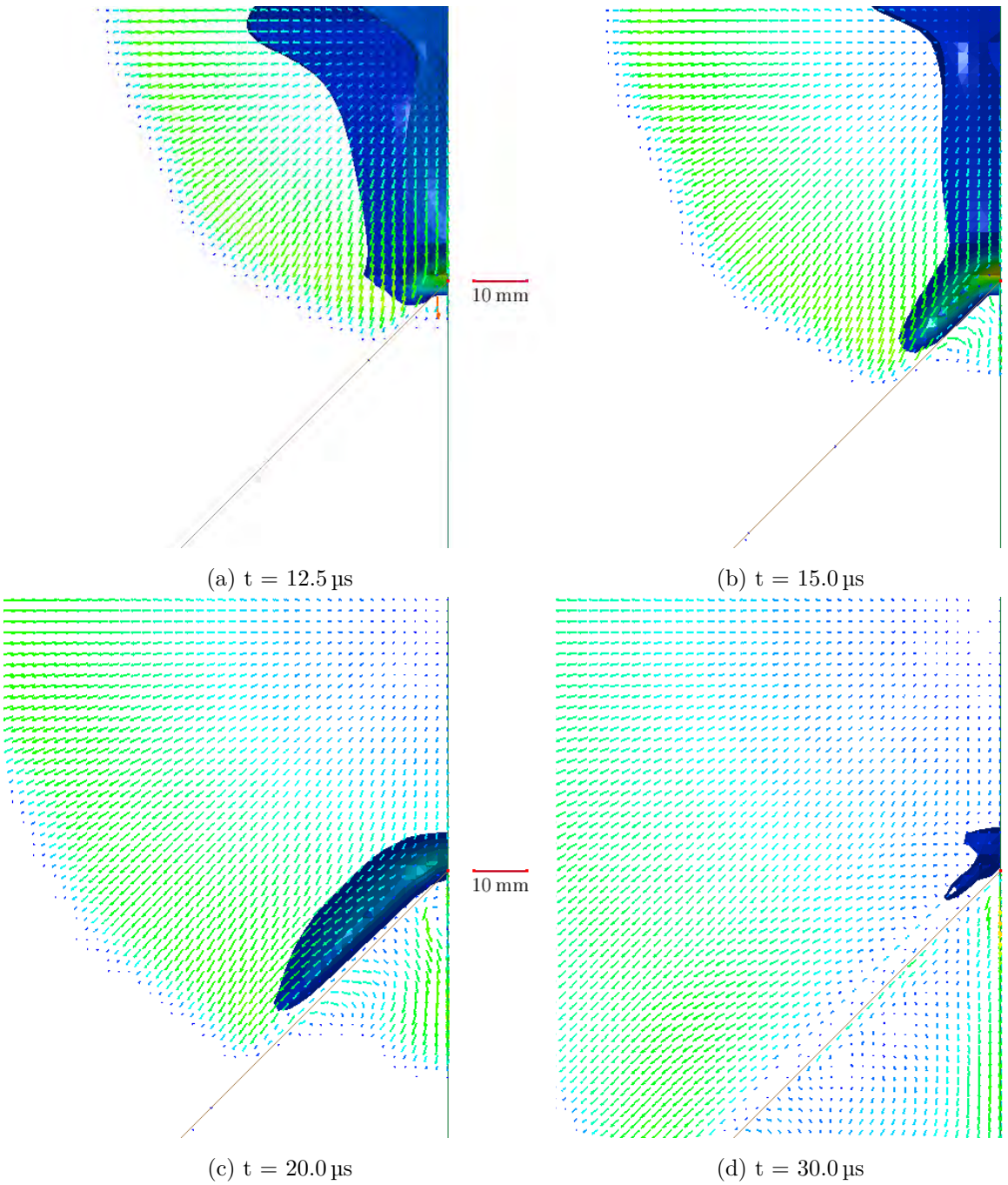

(a) t = 12.5 µs (b) t = 15.0 µs

(c) t = 20.0 µs (d) t = 30.0 µs

Figure 6.18: Crosscut profile view showing the pressure time history development and material velocity for a 90° V-plate with a bend radius of 0 mm and a 58 g charge

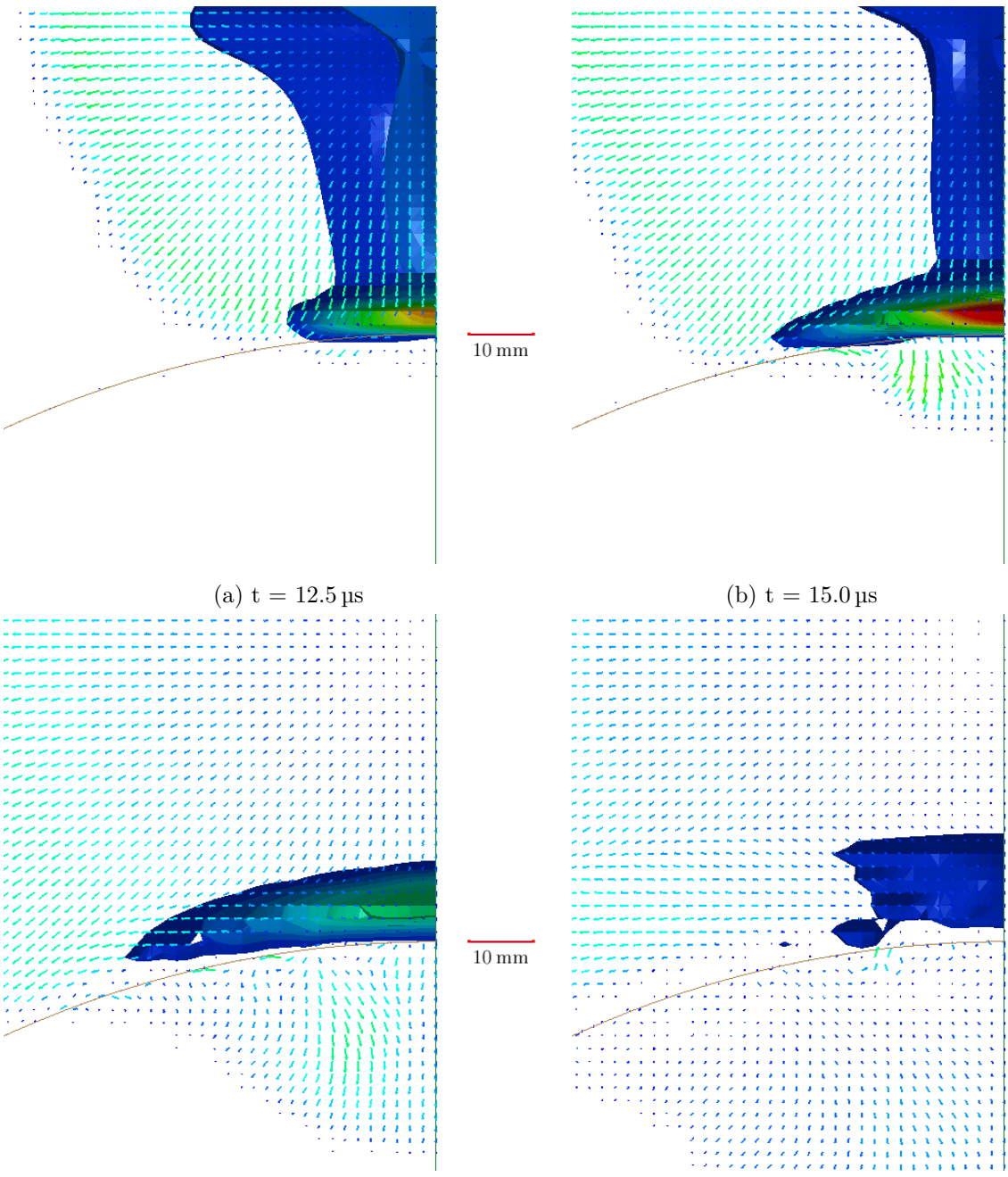

(a) t = 12.5 µs (b) t = 15.0 µs

(c) t = 20.0 µs (d) t = 30.0 µs

Figure 6.19: Crosscut profile view showing the pressure time history development and material velocity for a 90° V-plate with a bend radius of 160 mm and a 58 g charge

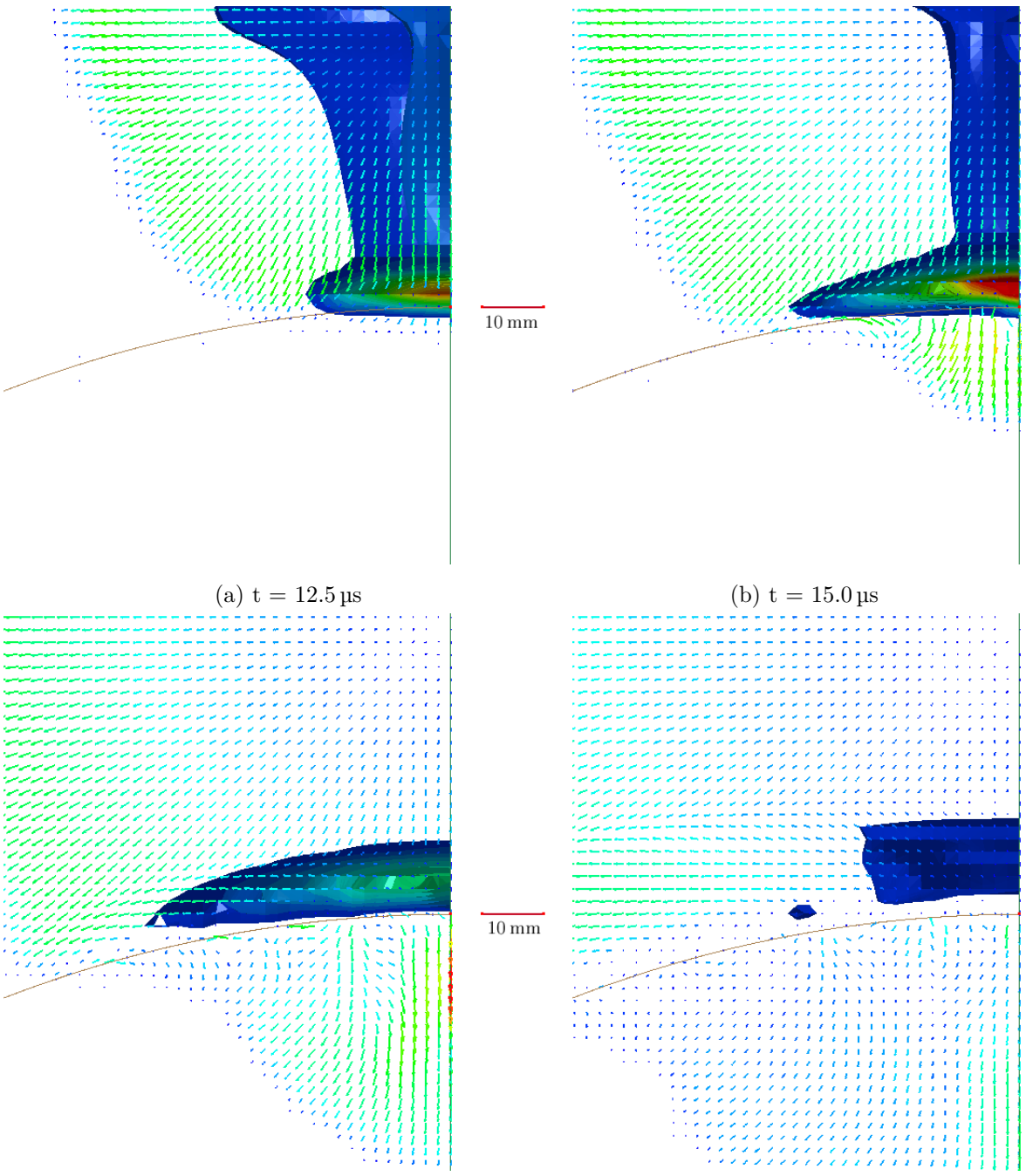

(a) t = 12.5 µs (b) t = 15.0 µs

(c) t = 20.0 µs (d) t = 30.0 µs

Figure 6.20: Crosscut profile view showing the pressure time history development and material velocity for a 90° V-plate with a bend radius of 200 mm and a 58 g charge

6.5.2 Velocity vector analysis

Figures 6.21 and 6.22 show zoomed in views of subfigures (b) and (d) in each of Figures 6.18 and 6.19 respectively. This was done to investigate the variation in the flow of the gas products for the different bend radii. It can be seen from Figure 6.21 that the gas products tended to follow the profile of the V-plate for the 0 mm bend radius. For large bend radii, more of the gas products travelled laterally rather than travelling down the plate, as shown in Figure 6.22. This effect becomes more pronounced as the bend radius increases.

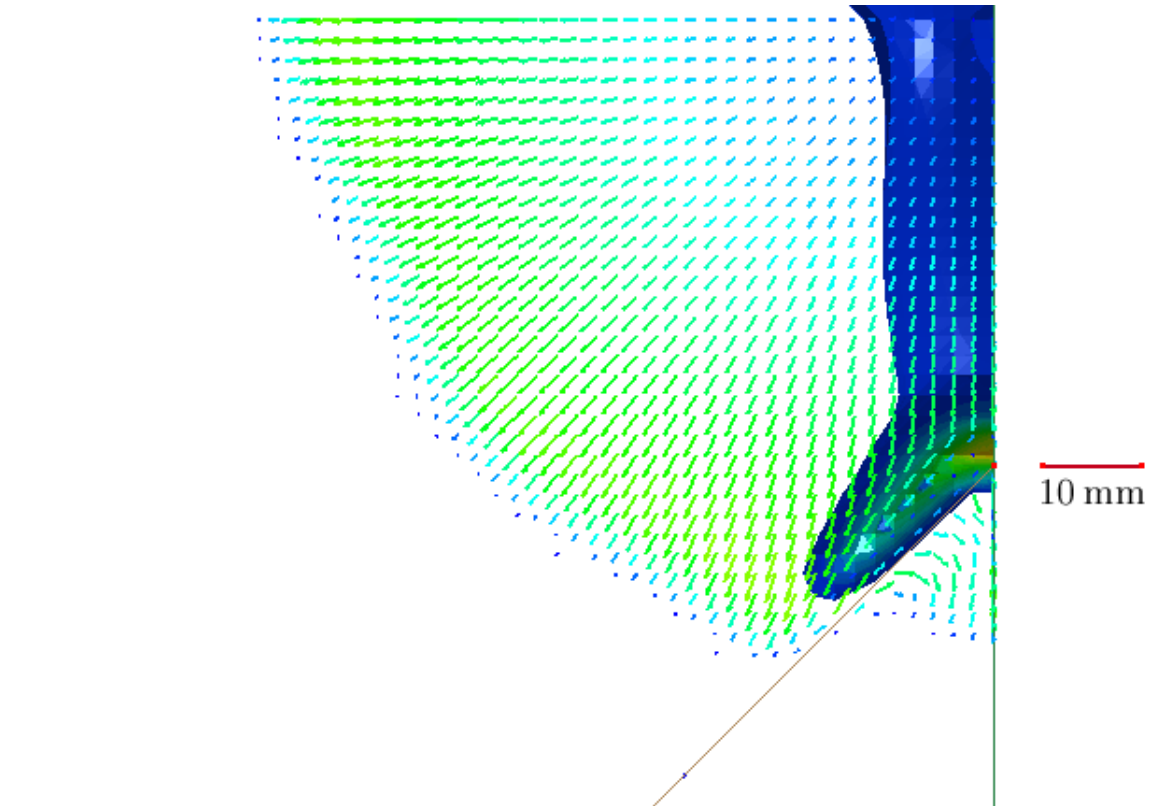

(a) t = 15 µs

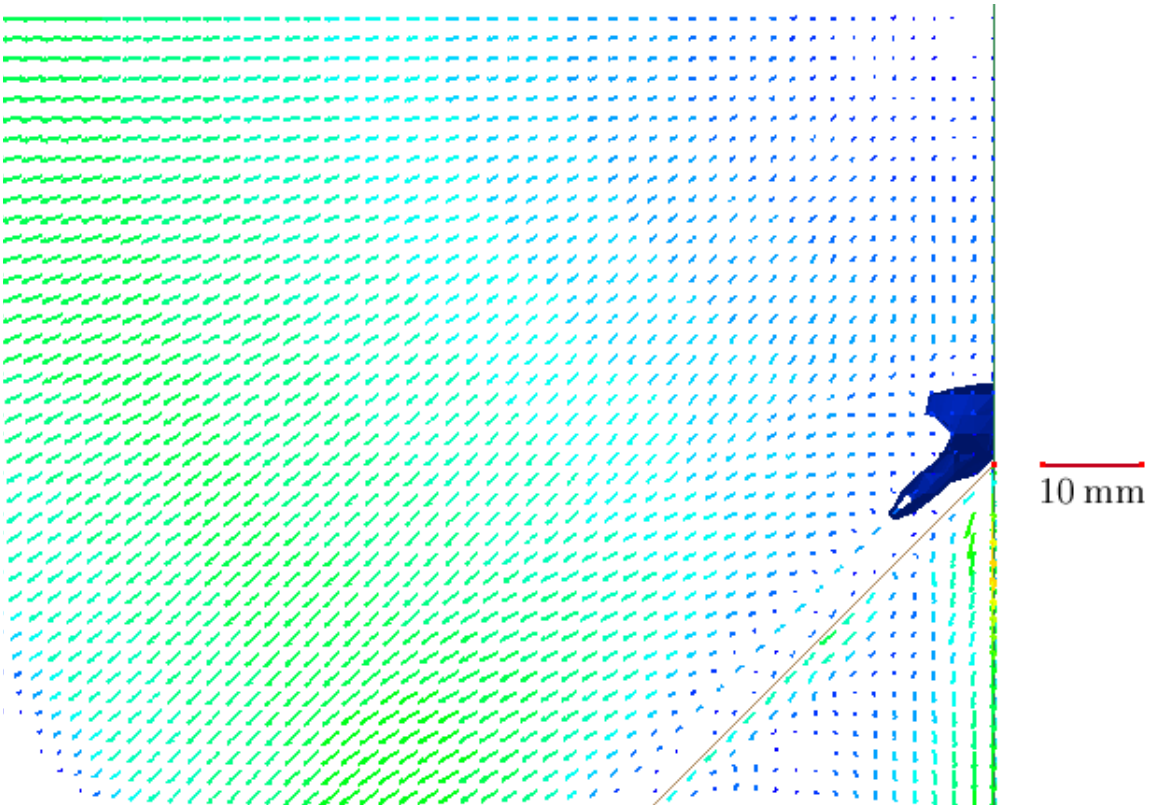

(b) t = 30 µs

Figure 6.21: Magnified view of the crosscut profile view showing the pressure time history development and material velocity for a 90° V-plate with a bend radius of 0 mm and a 58 g charge at 15 and 30 µs

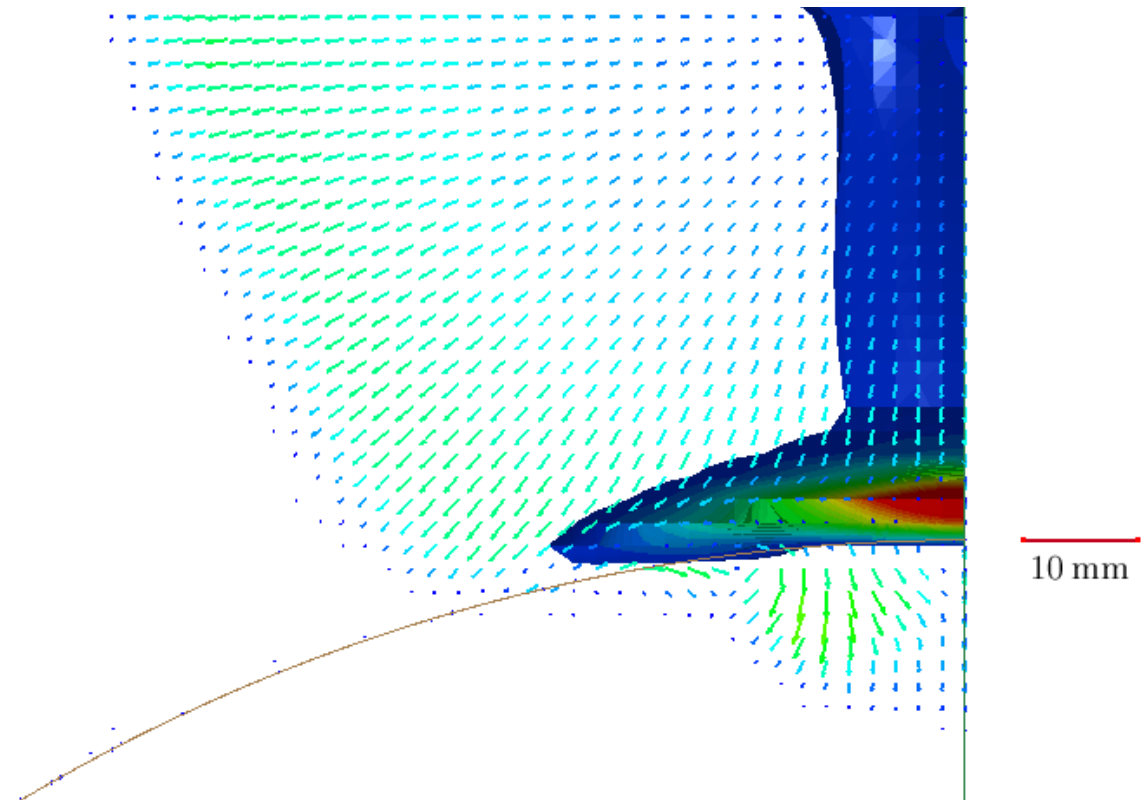

(a) t = 15 µs

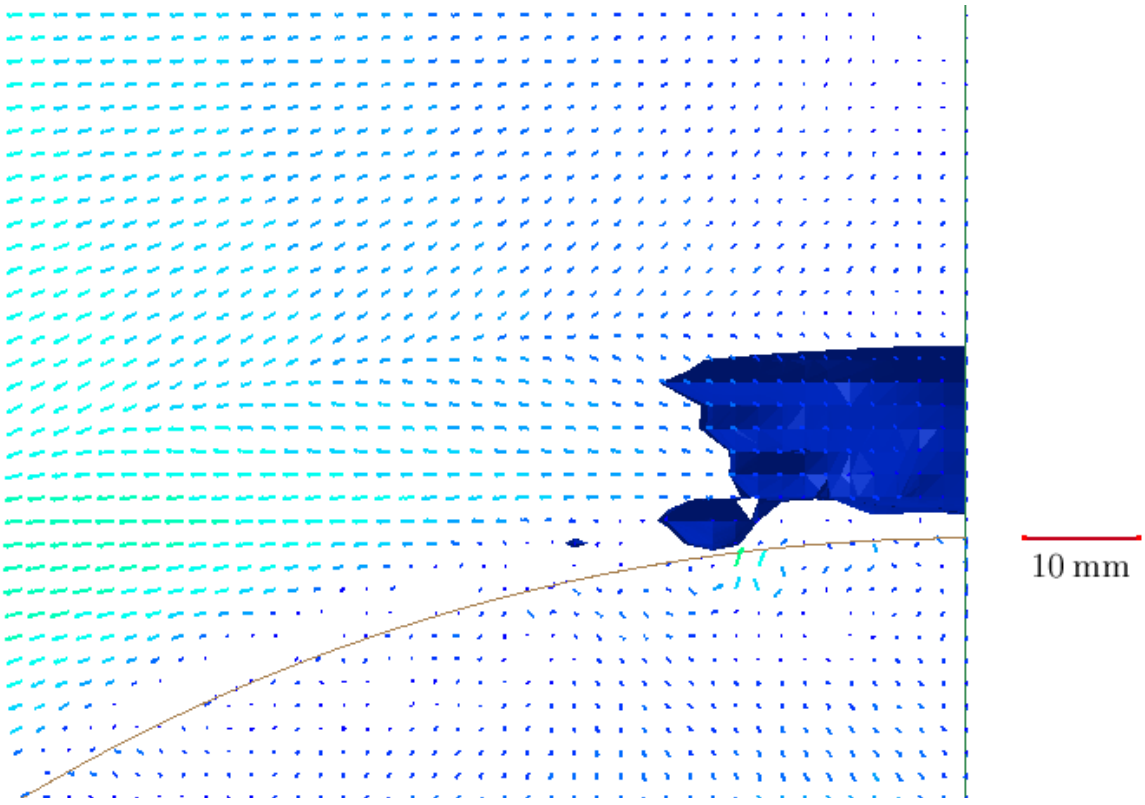

(b) t = 30 µs

Figure 6.22: Magnified view of the crosscut profile view showing the pressure time history development and material velocity for a 90° V-plate with a bend radius of 160 mm and a 58 g charge at 15 and 30 µs

6.5.3 Ridge profile views

The pressure and velocity time histories along the ridges of the V-plates for the minimum and maximum bend radii are shown in Figures 6.23 and 6.24. When Figure 6.23(a) is compared to Figure 6.24(a), it can be seen that there was an increase in the maximum pressure and the pressure distribution as the bend radius was increased from 0 mm to 200 mm. This was not observed for the 60° V-plate simulations. This greater distribution of the pressure wave continued throughout the loading, shown by comparing Figures 6.24(b) to (d) to Figures 6.23(b) to (d). The crosscut profile views show that the pressure had not dissipated for the plates with the larger bend radii after 30 µs. The same behaviour is observed for the ridge profile views. A possible explanation, for the pressure wave remaining at the V-tip for the larger bend radii, could be the lower velocities of the explosive material products.

For a 0 mm bend radius at 20 µs there appeared to be circulation behind the plate at the V-tip. These Eddies started to develop at 15 µs and appeared to dissipate by 30 µs. A similar effect was observed at a bend radius of 200 mm although the circulation was observed at 15 µs and the magnitude was much lower by 30 µs. A split was observed by 30 µs in the pressure distribution in Figure 6.22(d). This was the flow along the plate and the split is due to the view displayed.

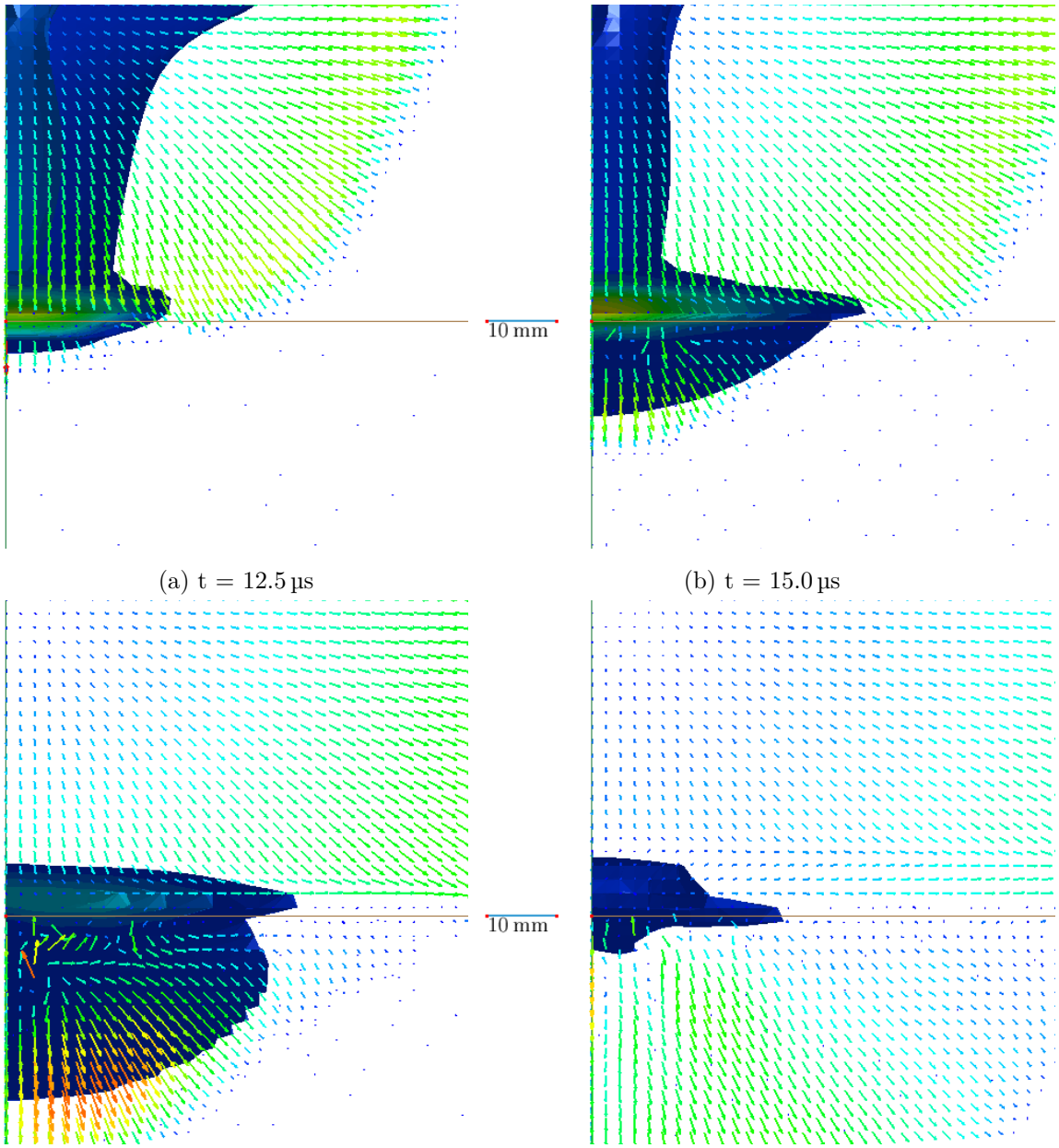

(a) t = 12.5 µs (b) t = 15.0 µs

(c) t = 20.0 µs (d) t = 30.0 µs

Figure 6.23: Ridge profile view showing the pressure time history development and material velocity for a 90° V-plate with a bend radius of 0 mm and a 58 g charge

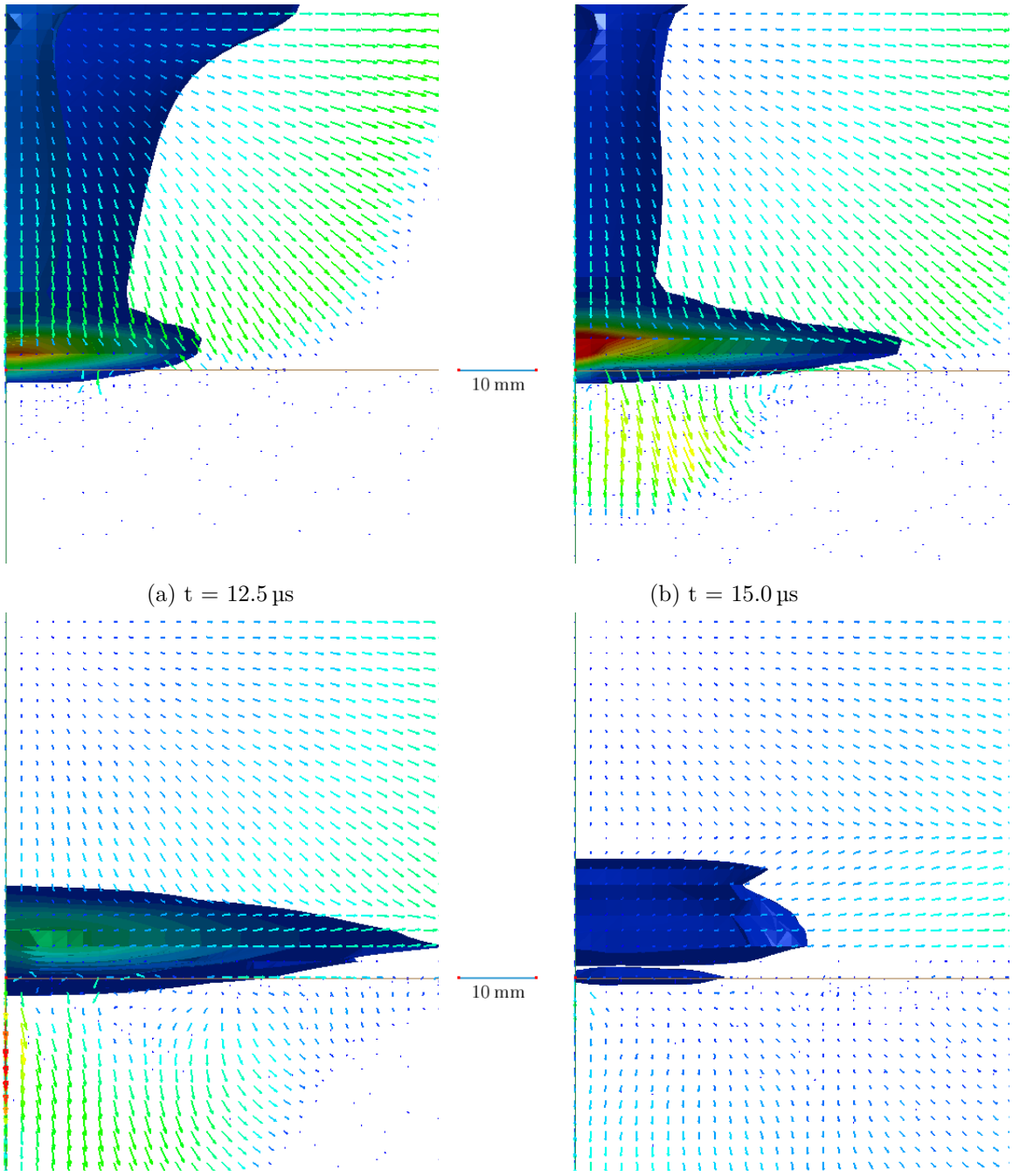

(a) t = 12.5 µs (b) t = 15.0 µs

(c) t = 20.0 µs (d) t = 30.0 µs

Figure 6.24: Ridge profile view showing the pressure time history development and material velocity for a 90° V-plate with a bend radius of 200 mm and a 58 g charge

6.6 120° V-plates

The 120° V-plates showed similar bend radius effects as the 60° and 90° V-plates, and the explosive material distributions for the full bend radii range are given in Appendix D.

6.6.1 Crosscut profile views

Some examples are shown at bend radii of 0, 160 and 280 mm, for a charge mass of 58 g, in Figures 6.25 to 6.27. Figure 6.25 shows the pressure distribution for the crosscut profile of a 120° V-plate with a 0 mm bend radius. In Figure 6.25(a) it can be seen that the maximum pressure acted over a larger area when compared Figure 6.9(a) and Figure 6.18(a). This is one of the reasons for the greater impulse observed for the larger V-angles. From Figures 6.25(b) and (c) it can be seen that the pressure distribution was similar to that observed for the 60° and 90° V-plates with a 0 mm bend radius, where the pressure wave travelled down the plate and decreased in magnitude. Finally it can be seen that, unlike Figure 6.9(d) and Figure 6.18(d), by 30 µs the pressure wave still remained at the tip of the V-plate and only dissipated by 35 µs.

Figures 6.26 and 6.27 show the pressure time-histories for 120° V-plates with a 160 mm and 280 mm bend radii respectively. The peak pressure at the V-tip was greater and acted over a larger area for the simulations with larger bend radii. Similar effects were observed for the 60° and 90° V-plates. By 30 µs, a greater portion of the pressure wave remained at the top of the plate for the two simulations with large bend radii, when compared to Figure 6.25. The velocity of the gas flow behind the V-plate at the V-tip appeared to be much greater for the 160 mm and 280 mm bend radii when compared to the 0 mm bend radius. The large velocities were observed at a later time for the 280 mm bend radius, although the circulation at the tip appears to be similar for the 160 mm and 280 mm bend radii.

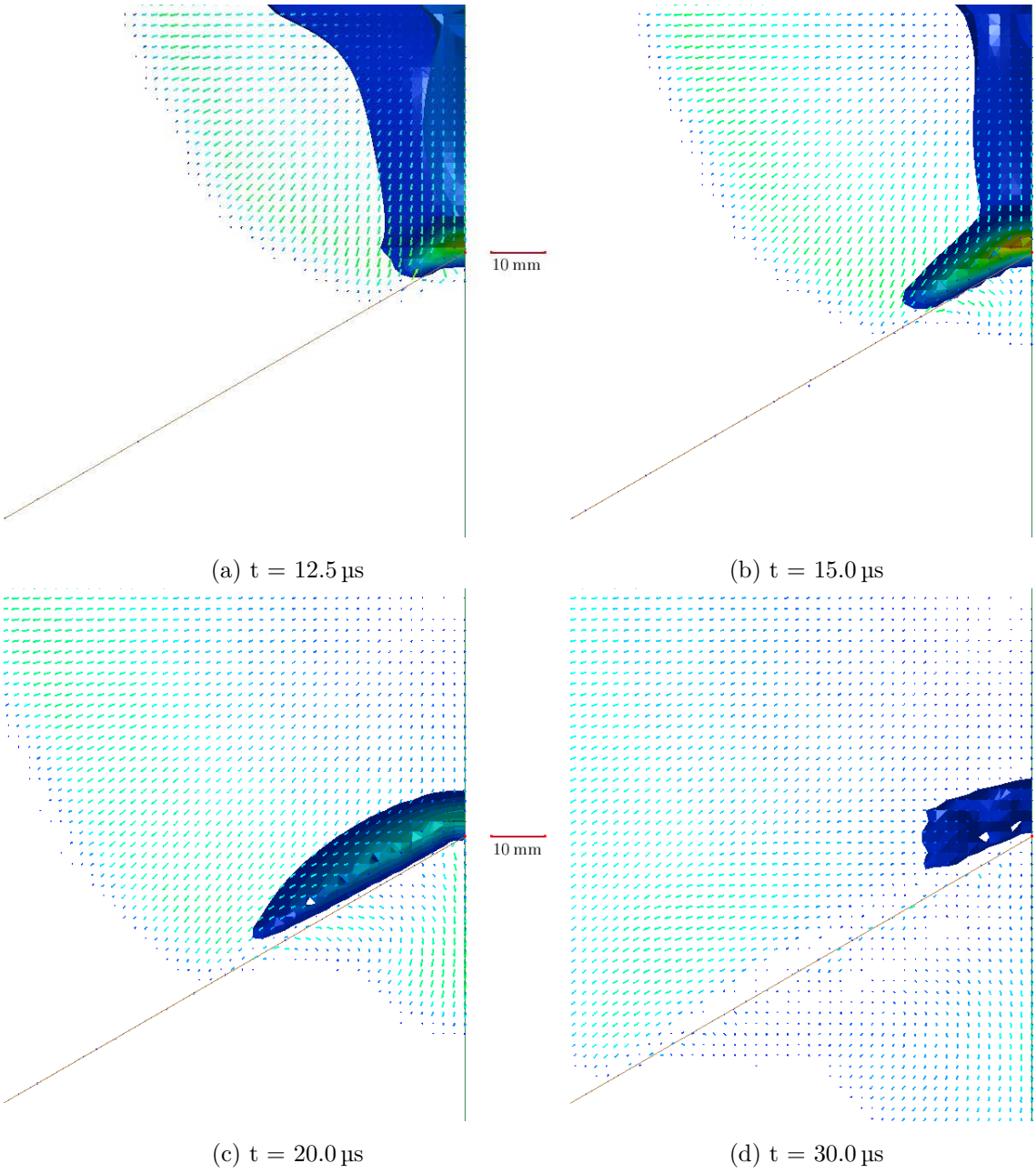

(a) t = 12.5 µs (b) t = 15.0 µs

(c) t = 20.0 µs (d) t = 30.0 µs

Figure 6.25: Crosscut profile view showing the pressure time history development and material velocity for a 120° V-plate with a bend radius of 0 mm and a 58 g charge

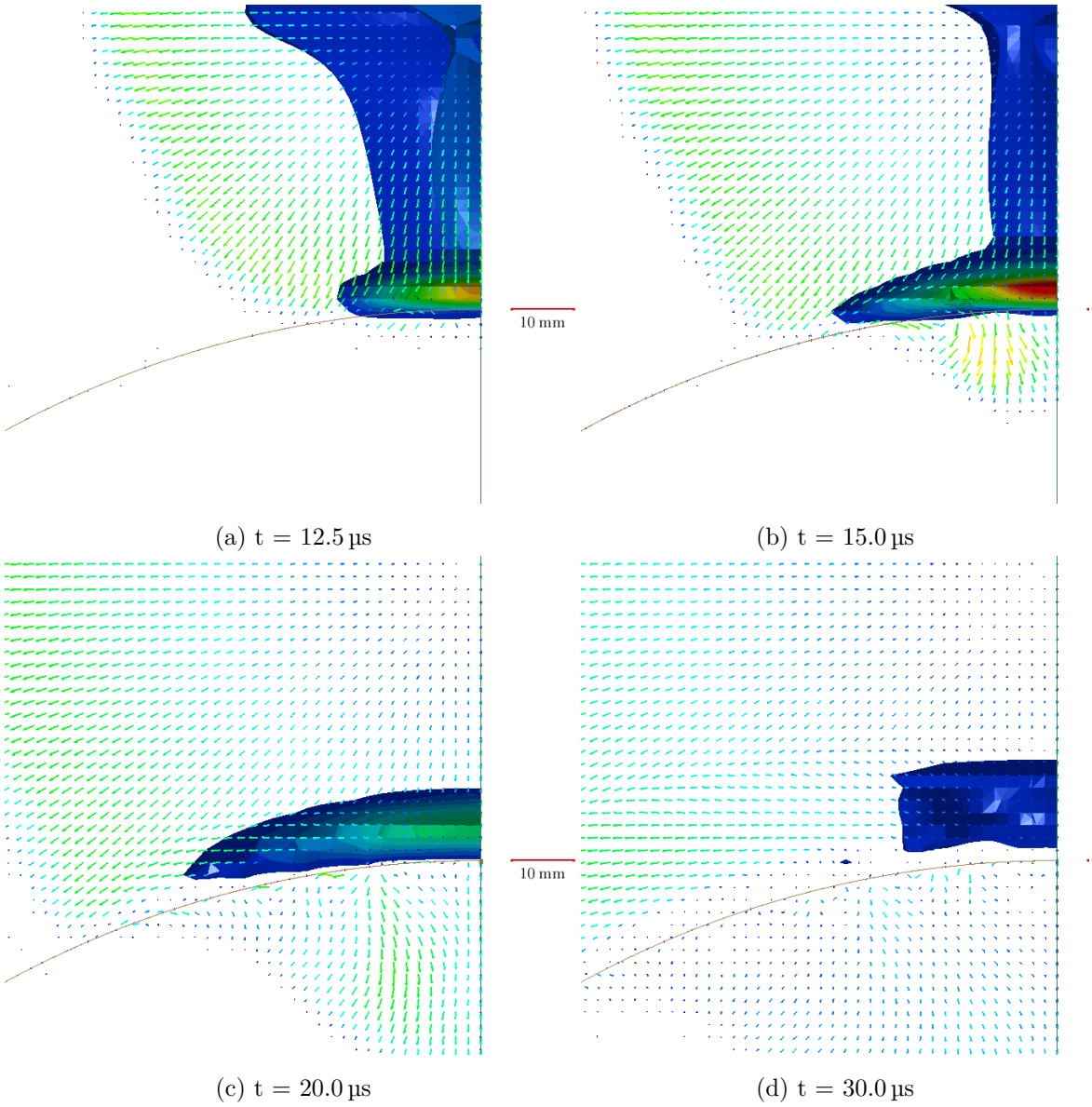

(a) t = 12.5 µs (b) t = 15.0 µs

(c) t = 20.0 µs (d) t = 30.0 µs

Figure 6.26: Crosscut profile view showing the pressure time history development and material velocity for a 120° V-plate with a bend radius of 160 mm and a 58 g charge

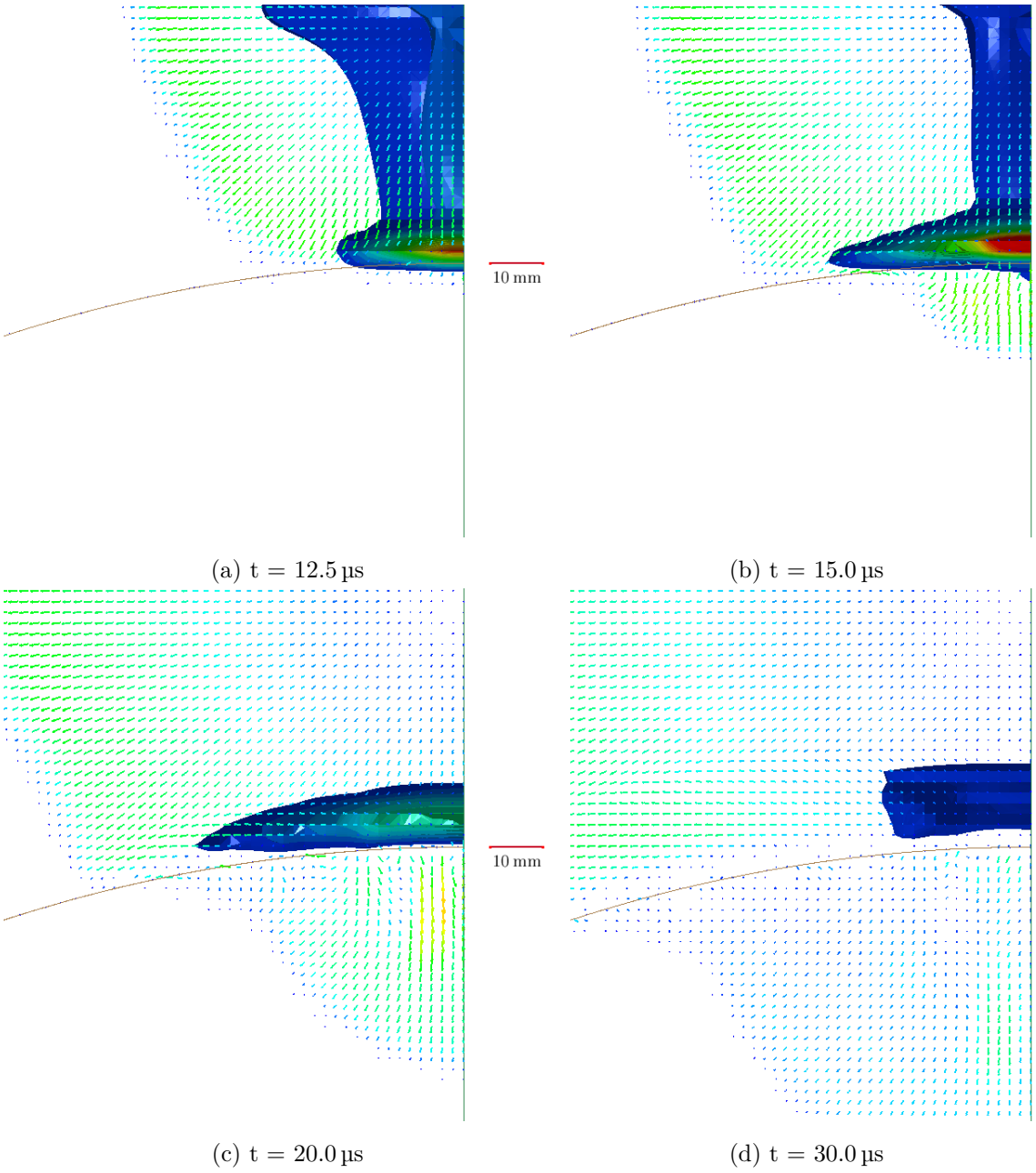

(a) t = 12.5 µs (b) t = 15.0 µs

(c) t = 20.0 µs (d) t = 30.0 µs

Figure 6.27: Crosscut profile view showing the pressure time history development and material velocity for a 120° V-plate with a bend radius of 280 mm and a 58 g charge

6.6.2 Velocity vector analysis

The velocity vectors of the gas products for the 120° V-plate simulations are shown in Figures 6.28 and 6.29 for bend radii of 0 and 280 mm. From Figure 6.28 it can be seen that, at a bend radius of 0 mm, the gas products tended to follow the profile of the V-plate in a similar manner to the 60° and 90° plates (shown in Figures 6.15 and 6.21). Figure 6.29 shows that, for a bend radius of 280 mm, most of the gas products were flowing at a shallower angle (than the slope of the V-plate). This is the same effect that was observed for the 60° and 90° V-plates.

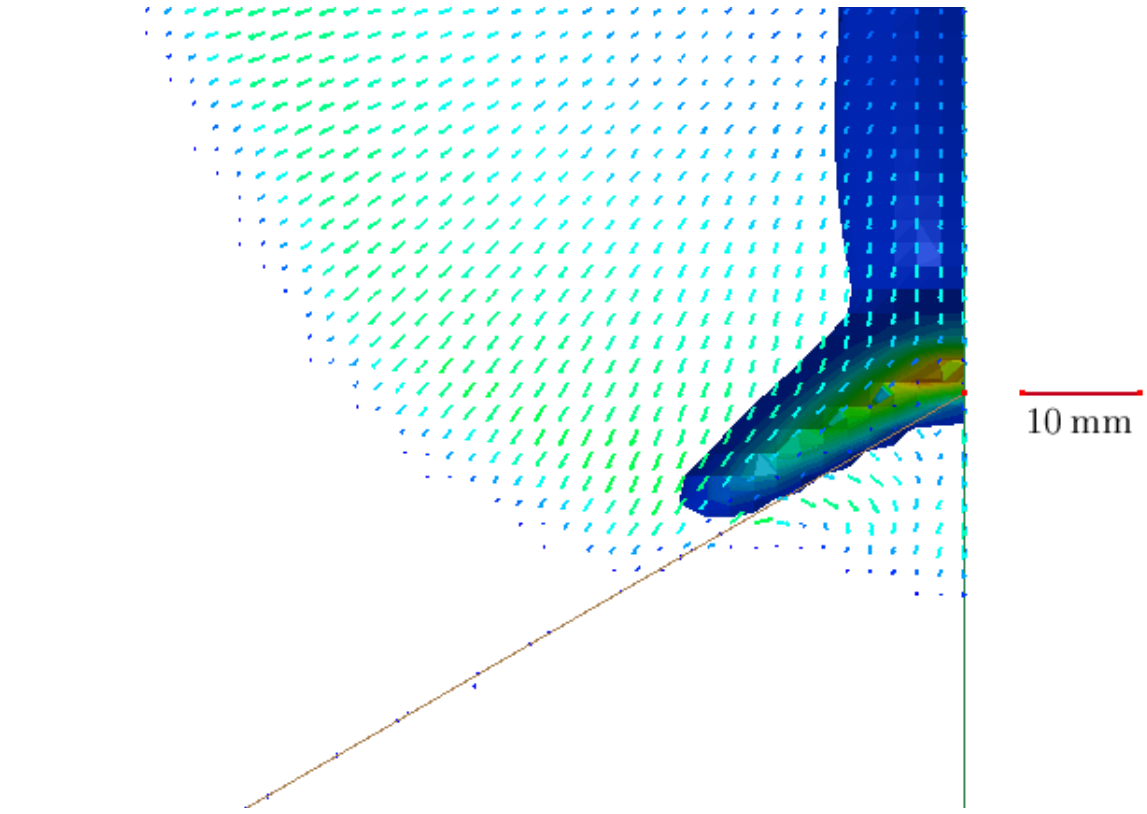

(a) t = 15 µs

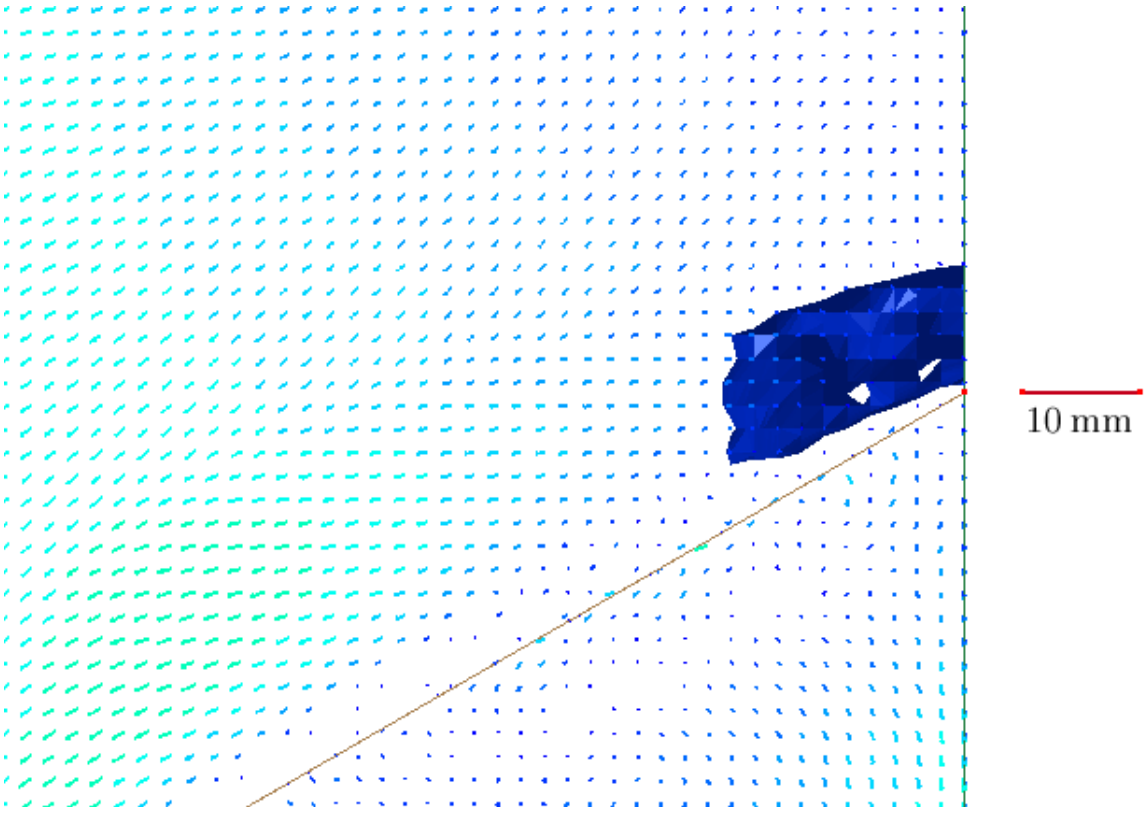

(b) t = 30 µs

Figure 6.28: Magnified view of the crosscut profile view showing the pressure time history development and material velocity for a 120° V-plate with a bend radius of 0 mm and a 58 g charge at 15 and 30 µs

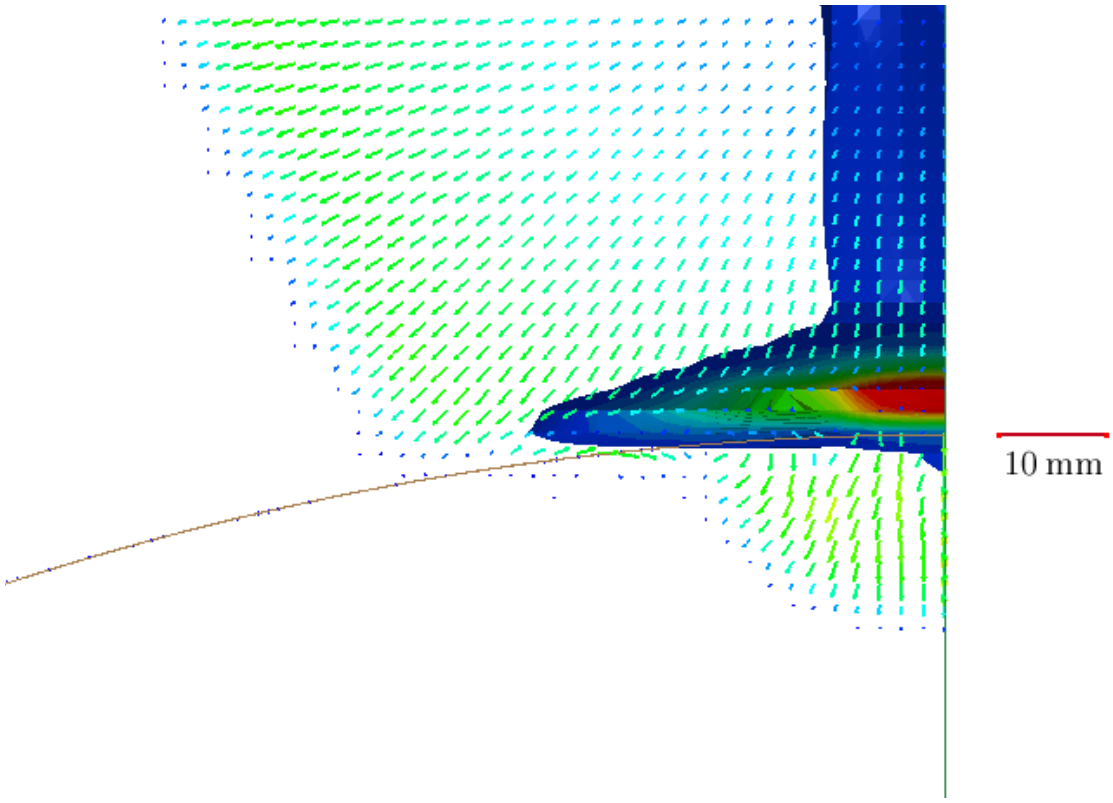

(a) t = 15 µs

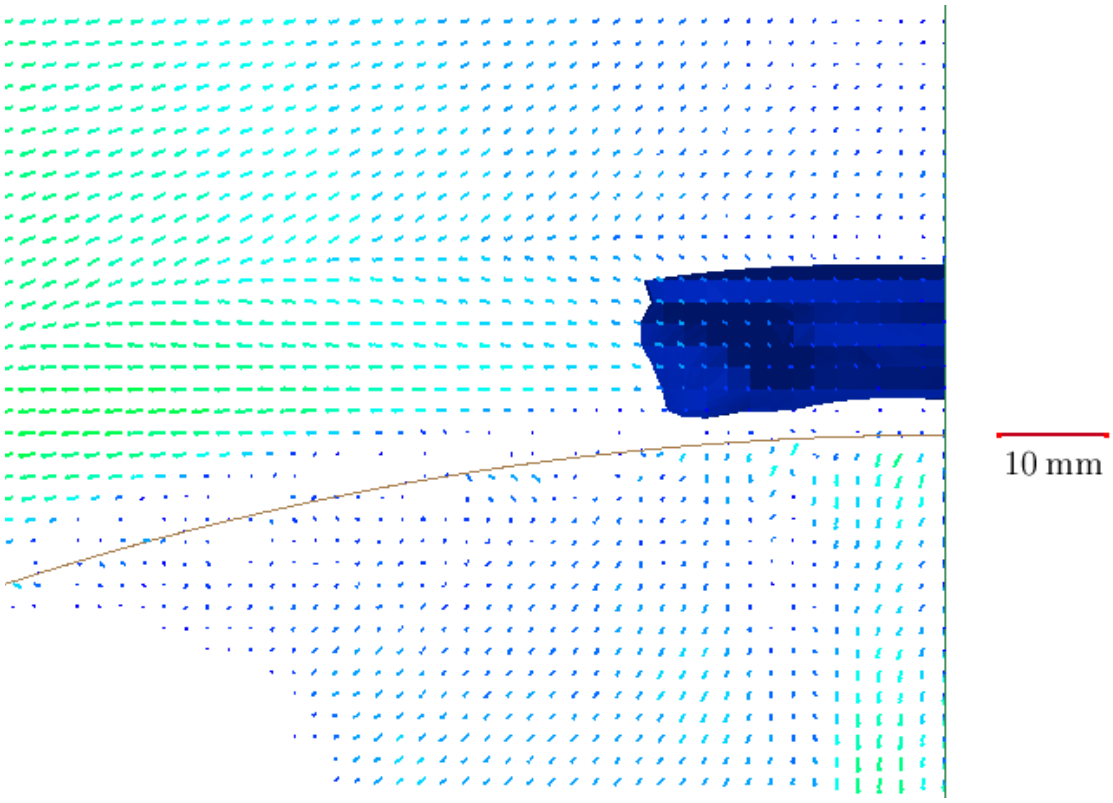

(b) t = 30 µs

Figure 6.29: Magnified view of the crosscut profile view showing the pressure time history development and material velocity for a 120° V-plate with a bend radius of 280 mm and a 58 g charge at 15 and 30 µs

6.6.3 Ridge profile views

The pressure and velocity time histories for the ridge profile views of the V-plates for the minimum and maximum bend radii investigated are shown in Figures 6.30 and 6.31. There was no significant difference in the maximum pressure or the pressure distribution as the bend radius is increased from 0 to 280 mm at 12.5 µs, as shown in Figure 6.30(a) and Figure 6.31(a). This matches the trend observed for the 60° simulations, but not what was observed for the 90° simulations. The pressure wave dissipated more slowly for the larger bend radii as observed in Figures 6.30(c) and (d) and Figures 6.31(c) and (d). Similar effects were observed for both the 60° and 90° simulations. The gas velocity behind the V-plate for a bend radius of 280 mm was observed to be large at 15 µs and the flow became more uniform by 30 µs. This is similar to the flow observed for the 60° and 90° V-plates with a large bend radius.

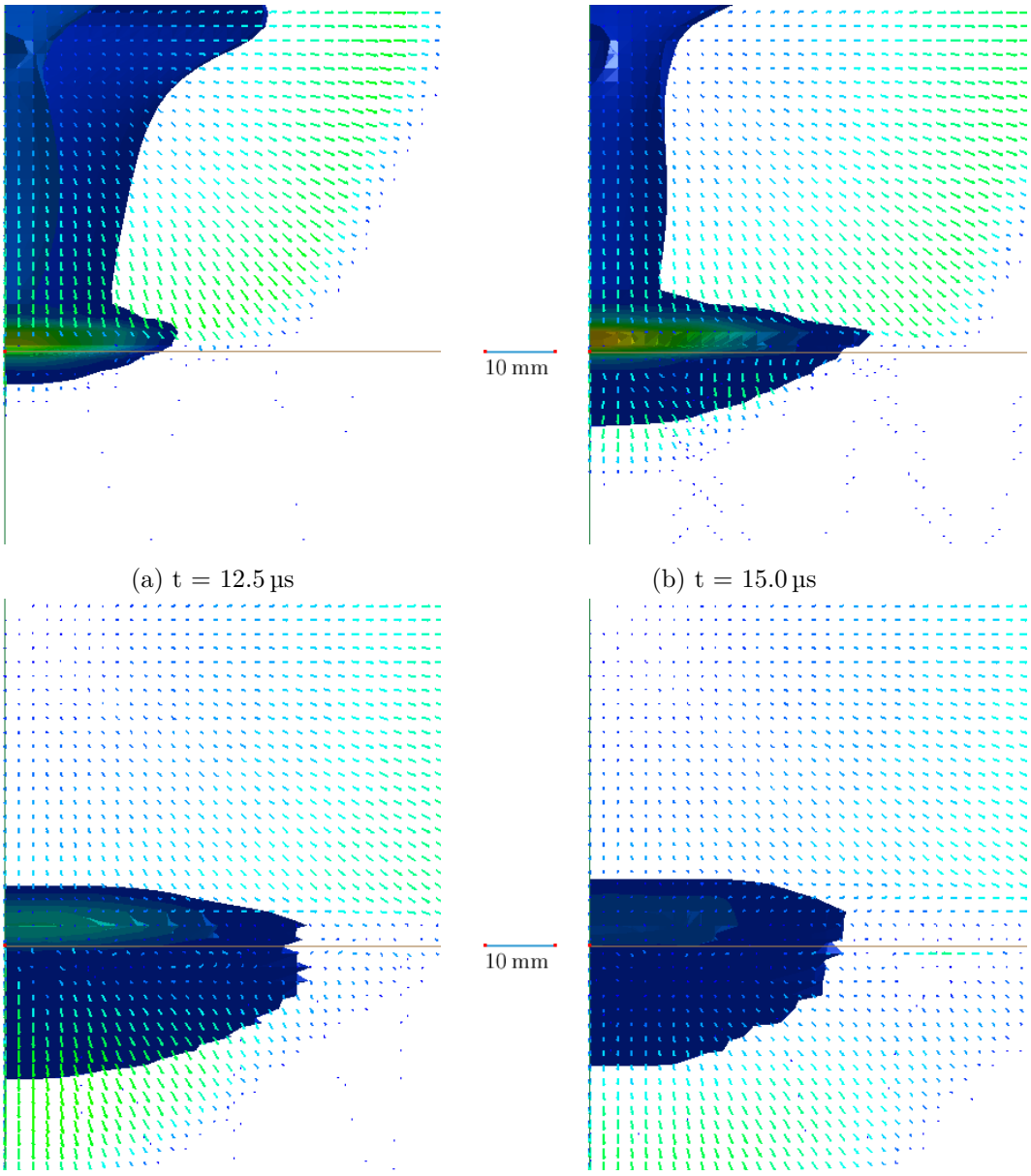

(a) t = 12.5 µs (b) t = 15.0 µs

(c) t = 20.0 µs (d) t = 25.0 µs

Figure 6.30: Ridge profile view showing the pressure time history development and material velocity for a 120° V-plate with a bend radius of 0 mm and a 58 g charge

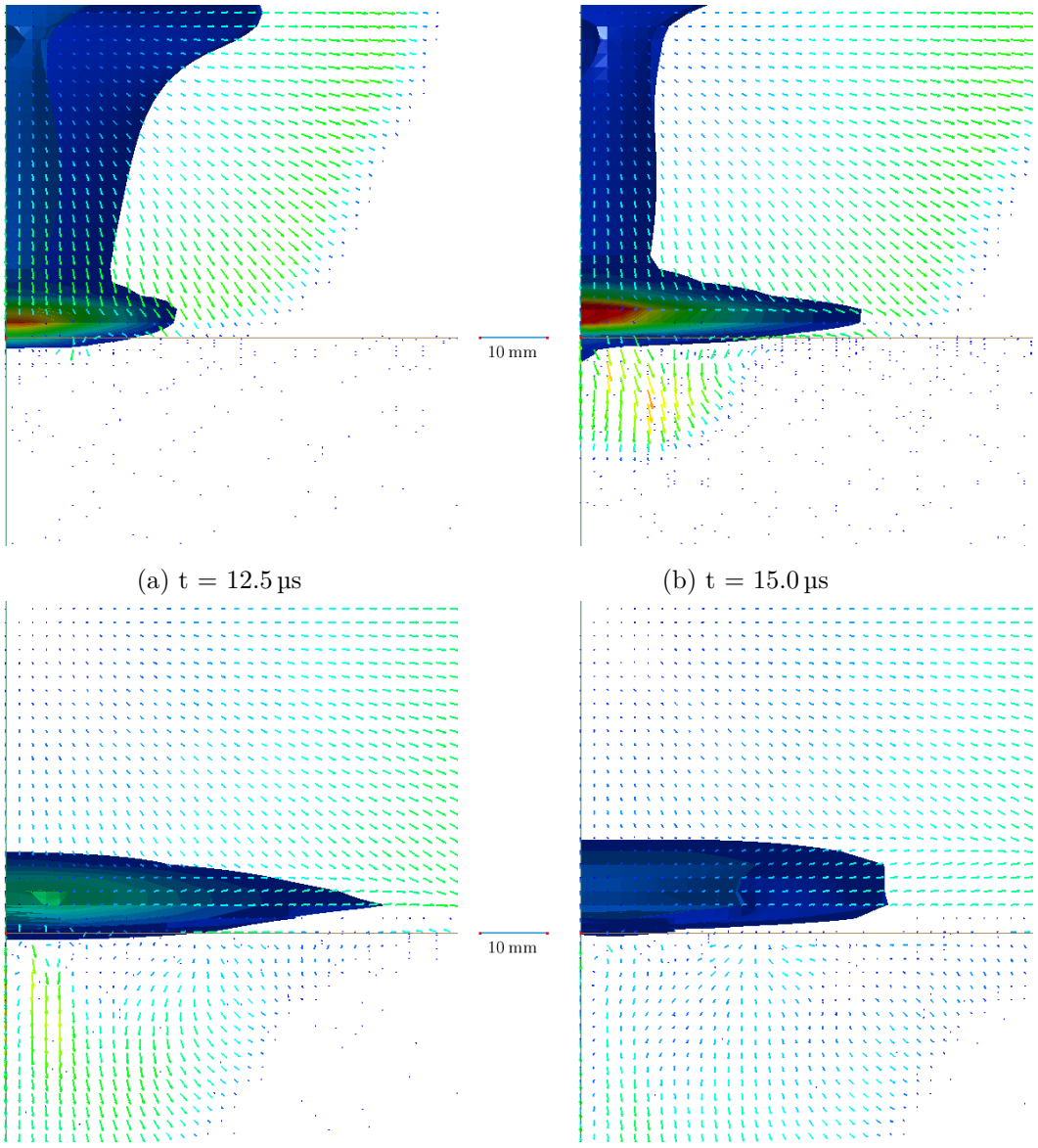

(a) t = 12.5 µs (b) t = 15.0 µs

(c) t = 20.0 µs (d) t = 25.0 µs

Figure 6.31: Ridge profile view showing the pressure time history development and material velocity for a 120° V-plate with a bend radius of 280 mm and a 58 g charge

Chapter 7

Discussion of numerical modelling results

This chapter discusses the influence of bend radius, V-plate angle and two different clamp frame designs (Shown in Figure 5.1 in Chapter 5) on the pressure loading and impulse transfer to V-plates. The numerical model developed in Chapter 5, with rigid V-plates and rigid clamp frames, was used to perform simulations to investigate these effects. The effect of explosive distance from the plate surface is also discussed, and looks at both 60° and 120° V-plates.

7.1 Influence of the bend radius

Three charge masses were used for all the simulations investigating the influence of bend radius, namely 19 g, 40 g and 58 g. Three V-angles were simulated (60°, 90° and 120°) using the new clamp frame design as shown in Figure 7.1. The stand-off distance was fixed at 34 mm from the tip of the V as defined in Figure 7.1 for various bend radii. Figure 7.1 shows that as bend radius is increased the distance of the charge from the tip of the V-plate remains fixed while the height from the base of the clamp frame decreases.

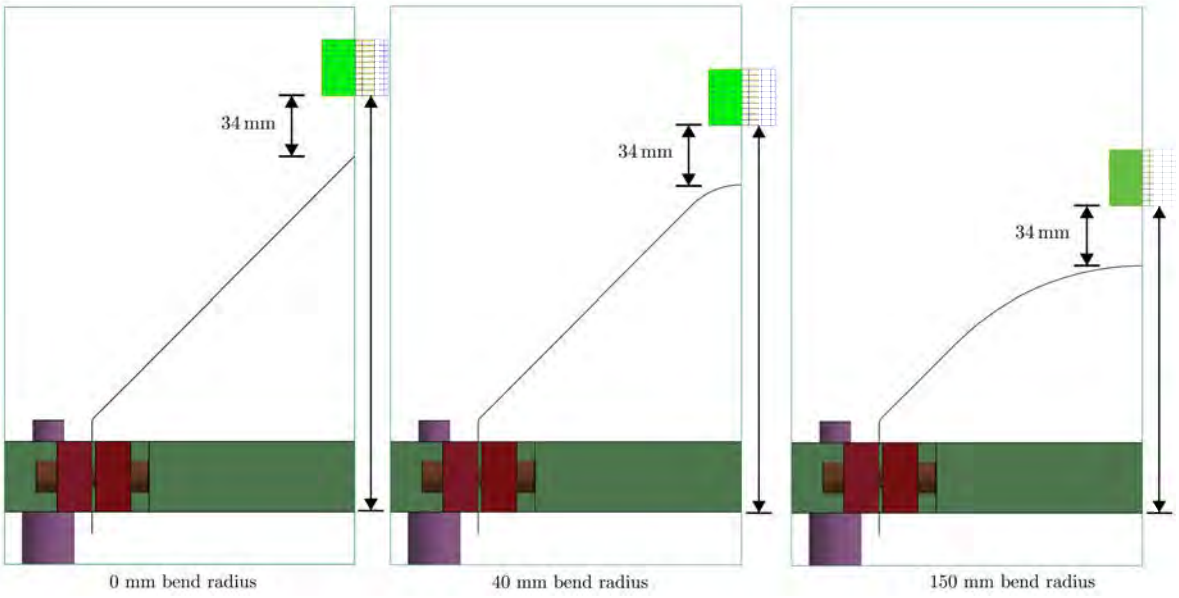

Figure 7.1: Figures of three 90° V-plates that were investigated with bend radii of 0 mm, 40 mm and 150 mm, showing the fixed SOD

Table 7.1 shows the predicted impulse values for all the simulations. For the 60° V-plates, the largest bend radius that could be used was 160 mm, while for the 90° and 120° V-plates larger bend radii (200 mm and 280 mm respectively) could be used. The analyses of the results for the different V-angles tested is shown in the following subsections. It is noted that, for large bend radii, at 100 mm and above (See Table 7.1) all the V-plates show similar impulse transfer characteristics. This would be expected as the curvature of the plate starts to have a greater effect over the V-angle as shown in Figure 6.2.

For a bend radius of 100 mm, there is a maximum difference of approximately 3% in impulse transferred for the three V-angles at each charge mass. As the bend radius is increased, the impulse increases, but the variation in impulse between the V-angles tested remains low ($<$ 5%). This trend continues up to a bend radius of 160 mm. This suggests that for bend radii between 100 mm and 160 mm the effect of V-angle on impulse transfer is negligible and that only the bend radius of the V-plate influences the impulse transferred. For bend radii greater than 160 mm the impulse continues to increase as the bend radius increases, although the rate of increase is reduced. The impulse also remains similar for the three V-angles as the bend radius

increases for bend radii in this range. When the bend radius is increased from 160 mm to ∞ (that is a flat plate), the impulse increases by approximately 10 to 20% for the three charge masses tested. This increase is much lower than the increase in impulse when the bend radius is increased from 0 mm to 160 mm. Thus for bend radii greater than 160 mm the effect of V-angle negligible and the effect of the bend radius is significantly reduced.

Table 7.1: Table showing the predicted impulse (in N s) for the rigid V-plates of different bend radii

	19 g			**40 g**			**58 g**		
Bend radius (mm)	**60°**	**90°**	**120°**	**60°**	**90°**	**120°**	**60°**	**90°**	**120°**
0	13.49	19.33	22.51	20.28	30.10	35.25	22.98	35.71	40.74
4			22.04			34.37			39.99
8	14.35	17.26		21.50	26.60		24.39	30.72	
12	15.35	14.94	21.73	23.02	22.53	34.20	26.35	25.59	39.85
16	16.01	15.25		24.18	22.94		27.61	26.04	
20		18.79	21.64		28.50	32.85		32.71	38.32
30	18.19			28.18			32.41		
40	19.22	20.62	23.69	29.87	31.66	35.59	34.23	36.13	41.40
60	20.65	21.10	22.68	32.43	32.52	35.23	37.48	37.35	40.85
80	22.00	22.05	24.37	34.79	34.39	38.28	40.29	39.46	44.40
100	23.13	23.09	23.70	36.35	35.92	37.41	42.38	41.55	43.19
120	23.95	23.97	25.12	37.97	37.66	39.85	44.00	43.34	46.04
140	24.66	24.74	24.62	39.13	39.14	38.72	45.54	45.66	45.23
150	24.90	25.10	24.69	40.02	39.57	38.76	46.65	45.97	45.09
160	25.30	25.44	25.80	40.24	40.60	40.86	46.69	47.23	47.58
180		25.37	25.35		39.98	40.34		46.53	47.27
200		25.12	25.77		40.03	40.98		46.64	47.77
280			26.03			41.85			49.06
∞[1]		29.24			48.90			58.85	

[1]Corresponds to a flat plate

7.1.1 60° V-plates

The impulses predicted for the 60° V-plates are shown in Table 7.2, along with the global stand-off distance (measured from the base of the V-plate to the bottom of the explosive charge) and reduction in height (Δh) of the V-plate for each bend radius investigated (as shown in Figure 7.1). The general trend shows an increase in the impulse with an increase in the bend radius. There is an 88% increase in the impulse transfer when the bend radius is increased from 0 mm to 160 mm for the 19 g charges, while the increase is 98% for the 40 g charges and 103% for the 58 g charges. A graph of impulse versus bend radii is shown in Figure 7.2. In general the impulse increases with increasing bend radii and allowed a second order polynomial to be fitted to the data points with coefficient of determination values exceeding 99%.

Table 7.2: Table showing the predicted impulse (in N s) for the 60° rigid V-plates of different bend radii

			Charge mass (g)		
Bend radius (mm)	**Global SOD (mm)**	**Δh (mm)[2]**	**19 g**	**40 g**	**58 g**
0	324.81	0	13.49	20.28	22.98
8	316.81	8	14.35	21.50	24.39
12	312.81	12	15.35	23.02	26.35
16	308.81	16	16.01	24.18	27.61
30	294.81	30	18.19	28.18	32.41
40	284.81	40	19.22	29.87	34.23
60	264.81	60	20.65	32.43	37.48
80	244.81	80	22.00	34.79	40.29
100	224.81	100	23.13	36.35	42.38
120	204.81	120	23.95	37.97	44.00
140	184.81	140	24.66	39.13	45.54
150	174.81	150	24.90	40.02	46.65
160	164.81	160	25.30	40.24	46.69
% Increase for 160 mm radius			**88**	**98**	**103**

[2] Δh = bend radius as a result of the geometry for the 60° V, this is generally not the case

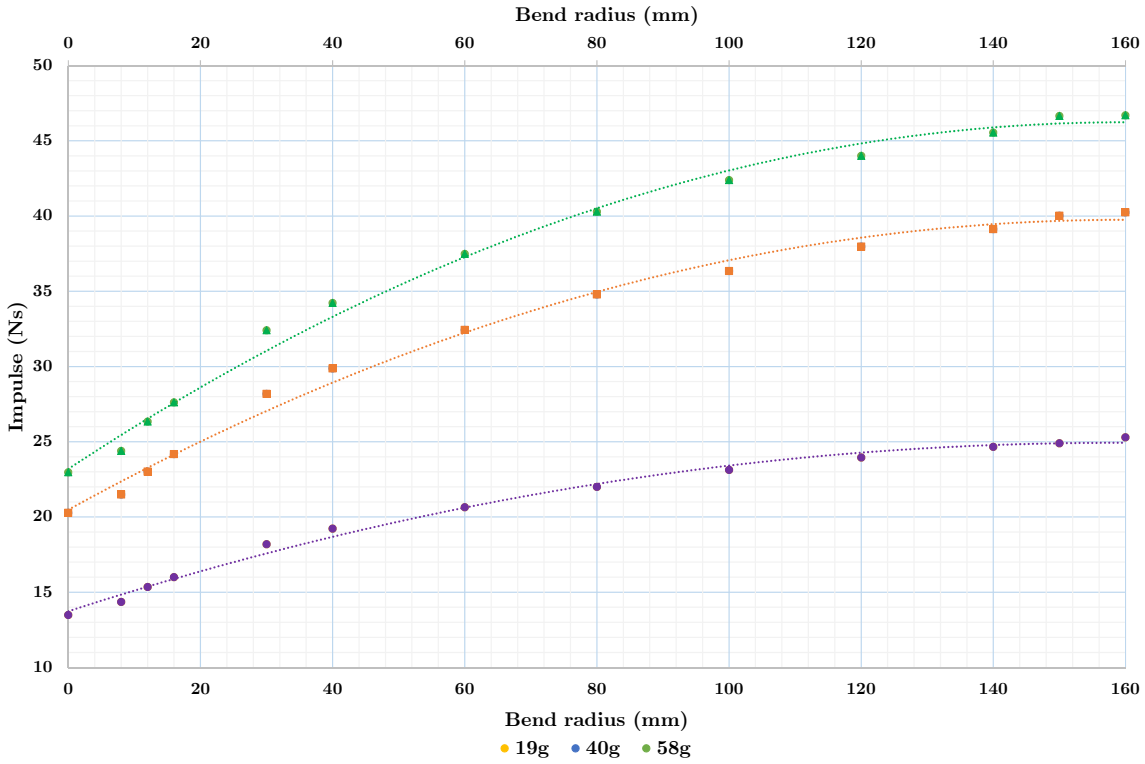

Figure 7.2: Graph showing the effect of bend radius on impulse transfer for 60° V-plates

As the bend radius increased beyond 100 mm, there was a smaller increase in the impulse transferred for the same reduction in total height. When Figure 6.12 is compared with Figure 6.11 was observed that the pressure histories along the V-profile are very similar. This explains why there is a small variation in the impulse transfer when the bend radius is increased from 100 mm to 160 mm: a reduction of 26% in total height resulted in only a 10% increase in the impulse transferred. The increase in impulse transfer can be attributed to the increased areas of the plate subjected to the maximum pressure (when the pressure wave reached the plate) and also to the slower pressure dissipation with increasing the bend radius. More of the gas products were directed horizontally, rather than travelling down the plate, hence an increase in plate area exposed to the maximum pressure. More of the energy from the blast was transferred horizontally (rather than vertically), which resulted in a smaller increase in impulse than might be expected.

7.1.2 90° V-plates

Table 7.3 shows the predicted impulses for the 90° V-plates. The larger included angle made it possible to investigate larger bend radii, since the reduction in height for an increase in the bend radius is lower. As with the 60° plates, there is a general increase in impulse calculated with an increase in bend radii, but with a dip in the impulse transfer for bend radii in the 0 to 20 mm range. The total increase in impulse transfer is approximately 30% from a 0 mm bend radius to a 200 mm bend radius. The percentage increase in impulse is also shown in Table 7.3.

Table 7.3: Table showing the predicted impulse (in N s) for the 90° rigid V-plates of different bend radii

			Charge mass (g)		
Bend radius (mm)	**Global SOD (mm)**	**Δ h (mm)**	**19 g**	**40 g**	**58 g**
0	215.00	0.00	19.33	30.10	35.71
8	211.69	3.31	17.26	26.60	30.72
12	210.03	4.97	14.94	22.53	25.59
16	208.37	6.63	15.25	22.94	26.04
20	206.72	8.28	18.79	28.50	32.71
40	198.43	16.57	20.62	31.66	36.13
60	190.15	24.85	21.10	32.52	37.35
80	181.86	33.14	22.05	34.39	39.46
100	173.58	41.42	23.09	35.92	41.55
120	165.29	49.71	23.97	37.66	43.34
140	157.01	57.99	24.74	39.14	45.66
150	152.87	62.13	25.10	39.57	45.97
160	148.73	66.27	25.44	40.60	47.23
180	140.44	74.56	25.37	39.98	46.53
200	132.16	82.84	25.12	40.03	46.64
% Increase for 200 mm radius			**30**	**33**	**31**

Figure 7.3 shows the impulse values plotted against the increasing bend radii for all three charge masses tested. The same trends were observed for the three charge masses including a decrease in impulse between 0 and 16 mm. A linear trend of increasing impulse transfer was observed between 20 mm and 160 mm. For bend radii greater than 160 mm it appears that the impulse values reach a plateau.

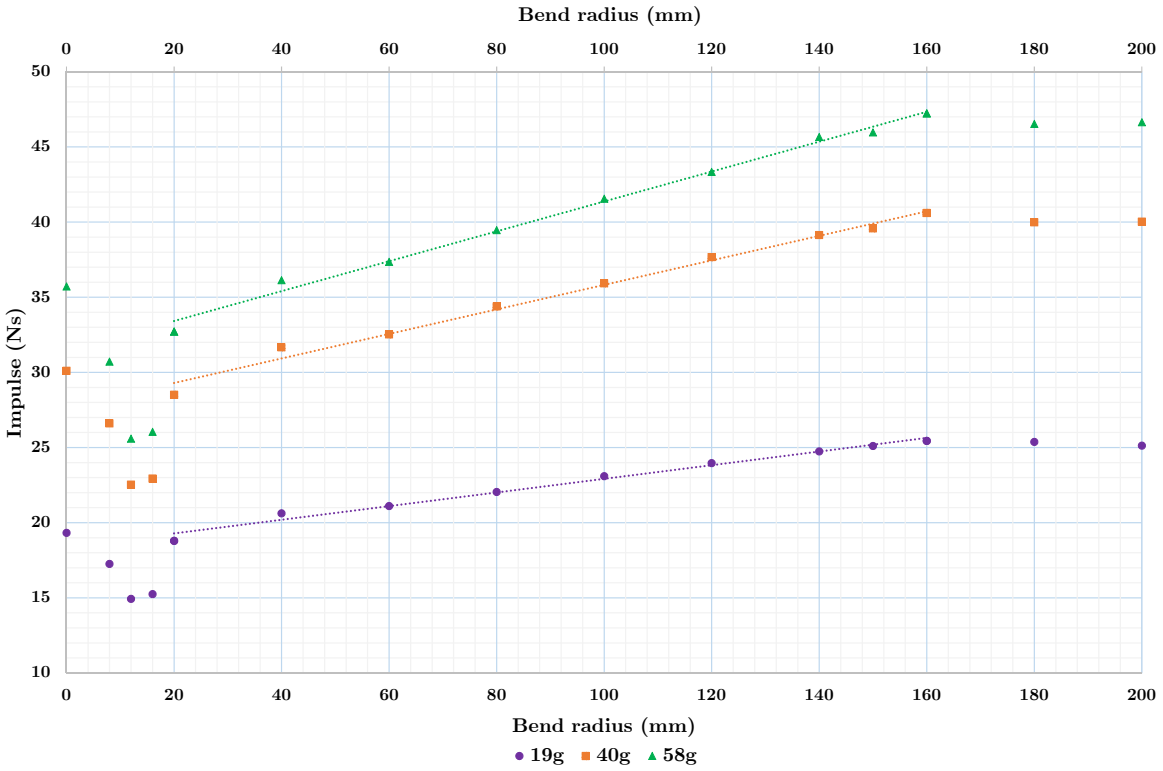

Figure 7.3: Graph showing the effect of bend radius on impulse transfer for 90° V-plates

Much like the 60° V-plates which showed a small variation in impulse transfer for bend radii greater than 100 mm, the 90° V-plates show a smaller change in the impulse transferred for bend radii greater than 160 mm. When Figures 6.19 and 6.20 (which show the pressure time history development for 90° V-plates with a 160 mm and 200 mm bend radius respectively) are compared it is evident that there were no significant variations in the pressure distributions and the peak pressure, hence little change in impulse transfer for bend radii above 160 mm. The reduction in height is lower though, due to the larger V-angle. This can be seen by a reduction of 13.5% in total height when the bend radius is increased from 150 mm to 200 mm, with only an increase in impulse of 1.5%. There is a 14.31% reduction in height when the bend radius is increased from 100 mm to 160 mm for the 90° V-plates with a 13.6% increase in impulse. This is a smaller reduction in height for a greater increase in impulse than the 60° V-plates for the same range of bend radii. The increasing impulse with bend radii up to 160 mm trend for the 90° V-plates was again attributed to the increased area exposed to the maximum pressure and the slower pressure dissipation as the bend radius increased. The dip in impulse for bend radii in the 0 mm to 20 mm range is discussed in Section 7.1.4.

7.1.3 120° V-plates

The calculated impulse values for the 120° V-plates are shown in Table 7.4. Since these 120° V-plates have a largest included angle it was possible to investigate bend radii up to 280 mm. Due to geometry, the total reduction in height is the lowest of the V-angles investigated. The general trend is an increase in impulse transfer with an increase in bend radii. There is a 15-20% increase in impulse transfer as the bend radius is increased from 0 mm to 280 mm for a 43 mm height reduction, also shown in Table 7.4.

Table 7.4: Table showing the predicted impulse (in N s) for the 120° rigid V-plates of different bend radii

			Charge mass (g)		
Bend radius (mm)	**Global SOD (mm)**	**Δ h (mm)**	**19 g**	**40 g**	**58 g**
0	151.60	0.00	22.51	35.25	40.74
4	150.98	0.62	22.04	34.37	39.99
12	149.75	1.86	21.73	34.20	39.85
20	148.51	3.09	21.64	32.85	38.32
40	145.41	6.19	23.69	35.59	41.40
60	142.32	9.28	22.68	35.23	40.85
80	139.23	12.38	24.37	38.28	44.40
100	136.13	15.47	23.70	37.41	43.19
120	133.04	18.56	25.12	39.85	46.04
140	129.94	21.66	24.62	38.72	45.23
150	128.40	23.21	24.69	38.76	45.09
160	126.85	24.75	25.80	40.86	47.58
180	123.76	27.85	25.35	40.34	47.27
200	120.66	30.94	25.77	40.98	47.77
280	108.29	43.32	26.03	41.85	49.06
% Increase for 280 mm radius			**16**	**19**	**20**

Figure 7.4 shows a graph of impulse versus bend radii for the three charge masses tested. The trends resemble the results of the 90° simulations. The results show a drop in impulse between 0 and 20 mm, followed by a general increase between 20 and 280 mm. The rate of increase appears to drop between 160 and 280 mm.

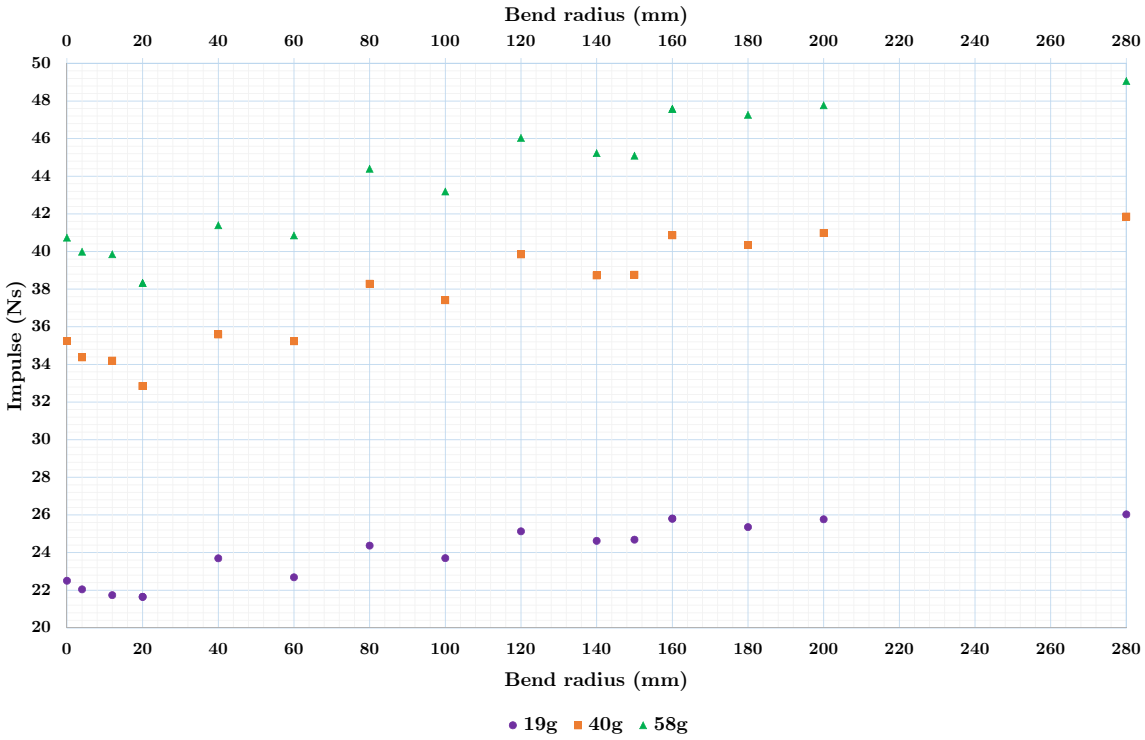

Figure 7.4: Graph showing the effect of bend radius on impulse transfer for 120° V-plates

The 120° plates exhibited a small change in the impulse transferred for bend radii greater than 160 mm. There are no significant variations in the pressure distributions, pressure flows and the peak pressures in between simulations at 160 mm and 280 mm as shown in Figures 6.26 and 6.27. Hence the calculated impulses do not vary significantly for bend radii greater than 160 mm. The total reduction in height is significantly lower than the 60° V-plates, due to the larger V-angle. This was observed by a reduction of 14.6% in total height when the bend radius is increased from 160 mm to 280 mm, with an increase in impulse of 3%. Additionally when the bend radius was increased from 0 mm to 280 mm, the impulse transferred increases by 20.4% while the height reduced by 28%. Similarly to the other V-angles the increased areas of the plate subjected to the maximum pressure and the slower rate of dissipation were the likely causes of the increased impulse. As with the 60° and 90° simulations, for large bend radii more of the gas products move laterally and do not transfer energy towards the V-plates.

7.1.4 Lowered impulse between 0-20 mm bend radii for the 90 and 120° V-plates

In an attempt to identify the reason for the reduced impulse values between 0 and 20 mm for both the 90 and the 120° V-plates, it was useful to look at the pressure and velocity distributions for a few cases in this range. Figures 7.5 and 7.6 show the pressure-time history of the crosscut profile view for a 90° V-plate with a 12 mm and 16 mm bend radius respectively. While Figure 7.9

shows the pressure-time history of the crosscut profile view for a 120° V-plate with a bend radius of 20 mm.

When Figures 7.5 and 7.6 are compared to Figure 6.18, it can be seen that as the bend radius is increased, the region over which the maximum pressure acts increased, although there was no significant variation in the pressure distribution along the plate for the timesteps shown. Additionally, as expected, the pressure wave takes longer to travel down the plate when compared to Figure 6.18.

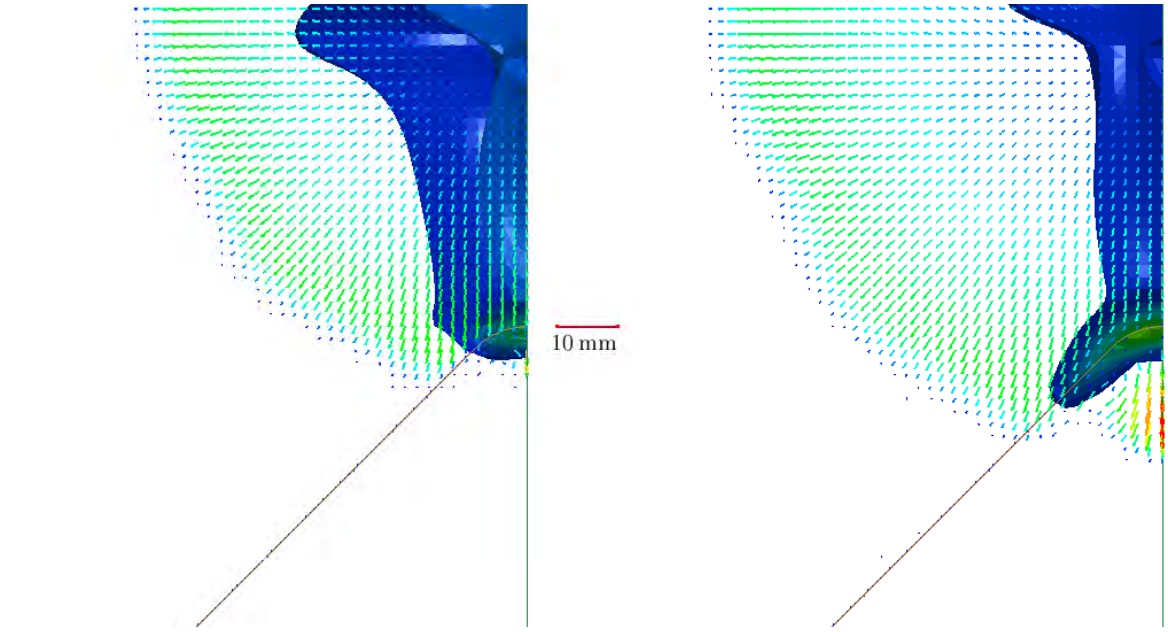

(a) t = 12.5 µs (b) t = 15.0 µs

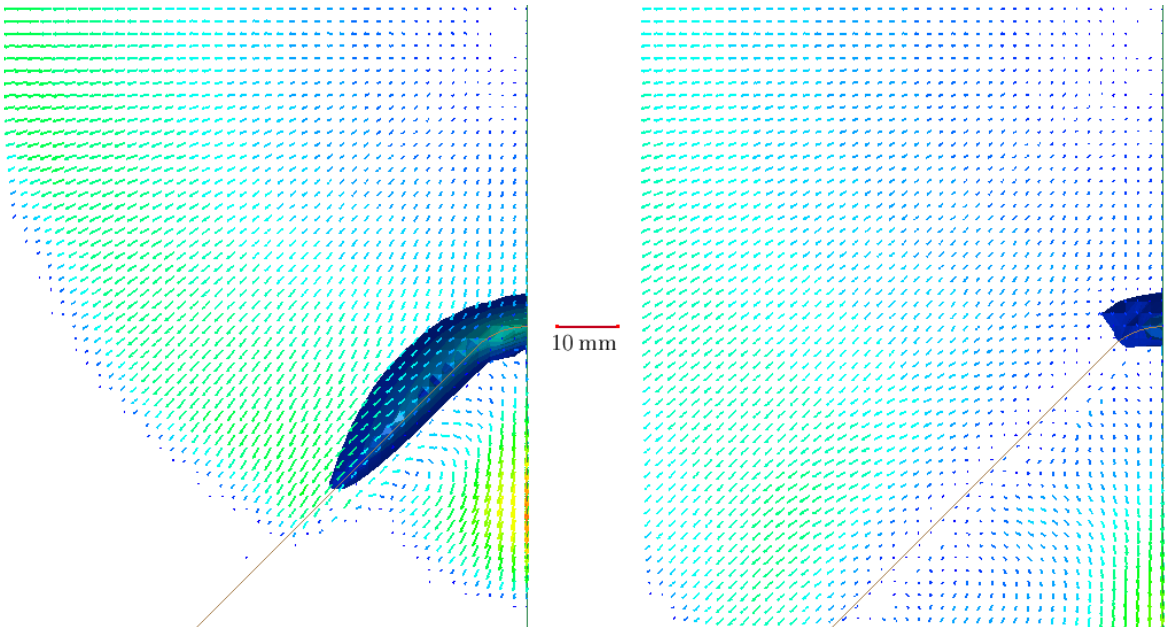

(a) t = 20.0 µs (b) t = 30.0 µs

Figure 7.5: Crosscut profile view showing the pressure time history development and material velocity for a 90° V-plate with a bend radius of 12 mm and a 58 g charge

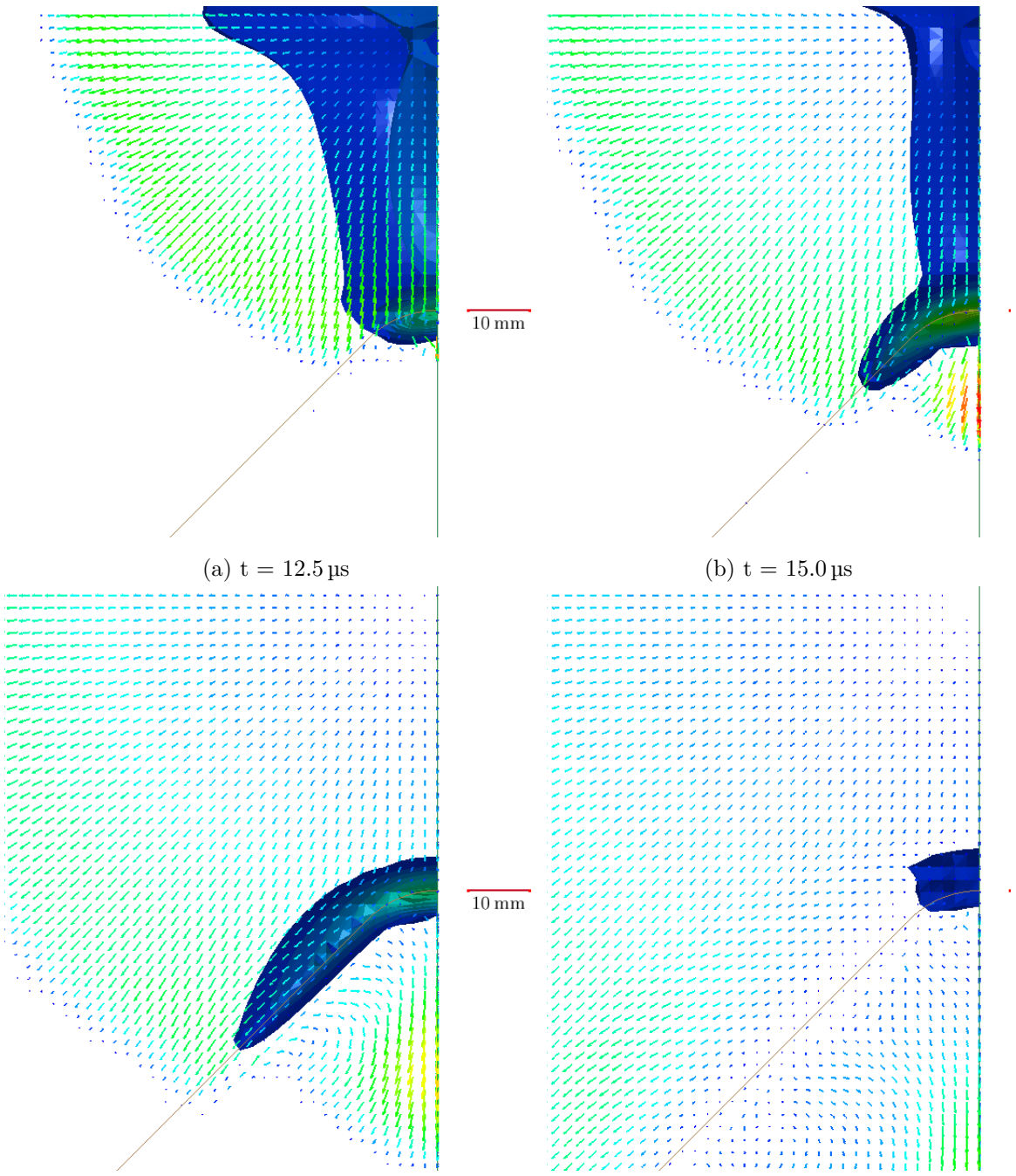

(a) t = 12.5 µs (b) t = 15.0 µs

(a) t = 20.0 µs (b) t = 30.0 µs

Figure 7.6: Crosscut profile view showing the pressure time history development and material velocity for a 90° V-plate with a bend radius of 16 mm and a 58 g charge

Figures 7.7 and 7.8 show zoomed in views of subfigures (b) and (d) in each of Figures 7.5 and 7.6 respectively. This was done to determine if the direction of the gas flow could explain the lower peak pressure at 12 and 16 mm. Figures 7.7 and 7.8 show that while the explosive products still appeared to be flowing in the same direction as in Figure 6.21, the velocity was lower (*i.e.* blue vectors as compared to green vectors). This also explains the longer duration in the pressure loading for the 12 and 16 mm bend radii tests.

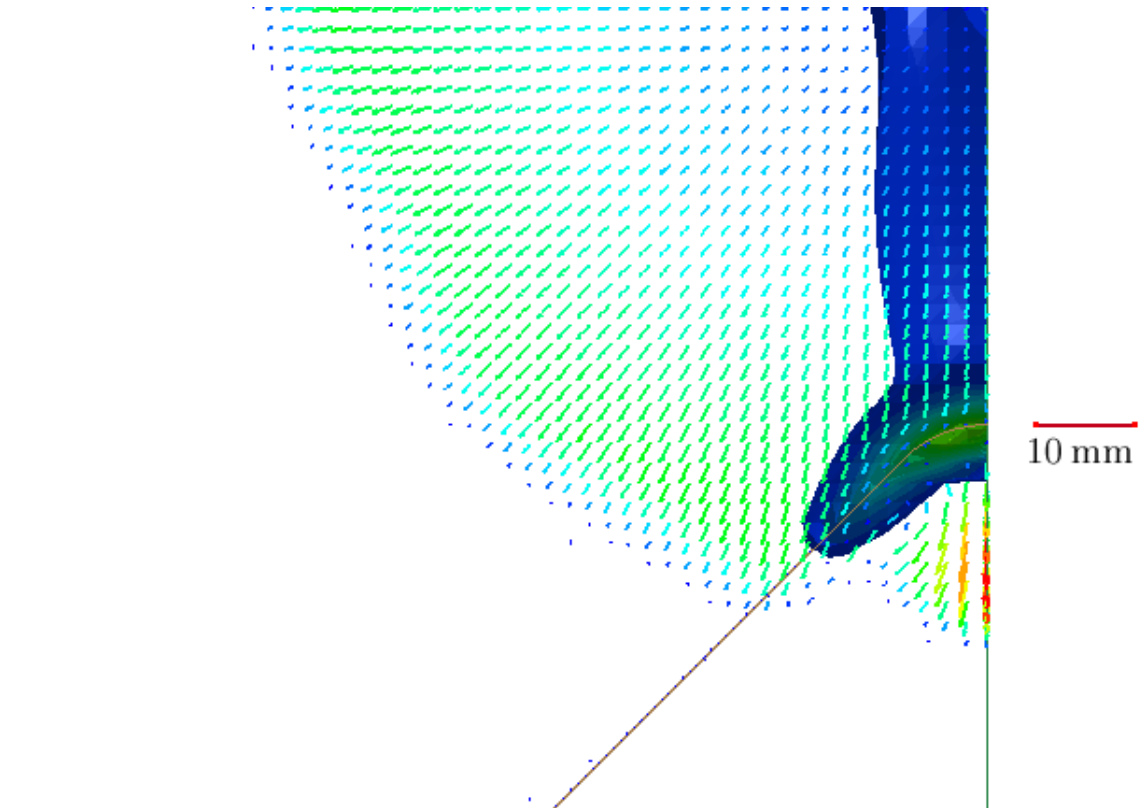

(a) t = 15.0 µs

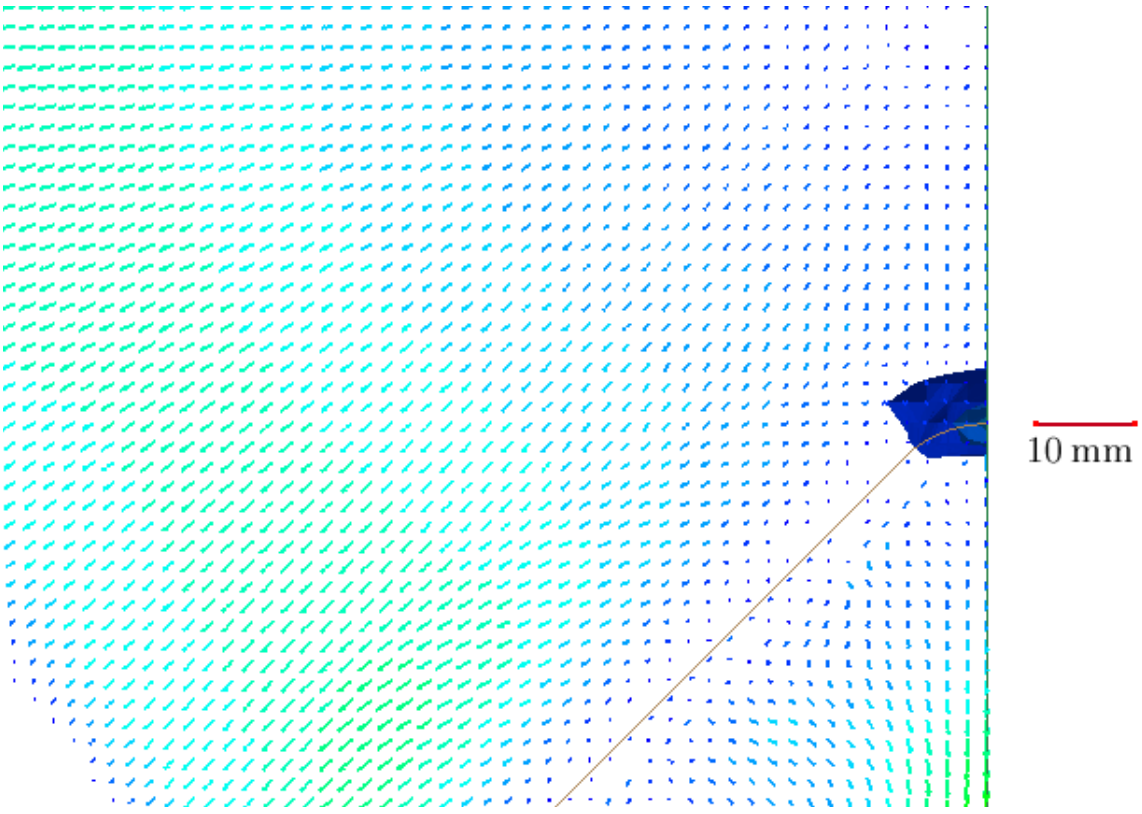

(b) t = 30.0 µs

Figure 7.7: Zoomed in view of the crosscut profile view showing the pressure time history development and material velocity for a 90° V-plate with a bend radius of 12 mm and a 58 g charge at 15.0 and 30.0 µs

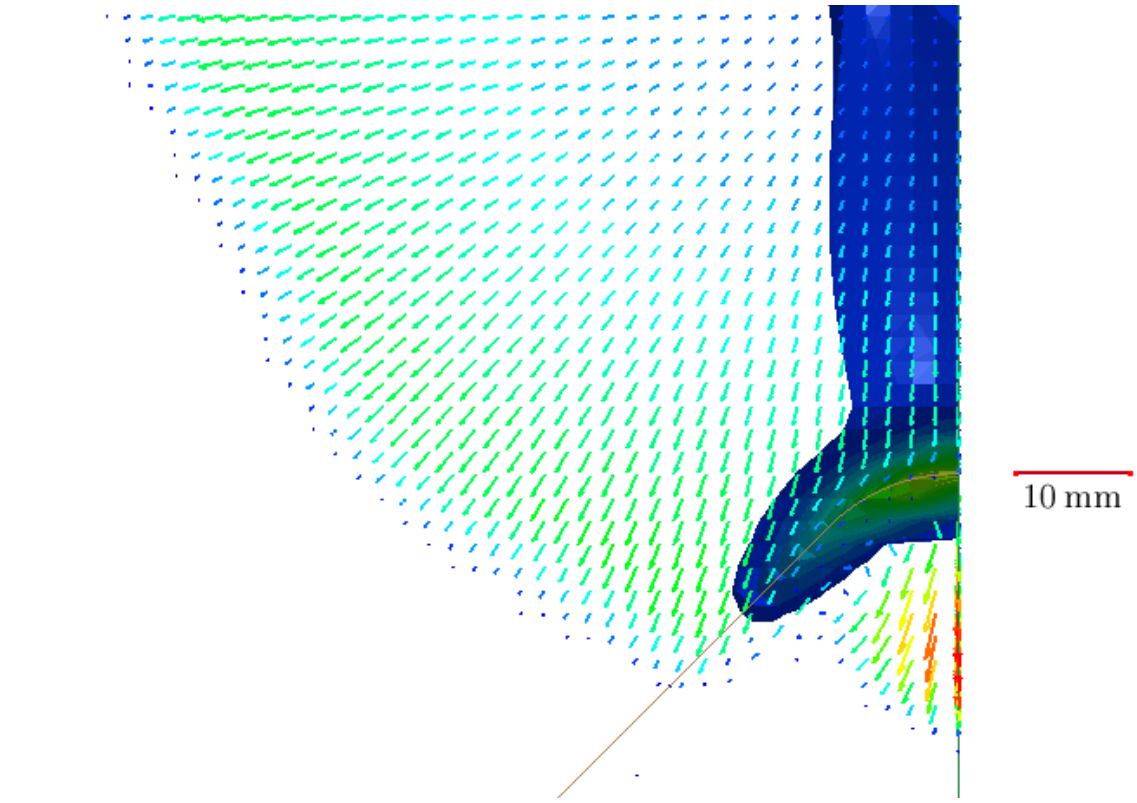

(a) t = 15.0 µs

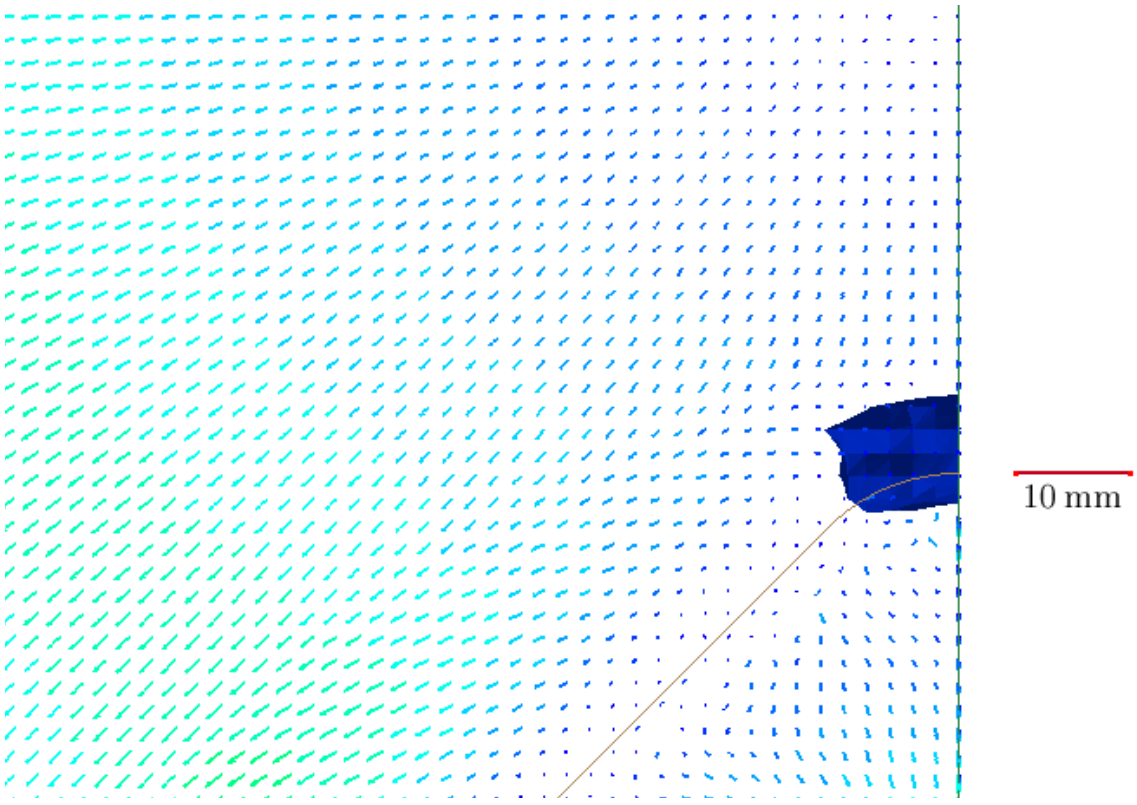

(b) t = 30.0 µs

Figure 7.8: Zoomed in view of the crosscut profile view showing the pressure time history development and material velocity for a 90° V-plate with a bend radius of 16 mm and a 58 g charge at 15.0 and 30.0 µs

The pressure histories for the crosscut profile of a 120° V-plate with a 20 mm bend radius are shown in Figure 7.9. From Figures 7.9(a) and (b), it can be seen that the maximum pressure occurs at the V-tip, but acts over a larger area. When Figure 7.9(d) is compared to Figure 6.25(d) in Chapter 6 it can be seen that the pressure has dissipated more for the plate with a 20 mm bend radius by 30.0 µs. This might explain the lower impulse observed at this bend radius.

To determine if the gas flow could explain the lower impulse transfer values obtained for the simulations with a bend radius of 20 mm it was useful to look at zoomed in views of some of the sub-figures of Figure 7.9 as shown in Figure 7.10. Figure 7.10 shows that the gas products were flowing in the same direction as the 0 mm radius (in Figure 6.28 in Chapter 6), but the velocity was higher (*i.e.* green vector arrows), hence the pressure dissipated faster at this bend radius.

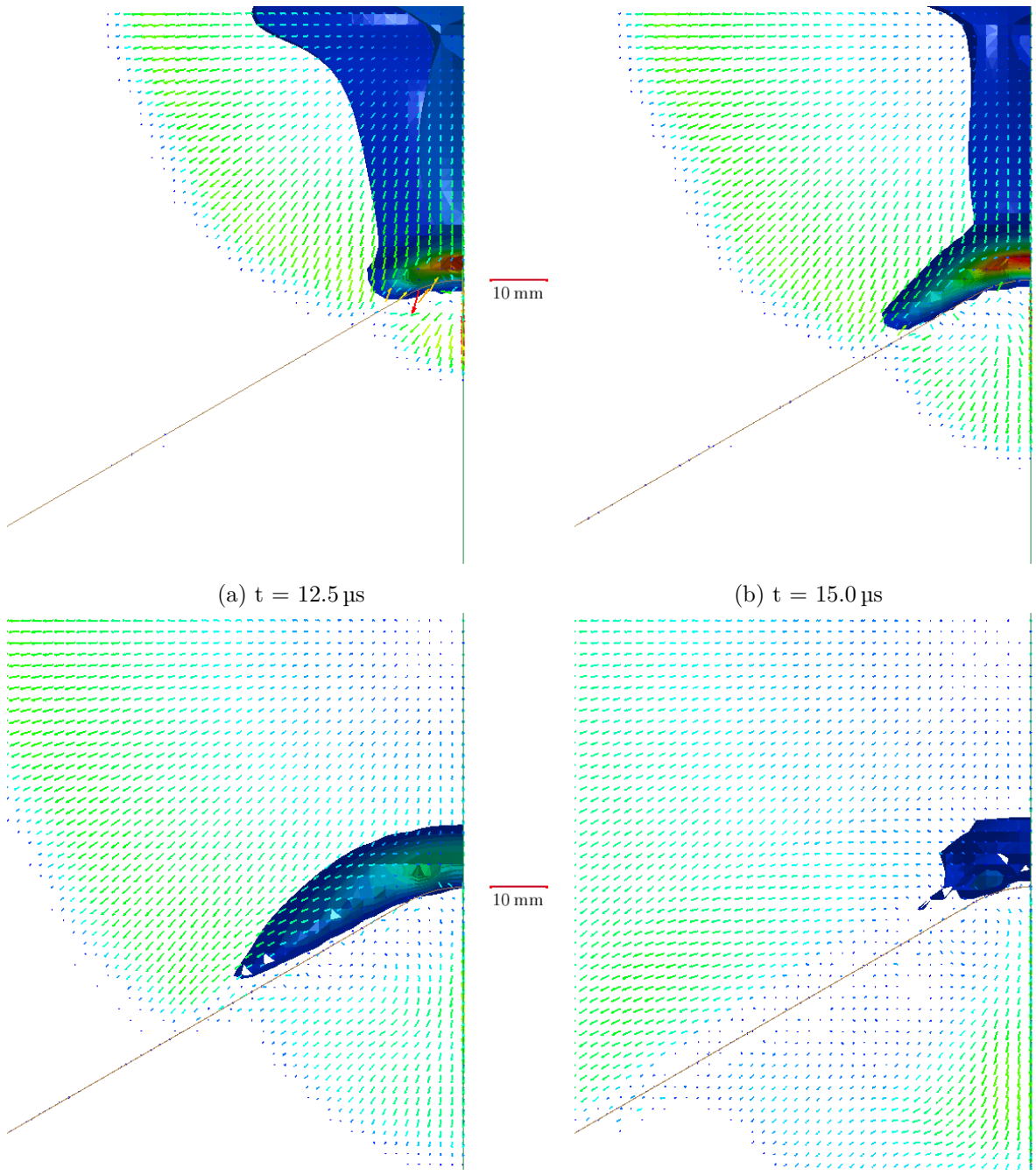

(a) t = 12.5 µs (b) t = 15.0 µs

(c) t = 20.0 µs (d) t = 30.0 µs

Figure 7.9: Crosscut profile view showing the pressure time history development and material velocity for a 120° V-plate with a bend radius of 20 mm and a 58 g charge

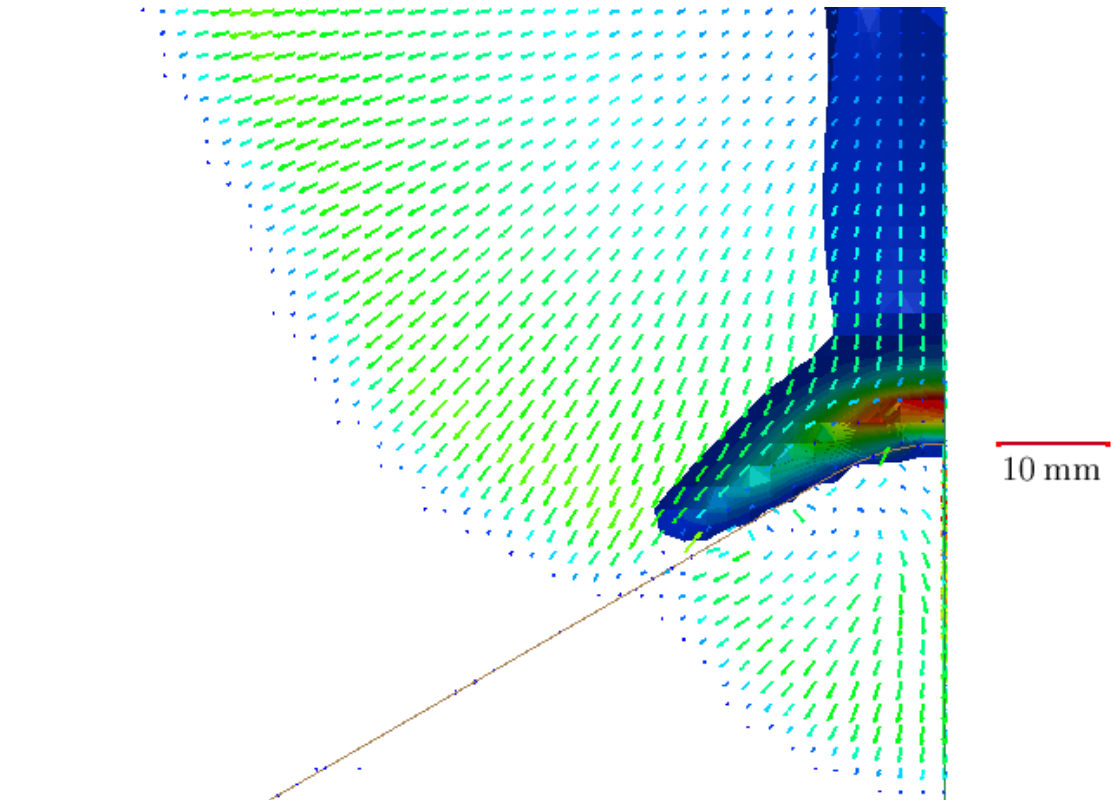

(a) t = 15.0 µs

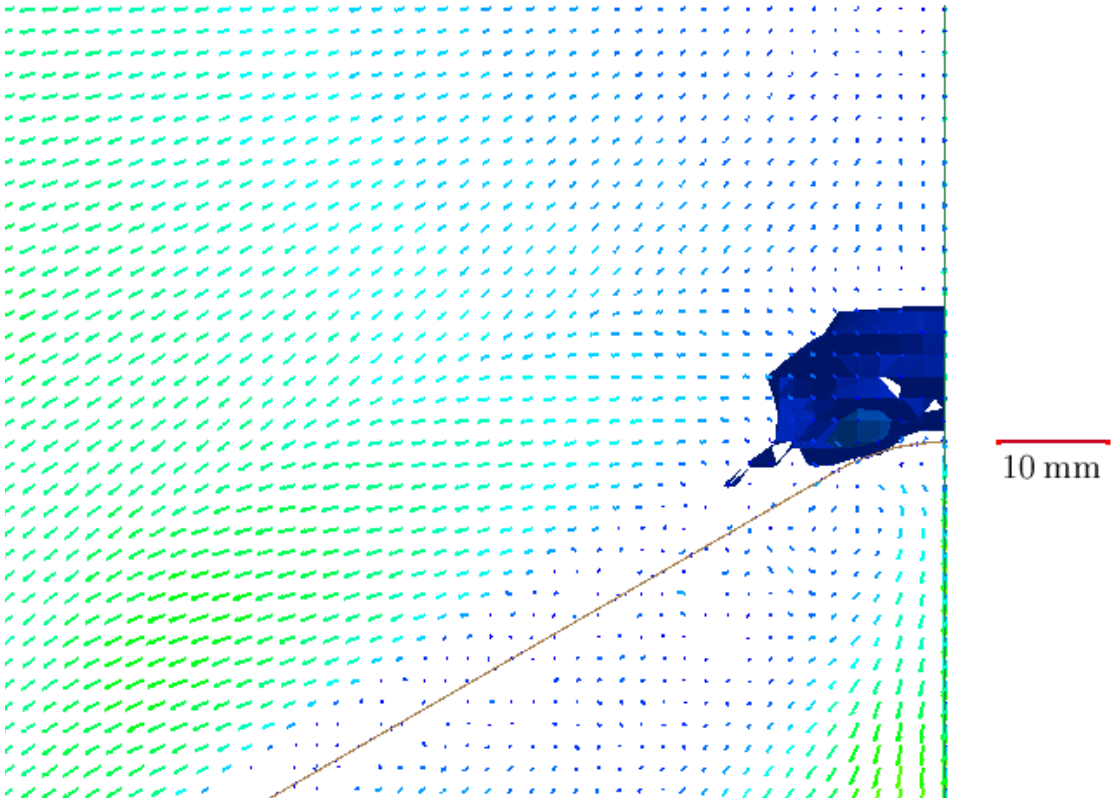

(b) t = 30.0 µs

Figure 7.10: Zoomed in view of the crosscut profile view showing the pressure time history development and material velocity for a 120° V-plate with a bend radius of 20 mm and a 58 g charge at 15.0 and 30.0 µs

The peak pressures at a tracer point located 1 mm above the tip of the V-plate (See Figure 4.3), for plates with 0, 12, 16 and 100 mm bend radii for the 90° V-plates are shown in Figure 7.11. It can be seen from Figure 7.11 that the peak pressure is 180 MPa lower for the 12 mm plates than for the 16 mm radius plates. The duration of the loading is longer for the test with the plate with a 12 mm bend radius compared to the one with a 16 mm bend radius. It is interesting to note that the peak pressures for bend radii of 12 and 16 mm are lower than the peak pressure at 0 mm. This could explain why the impulse transfer at these bend radii is lower. As expected the peak pressures for a bend radius of 100 mm is approximately 700 MPa greater than for a 0 mm bend radius. This causes the greater magnitude of the impulse transferred when combined with the additional area of impingement in the central region of the V. For the 120° simulations the lower impulses calculated for bend radii between 0 and 20 mm was due to the reduced peak pressures at the V-tip and the increased rate of gas flow down the plate.

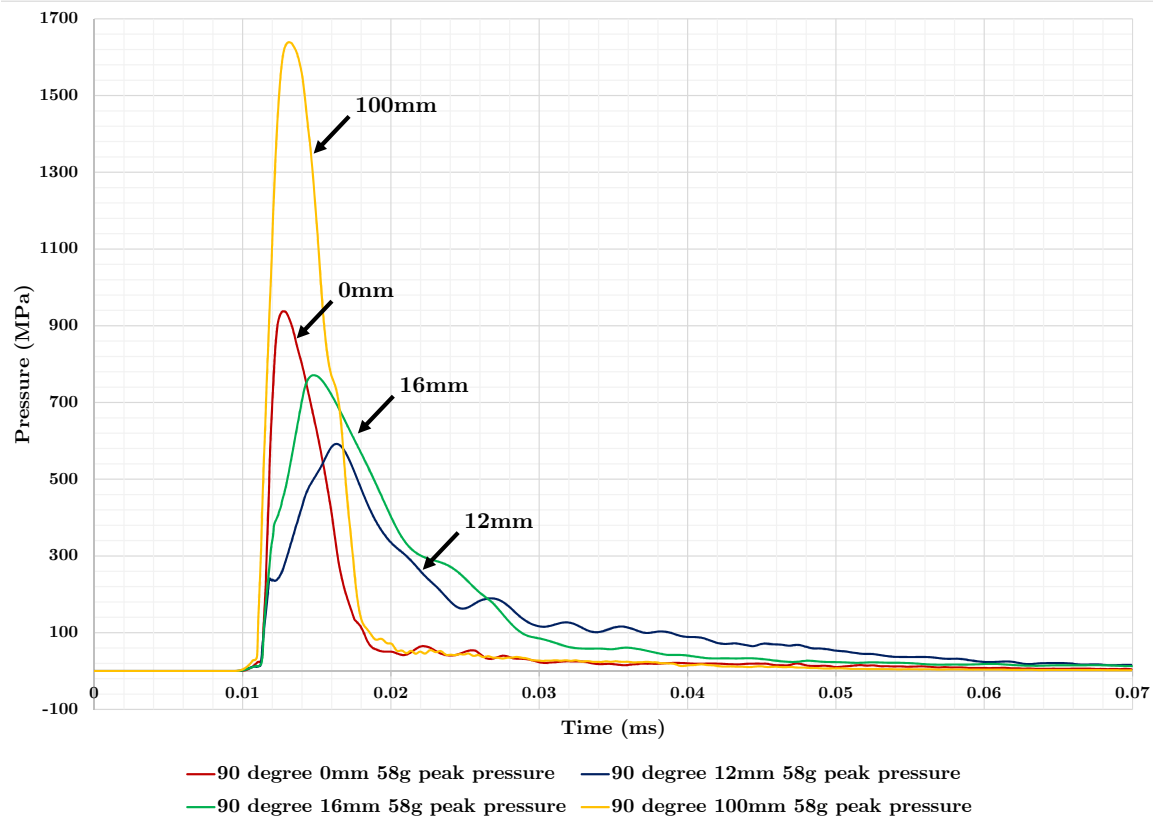

Figure 7.11: Graph showing the peak pressures for 90° V-plates with bend radii of 0, 12, 16 and 100 mm, subjected to a 58 g detonation

7.2 Influence of clamp frame designs

From the initial analyses in Chapter 5 it was identified that it was acceptable to model both the V-plates and the clamp frames with a rigid material. For two different clamp frame designs, V-plates with an internal angle of 60°, 90° and 120° were subjected to detonations of 19, 40 and 58 g of PE4 using numerical simulations.

Table 7.5 shows the impulses measured for the different simulations using the two different clamp frame designs. It can be seen that the impulse values are almost identical for the 60 and 90° V-plates, while the old clamp frame impulses are approximately 5% larger for the 120° V-plates. Furthermore, from Figures 7.12 to 7.14, it can be seen that the force histories obtained from the two different clamp frame designs are virtually identical. This was observed in all the tests performed, so it was concluded that the results obtained from the two clamp frame designs can be accurately compared. This means that if it is easier to manufacture a test panel in one configuration over the other, the sets of results should be comparable.

Table 7.5: Table showing the comparison of the impulse transferred in N s when using the old versus the new clamp frame designs

	60°		**90°**		**120°**	
Charge mass (g)	**New**	**Old**	**New**	**Old**	**New**	**Old**
19	13.49	13.30	19.33	19.30	22.51	23.13
40	20.28	19.68	30.10	30.28	35.25	36.97
58	22.98	22.19	35.71	34.70	40.74	43.34

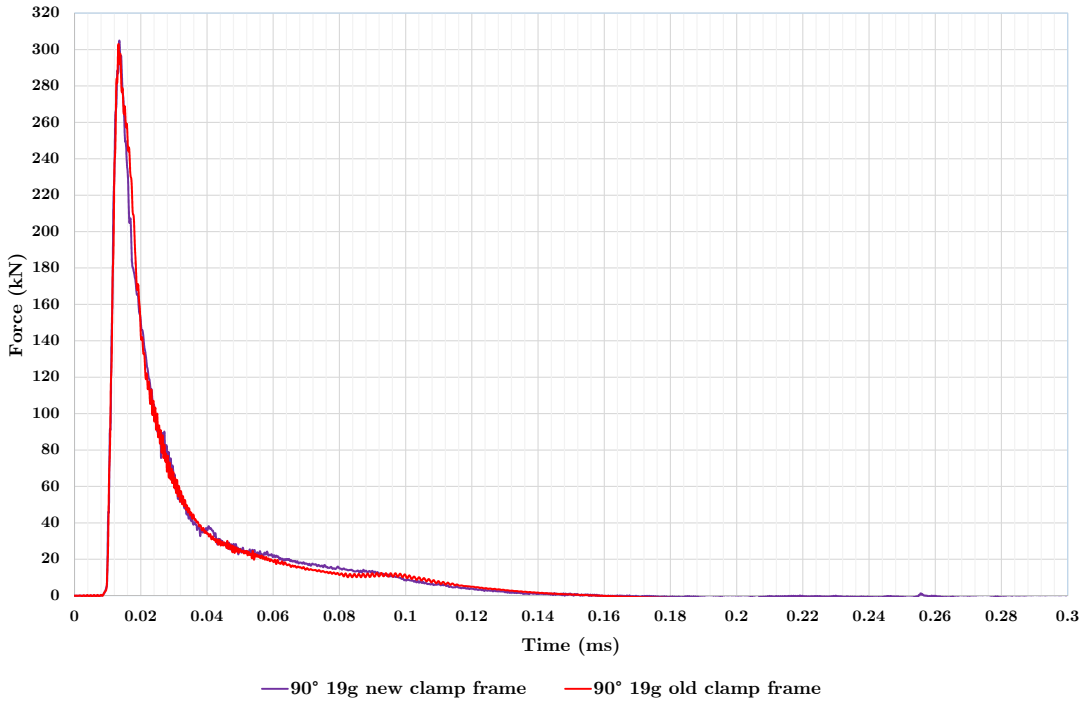

Figure 7.12: Graph showing the comparison in the force history between the new and old clamp frame designs for a 90° V-plate with a 19 g charge

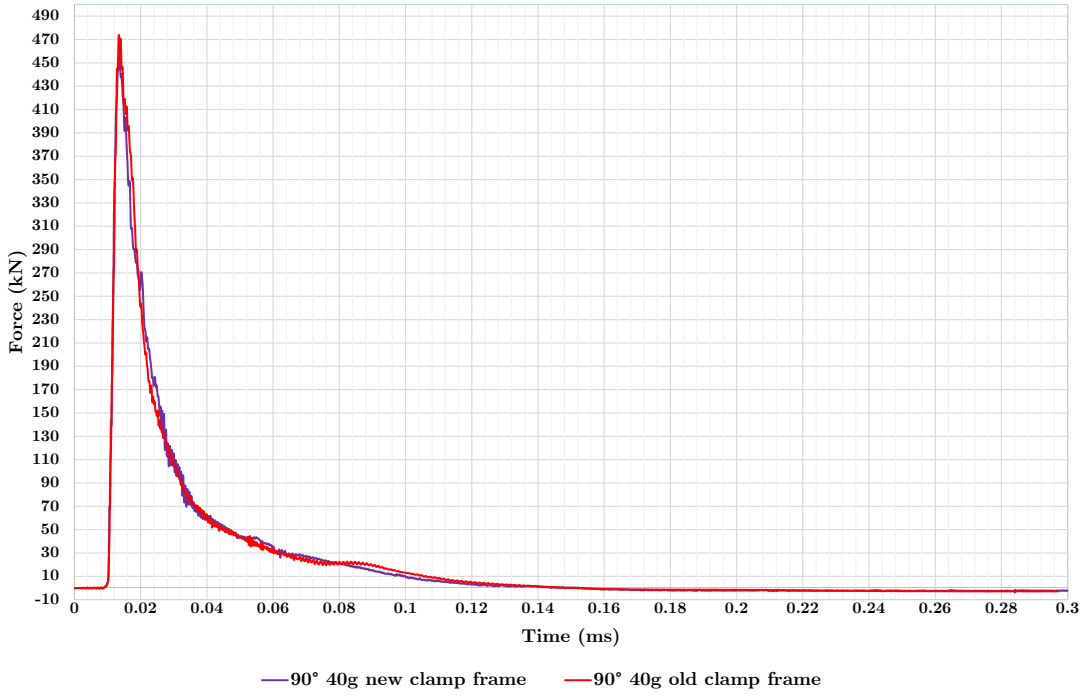

Figure 7.13: Graph showing the comparison in the force history between the new and old clamp frame designs for a 90° V-plate with a 40 g charge

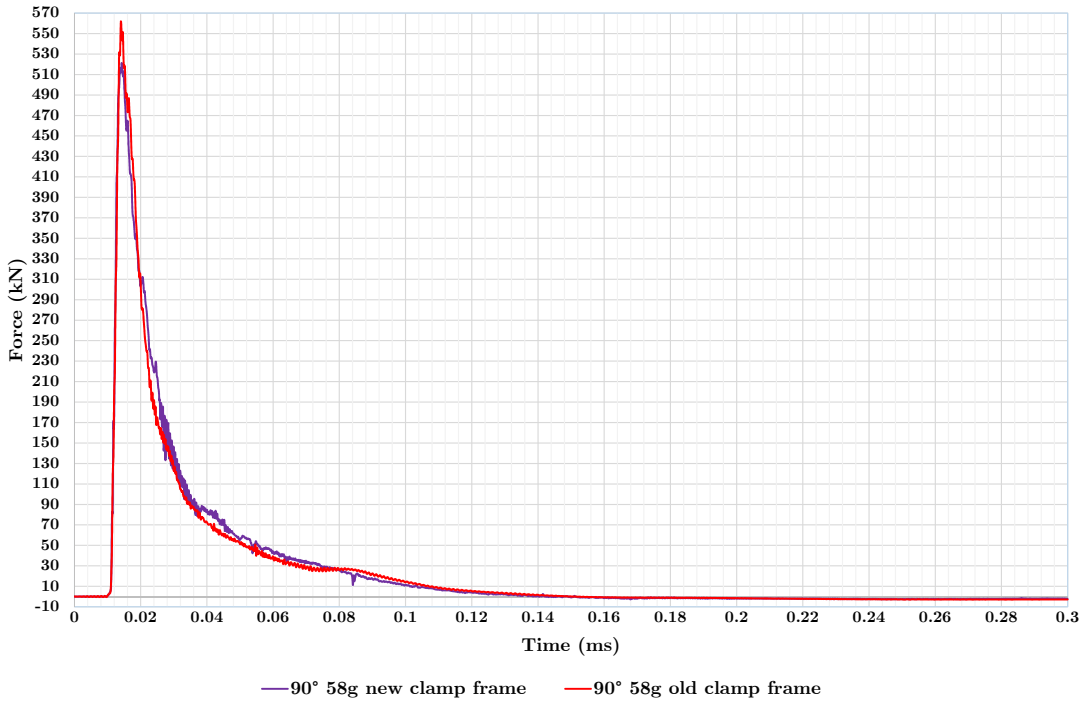

Figure 7.14: Graph showing the comparison in the force history between the new and old clamp frame designs for a 90° V-plate with a 58 g charge

7.3 Fixed height of the explosive

7.3.1 Total impulse analysis

The stand-off distance between the top of the V-plate and the bottom of the charge was fixed at 34 mm in the analyses presented in Section 7.1 as shown in Figures 6.2 and 7.1. It is also possible to fix the height of the explosive relative to the clamp frame, meaning that when the bend radius of the plate was increased, the stand-off distance increased. This is useful to determine if fixing the ride height of the crew compartment of a vehicle and varying the bend radius of the V-hull would affect the impulse transferred to the occupants of the vehicle.

Simulations on 60° V-plates with bend radii of 0, 40, 100 and 160 mm and 120° V-plates with a bend radii of 0, 40, 100, 160 and 200 mm, tested with a charge mass of 58 g were performed. Three of these cases are shown in Figure 7.15.

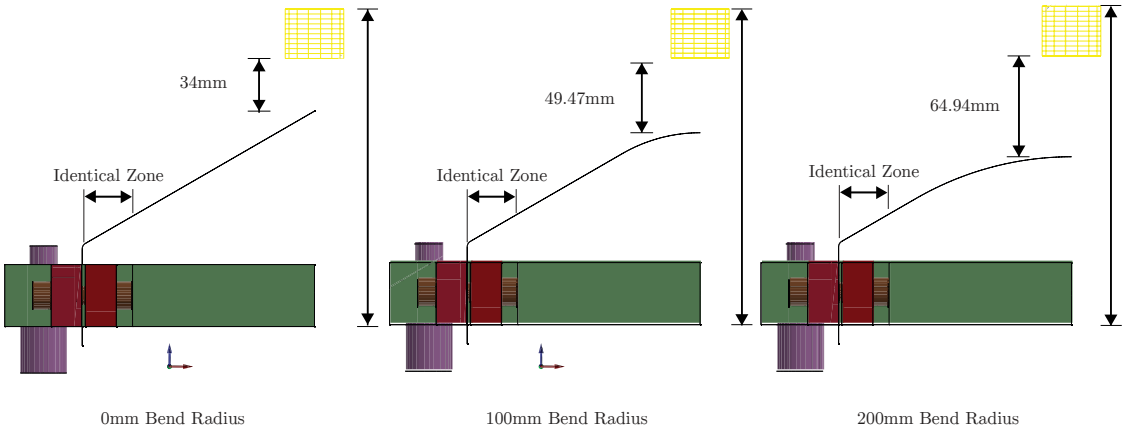

Figure 7.15: Schematic showing the fixed position (at 185.6 mm) of the explosive and the varying stand-off distance for the 120° V-plates of 0, 100 and 200 mm bend radii

Table 7.6 shows the impulse transferred and the stand-off distance for the simulations. For both the 60° and 120° simulations, it was observed that the total impulse was very similar as the stand-off distance is increased. Additionally, Figures 7.16 and 7.17 show that as the bend radius and stand-off distance increased, the peak force dropped, but the duration of the loading increased. This occurred for both the 60° and 120° simulations. Hence, the impulse varies far less than the peak force and duration because it smears any variation in pressure loading history. The effect is more pronounced for the 60° simulations as the change in the stand-off distance is greater. The peak forces and loading durations are also shown in Table 7.6.

Table 7.6: Table showing the effect of changing the bend radius and fixing the height (at 185.6 mm and 358.8 mm for the 60 and 120° V-plates respectively) of the explosive on the impulse transferred

	60°				120°			
Bend radius (mm)	**SOD (mm)**	**Impulse (N s)**	**t_{dur} (µs)**	**F_{peak} (kN)**	**SOD (mm)**	**Impulse (N s)**	**t_{dur} (µs)**	**F_{peak} (kN)**
0	34	22.97	149.86	410.05	34	40.73	101.87	793.36
40	74	22.76	161.42	304.99	40.19	38.91	102.64	766.73
100	134	22.96	158.41	163.90	49.47	38.75	101.36	528.86
160	194	23.20	209.05	122.70	58.75	39.83	104.92	490.23
200					64.94	39.70	106.29	435.59

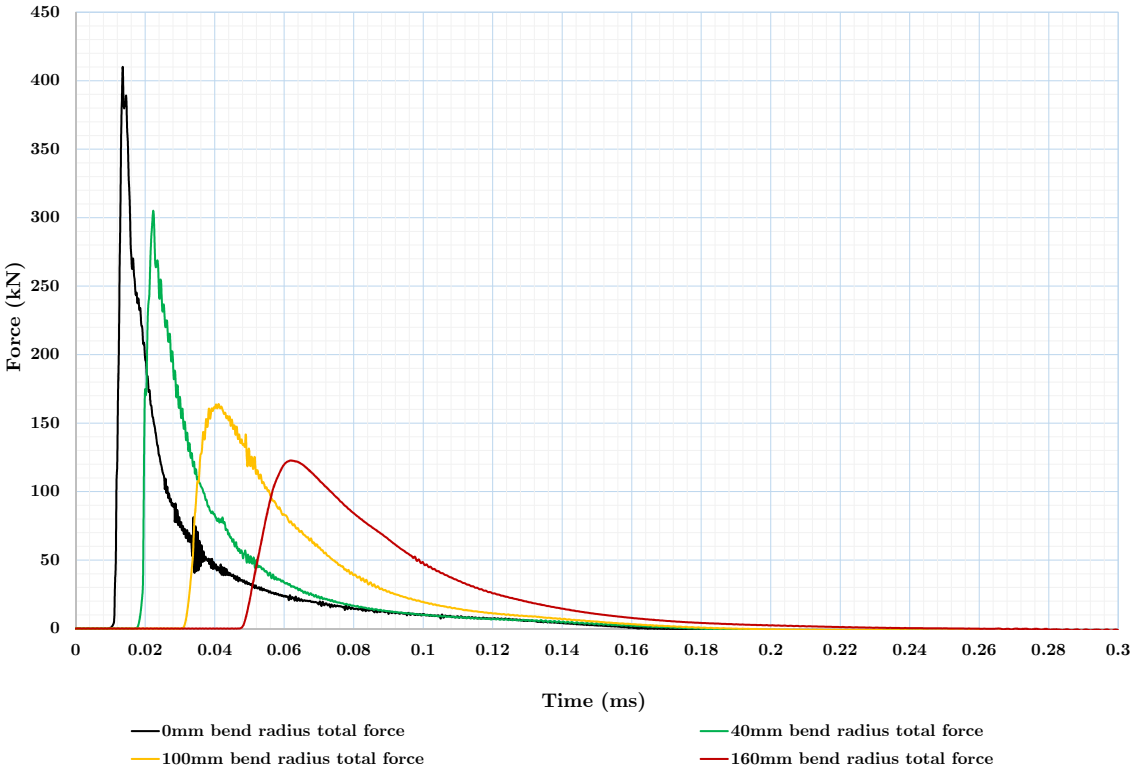

Figure 7.16: Graph showing the effect of varying the bend radius and fixing the total stand-off distance on the total force-time history for a 60° V-plate with a 58 g charge

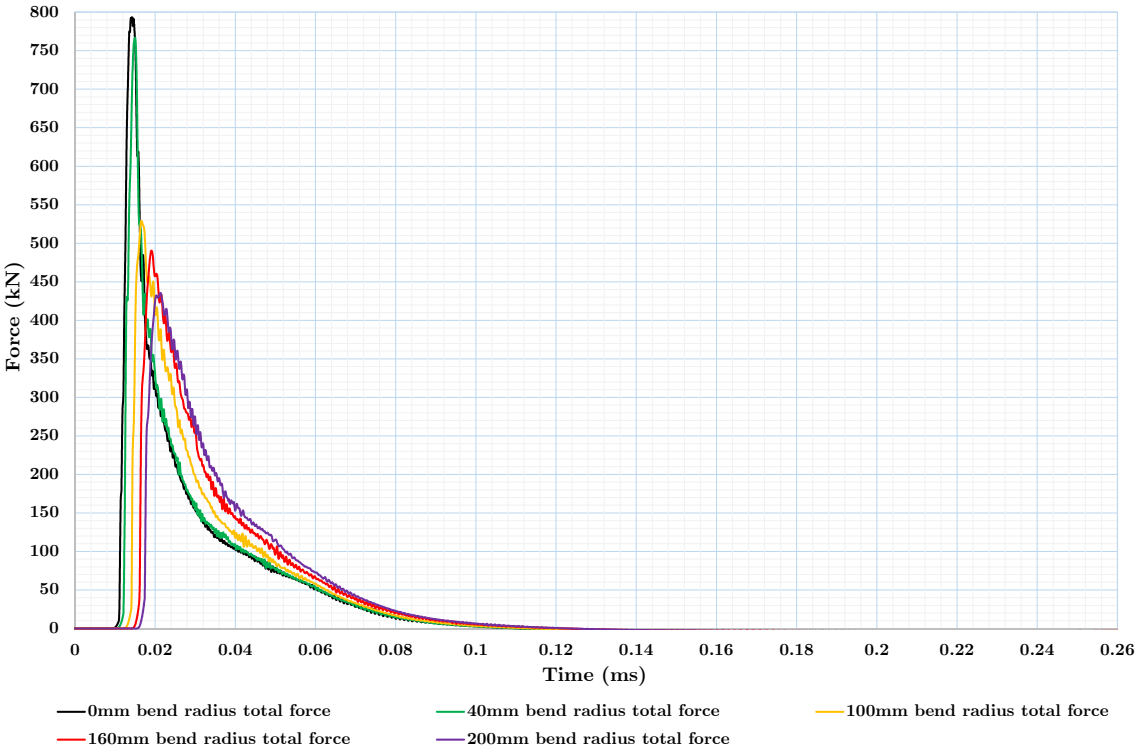

Figure 7.17: Graph showing the effect of varying the bend radius and fixing the total stand-off distance on the total force-time history for a 120° V-plate with a 58 g charge

From these tests, it can be concluded that if the ride height of the armoured vehicle is kept the same, but the bend radius of the hull is increased, the performance of the V-hull will be similar when impulse is the dominant factor determining occupant safety. If both the stand-off distance and the bend radius were varied it may be possible to find an optimised bend radius/stand-off distance combination.

7.3.2 Zonal impulse analysis

Figure 7.18 shows an example of the air meshes used by Pickering [6]. The air meshes were 100 mm x 100 mm blocks of varying heights and covered a portion of the plates which had projected areas of 150 mm x 150 mm. It was decided that it would be useful to determine if due to the fact that the air mesh did not cover the entire plate, there would be a significant reduction in the impulse measured.

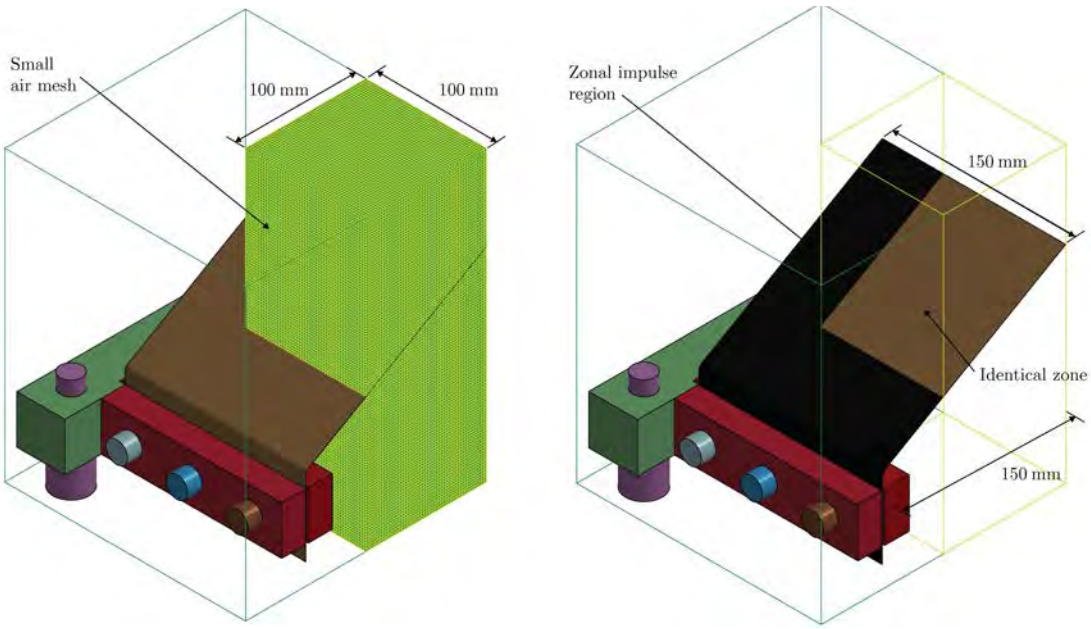

Figure 7.18: Schematic, showing the air mesh used by Pickering [6] and Warncke [9], and the region analysed

In Figure 7.18 there is a region labelled the "Identical zone". This was done to determine two things. The first was whether the impulse transferred from regions further away from the explosive charge were identical. The second was to determine if this impulse (labelled the zonal impulse) was significant in terms of the total impulse transferred. The results for the impulse in this region and the percentage of these values in terms of the total impulse from Table 7.6 are shown in Table 7.7.

Table 7.7: Table showing the effect of changing the bend radius and fixing the height of the explosive on the impulse transferred from the zonal impulse region on each the plate

	60°			120°		
Bend radius (mm)	**SOD (mm)**	**Impulse (N s)**	**% of total impulse**	**SOD (mm)**	**Impulse (N s)**	**% of total impulse**
0	34	2.56	11.13	34	3.28	8.05
40	74	2.45	10.79	40.19	3.25	8.36
100	134	2.25	9.79	49.47	3.30	8.51
160	194	2.67	11.49	58.75	3.24	8.14
200				64.94	3.24	8.17

The impulse values are very similar for both the 60° and the 120° simulations, which suggests that the loading is similar for regions further away from the detonation at the extremities of the plate. Figures 7.19 and 7.20 shows that the force histories in the same zone are also very similar for the different simulations. In terms of the percentage of the total impulse, the zonal impulse varies between 8 and 11% for all the cases considered, which represents a significant portion of the total impulse.

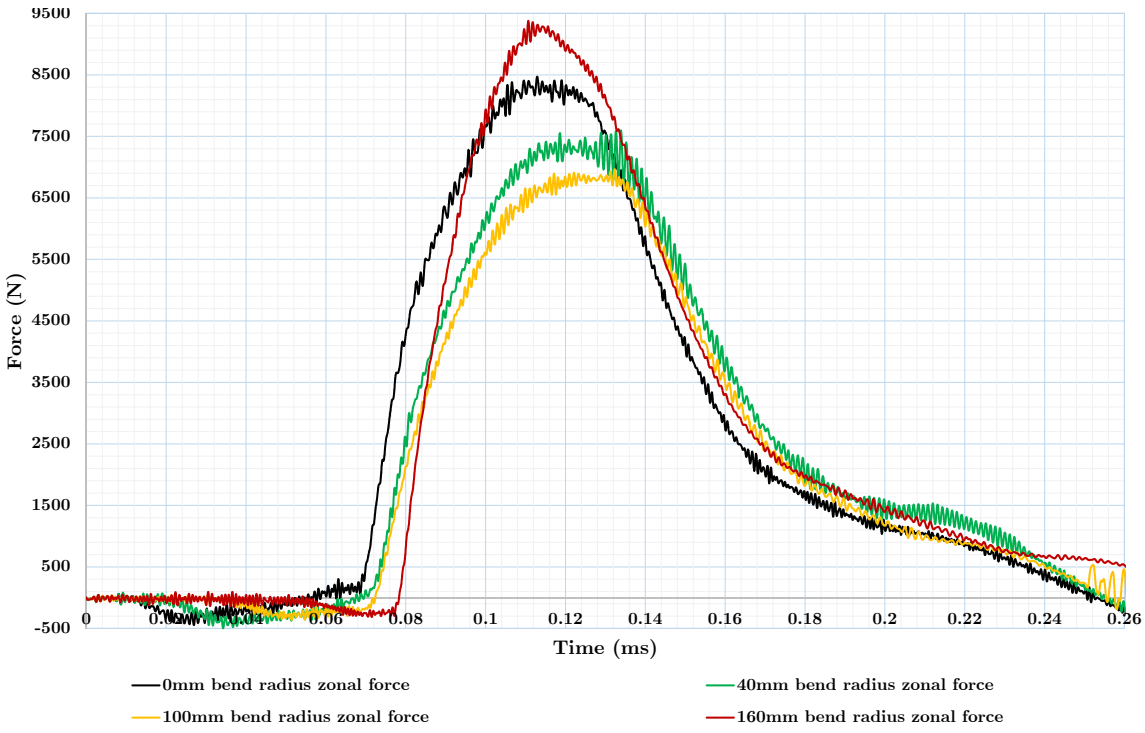

Figure 7.19: Graph showing the effect of varying the bend radius and fixing the total stand-off distance on the zonal force-time history for a 60° V-plate with a 58 g charge

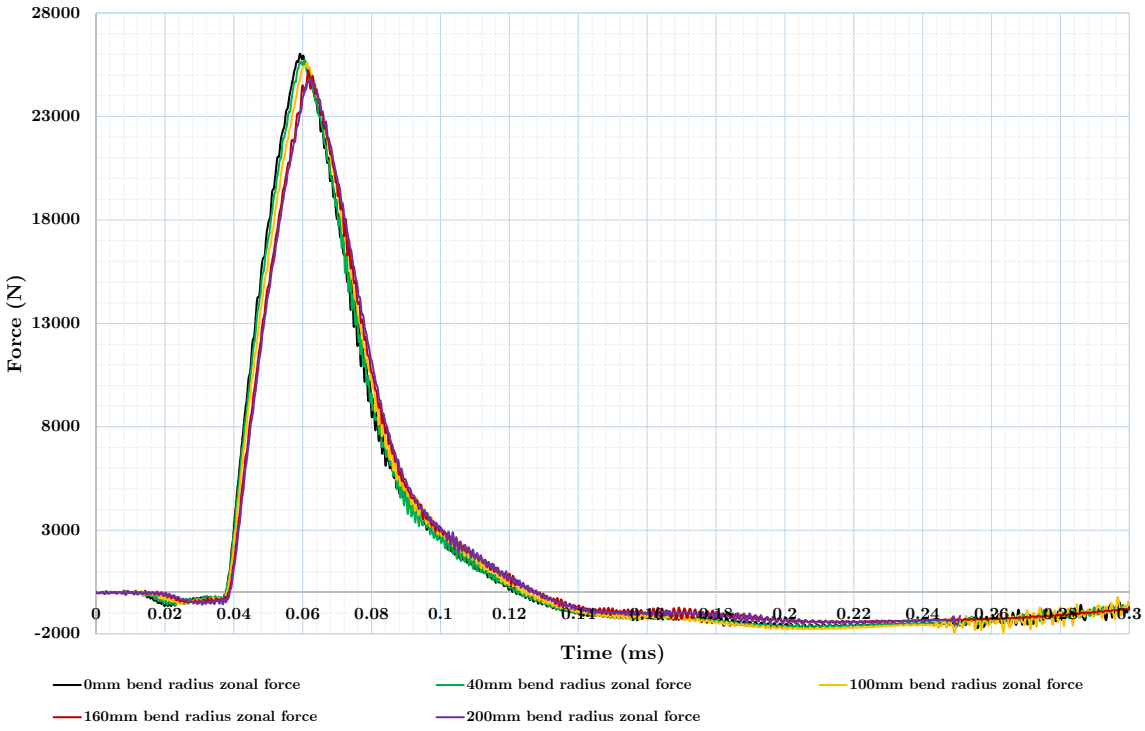

Figure 7.20: Graph showing the effect of varying the bend radius and fixing the total stand-off distance on the zonal force-time history for a 120° V-plate with a 58 g charge

Chapter 8

Conclusions

A numerical model was developed using LS-DYNA. The model was validated using experimental tests performed on rigid V-plates. This model was then used to investigate the objectives stated in Chapter 1.

1. *Effects of the V-tip radius on the impulse transfer characteristics of V-plates with varying included angles.*

   The impulse transferred generally increased as the bend radius was increased, for all three V-angles investigated. The 60° V-plates showed the greatest sensitivity to bend radius effects. A possible explanation for this could be due to the greater reduction in total height for an increasing bend radius.

   It was also observed that the 90° and 120° V-plates showed very small increases in impulse transferred for bend radii greater than 160 mm. A similar trend was not observed for the 60° V-plates as it was not possible to investigate bend radii greater than 160 mm. Larger bend radii could not fit in the profile due to the geometry of these V-plates.

2. *V-angle and charge mass effects*

   As expected, the larger V-angles resulted in higher impulse transfer. Furthermore, as expected, an increase in the charge mass resulted in an increase in the impulse transfer.

   Both the V-angle and the bend radius influence the impulse transfer for bend radii between 0 and 80 mm. For larger bend radii (that is between than 100 and 160 mm), bend radius effects appear to dominate, with the V-angle having little to no effect, as the predicted impulse values are very similar for the different V-angles investigated. For bend radii above 160 mm the rate of increase in impulse for an increase in bend radius is significantly reduced and tends to plateau. Once again the V-angle continues to have no effect for bend radii in this range. These observations are summarised in Table 8.1.

Table 8.1: Table showing the trends for V-angle and bend radius effects on impulse for ranges of V-tip radii

Bend radius range	**V-angle effects**	**Bend radius effects**
< 100 mm	↑ V-angle ⇒ ↑ Impulse transferred	↑ Bend radius ⇒ ↑ Impulse transferred
100 mm to 160 mm	↑ V-angle ⇒ no significant change in impulse	↑ Bend radius ⇒ ↑ Impulse transferred
> 160 mm	↑ V-angle ⇒ no significant change in impulse	↑ Bend radius ⇒ ↑ impulse transferred; rate of increase is reduced significantly almost plateauing

3. *Effects of two clamp frame designs on the impulse transfer and pressure distributions of V-plates with different V-angles.*

   From the study it was found that the clamp frame design had no significant effect on impulse transfer, which suggests that impulse values obtained from similar tests performed with either design should be comparable. The lower impulses measured by Hobson [8] were probably not due to the different clamp frame used in the experiments.

   The clamp frame should be included in the model as the pressure profile across the plate changed when the clamp frame is not included. These pressures in the clamp frame region were two orders of magnitude smaller than the peak pressure at the V-tip. When the numerical model was being developed, it was observed that when the clamp frame was not included, the predicted impulses were significantly lower (See Table 5.9 on page 73 in Section 5.2.2).

4. *Effects of fixing the position of the explosive charge relative to the clamp frame while increasing the bend radius of the V-plates on the impulse transfer and pressure-time characteristics of the blast test.*

   This was investigated to determine if the height of the crew compartment of an APC could be fixed (See Section 7.3). It was observed that the impulse did not vary when the bend radius was increased. When impulse alone was used as a measure of performance, it obscured the differences observed in the pressure distribution and the temporal characteristics. As the stand-off distance increased due to the increase in bend radius, the peak pressure dropped, but the duration of the loading increased. The variation in the pressure loading of the V-hulls would be significant in terms of damage that they would experience (such as plastic deformation or tearing failure) but not for general occupant safety (as this is primarily due to the total impulse) [14].

5. *Effects of plate geometry on the impulse transfer at regions remote from the detonation point.*

   Similar force-time histories were predicted by the models for regions remote from the detonation point. Additionally no variation in impulse was observed in these regions. This indicates that while the geometry (V-angle and bend radius) affects the total impulse, there is no variation in the impulse measured for regions far away from the detonation point for a given charge mass and stand-off distance.

6. *Explaining the lowered impulse values obtained by Pickering [6] in numerical simulations performed.*

   In this study the air mesh covered the entire plate and the impulse was measured across the entire plate. Additionally the impulses were considered in two zones for comparison with work by Pickering [6]. A fixed zone that covered the difference in area between the air mesh used by Pickering [6] and the one used in these simulations were considered. It was found that the zonal impulse values were between 8 and 11% of the total impulse. Hence the lower impulses predicted by Pickering [6] were attributed to the smaller air mesh used (which did not cover the entire plate).

This page has been intentionally left blank.

Chapter 9

Recommendations

The following recommendations are based on the results, discussion and conclusions of this work. They are listed as follows:

1. *Experiments*

    - Conduct experiments using DOMEX-700 MC steel V-plates with varying bend radii, to confirm the trends observed for the predicted impulses in the numerical simulations.

    - Carry out experiments where the distance of the explosive from the clamp frame is fixed and the bend radius is increased, to confirm the trends observed in the simulations.

    - Choose an optimum bend radius and stand-off distance combination for each V-plate investigated that results in minimum deformation or damage.

2. *Numerical simulations*

    - Modify the numerical model to include the explosive used in the detonator or to model the detonation as a line detonation rather than a point detonation.

    - Extend the bend radius analysis to include the effects of the deformation of the V-plates, by using the Johnson-Cook material model for DOMEX-700 MC steel.

    - Add a material model for the fibreglass composite used by Hobson [8] to the numerical models, and use it to investigate the damage characteristics of composite V-plates as tested by Hobson [8].

This page has been intentionally left blank.

References

[1] Stiff, P. *Taming the Landmine*. Galago, 1986. ISBN: 9780947020040.

[2] Livesey, J. *The Illustrated Guide to Armoured Fighting Vehicles of the World*. Hermes House, 2006. ISBN: 9781844779444.

[3] Beem, A. van. *GKN-Sankey FV432 APC*. Online. July 2010.

[4] McCree, J. *A Senior Airman (standing) and an Airman 1st Class patrol in an M-113 Armored Personnel Carrier at the Theater Internment Facility at Camp Bucca, Iraq*. Online. Feb. 2008.

[5] O'Lionnain, E. *Armoured car, Army Museum Stockholm*. Online. Aug. 2008.

[6] Pickering, E. G. *The Response of V-Shaped Plate Structures to Localised Blast Loading*. Tech. rep. Department of Mechanical Engineering, University of Cape Town, Oct. 2009.

[7] Naidoo, K. *Response of Shallow "V" Plates to Blast Load*. Tech. rep. Department of Mechanical Engineering, University of Cape Town, 2012.

[8] Hobson, L. *Response of Composite Panels to Blast Loading*. Tech. rep. Department of Mechanical Engineering, University of Cape Town, 2013.

[9] Warncke, D. *The Design And Testing Of Novel Shallow V-Shape Structures*. Tech. rep. Department of Mechanical Engineering, University of Cape Town, 2013.

[10] Keeley, R. *Understanding landmines and mine action*. Tech. rep. September. 2003.

[11] GICHD. *Guide to Mine Action*. 5th ed. GICHD (Geneva International Centre for Humanitarian Demining), Mar. 2014.

[12] Youngblood IV, N. E. "The development of landmine warfare". PhD thesis. Texas Tech University, 2002.

[13] Croll, M. *The History of Landmines*. Leo Cooper, 1998.

[14] Lester, C. *Protection of Light Skinned Vehicles Against Landmines - A Review*. Tech. rep. DTIC Document, 1997.

[15] ICRC. *Anti-personnel Landmines: Friend Or Foe?: A Study of the Military Use and Effectiveness of Anti-personnel Mines*. Vol. 72. ICRC publications 4. ICRC (International Committee of the Red Cross), 1996, p. 100.

[16] Ramasamy, A., Masouros, S. D., Newell, N., Hill, A. M., Proud, W. G., Brown, K. A., Bull, A. M. J., and Clasper, J. C. "In-vehicle extremity injuries from improvised explosive devices: current and future foci". In: *Philos. Trans. R. Soc. B Biol. Sci.* 366.1562 (2011), pp. 160–170.

[17] Wilson, C. *Improvised Explosive Devices (IEDs) in Iraq: Effects and Countermeasures: CRS Report for Congress*. Tech. rep. DTIC, 2006.

[18] Wilson, C. *Improvised Explosive Devices (IEDs) in Iraq and Afghanistan: Effects and Countermeasures: CRS Report for Congress*. Tech. rep. DTIC, 2006.

[19] DTIC. "A Military Guide to Terrorism in the Twenty-First Century". In: *US Army TRADOC G2 Handb.* 1 (2007).

[20] Rupiah, M. R. "A Historical Study of Land-Mines in Zimbabwe, 1963-1995". In: 2.May 1994 (1995), pp. 9–11.

[21] Ramasamy, A., Hill, A. M., Masouros, S. D., Gordon, F., Clasper, J. C., and Bull, A. M. J. "Evaluating the ezffect of vehicle modification in reducing injuries from landmine blasts. An analysis of 2212 incidents and its application for humanitarian purposes". In: *Accid. Anal. Prev.* 43.5 (2011), pp. 1878–1886.

[22] Hohl, G. H. "Military Terrain Vehicles". In: *J. terramechanics* 44.1 (2007), pp. 23–34.

[23] O'Malley, T. J. and O'Malley, T. J. *Fighting Vehicles: Armoured Personnel Carriers & Infantry Fighting Vehicles*. Greenhill Books, 1996.

[24] Smith, M. *A British Standard Beaverette armored car at RAF Duxford*. Online. 2006.

[25] Robledo, L, Carrasco, M, and Mery, D. "A Survey of Land Mine Detection Technology". In: *Int. J. Remote Sens.* 30.9 (2009), pp. 2399–2410.

[26] Blakeman, S. T., Gibbs, A. R., and Jeyasingam, J. "Study of the Mine Resistant Ambush Protected (MRAP) Vehicle Program as a Model for Rapid Defense Acquisitions". PhD thesis. Monterey, California: Naval Postgraduate School, 2008.

[27] Roux, N. *The Rhodesian Leopard landmine resisting or 'anti-landmine' vehicle. Photo taken at the South African National Museum of Military History*. Feb. 2007.

[28] Gorelik, B. *Casspir at the South African Police Museum, Pretoria. A view from the back*. Online. Sept. 2008.

[29] Baker, W. E. *Explosions in Air*. University of Texas Press Austin, 1973.

[30] Kinney, G. F. and Graham, K. J. *Explosive Shocks in Air*. Springer, Verlag, 1985.

[31] Gregory, C. E. *Explosives for Engineers*. Vol. 10. Trans Tech Publications, 1993.

[32] Akhavan, J. *The Chemistry of Explosives*. RSC Paperbacks Series. Royal Society of Chemistry, 2011.

[33] Zukas, J. A. and Walters, W. P. *Explosive Effects and Applications*. Springer, 2002.

[34] Cooper, P. W. *Explosives Engineering*. Wiley-VCH, 1996.

[35] Jacob, N., Chung Kim Yuen, S., Nurick, G. N., Bonorchis, D., Desai, S., and Tait, D. "Scaling aspects of quadrangular plates subjected to localised blast loads - Experiments and predictions". In: *Int. J. Impact Eng.* 30.8 (2004), pp. 1179–1208.

[36] Langdon, G. S., Yuen, S. C. K., and Nurick, G. N. "Experimental and numerical studies on the response of quadrangular stiffened plates. Part II: localised blast loading". In: *Int. J. Impact Eng.* 31.1 (2005), pp. 85–111.

[37] Zakrisson, B. "Numerical and Experimental Studies of Blast Loading". PhD thesis. LuleåUniversity of Technology, 2010.

[38] Zakrisson, B., Wikman, B., and Häggblad, H. K. “Numerical simulations of blast loads and structural deformation from near-field explosions in air”. In: *Int. J. Impact Eng.* 38.7 (2011), pp. 597–612.

[39] Jacob, N., Nurick, G. N., and Langdon, G. S. “The effect of stand-off distance on the failure of fully clamped circular mild steel plates subjected to blast loads”. In: *Eng. Struct.* 29.10 (2007), pp. 2723–2736.

[40] James Madison University - CISR Reference. “Landmines - Afghanistan Ordnance Identification Guide”. In: (). URL: `http://www.jmu.edu/cisr/\_pages/research/munitions.shtml`.

[41] Jacinto, A. C., Ambrosini, R. D., and Danesi, R. F. “Experimental and computational analysis of plates under air blast loading”. In: *Int. J. Impact Eng.* 25.10 (2001), pp. 927–947.

[42] Chung Kim Yuen, S., Langdon, G. S., Nurick, G. N., Pickering, E. G., and Balden, V. “Response of V-shape Plates to Localised Blast Load: Experiments and Numerical Simulation”. In: *Int. J. Impact Eng.* 46 (2012), pp. 97–109.

[43] Langdon, G. S., Yuen, S. C. K., Nurick, G. N., and Naidoo, K. “Some Insights into the Response of "Shallow V Shape" Structures to Air Blast Loading”. In: *Proc. Natl. Acad. Sci.* (2013), pp. 695–703.

[44] Anderson Jr, C. E., Behner, T., Weiss, C. E., Chocron, S., and Bigger, R. P. *Mine Blast Loading: Experiments and Simulations*. Tech. rep. April. 2010.

[45] Anderson Jr, C. E., Behner, T., and Weiss, C. E. “Mine Blast loading Experiments”. In: *Int. J. Impact Eng.* 38.8 (2011), pp. 697–706.

[46] Follett, S. “Blast Analysis Of Composite V-shaped Hulls: An Experimental And Numerical Approach”. PhD thesis. Department of engineering and applied science, Cranfield university, 2012.

[47] Tabatabaei, Z. S. and Volz, J. S. “A Comparison between Three Different Blast Methods in LS-DYNA®: LBE, MM-ALE, Coupling of LBE and MM-ALE”. In: *12th Int. LS-DYNA Users Conf.* 3 (2012), pp. 1–10.

[48] Williams, K., McClennan, S., Durocher, R., St-Jean, B., and Tremblay, J. “Validation of a Loading Model for Simulating Blast Mine Effects on Armoured Vehicles”. In: *7th Int. LS-DYNA Users Conf.* (2002), pp. 35–44.

[49] Ozinsky, A. “The Response of Partially-confined Right-circular Cylinders to Internal Blast Loading”. PhD thesis. Department of Mechanical Engineering, University of Cape Town, Dec. 2012.

[50] Volschenk, G. *Material Characterization and Blast Modelling of Multi-Layered DOMEX-550 MC and 700 MC Plates*. Tech. rep. Department of Mechanical Engineering, University of Cape Town, 2013.

[51] Geretto, C. “The Effects Of Different Degrees Of Confinement On The Deformation Of Square Plates Subjected To Blast Loading”. PhD thesis. Department of Mechanical Engineering, University of Cape Town, 2012, p. 140.

[52] Showichen, A. “Numerical analysis of vehicle bottom structures subjected to anti-tank mine explosions”. PhD thesis. Cranfield University, 2008.

[53] Paykani, A., Khosravi, M., Saeimi-Sadigh, M.-A., and Mahmoodi-Kaleibar, M. "Dynamic analysis and design of V-shape plates under blast loading". In: *J. Vibroengineering* 15.2 (2013), pp. 971–978.

[54] Saeimi-Sadigh, M.-A., Paykani, A., Afkar, A., and Aminollah, D. "Design and energy absorption enhancement of vehicle hull under high dynamic loads". In: *J. Cent. South Univ.* 21.4 (2014), pp. 1307–1312.

[55] Barsotti, M. A., Puryear, J. M. H., Stevens, D. J., Alberson, R. M., and Mcmahon, P. "Modeling mine blast with SPH". In: *Proc. 12th Int. LS-DYNA User Conf.* 1. 2012, pp. 1–12.

[56] SSAB. *Safety Data Sheet for Hot Rolled and Cold Rolled Sheet Steel*. Tech. rep., pp. 2–3.

[57] Livermore Software Technology Corporations (LSTC). *LS-DYNA®Keyword User's Manual Volume II Material Models*. Vol. II. February. May 2013. ISBN: 9254492507.

[58] Hallquist, J. *LS-DYNA®Theory Manual*. March. May 2006, p. 680. ISBN: 9254492507. URL: `http://www.dynasupport.com/manuals/additional/ls-dyna-theory-manual-2005-beta/at\_download/file`.

[59] Dobratz, B. M. and Laboratory, L. L. N. *LLNL Explosives Handbook: Properties of Chemical Explosives and Explosive Simulants*. Lawrence Livermore National Laboratory, University of California, 1985.

[60] Hearn, E. *Mechanics of Materials Volume 1: An Introduction to the Mechanics of Elastic and Plastic Deformation of Solids and Structural Materials*. 1997. ISBN: 9780080523996.

Appendix A

Numerical model refinement

This appendix contains detailed explanations of the numerical model development, including the choice of element size for the final model, the ANSA pre-processor which was used to mesh the plates and clamp frames, the different LS-DYNA cards that were used in the model, the values used in the key cards and why they were chosen.

A.1 V-plate and clamp frame meshing

All the simulations that were performed, were based on a quarter symmetry model of the plate and clamp frame arrangement. The geometry of the plates was created using LS-PrePost, while the meshing was done in ANSA.

A.1.1 Drawing of a V-plate

The following section details the process of creating a plate using LS-PrePost. The first step was to create a side profile of the plate. This was done by defining the points representing the corners of the plate. These points were then connected with lines as shown in Figures A.1 and A.2.

Figure A.1: Creating a V-plate profile: The corner points

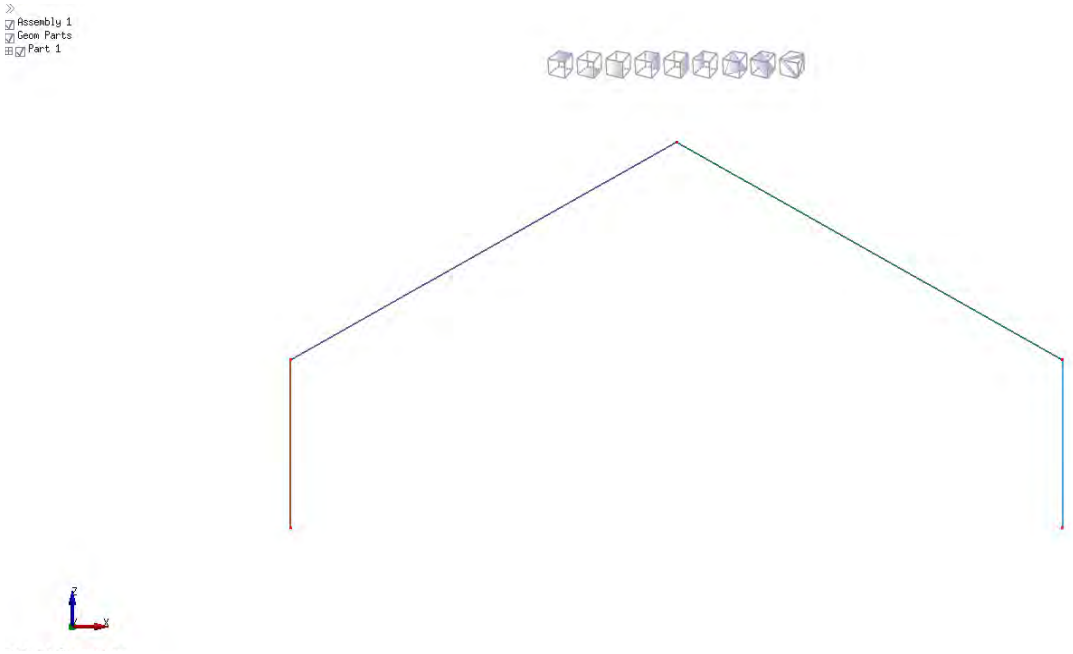

Figure A.2: Creating a V-plate profile: The profile of the plate without corner radii

The bend radii were added as fillets and an additional line is drawn in the middle to allow the

profile to be cut in half. The Trim tool was then used to remove the additional features and then the Merge Curve tool was used to create a single curve as shown in Figures A.3 to A.5.

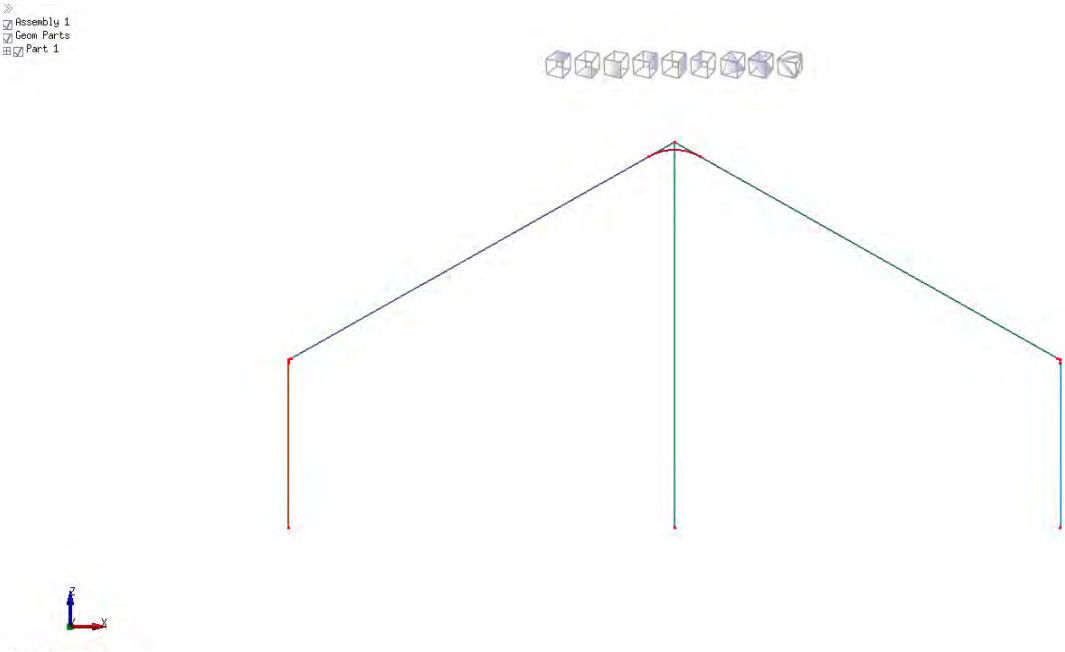

Figure A.3: Creating a V-plate profile: The profile of the plate with corner radii

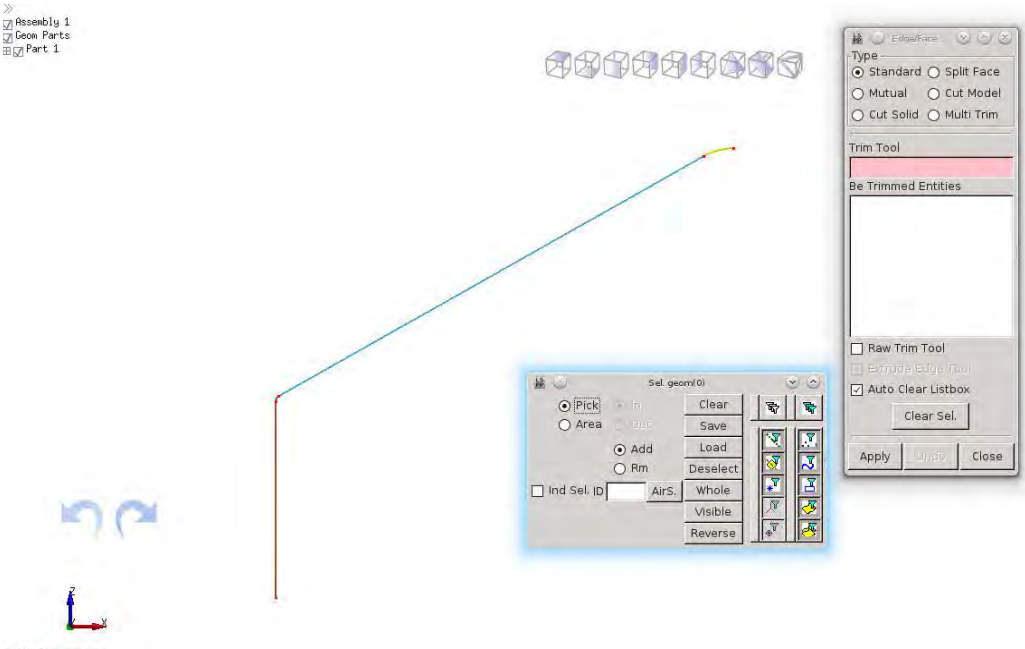

Figure A.4: Creating a V-plate profile: Half the plate profile showing the trim tool

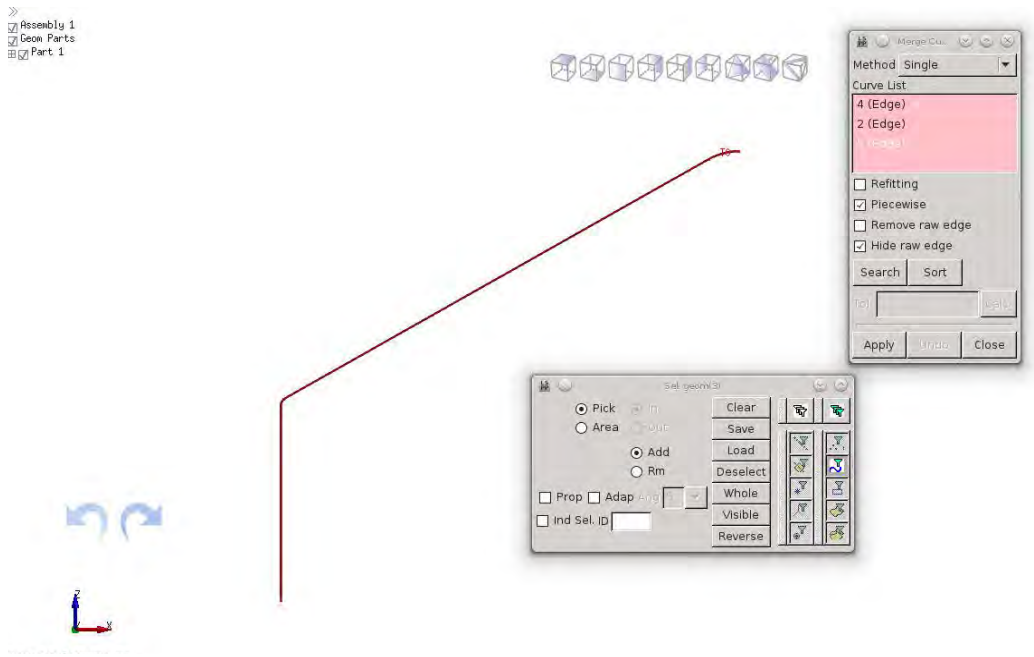

Figure A.5: Creating a V-plate profile: Merged curve representing the side profile for a 120°V-plate with a 20 mm bend radius

A.1.2 Meshing of a V-plate

The profile shown in Figure A.5 was extruded and saved as a STEP-File, and subsequently imported into ANSA. Holes for the bolts were cut into the plate using the Intersect and Delete tools under the Faces tab as shown in Figure A.6. ANSA was used to mesh the plates because LS-PrePost could not mesh the regions around the holes with only quadrilateral elements.

The Mesh module in ANSA was then selected and the plate cut into sections using the Cut tool under the Macros tab, to ensure that the regions around the holes were meshed with only quadrilateral elements as shown in Figure A.7. Then the edges were seeded with the correct number of nodes, using the Length tool (under the Perimeters tab). The length of all edges were set to 1.0 mm apart from the two curved edges near the clamped region. The length of the elements on these edges was set at 0.5 mm.

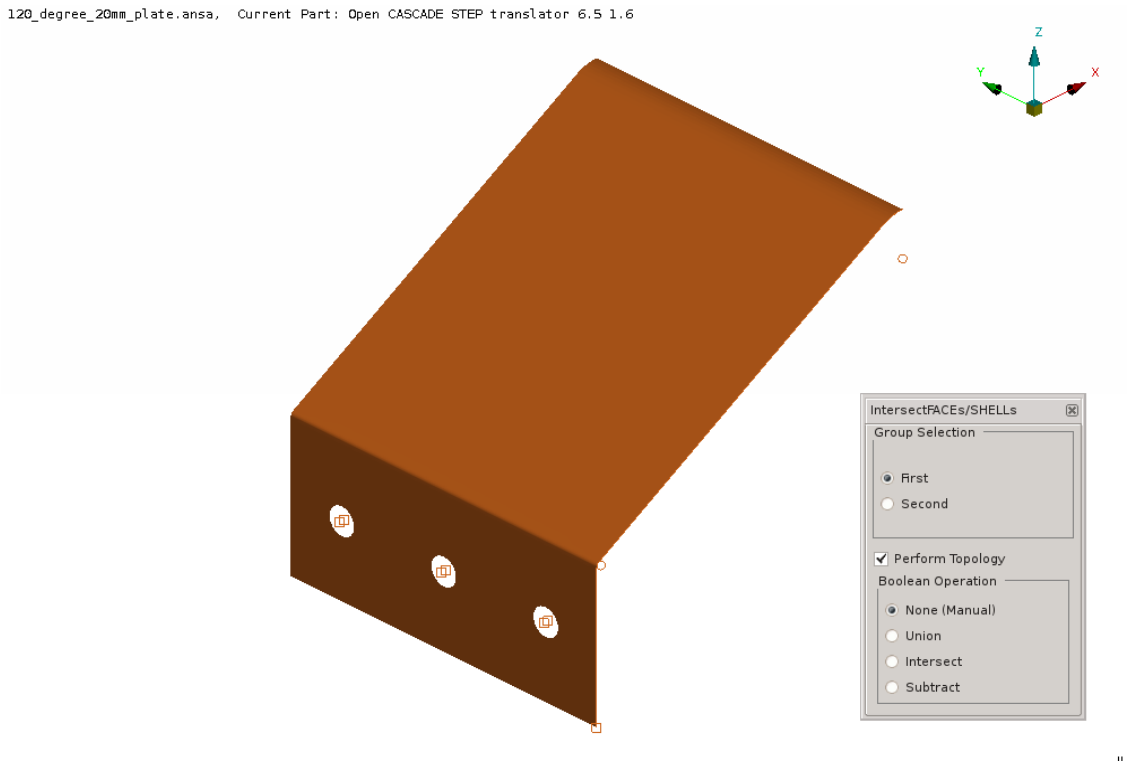

Figure A.6: Creating a meshed quarter symmetry model of a V-plate: Making the bolt holes in the plate

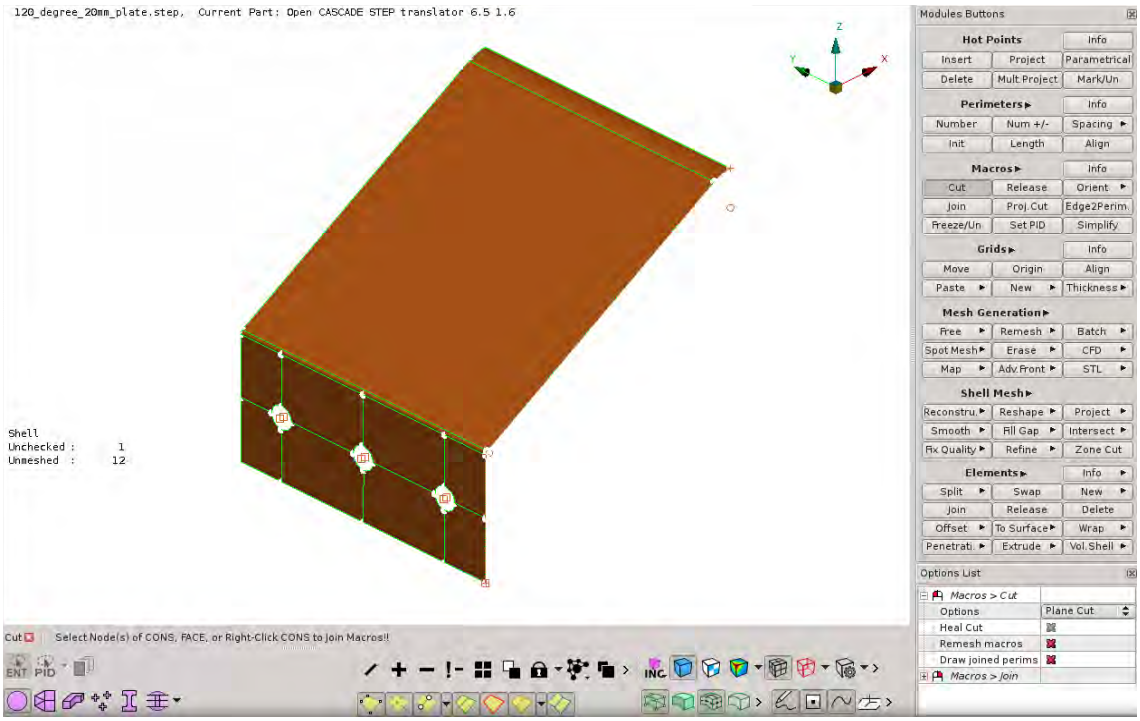

Figure A.7: Creating a meshed quarter symmetry model of a V-plate: Cutting the plate into sections to ensure uniform meshing

The plate was meshed with first order quadrilateral elements using the Map and Batch meshing tools (under the Mesh Generation tab). The Map meshing tool was used to mesh the rectangular regions of the plate as shown in Figure A.8, and the Batch meshing tool was used to mesh the regions of the plate containing the holes as shown in Figure A.9. After meshing, the part was saved into an LS-DYNA format.

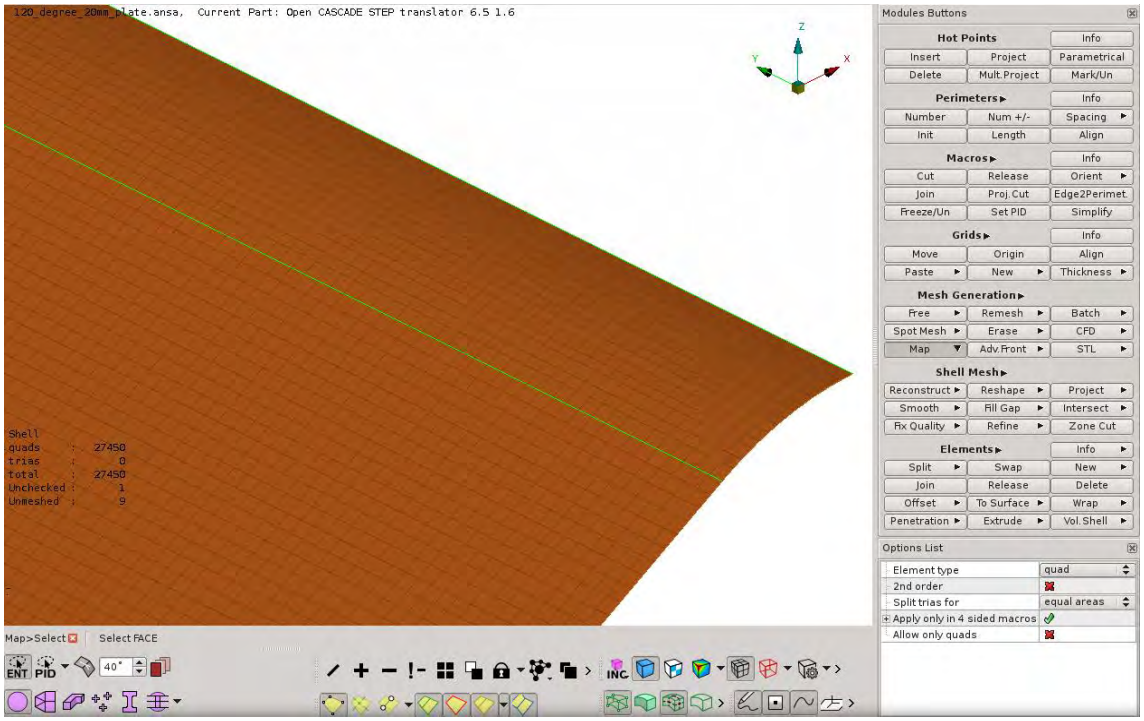

Figure A.8: Creating a meshed quarter symmetry model of a V-plate: Using the Map meshing tool to mesh the plate

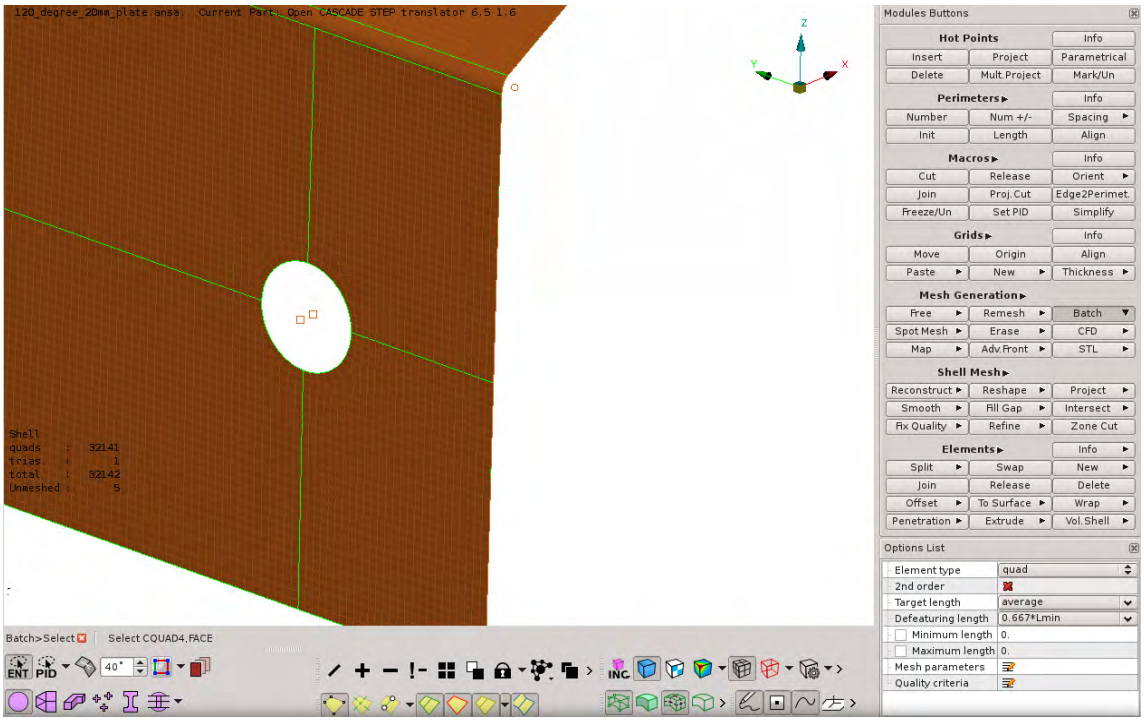

Figure A.9: Creating a meshed quarter symmetry model of a V-plate: Using the Batch meshing tool to mesh the region around the holes

A.1.3 Drawing and meshing the clamp frames

The clamp frames were drawn and meshed in a similar way to the V-plates. The cross-sectional profile was created by defining the corners with points and connecting the points together. A surface was then created from this profile. The surface was once again cut into regions like the plate. A cross-sectional profile of the side frame is shown in Figure A.10.

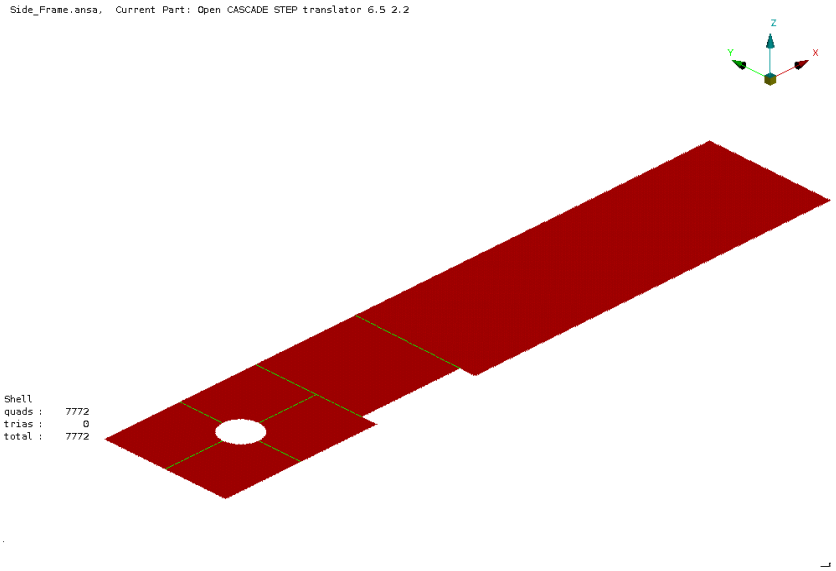

Figure A.10: Meshing a clamp frame: Cross-sectional profile of the side frame

Figure A.11 shows a close up view of the meshed profile of the side frame. The Batch and Map meshing tools were again used to mesh the profile with 1 mm length elements. The profile was then extruded using the Translate tool under the Structured Mesh tab as shown in Figure A.12. There was no biasing as all the elements were of the same size. The number of steps was set to be identical to the extruded length as the element length was 1.0 mm. Figures A.13 and A.14 show the meshed clamp frame. The same process was repeated for all the components for both the old and new clamp frames.

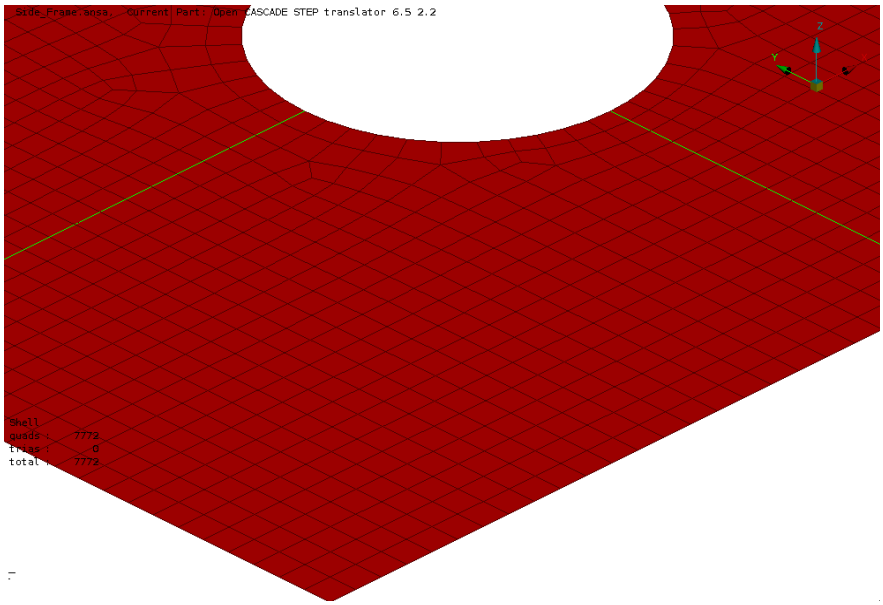

Figure A.11: Meshing a clamp frame: Close up view showing meshed cross-section of the side frame

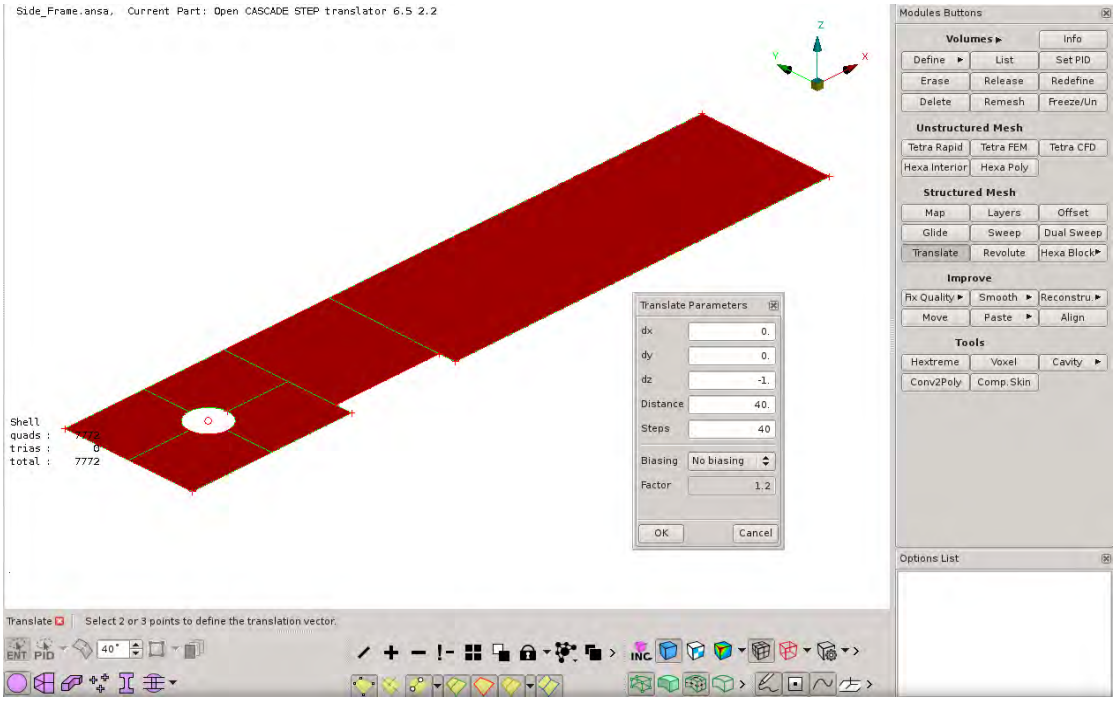

Figure A.12: Meshing a clamp frame: Using the Translate tool to generate the solid elements

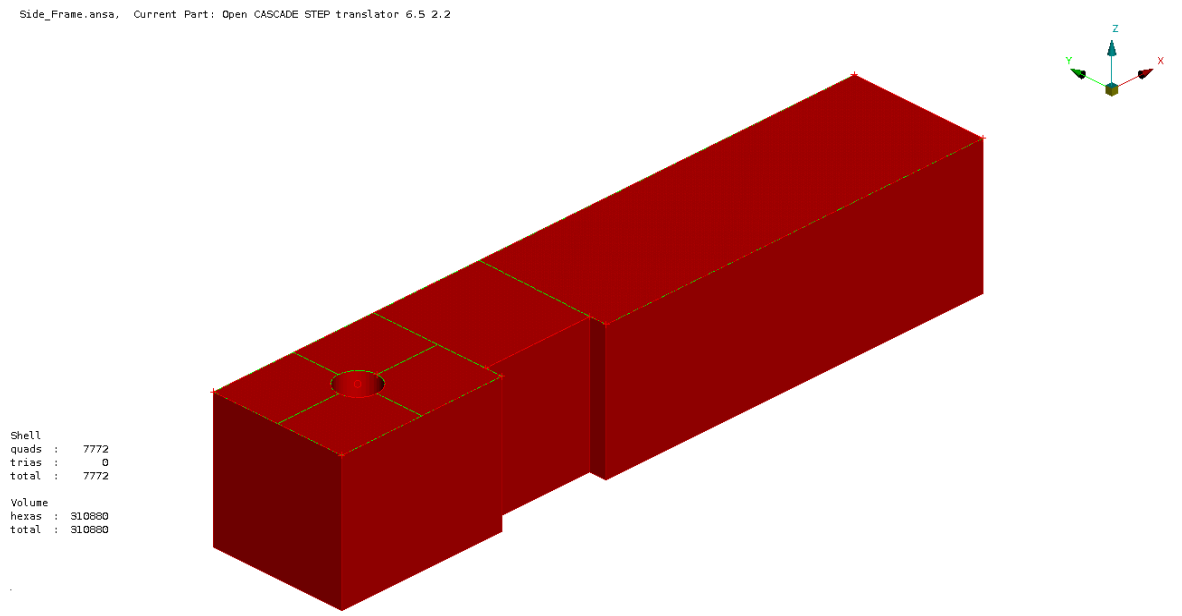

Figure A.13: Meshing a clamp frame: Meshed side frame

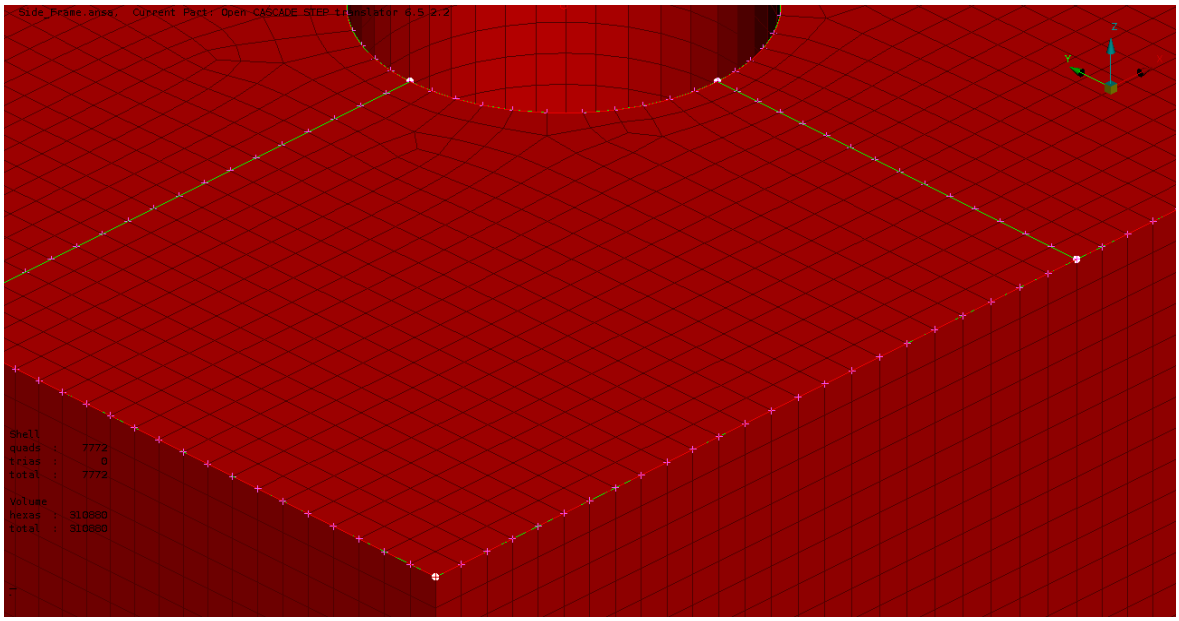

Figure A.14: Meshing a clamp frame: Close up view of the side frame showing the uniform elements

A.1.4 Assembled test setup

Once the clamp frames, V-plates and bolts were drawn and meshed they were included in the same LS-DYNA keyword file. This was done using the DEFINE_TRANSFORMATION and INCLUDE_TRANSFORM keycards as shown in Listings A.1 and A.2. The benefit of doing this is that parts that are reused do not have to remeshed when a single component in the simulation is changed. Figure A.15 shows the numerical models used for the blast simulations.

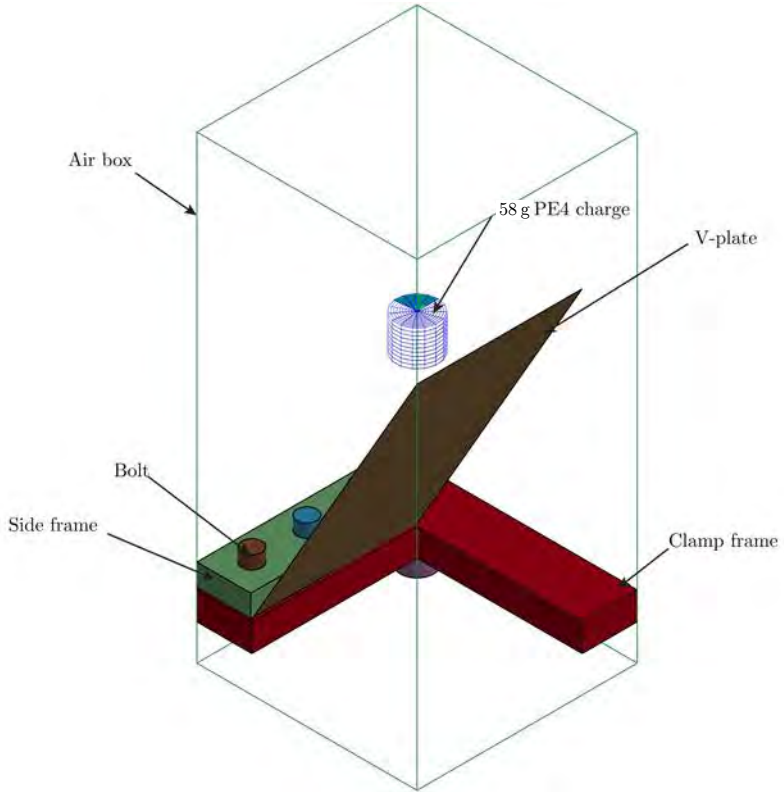

(a) Old clamp frame design, with 60° V-plate (test arrangement used by Pickering [6])

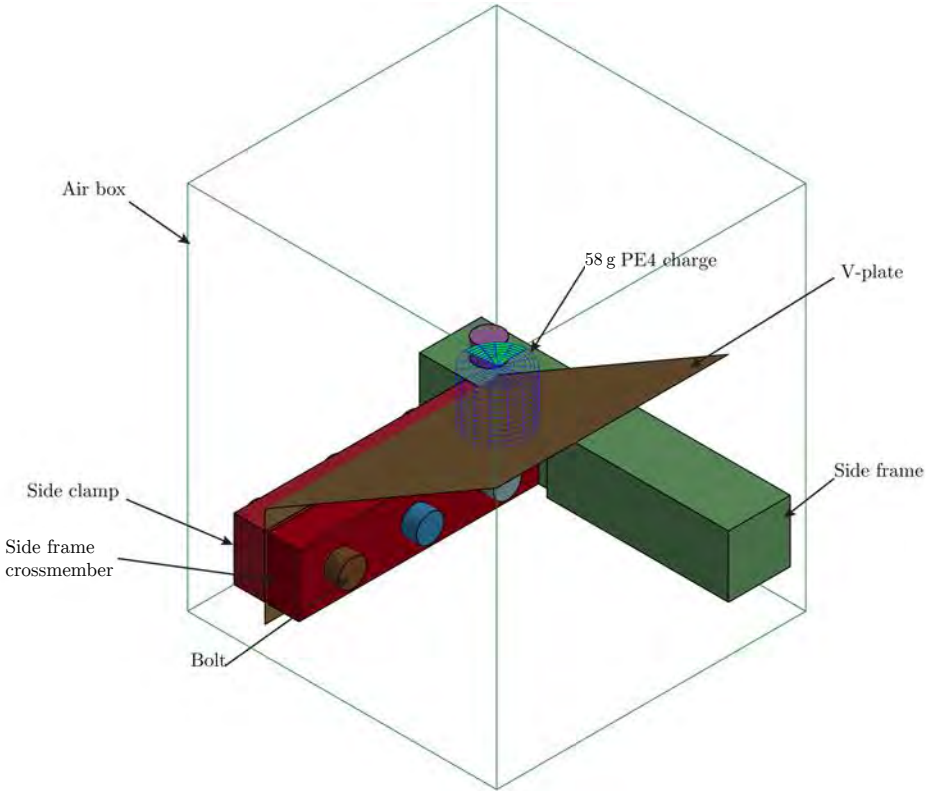

(b) New clamp frame design, with 120° V-plate (test arrangement used by Hobson [8])

Figure A.15: Numerical models, showing V-plates and 58g PE4 explosive discs with the air meshes shown as bounding boxes

A.2 Essential LS-DYNA keywords

This section contains some of the LS-DYNA keycards required to setup an blast simulation. These include cards that control the timestep and termination of the simulation, database cards that determine the outputs of the simulations as well as cards that determine how the various parts in the model interact with one another. The consistent set of units used for the models are shown in Table A.1.

Table A.1: Consistent units used for the model and keyword files

Time	Mass	Length	Force	Stress	Energy
ms	g	mm	N	MPa	N mm

A.2.1 Include and transformation cards

The INCLUDE_TRANSFORM card is used to add parts to the model and shifts the node, element and part IDs, while the DEFINE_TRANSFORMATION card is used to rotate, translate and scale the part. These two card allow parts that have been designed and meshed individually, to be assembled before the simulation is performed.

Listing A.1: DEFINE_TRANSFORMATION card in LS-DYNA

```
*DEFINE_TRANSFORMATION
$   TRANID                          New_Bolts_Spacer
$#   tranid
         80
$   OPTION
$# option        a1          a2          a3          a4          a5          a6          a7
TRANSL     -175.000    170.000    -17.500      0.000      0.000      0.000      0.000
```

Listing A.2: INCLUDE_TRANSFORM card in LS-DYNA

```
*Include_Transform
Side_Frame.k
$   INDOFF    IDEOFF    INPOFF    IDMOFF    INSOFF    IDFOFF    IDDOFF
   2000000, 2000000,    19,        0,        19,        0,        0
$   IDROFF
     0
$   FCTMAS   FCTTIM   FCTLEN   FCTTEM   INCout
       0.0
$   TRANID
         20
```

A.2.2 ALE, explosive and detonation setup cards

These cards are used to setup the multi-material ALE groups, as well as to define the geometry of the explosive and the detonation point. The first cards shown in Listing A.3 are used to define the two parts occupying the Eulerian mesh region (*i.e.* The air and the explosive).

Listing A.3: MULTI_MATERIAL_GROUP cards in LS-DYNA

```
*SET_MULTI_MATERIAL_GROUP_LIST
$#   ammsid
         1
$# ammgid1    ammgid2    ammgid3    ammgid4    ammgid5    ammgid6    ammgid7    ammgid8
         1          0          0          0          0          0          0          0
*SET_MULTI_MATERIAL_GROUP_LIST
$#   ammsid
         2
$# ammgid1    ammgid2    ammgid3    ammgid4    ammgid5    ammgid6    ammgid7    ammgid8
         2          0          0          0          0          0          0          0
*ALE_MULTI-MATERIAL_GROUP
$#      sid    idtype   gpname
        90         1   air
*ALE_MULTI-MATERIAL_GROUP
$#      sid    idtype   gpname
       100         1   explosive
*Set_Part_List
$     SID
      9010
$    PID1    PID2
        90,     100
```

The geometry of the explosive and its location in the ALE mesh are defined in the INITIAL_VOLUME_FRACTION_GEOMETRY card as shown in Listing A.4. In this card, "conttyp" defines the geometry of the explosive (*i.e.* Conical, spherical or rectangular). For a charge with a cylindrical shape, the values of "r1" and "r2" are identical and are set to the radius of the cylinder. The location and time of the detonation are set in the INITIAL_DETONATION card shown in Listing A.5. The value of "lt" defines the time at which the explosive detonates, while the location of the detonation point is set by the values of "x, y and z".

Listing A.4: INITIAL_VOLUME_FRACTION_GEOMETRY card in LS-DYNA

```
*INITIAL_VOLUME_FRACTION_GEOMETRY
$#    fmsid    fmidtyp      bammg     ntrace
        90          1          1         10
$# conttyp    fillopt      fammg         vx         xy         xz     radvel     unused
         4          0          2      0.000      0.000      0.000          0
$#      x1         y1         z1         x2         y2         z2         r1         r2
     0.000      0.000 358.80762      0.000      0.000 369.27180 19.000000 19.000000
```

Listing A.5: INITIAL_DETONATION card in LS-DYNA

```
*INITIAL_DETONATION
$#     pid           x           y           z          lt
       100       0.000       0.000 368.27180       0.000
```

The CONSTRAINED_LAGRANGE_IN_SOLID_EDGE card is used to define how a Lagrangian solid in the Eulerian mesh interacts with the air and explosive products. Two examples of this card are shown in Listing A.6. These cards are required for every Lagrangian part that interacts with the ALE mesh. The parameter "ctype" defines the type of coupling used between the Lagrangian and Eulerian parts. In this example a penalty coupling is used. The number of coupling points is defined by the parameter "nquad", while the direction of the coupling is set with the value of the "direc" parameter.

Listing A.6: CONSTRAINED_LAGRANGE_IN_SOLID_EDGE card in LS-DYNA

```
*CONSTRAINED_LAGRANGE_IN_SOLID_EDGE_TITLE
$#   coupid                title
         0         Lag in solid
$#   slave     master      sstyp      mstyp      nquad      ctype      direc      mcoup
        10       9010          0          0          2          4          3         -1
$#   start        end       pfac       fric     frcmin       norm    normtyp       damp
    0.0001 1.0000E+10   0.100000      0.000   0.100000          0          1      0.000
$#      cq       hmin       hmax      ileak      pleak    lcidpor      nvent   blockage
    0.000      0.000      0.000          0   0.000000          0          0          0
$#  iboxid   ipenchk    intforc    ialesof     lagmul     pfacmm       thkf
         0          0          0          0      0.000          0     2.0000
*CONSTRAINED_LAGRANGE_IN_SOLID_EDGE_TITLE
$#   coupid                title
         1         Lag in solid
$#   slave     master      sstyp      mstyp      nquad      ctype      direc      mcoup
        10       9010          0          0          2          4          3         -2
$#   start        end       pfac       fric     frcmin       norm    normtyp       damp
    0.0001 1.0000E+10   0.100000      0.000   0.100000          0          1      0.000
$#      cq       hmin       hmax      ileak      pleak    lcidpor      nvent   blockage
    0.000      0.000      0.000          2   0.200000          0          0          0
$#  iboxid   ipenchk    intforc    ialesof     lagmul     pfacmm       thkf
        90          0          0          0      0.000          0     2.0000
```

A.2.3 Database cards

The various outputs of the simulations are defined using the database cards. This includes which results are stored as well as their frequency. The DATABASE_TRACER card is used to set tracer point locations, while the DATABASE_TRHIST card is used to setup the frequency of the tracer history outputs (See Listings A.7 and A.8). These tracer points can be tied to a deformable Lagrangian part or they can be fixed in space. Each tracer point records a number of outputs including the pressure history at its location.

Listing A.7: DATABASE_TRHIST card in LS-DYNA

```
*DATABASE_TRHIST
$#      dt    binary      lcur     ioopt
 1.0000E-5         0         0         1
```

Listing A.8: DATABASE_TRACER card in LS-DYNA

```
*DATABASE_TRACER
$#    time     track         x         y         z      ammg       nid
     0.000         1    0.0000    0.0000 325.80762         0         0
*DATABASE_TRACER
$#    time     track         x         y         z      ammg       nid
     0.000         1    0.0000  150.0000 325.80762         0         0
*DATABASE_TRACER
$#    time     track         x         y         z      ammg       nid
     0.000         1 -150.0000    0.0000  66.00000         0         0
*DATABASE_TRACER
$#    time     track         x         y         z      ammg       nid
     0.000         1 -150.0000  150.0000  66.00000         0         0
```

The DATABASE_FSI card is used to output the fluid-structure interaction forces and leakage forces in each of the principal directions (See Listing A.9). The regions or parts for which the FSI forces are required are set with the "sid" parameter, while the "dt" parameter is used to set the frequency of the outputs. The DATABASE_BINARY_D3PLOT card is used to set the frequency of the field outputs and is shown in Listing A.10.

Listing A.9: DATABASE_FSI card in LS-DYNA

```
*DATABASE_FSI
$#      dt
 1.0000E-4
$#dbsfi_id       sid     stype      swid    convid
         0        10         2         0         0
         1        11         2         0         0
```

Listing A.10: DATABASE_BINARY_D3PLOT card in LS-DYNA

```
*DATABASE_BINARY_D3PLOT
$#      dt      lcdt      beam     npltc    psetid
  2.500E-2         0         0         0         0
$#    iopt
         0
```

A.2.4 Control cards

The control cards are used to setup global parameters of the numerical simulation, such as the timestep, the termination time and global ALE parameters. In the CONTROL_ALE card (shown in Listing A.11) properties such as the reference pressure (set with the "pref" parameter) and the number of advection cycles per calculation (set with the "nadv" value) are specified.

Listing A.11: CONTROL_ALE card in LS-DYNA

```
*CONTROL_ALE
$#      dct      nadv      meth      afac      bfac      cfac      dfac      efac
         -1         1         3 -1.000000     0.000     0.000     0.000     0.000
$#    start       end     aafac      vfact      prit       ebc      pref   nsidebc
    0.0001.0000E+20     1.000     0.000         0         0    0.1013         0
$#     ncpl      nbkt    imascl    checkr
         1        50         0     0.000
```

The termination time is set in the CONTROL_TERMINATION card as shown in Listing A.12, while the timestep is set in the CONTROL_TIMESTEP card (See Listing A.13). If the CONTROL_TIMESTEP card is excluded, LS-DYNA determines the critical timestep based on the length of the smallest element.

Listing A.12: CONTROL_TERMINATION card in LS-DYNA

```
*CONTROL_TERMINATION
$#  endtim    endcyc     dtmin    endeng    endmas
       0.3         0     0.000     0.000     0.000
```

Listing A.13: CONTROL_TIMESTEP card in LS-DYNA

```
*CONTROL_TIMESTEP
$#  dtinit    tssfac      isdo    tslimt    dt2ms      lctm     erode     ms1st
      1e-5  0.670000         0     0.000    0.000         0         0         0
$#  dt2msf   dt2mslc    imscl
    0.000         0         0
```

A.2.5 Section and material cards

Section and material cards are required to fully define all parts in LS-DYNA. Additionally some parts require an Equation of State card as well. Two examples of section cards are shown below in Listings A.14 and A.15. The "elform" parameter is used to set the element formulation used for the part. In the SECTION_SHELL card the "nip" value is set to the number of through thickness integration points for the shell part.

Listing A.14: SECTION_SHELL card in LS-DYNA

```
*SECTION_SHELL_TITLE
Steel
$#    secid     elform      shrf       nip     propt    qr/irid     icomp     setyp
        10          2  0.833330         5         1          0         0         1
$#      t1        t2        t3        t4      nloc     marea      idof    edgset
  2.000000  2.000000  2.000000  2.000000       1.0     0.000  1.000000         0
```

Listing A.15: SECTION_SOLID_ALE card in LS-DYNA

```
*SECTION_SOLID_ALE_TITLE
air section
$#    secid     elform       aet
      9010         11         1
$#     afac      bfac      cfac      dfac     start       end      aafac
     0.000     0.000     0.000     0.000     0.000     0.000     0.000
```

A number of material cards are required for a blast simulation. A rigid material can be used for the clamp frames and bolts and is setup using the MAT_RIGID card as shown in Listing A.16. The parameters "con1 and con2" are used to constrain the plate in all rotational and translational degrees-of-freedom. The remaining parameters in this card are those of a generic steel. The MAT_HIGH_EXPLOSIVE_BURN card is used to set the properties of the explosive used. The properties used in Listing A.17 are for PE4 and are given in Table 5.5. These include the density, detonation velocity and CJ pressure.

Listing A.16: MAT_RIGID card in LS-DYNA

```
*MAT_RIGID_TITLE
Rigid Plate Material
$#      mid        RO         E        PR    N  COUPLE    M
         10 7.8700E-3 2.1000E+6  0.330000    0         0    0
$       cmo      con1      con2
        1.0         7         7
$        A1        A2        A3
         0         0         0
```

Listing A.17: MAT_HIGH_EXPLOSIVE_BURN card in LS-DYNA

```
*MAT_HIGH_EXPLOSIVE_BURN_TITLE
explosive
$#      mid        ro         d       pcj      beta         k         g      sigy
        100 1.6010E-3 8193.0000 28000.000     0.000     0.000     0.000     0.000
```

This page has been intentionally left blank.

Appendix B

Impulse derivations

The impulse transferred to the pendulum can be obtained by treating the ballistic pendulum as a single degree of freedom (SDOF) vibration problem and relating the measured quantities to the geometry of the arrangement. Figure B.1 shows a schematic of the geometry of the pendulum.

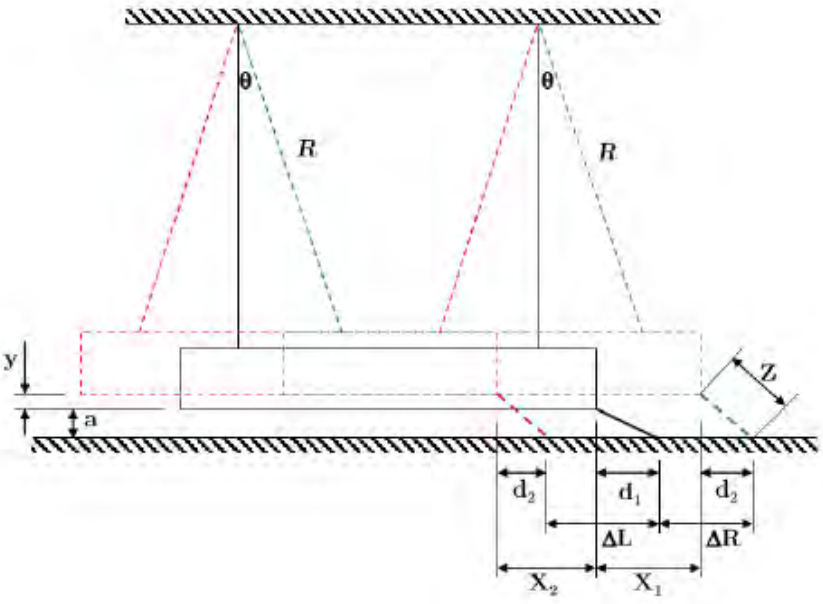

Figure B.1: Schematic showing the geometry of the ballistic pendulum [49]

$$\ddot{X} + 2\beta\dot{X} + \omega_n^2 = 0 \tag{B.1}$$

Where the natural frequency of pendulum is given by,

$$\omega_n = \frac{2\pi}{T} \tag{B.2}$$

While β is defined as the ratio of the viscous damping coefficient (C) to twice the mass of the pendulum (M_p),

$$\beta = \frac{C}{2M_p} \tag{B.3}$$

The solution to the differential equation given in Equation (B.1) is,

$$X = \frac{\left(e^{-\beta t}\right) \dot{X}_0 sin(\omega_d t}{\omega_d}) \tag{B.4}$$

Where the damped frequency (ω_d) is given by,

$$\omega_d = \sqrt{\omega_n^2 - \beta^2} \tag{B.5}$$

The maximum forward displacement of the pendulum occurs at $t = \frac{T}{4}$ and is given by X_1, while the maximum backward displacement occurs at $t = \frac{3T}{4}$ and is given by X_2. Substitution into Equation (B.4) results in the following pair of equations.

$$X_1 = \frac{\dot{X}_0 T}{2\pi} e^{-\beta \frac{T}{4}} \tag{B.6}$$

$$X_2 = -\frac{\dot{X}_0 T}{2\pi} e^{-\beta \frac{3T}{4}} \tag{B.7}$$

β can be expressed in terms of X_1 and X_2 using Equations (B.6) and (B.7).

$$\beta = \frac{2}{T} \ln\left(\frac{X_1}{X_2}\right) \tag{B.8}$$

In order to obtain the impulse the initial velocity is required. This can be obtained by rearranging Equation (B.5).

$$\dot{X}_0 = \frac{2\pi}{T} X_1 e^{\beta \frac{T}{4}} \tag{B.9}$$

The impulse transferred to the pendulum can then be found.

$$I = M_p \dot{X}_0 \tag{B.10}$$

By displacing the pendulum and recording the time taken for it to complete 10 oscillations, the natural period (T) of the pendulum can be obtained. The pen traces a line, of which the maximum forward length is ΔR and the maximum backward length is ΔL. However these do not correspond to the maximum and minimum displacements of the pendulum (X_1 and X_2). By using the geometry of the pendulum these quantities can be related.

The horizontal distance between the end of the pendulum and the tip of the pen is related using the height of the pendulum from the ground and the length of the pen.

$$d_1 = \sqrt{Z^2 - a^2} \tag{B.11}$$

This distance reduces to d_2 when the pendulum is at its maximum forward displacement.

$$d_2 = \sqrt{Z^2 - (a + y)^2} \tag{B.12}$$

It is assumed that the angle of rotation of the cables is small, thus $\sin\theta \approx \theta$.

$$X_1 = R\theta \tag{B.13}$$

$$y = \frac{R\theta^2}{2} \tag{B.14}$$

$$\therefore y = \frac{X_1^2}{2R} \tag{B.15}$$

Equation (B.15) can be substituted into Equation (B.11).

$$d_2 = \sqrt{Z^2 - \left(a + \frac{X_1^2}{2R}\right)^2} \tag{B.16}$$

From the geometry of the pendulum arrangement, the quantities X_1, X_2 can be expressed in terms of ΔR, ΔL, d_1 and d_2. The constants d_1 and d_2 can then be eliminated using Equations (B.11) and (B.16). The final two equations can be solved using a recursive solver.

$$X_1 = \Delta R + d_1 - d_2 \tag{B.17}$$

$$X_2 = \Delta L - d_1 + d_2 \tag{B.18}$$

$$X_1 = \Delta R + \sqrt{Z^2 - a^2} - \sqrt{Z^2 - \left(a + \frac{X_1^2}{2R}\right)^2} \tag{B.19}$$

$$X_2 = \Delta L - \sqrt{Z^2 - a^2} + \sqrt{Z^2 - \left(a + \frac{X_1^2}{2R}\right)^2} \tag{B.20}$$

Appendix C

Detailed experimental results

This appendix contains the detailed results of the experiments (See Chapter 3) and are shown in Tables C.3, C.4 and C.6. The testing was done in three sets, with minor variations in the values of the lengths involved, shown in Tables C.2 and C.5. The masses of the rigid V-plates, the pendulum and the counterbalance masses are shown in Table C.1.

Table C.1: Table showing the masses the rigid V-plates, the pendulum and the counterbalance masses

$M_{pendulum}$	112.82	kg			
$M_{60°}$	46.16	kg	$M_{counterbalance}$	47.58	kg
$M_{90°}$	37.68	kg	$M_{counterbalance}$	37.70	kg
$M_{120°}$	34.48	kg	$M_{counterbalance}$	34.50	kg

Table C.2: Table containing the values of the lengths required for the impulse calculations for the first and second sets of experiments

a	122	mm
Z	204	mm
R	2763	mm

Table C.3: Detailed results for the first set of experiments performed on a rigid 60° V-plate

Charge Mass (g)	ΔR **(mm)**	ΔL **(mm)**	X_1 **(mm)**	X_1 **(Trial) (mm)**	X_2 **(mm)**	β	$\dot{X}_0$ **(m s^{-1})**	**I (N s)**
10	18.40	13.50	18.45	18.45	13.45	0.20	0.04	**8.76**
19	27.75	23.55	27.85	27.85	23.45	0.11	0.06	**12.31**
29	35.65	30.15	35.82	35.82	29.98	0.11	0.08	**15.88**
40	42.05	32.75	42.29	42.29	32.51	0.16	0.09	**19.56**

Table C.4: Detailed results for the second set of experiments performed on a rigid 120° V-plate

Charge Mass (g)	ΔR **(mm)**	ΔL **(mm)**	X_1 **(mm)**	X_1 **(Trial) (mm)**	X_2 **(mm)**	β	$\dot{X}_0$ **(m s^{-1})**	**I (N s)**
19	51.34	46.28	51.70	51.66	45.92	0.07	0.10	**18.19**
29	70.38	68.90	71.07	71.07	68.21	0.02	0.13	**24.07**
40	84.34	73.60	85.33	85.33	72.61	0.09	0.17	**30.70**
58	94.02	92.38	95.26	95.26	91.14	0.03	0.18	**32.32**

Table C.5: Table containing the values of the lengths required for the impulse calculations for the third set of experiments

a	153	mm
Z	204	mm
R	2995	mm

Table C.6: Detailed results for the third set of experiments performed

V-angle (°)	**Charge Mass (g)**	ΔR **(mm)**	ΔL **(mm)**	X_1 **(mm)**	X_1 **(Trial) (mm)**	X_2 **(mm)**	β	$\dot{X}_0$ **(m s^{-1})**	**I (N s)**
60	**45**	45.80	37.50	46.21	46.21	37.09	0.14	0.10	**20.91**
	58	48.32	42.50	48.77	48.77	42.05	0.09	0.10	**21.30**
90	**19**	43.22	37.08	43.58	43.58	36.72	0.10	0.09	**16.64**
	40	65.15	63.22	65.98	65.98	62.39	0.03	0.13	**23.78**
	58	75.24	66.58	76.35	76.35	65.47	0.09	0.15	**28.90**
120	**45**	88.02	84.88	89.10	89.10	83.80	0.04	0.17	**30.49**

Appendix D

Explosive material development

This appendix contains figures showing the explosive development and flow of the gas products over the plates for a selection of the numerical simulations performed. All simulations shown are for a charge mass of 58 g and include the maximum and minimum bend radii that were investigated for each V-angle. Figure D.1 shows the fringe levels used for all the figures, where 0 means there are no explosive products in that portion of the ALE mesh and 1 means that it is entirely explosive products in that area.

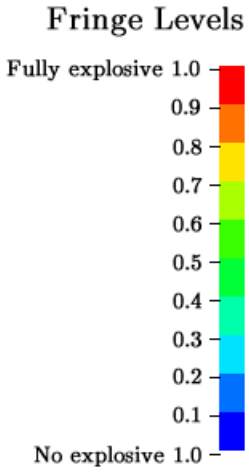

Figure D.1: Fringe levels used for all the figures in this appendix

D.1 60° explosive development

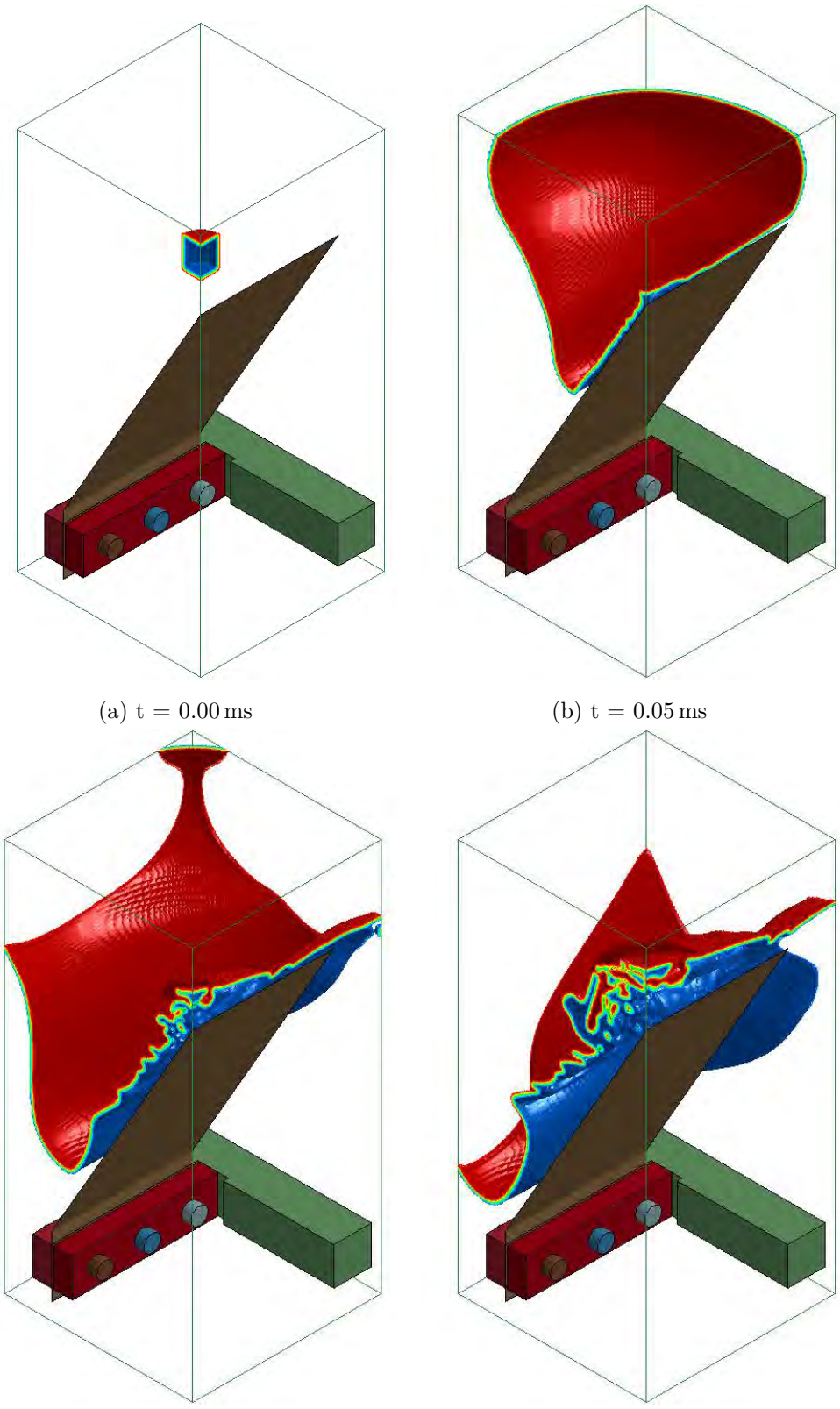

(a) t = 0.00 ms (b) t = 0.05 ms

(c) t = 0.10 ms (d) t = 0.15 ms

Figure D.2: Explosive development for a 60° V-plate with a bend radius of 0 mm and a 58 g charge from 0 to 0.30 ms

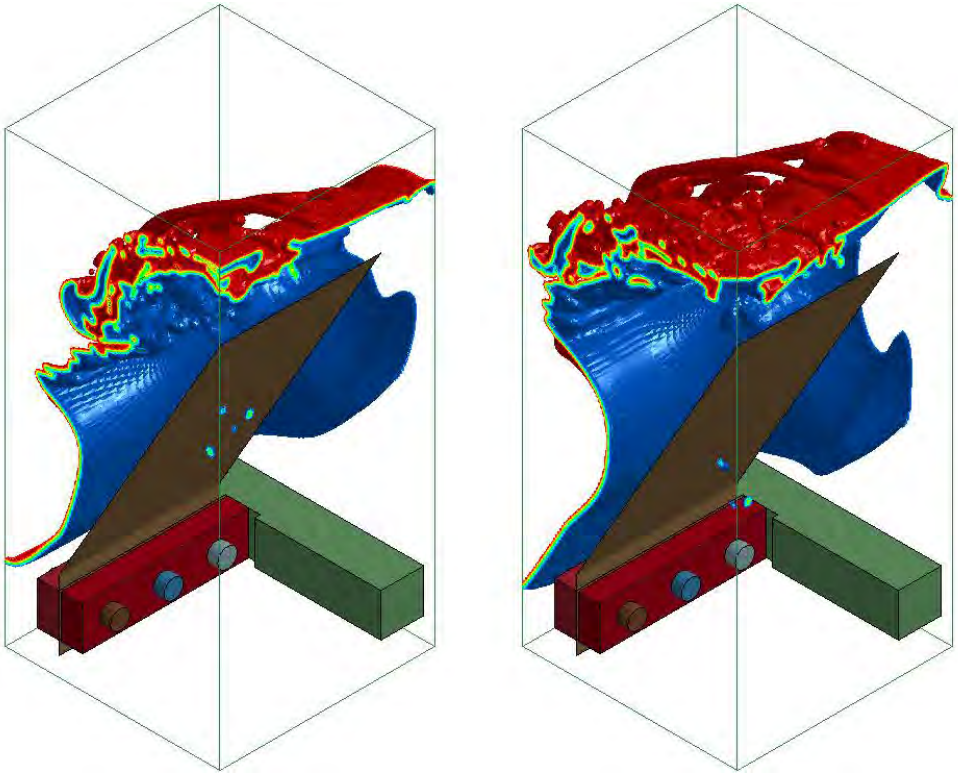

(e) t = 0.20 ms (f) t = 0.25 ms

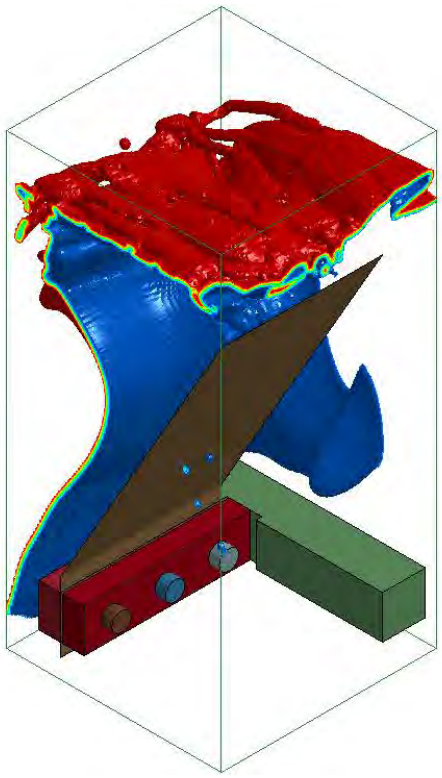

(g) t = 0.30 ms

Figure D.2: Explosive development for a 60° V-plate with a bend radius of 0 mm and a 58 g charge from 0 to 0.30 ms

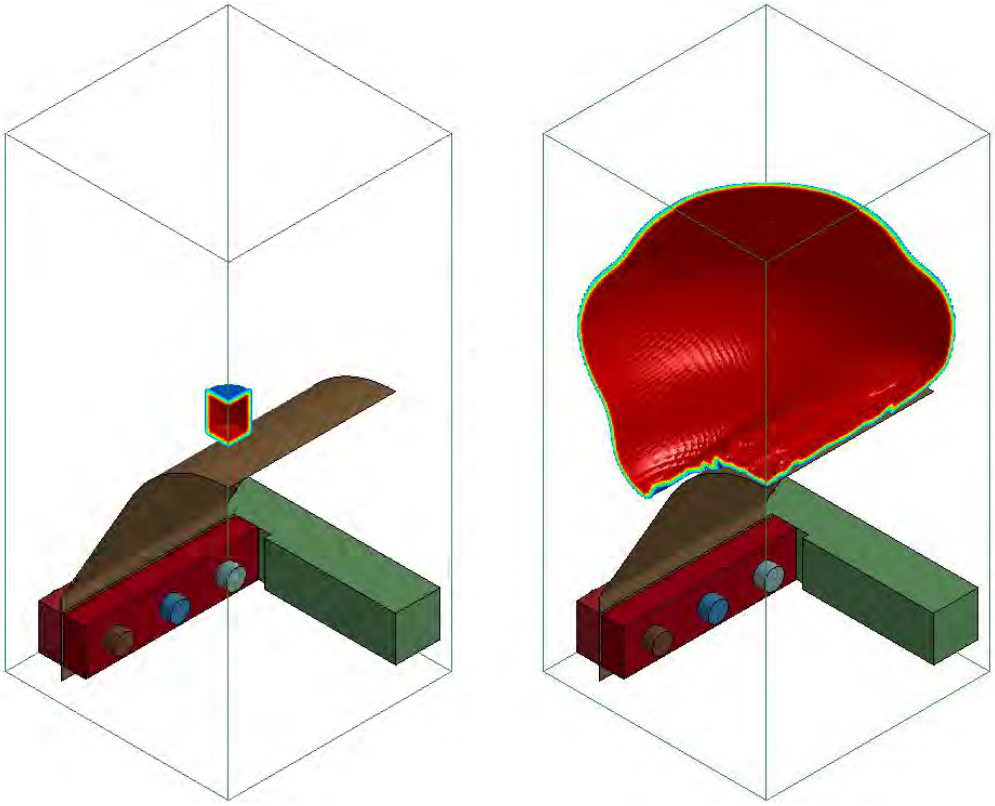

(a) t = 0.00 ms (b) t = 0.05 ms

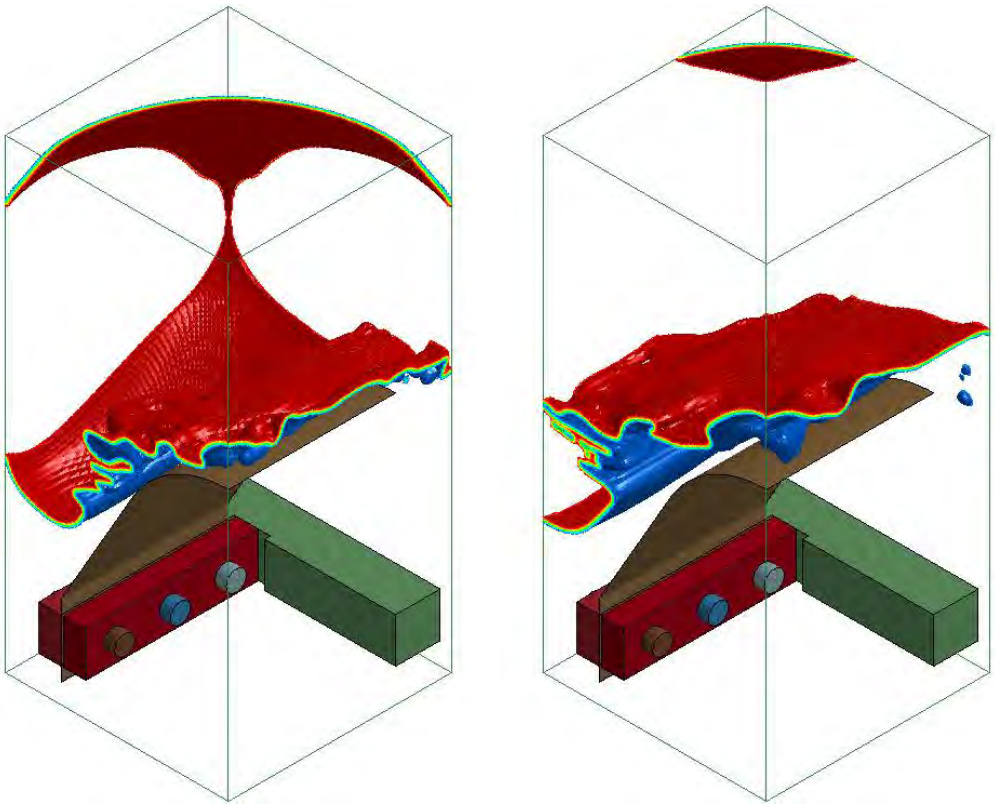

(c) t = 0.10 ms (d) t = 0.15 ms

Figure D.3: Explosive development for a 60° V-plate with a bend radius of 100 mm and a 58 g charge from 0 to 0.30 ms

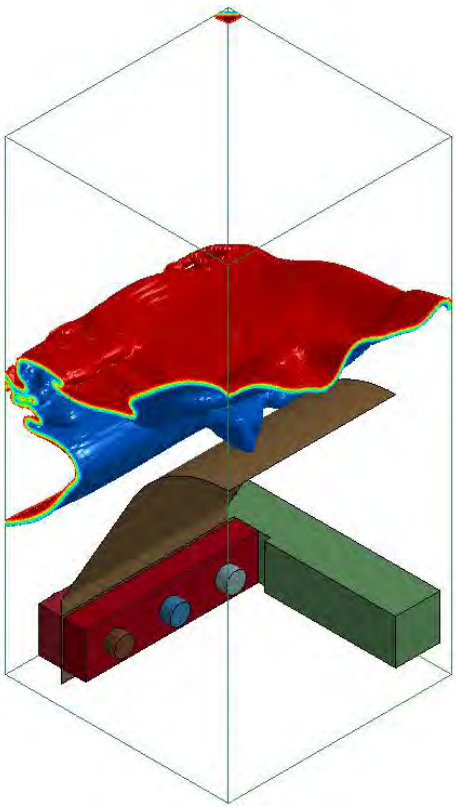

(e) t = 0.20 ms

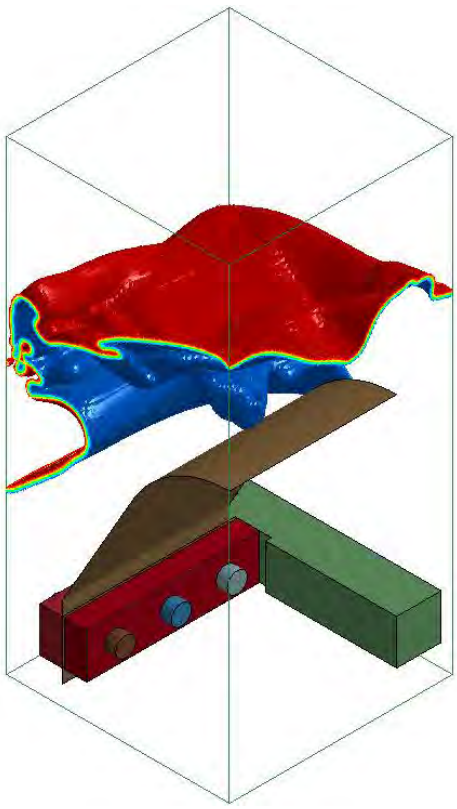

(f) t = 0.25 ms

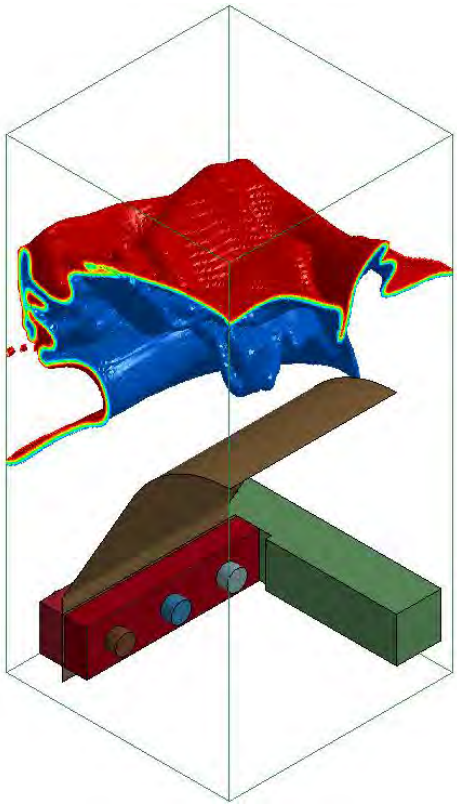

(g) t = 0.30 ms

Figure D.3: Explosive development for a 60° V-plate with a bend radius of 100 mm and a 58 g charge from 0 to 0.30 ms

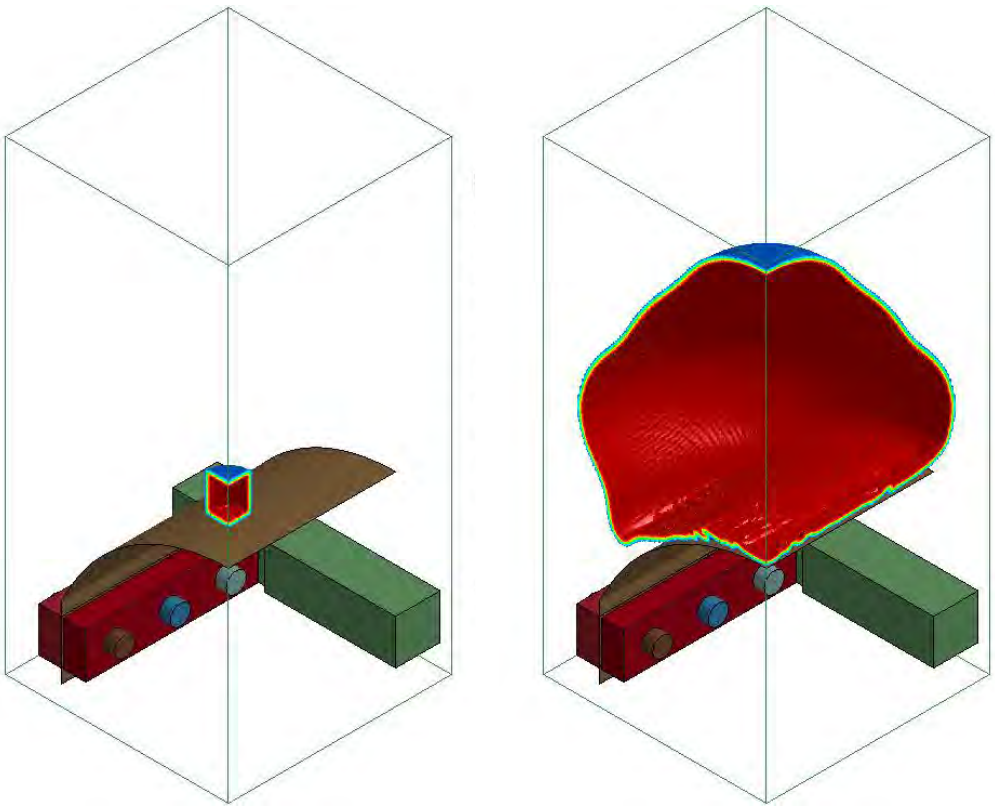

(a) t = 0.00 ms (b) t = 0.05 ms

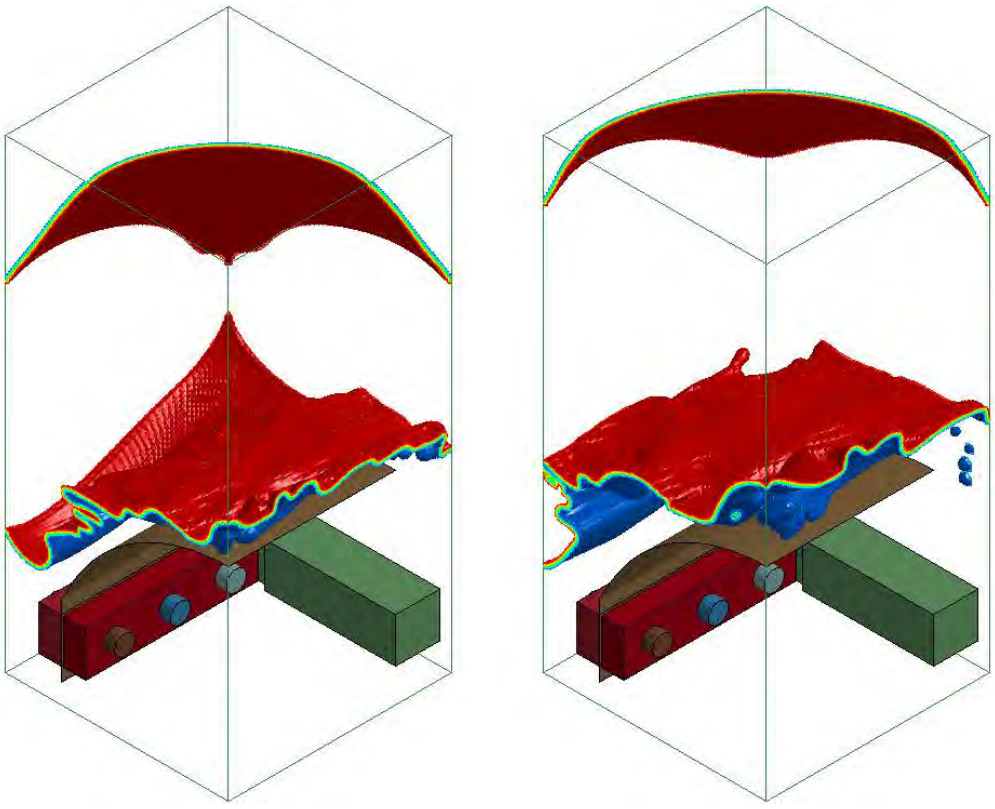

(c) t = 0.10 ms (d) t = 0.15 ms

Figure D.4: Explosive development for a 60° V-plate with a bend radius of 160 mm and a 58 g charge from 0 to 0.30 ms

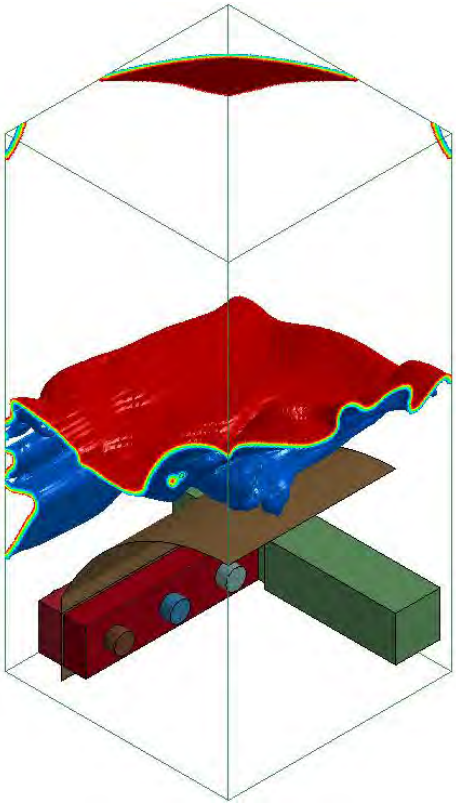

(e) t = 0.20 ms

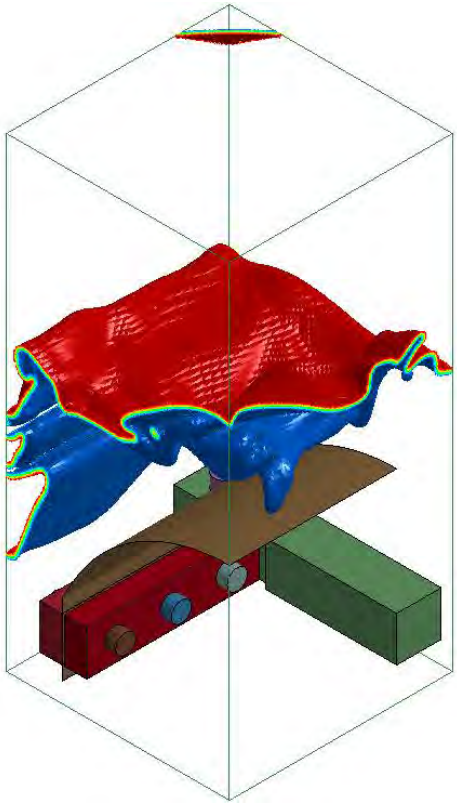

(f) t = 0.25 ms

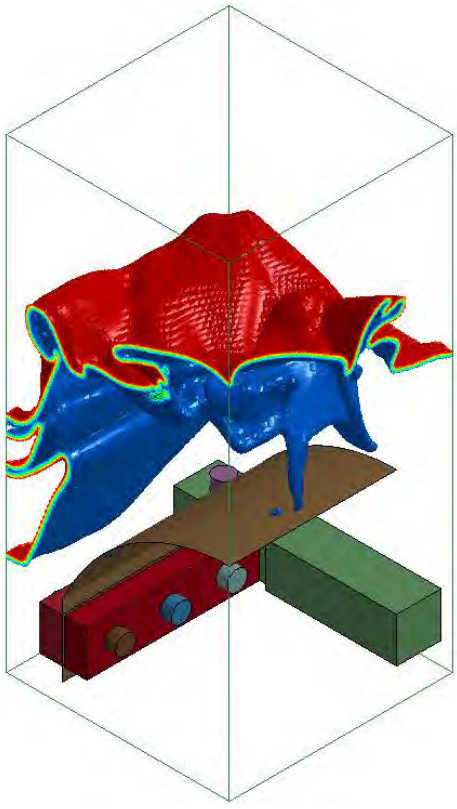

(g) t = 0.30 ms

Figure D.4: Explosive development for a 60° V-plate with a bend radius of 160 mm and a 58 g charge from 0 to 0.30 ms

D.2 90° explosive development

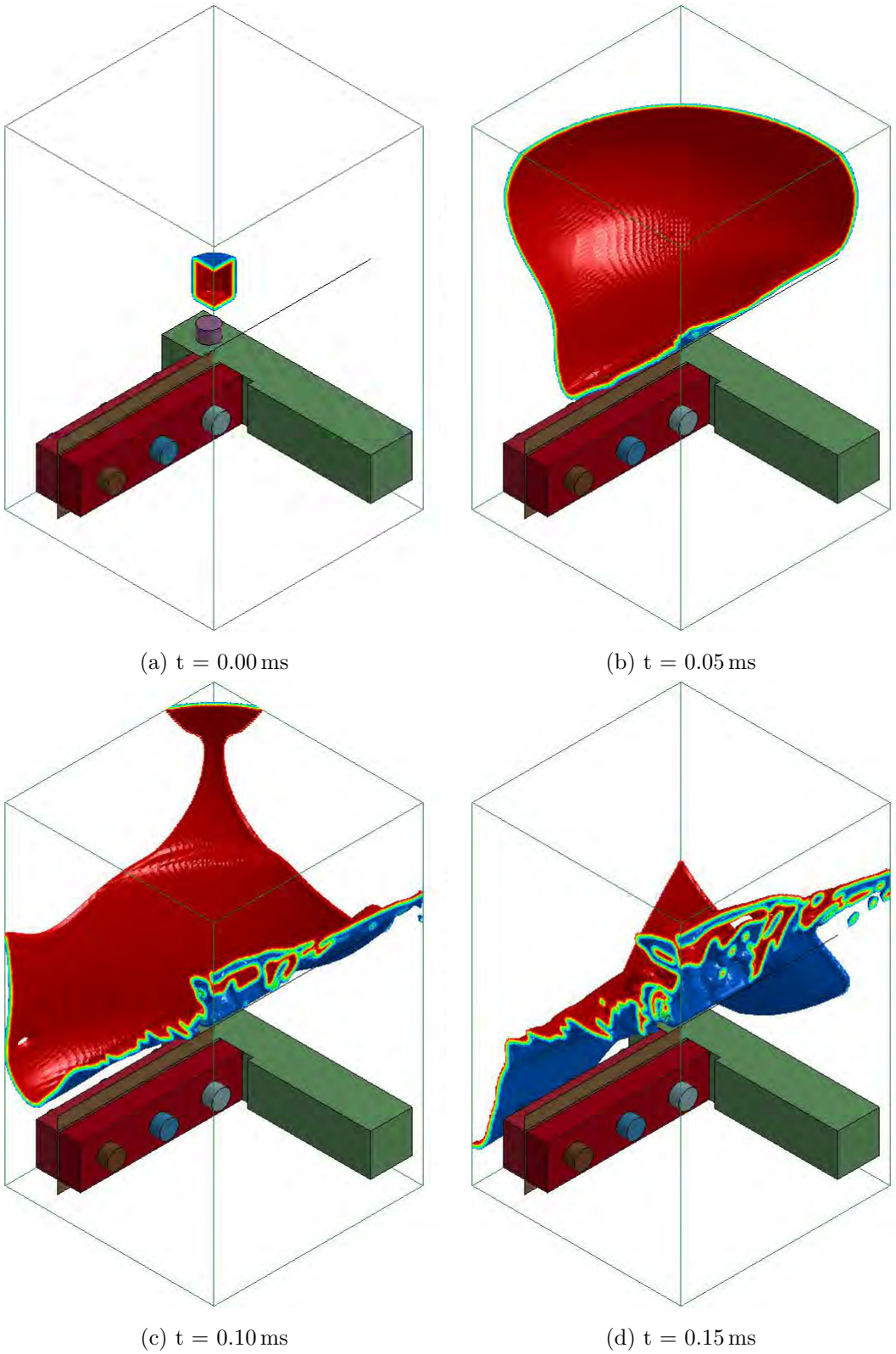

(a) t = 0.00 ms (b) t = 0.05 ms

(c) t = 0.10 ms (d) t = 0.15 ms

Figure D.5: Explosive development for a 90° V-plate with a bend radius of 0 mm and a 58 g charge from 0 to 0.30 ms

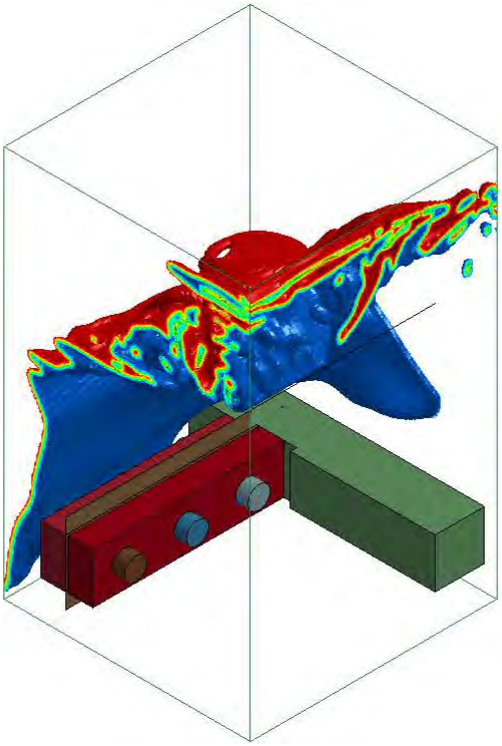

(e) t = 0.20 ms

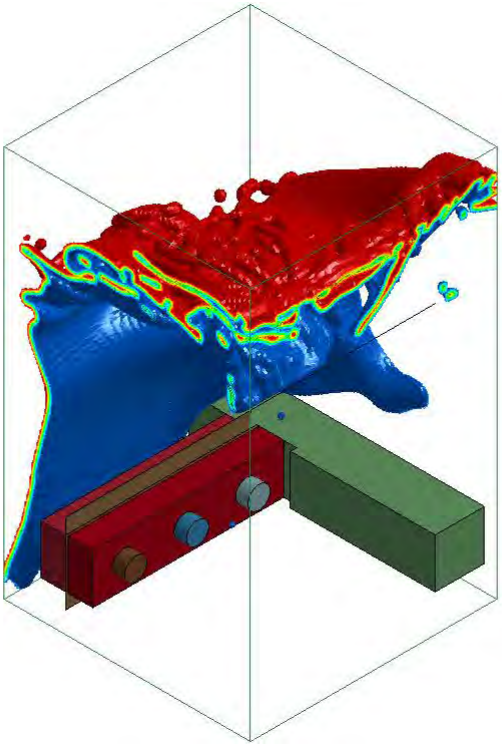

(f) t = 0.25 ms

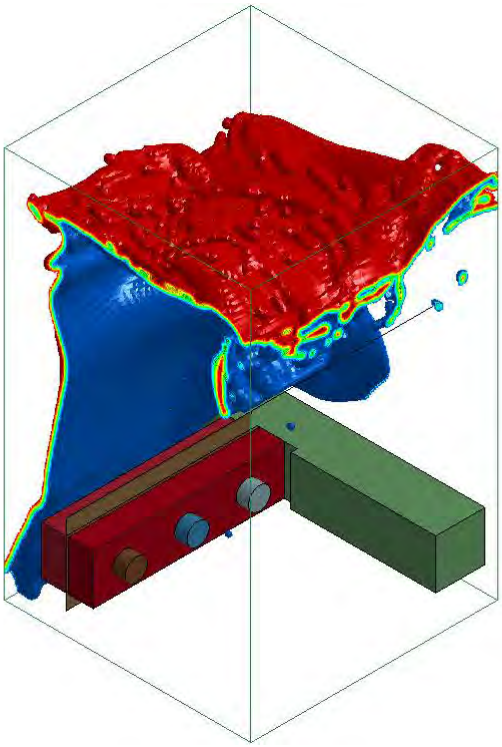

(g) t = 0.30 ms

Figure D.5: Explosive development for a 90° V-plate with a bend radius of 0 mm and a 58 g charge from 0 to 0.30 ms

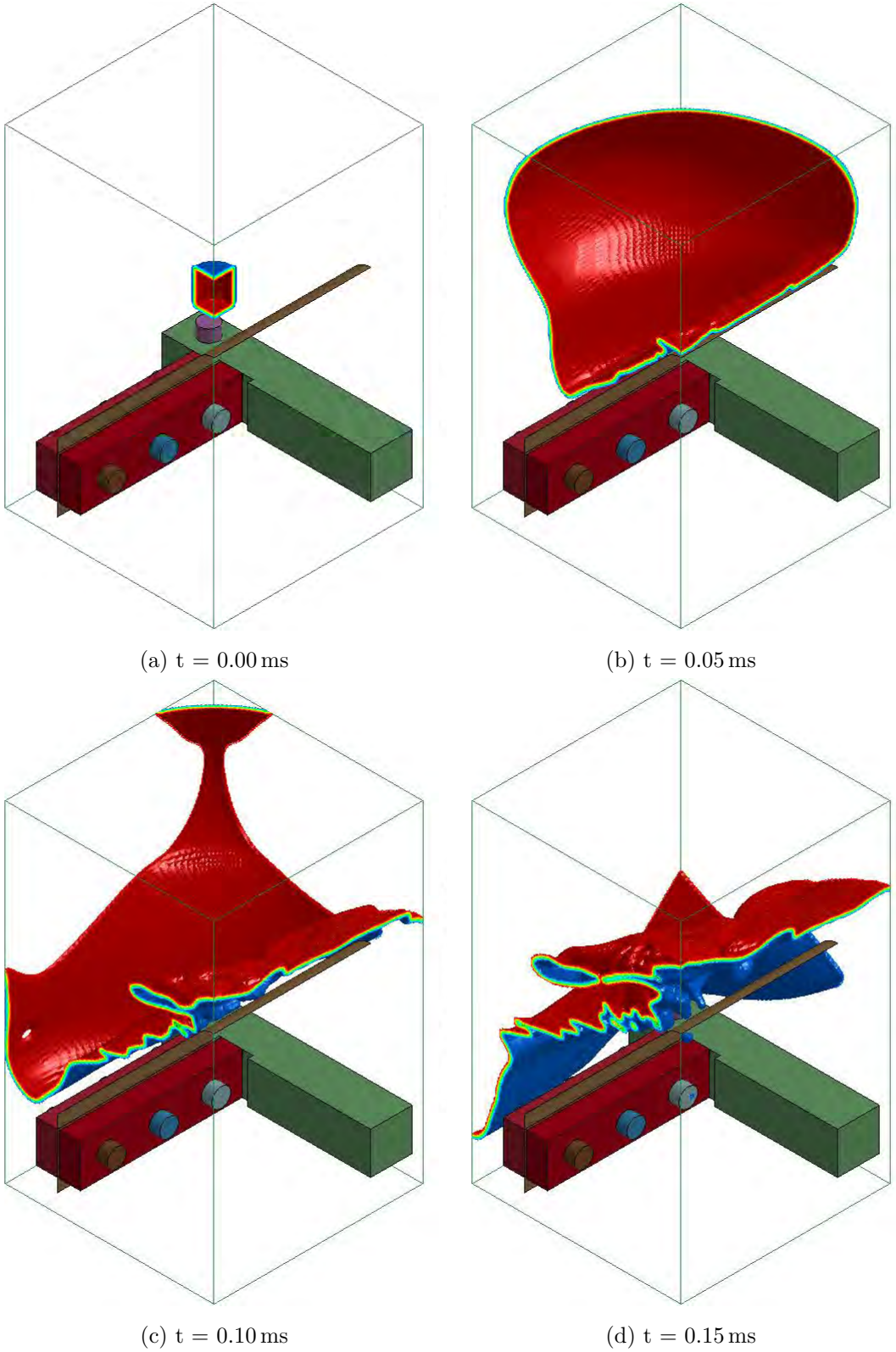

(a) t = 0.00 ms (b) t = 0.05 ms

(c) t = 0.10 ms (d) t = 0.15 ms

Figure D.6: Explosive development for a 90° V-plate with a bend radius of 20 mm and a 58 g charge from 0 to 0.30 ms

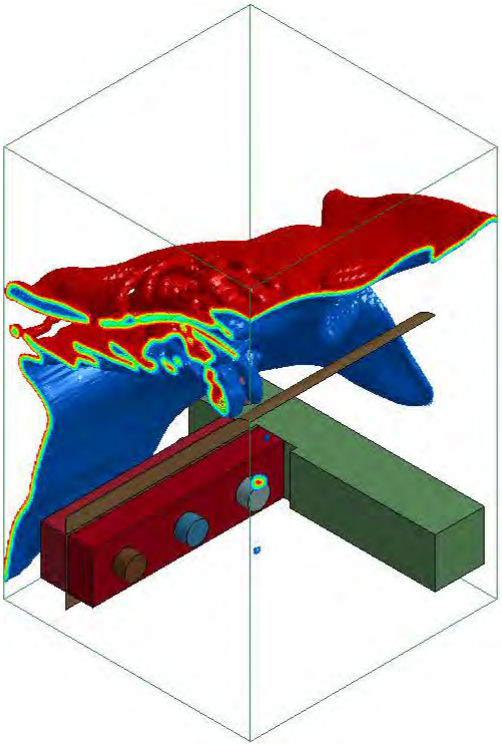

(e) t = 0.20 ms

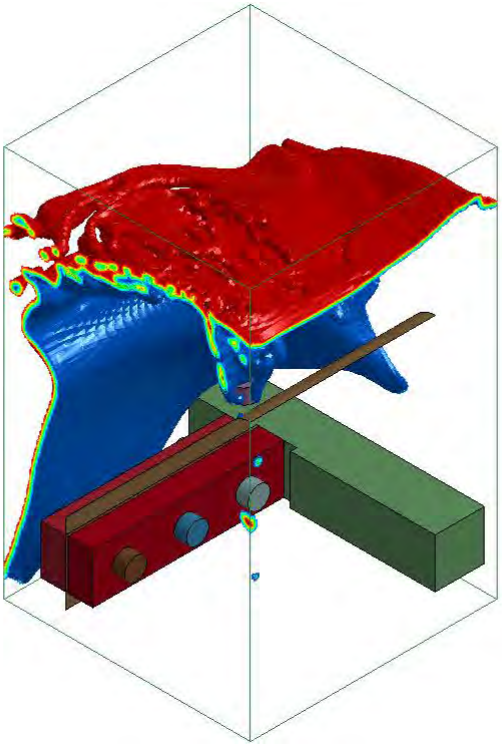

(f) t = 0.25 ms

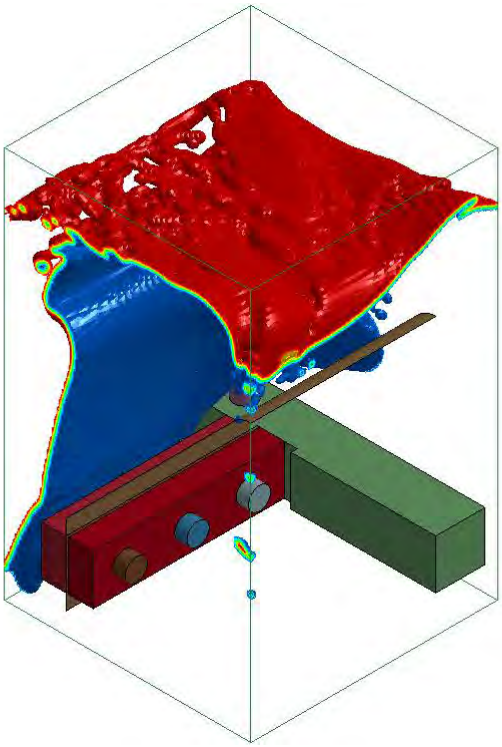

(g) t = 0.30 ms

Figure D.6: Explosive development for a 90° V-plate with a bend radius of 20 mm and a 58 g charge from 0 to 0.30 ms

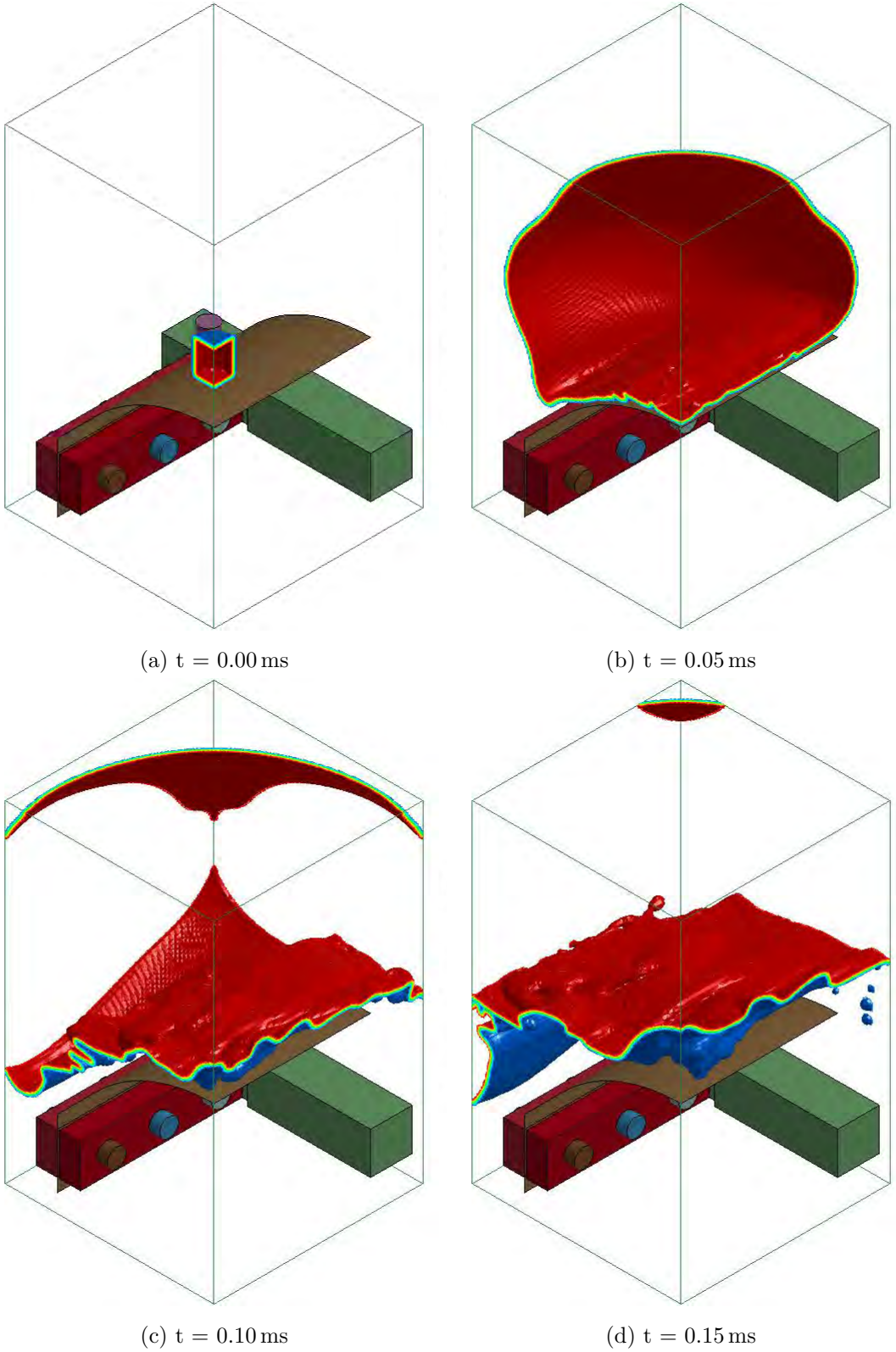

(a) t = 0.00 ms (b) t = 0.05 ms

(c) t = 0.10 ms (d) t = 0.15 ms

Figure D.7: Explosive development for a 90° V-plate with a bend radius of 160 mm and a 58 g charge from 0 to 0.30 ms

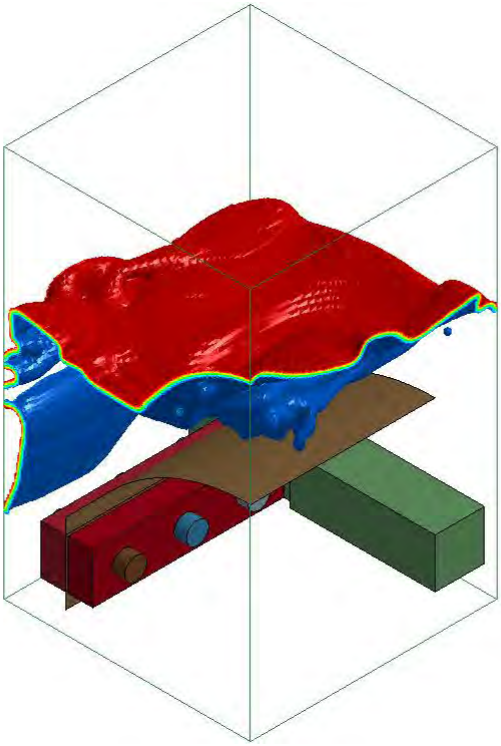

(e) t = 0.20 ms

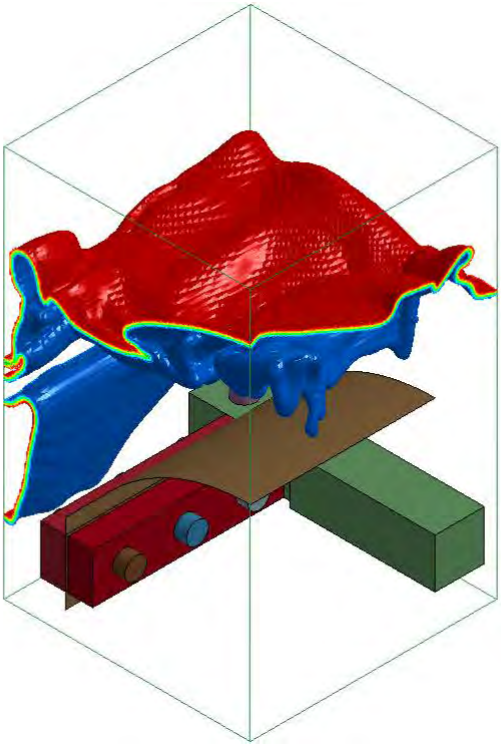

(f) t = 0.25 ms

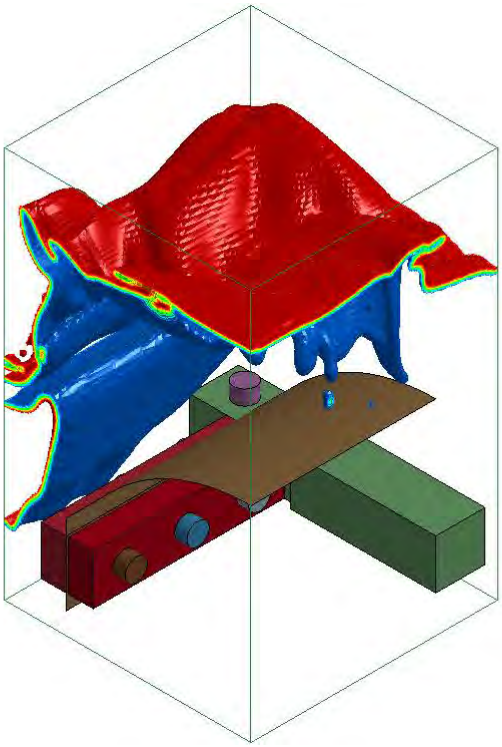

(g) t = 0.30 ms

Figure D.7: Explosive development for a 90° V-plate with a bend radius of 160 mm and a 58 g charge from 0 to 0.30 ms

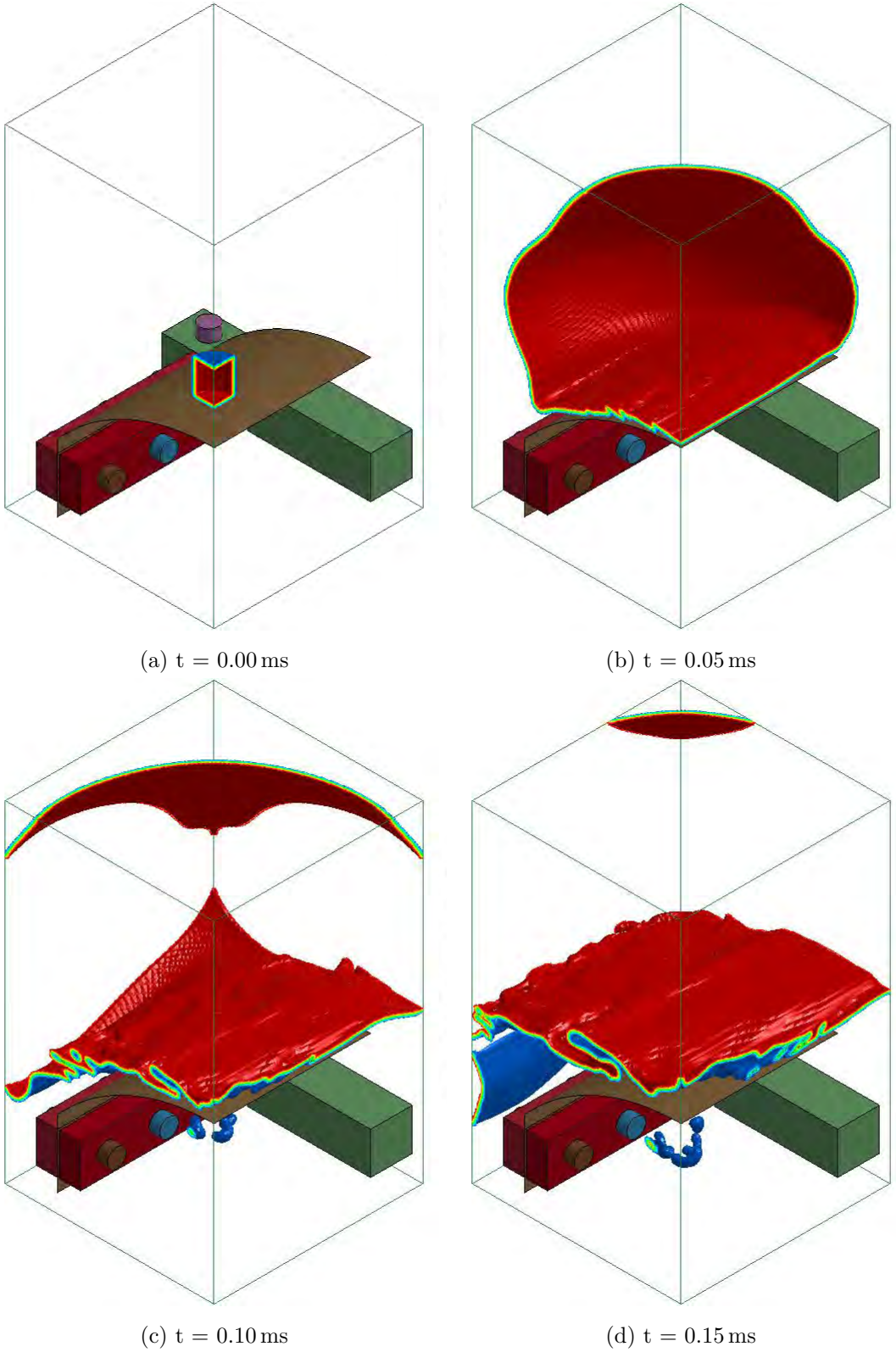

(a) t = 0.00 ms (b) t = 0.05 ms

(c) t = 0.10 ms (d) t = 0.15 ms

Figure D.8: Explosive development for a 90° V-plate with a bend radius of 200 mm and a 58 g charge from 0 to 0.30 ms

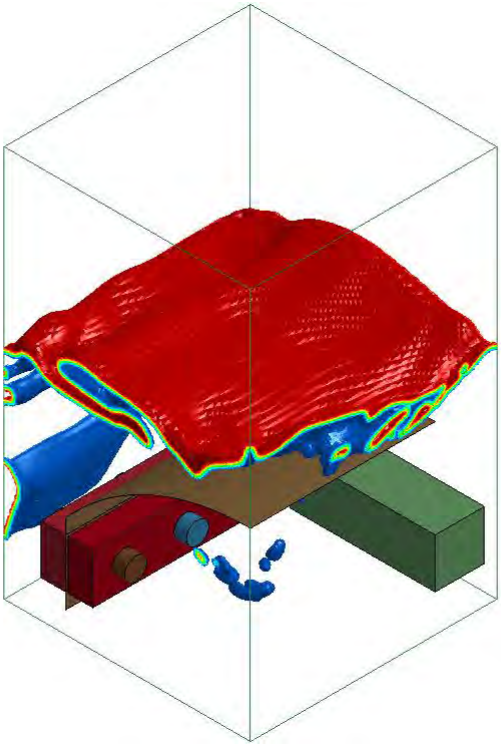

(e) t = 0.20 ms

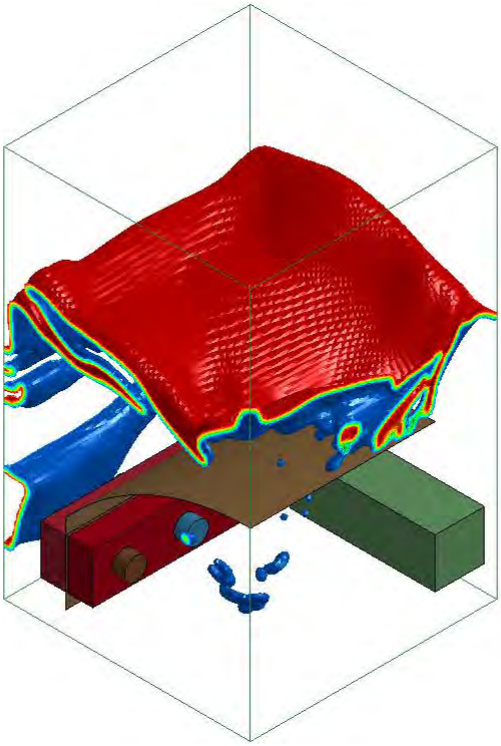

(f) t = 0.25 ms

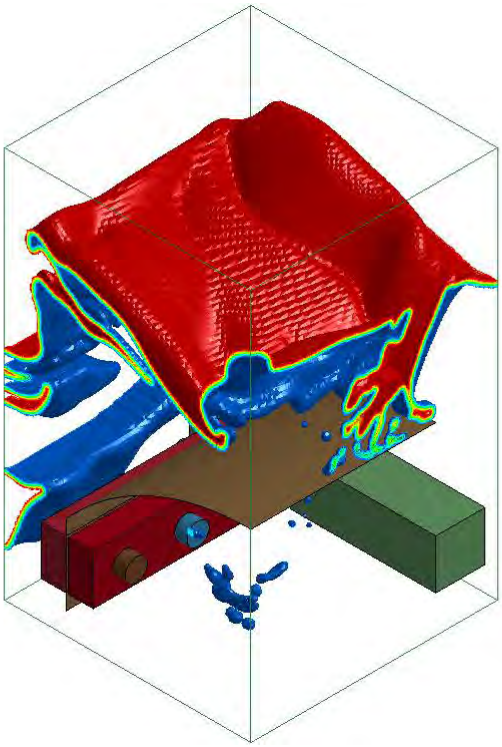

(g) t = 0.30 ms

Figure D.8: Explosive development for a 90° V-plate with a bend radius of 200 mm and a 58 g charge from 0 to 0.30 ms

D.3 120° explosive development

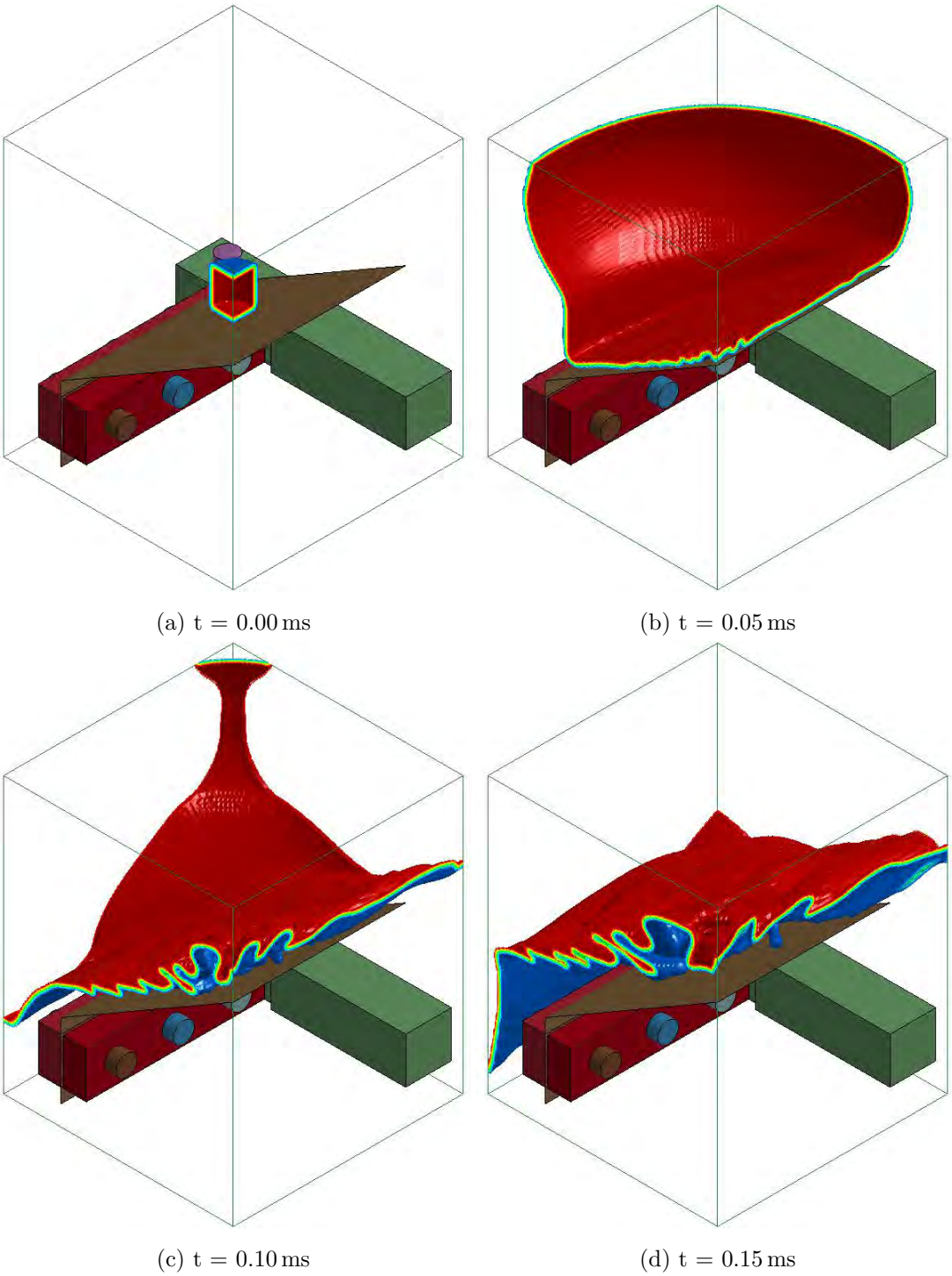

(a) t = 0.00 ms (b) t = 0.05 ms

(c) t = 0.10 ms (d) t = 0.15 ms

Figure D.9: Explosive development for a 120° V-plate with a bend radius of 0 mm and a 58 g charge from 0 to 0.30 ms

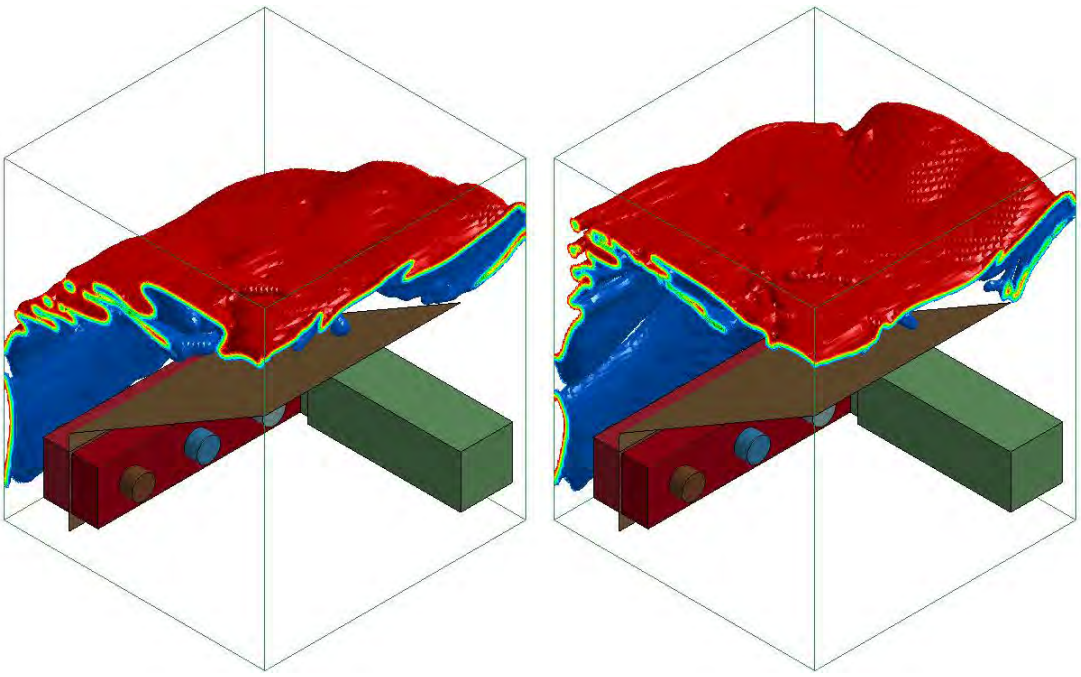

(e) t = 0.20 ms (f) t = 0.25 ms

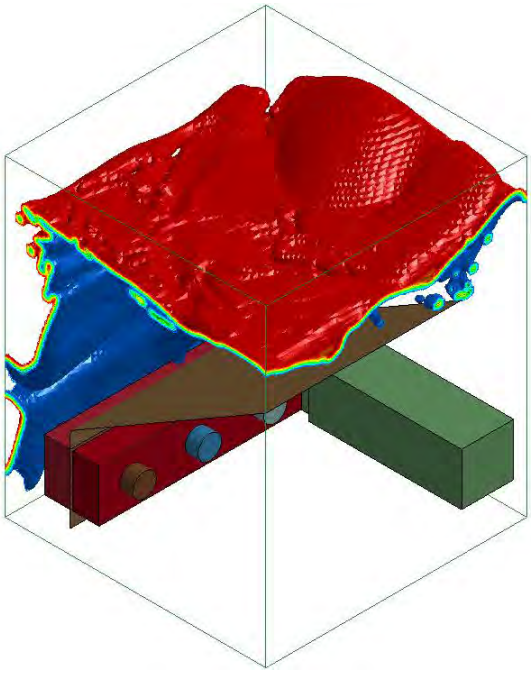

(g) t = 0.30 ms

Figure D.9: Explosive development for a 120° V-plate with a bend radius of 0 mm and a 58 g charge from 0 to 0.30 ms

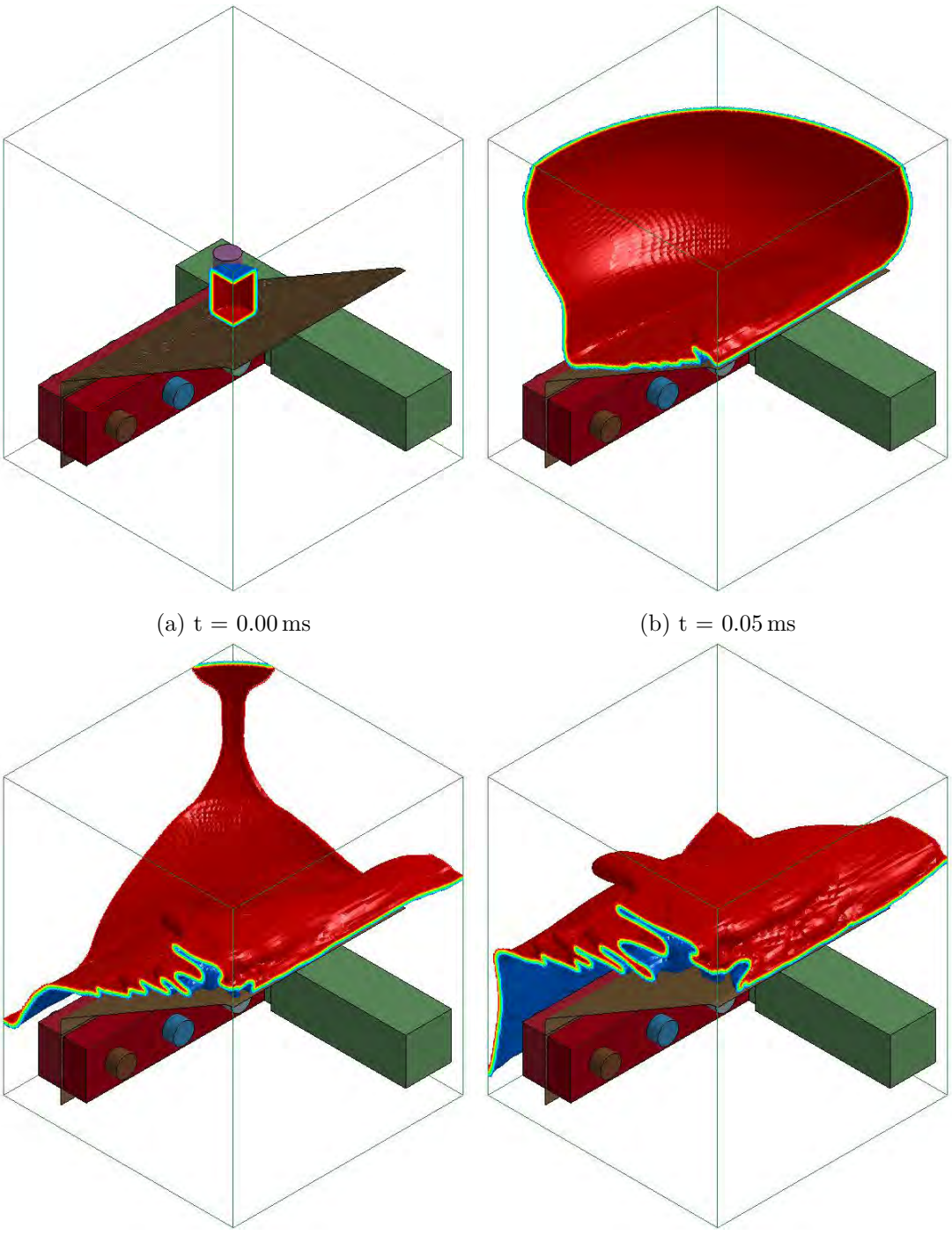

(a) t = 0.00 ms (b) t = 0.05 ms

(c) t = 0.10 ms (d) t = 0.15 ms

Figure D.10: Explosive development for a 120° V-plate with a bend radius of 20 mm and a 58 g charge from 0 to 0.30 ms

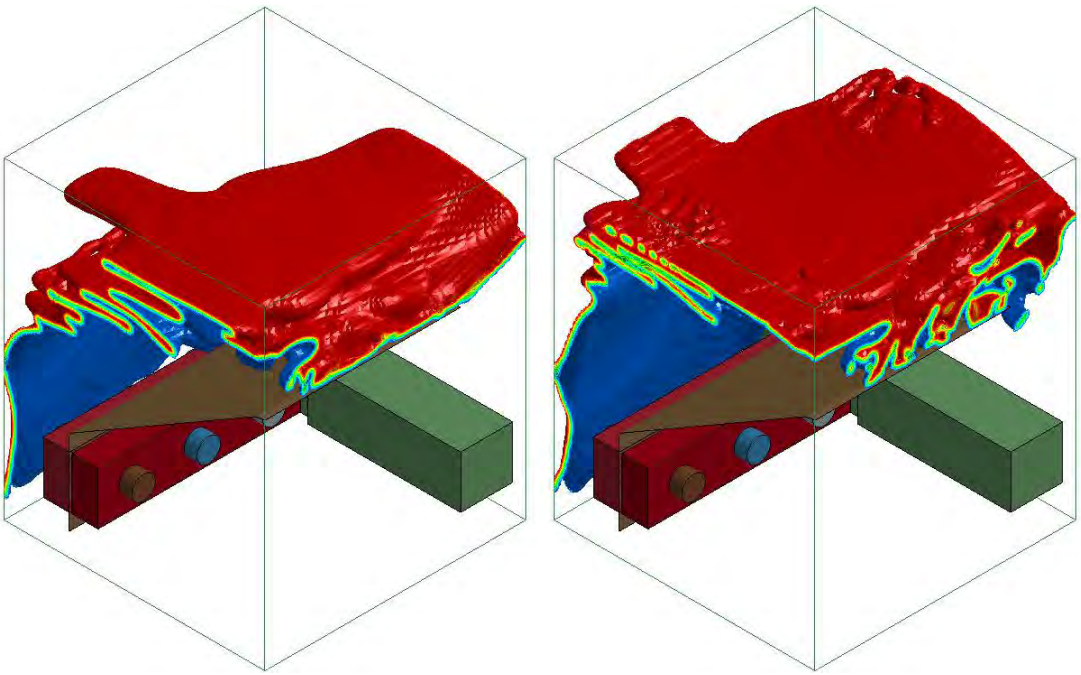

(e) t = 0.20 ms (f) t = 0.25 ms

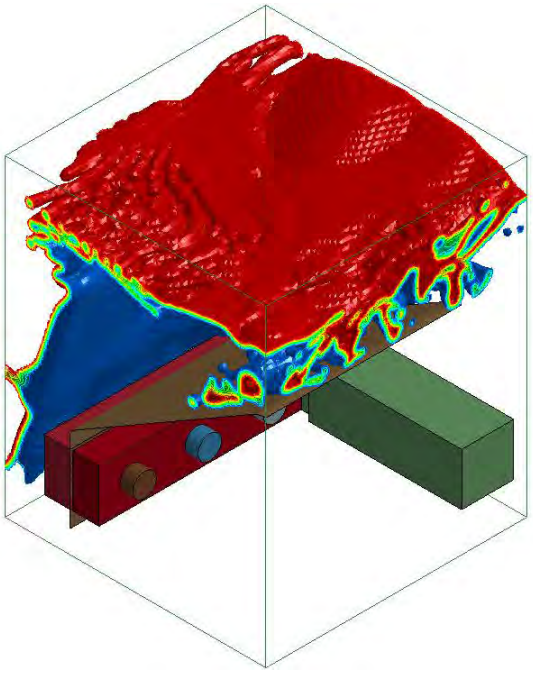

(g) t = 0.30 ms

Figure D.10: Explosive development for a 120° V-plate with a bend radius of 20 mm and a 58 g charge from 0 to 0.30 ms

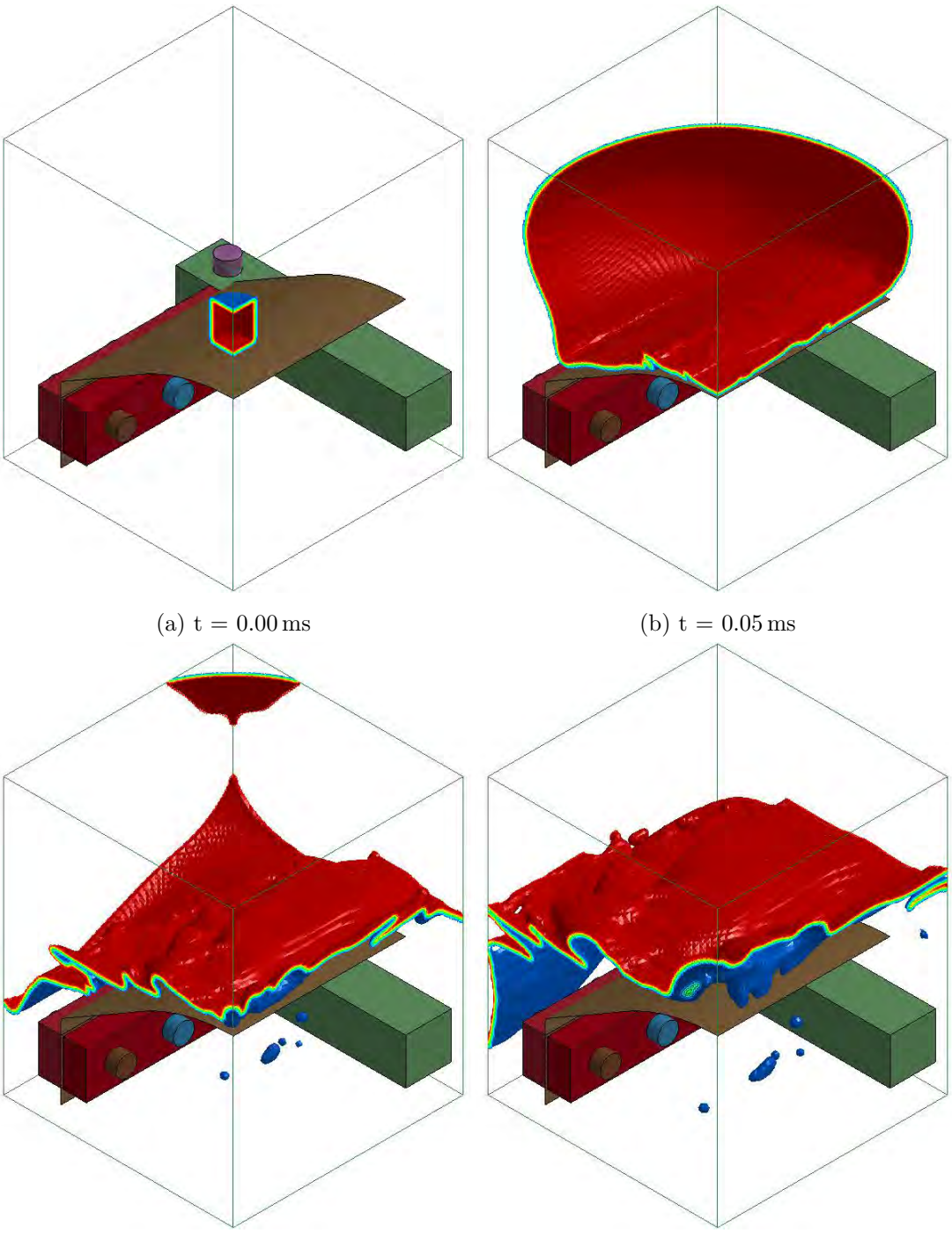

(a) t = 0.00 ms (b) t = 0.05 ms

(c) t = 0.10 ms (d) t = 0.15 ms

Figure D.11: Explosive development for a 120° V-plate with a bend radius of 160 mm and a 58 g charge from 0 to 0.30 ms

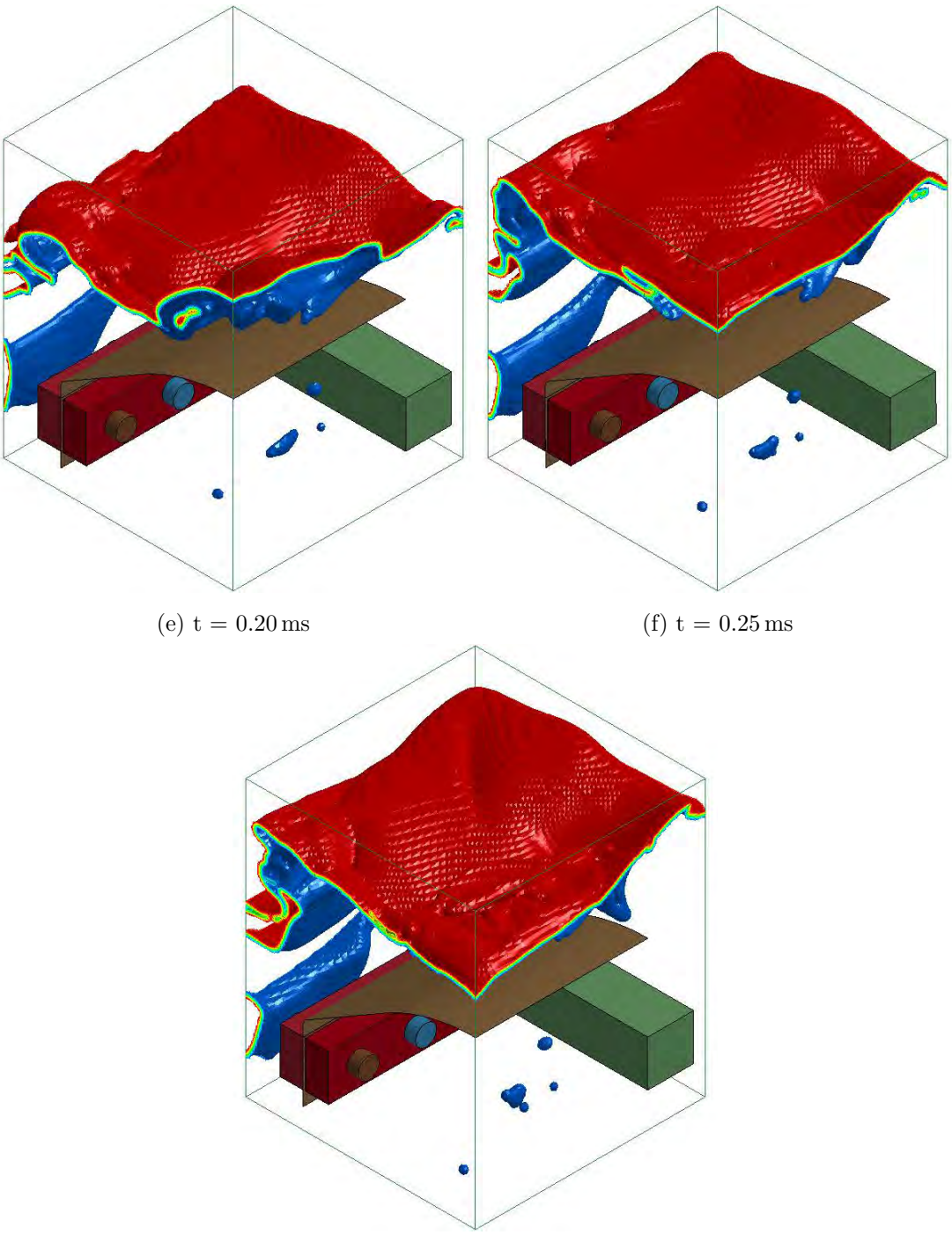

(e) t = 0.20 ms (f) t = 0.25 ms

(g) t = 0.30 ms

Figure D.11: Explosive development for a 120° V-plate with a bend radius of 160 mm and a 58 g charge from 0 to 0.30 ms

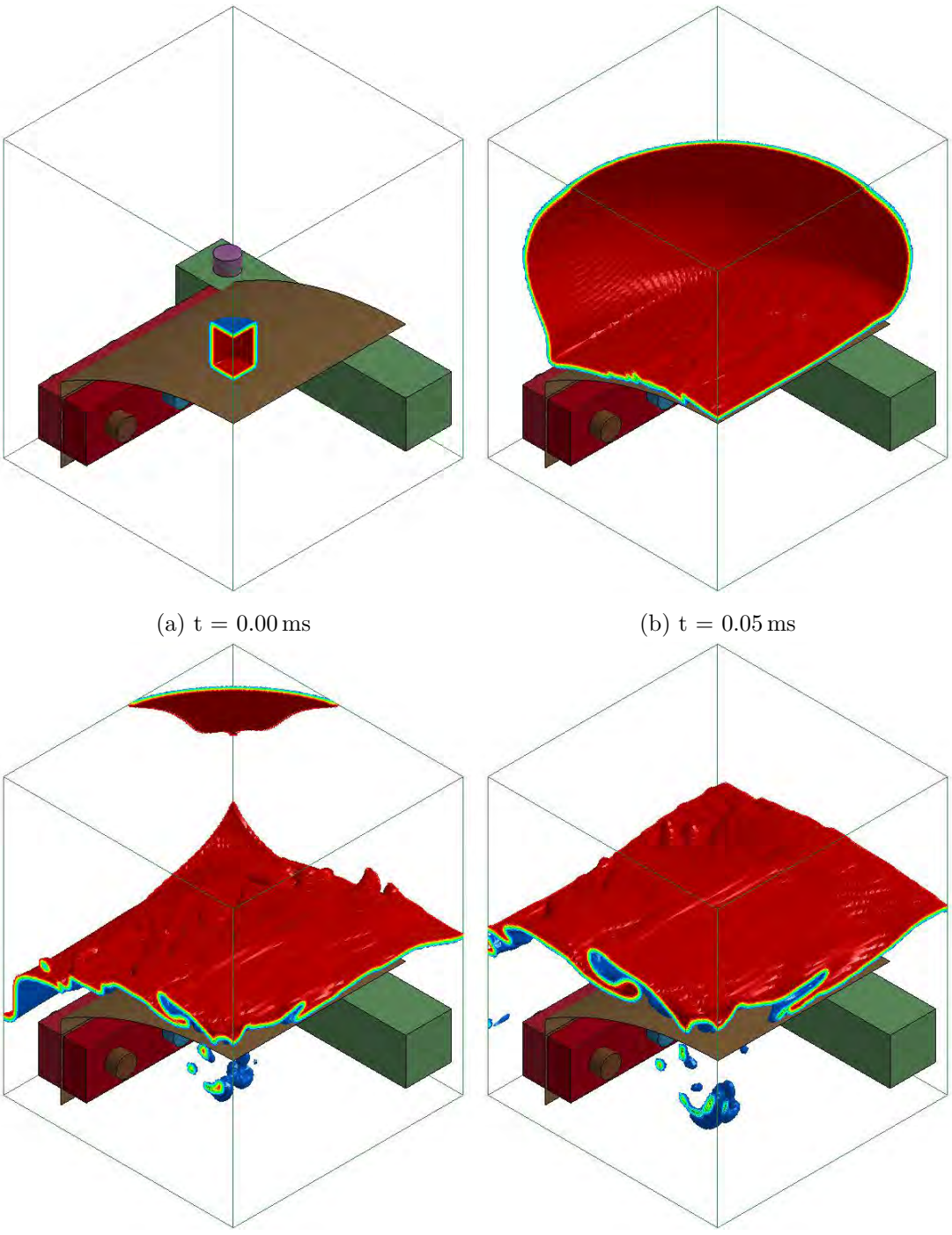

(a) t = 0.00 ms (b) t = 0.05 ms

(c) t = 0.10 ms (d) t = 0.15 ms

Figure D.12: Explosive development for a 120° V-plate with a bend radius of 280 mm and a 58 g charge from 0 to 0.30 ms

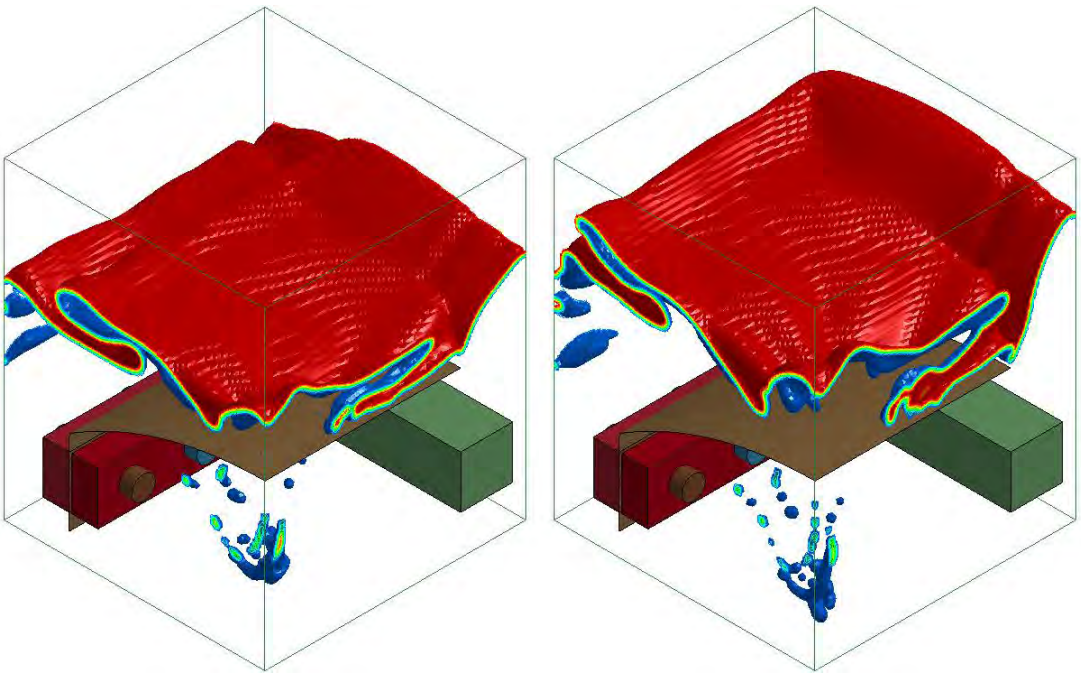

(e) t = 0.20 ms (f) t = 0.25 ms

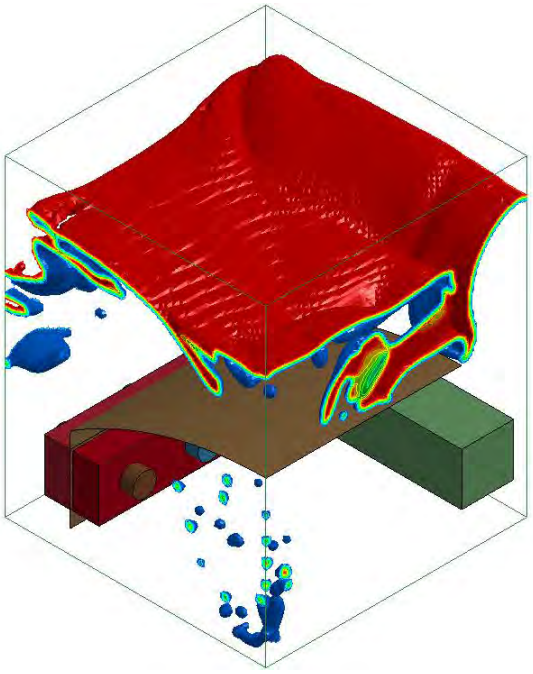

(g) t = 0.30 ms

Figure D.12: Explosive development for a 120° V-plate with a bend radius of 280 mm and a 58 g charge from 0 to 0.30 ms

This page has been intentionally left blank.

Appendix E

Rigid V-plate drawings

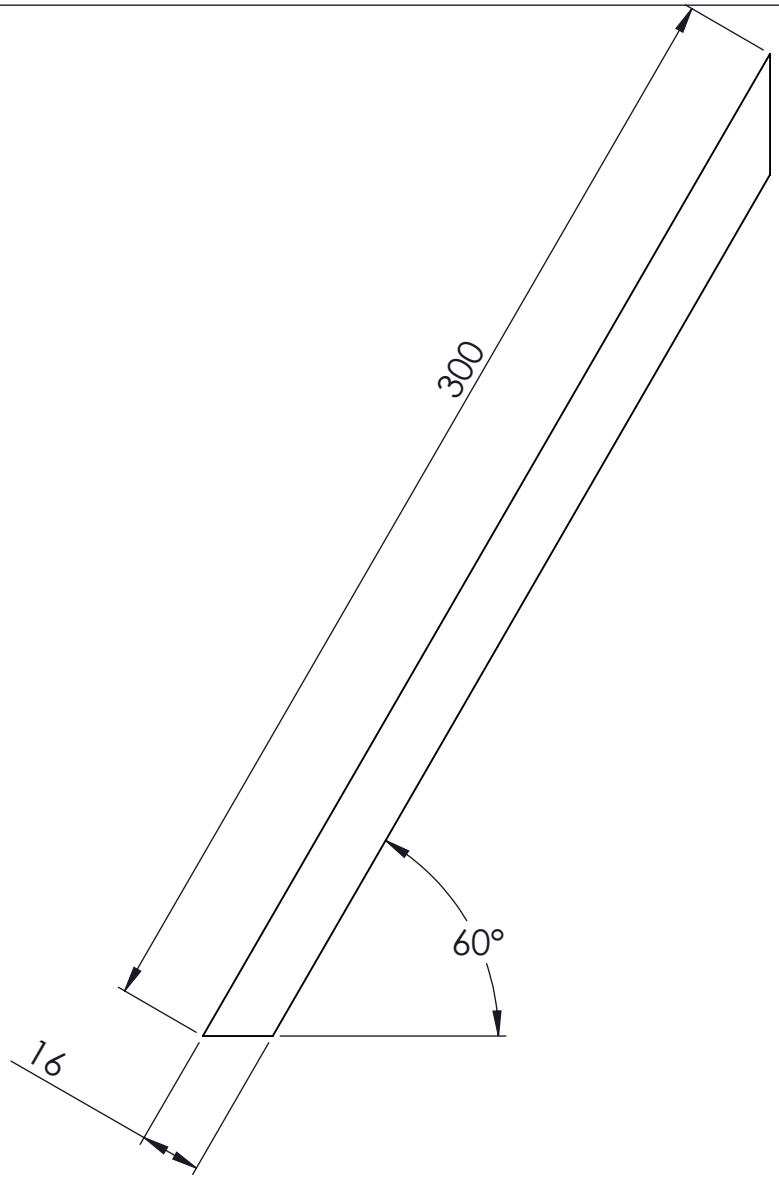

A4 Landscape	University of Cape Town Department of Mechanical Engineering			
	Title: 60_deg_V			
Part Finish	Scale: 1:2	Date: 2014/04/18	Sheet 1	of 1
Material: Mild Steel	Drawn By: Vinay Shekhar		Drawing Number 60-01	

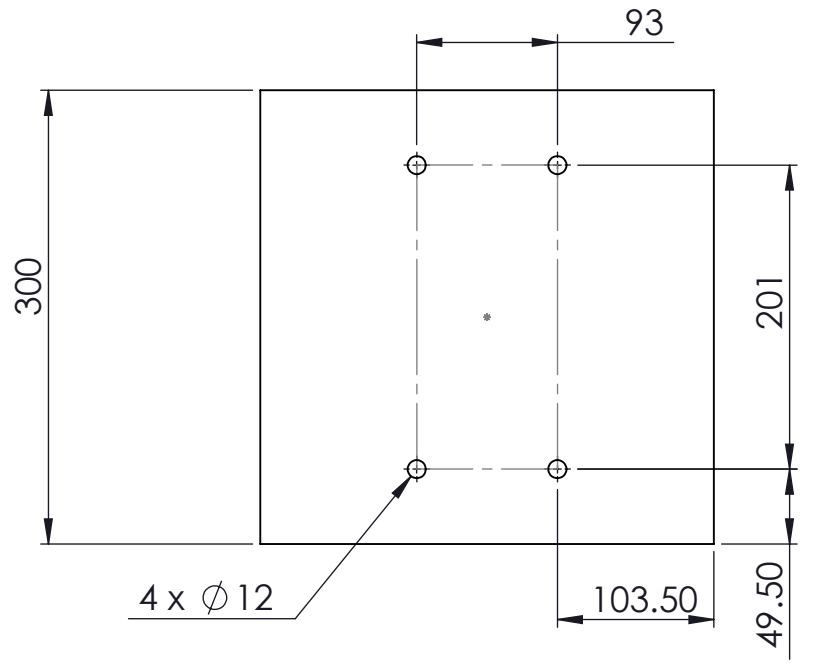

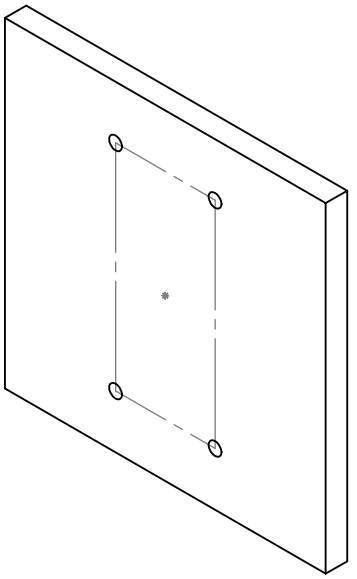

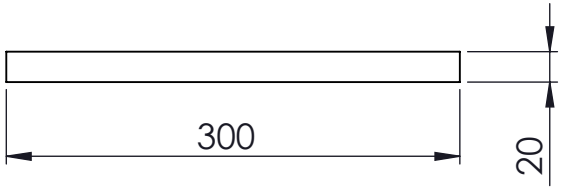

A4 Landscape	University of Cape Town Department of Mechanical Engineering			
	Title: Base_Section			
Part Finish	Scale: 1:5	Date: 2014/04/18	Sheet 1	of 1
Material: Mild Steel	Drawn By: Vinay Shekhar		Drawing Number 60-03	

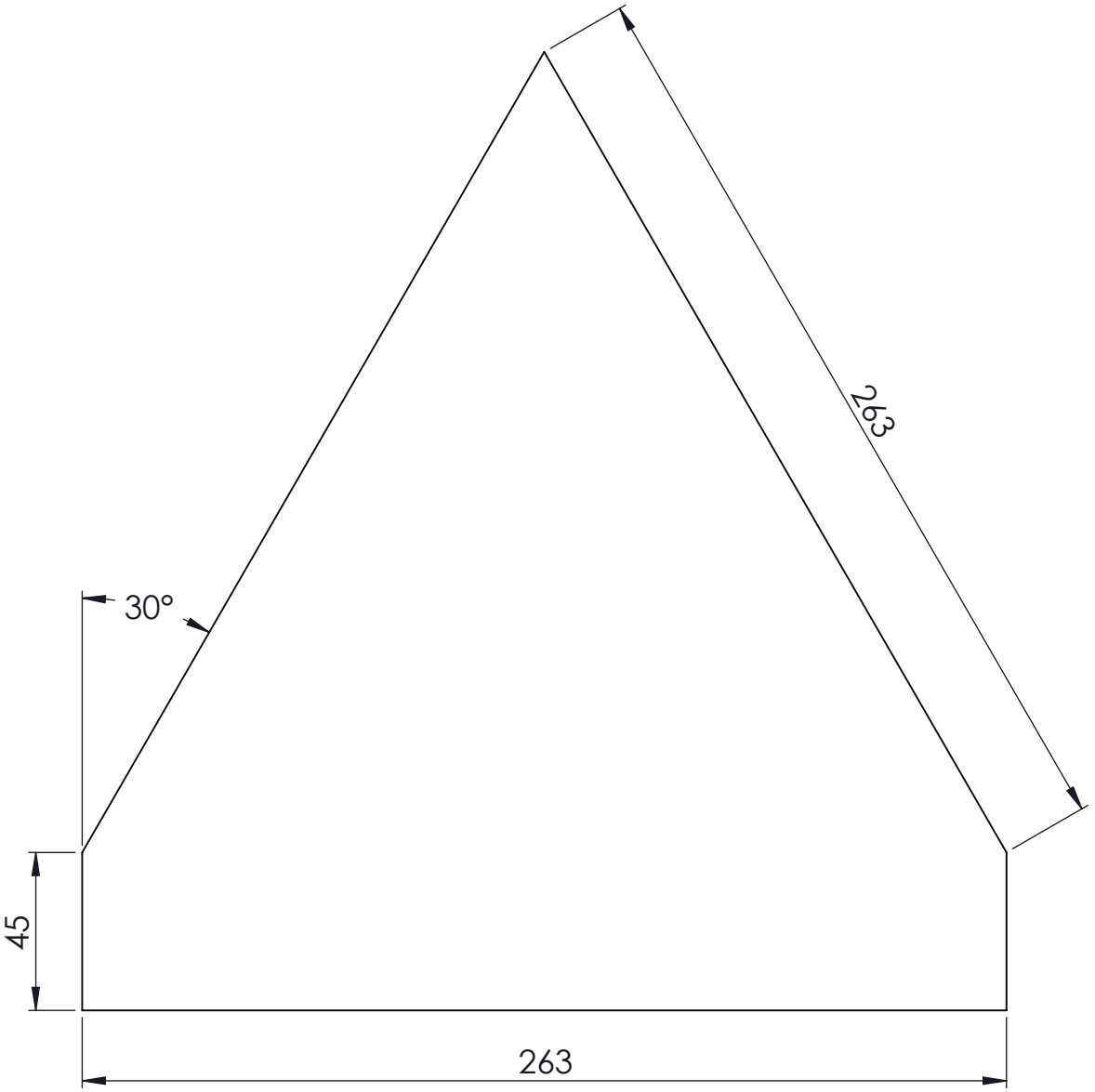

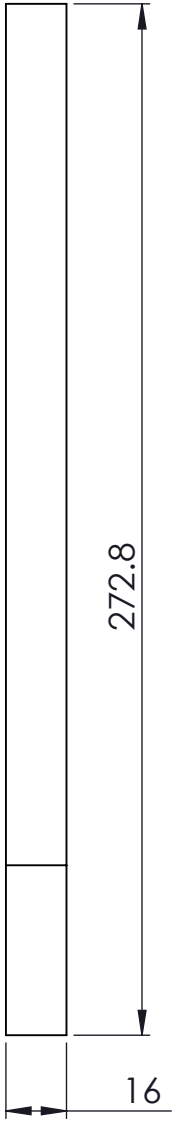

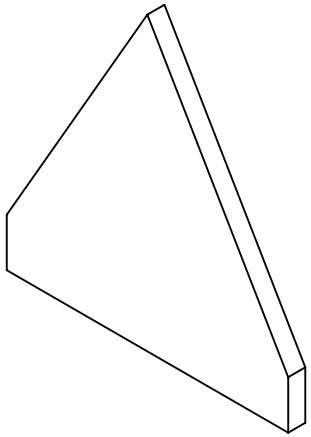

A4 Landscape	University of Cape Town Department of Mechanical Engineering			
	Title: Bridge_support			
Part Finish	Scale: 1:2	Date: 2014/04/18	Sheet 1	of 1
Material: Mild Steel	Drawn By: Vinay Shekhar		Drawing Number 60-04	

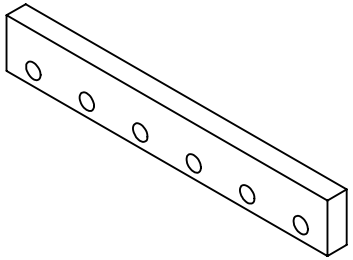

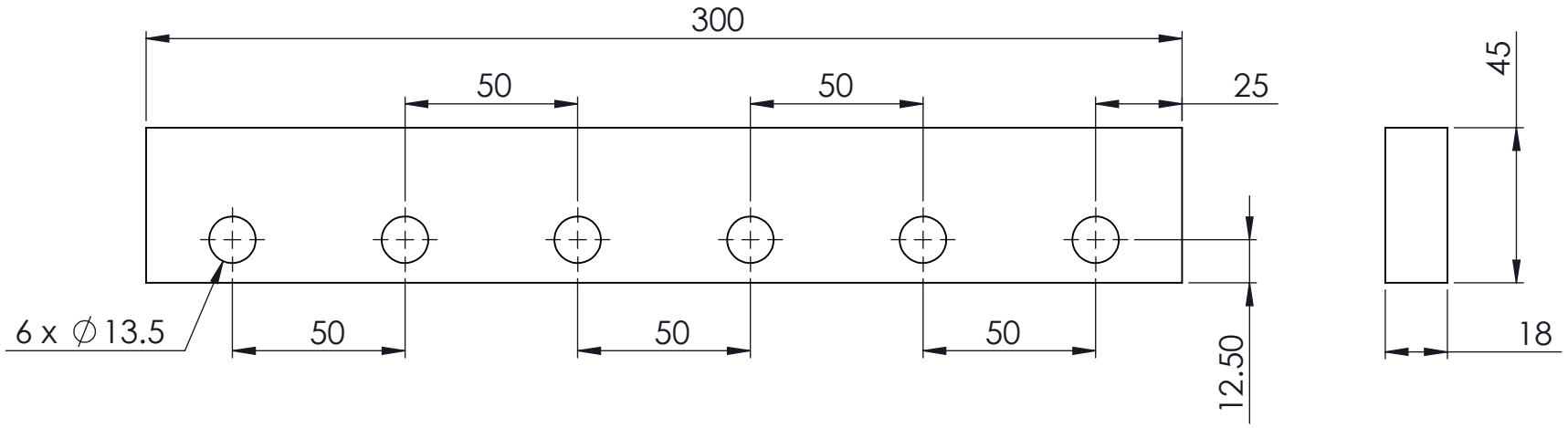

A4 Landscape	University of Cape Town Department of Mechanical Engineering			
	Title: Clamp_Region			
Part Finish	Scale: 1:2	Date: 2014/04/18	Sheet 1	of 1
Material: Mild Steel	Drawn By: Vinay Shekhar		Drawing Number 60-02	

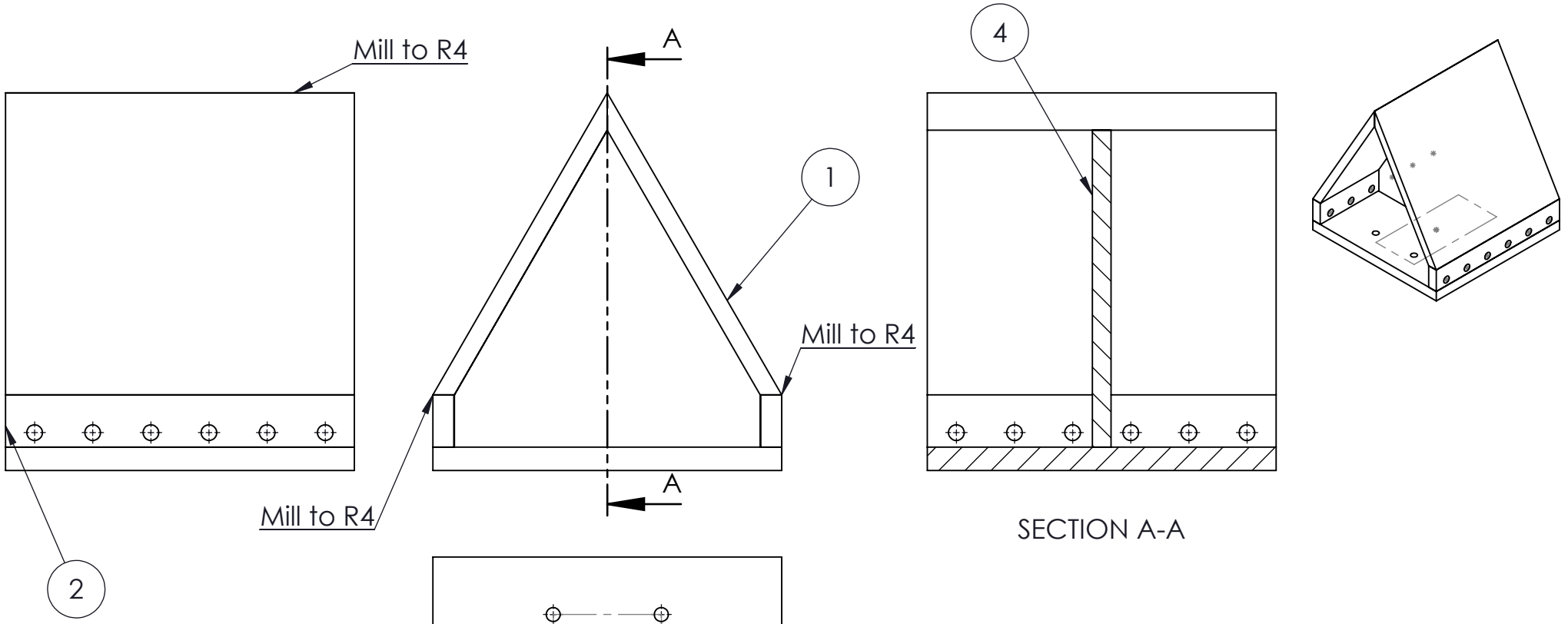

SECTION A-A

Notes:

All joints to be welded

ITEM NO.	PART NUMBER	DESCRIPTION	QTY.
1	60_deg_V		2
2	Clamp_Region		2
3	Base_Section		1
4	Bridge_support		1

A4 Landscape	**University of Cape Town** **Department of Mechanical Engineering**			
	Title: **Rigid_60_deg_V**			
Assembly Drawing	**Scale:** **1:5**	**Date:** **2014/04/18**	Sheet 1	of 1
	Drawn By: Vinay Shekhar		**Drawing Number** 60-00	

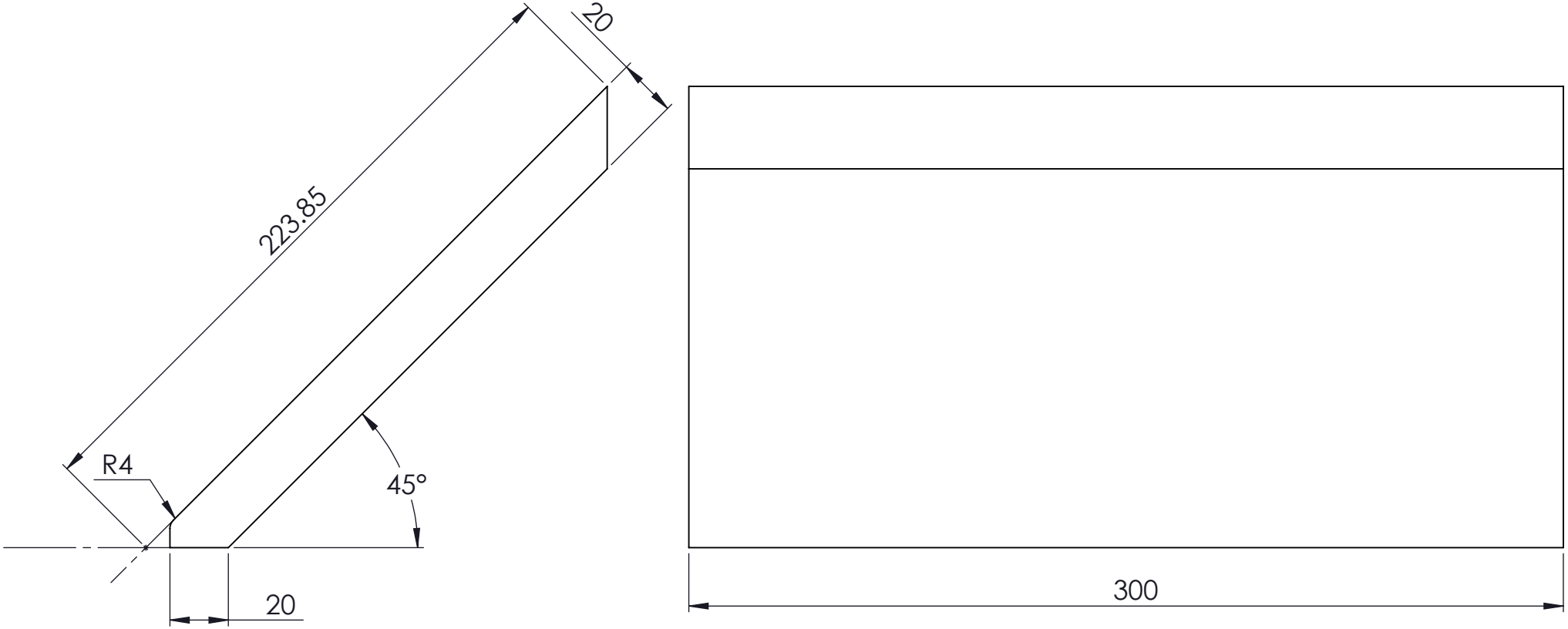

A4 Landscape	University of Cape Town Department of Mechanical Engineering			
	Title: 90_deg_V			
Part Finish	Scale: 1:2	Date: 2014/04/18	Sheet 1	of 1
Material: Mild Steel	Drawn By: Vinay Shekhar		Drawing Number 90-01	

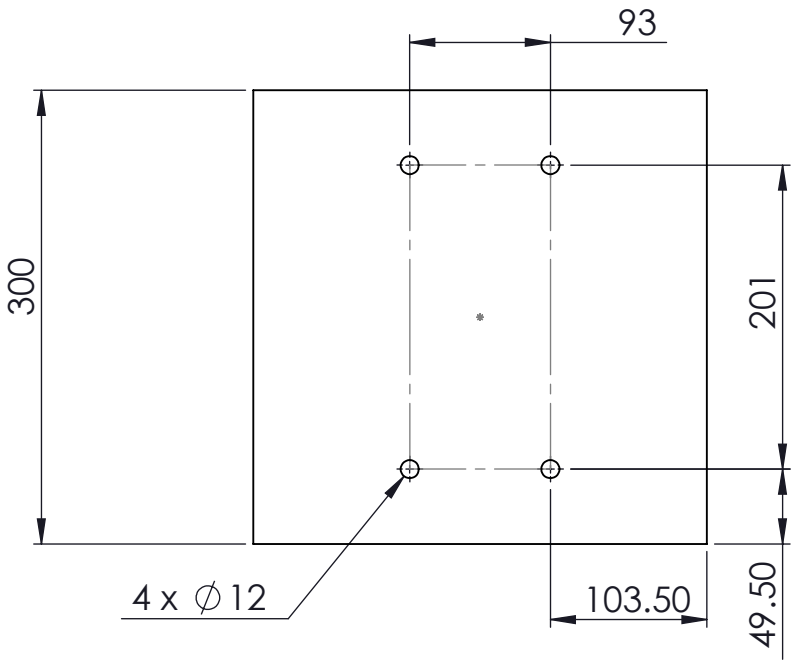

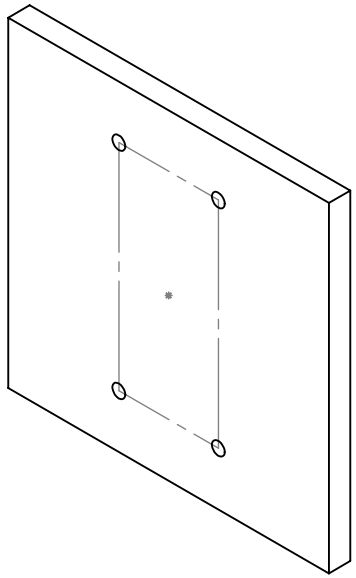

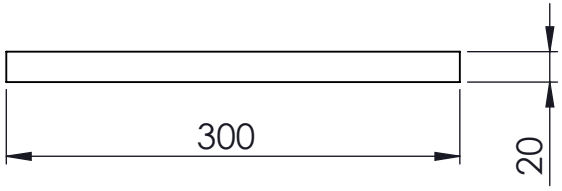

A4 Landscape	University of Cape Town Department of Mechanical Engineering			
	Title: Base_Section			
Part Finish	Scale: 1:5	Date: 2014/04/18	Sheet 1	of 1
Material: Mild Steel	Drawn By: Vinay Shekhar		Drawing Number 90-03	

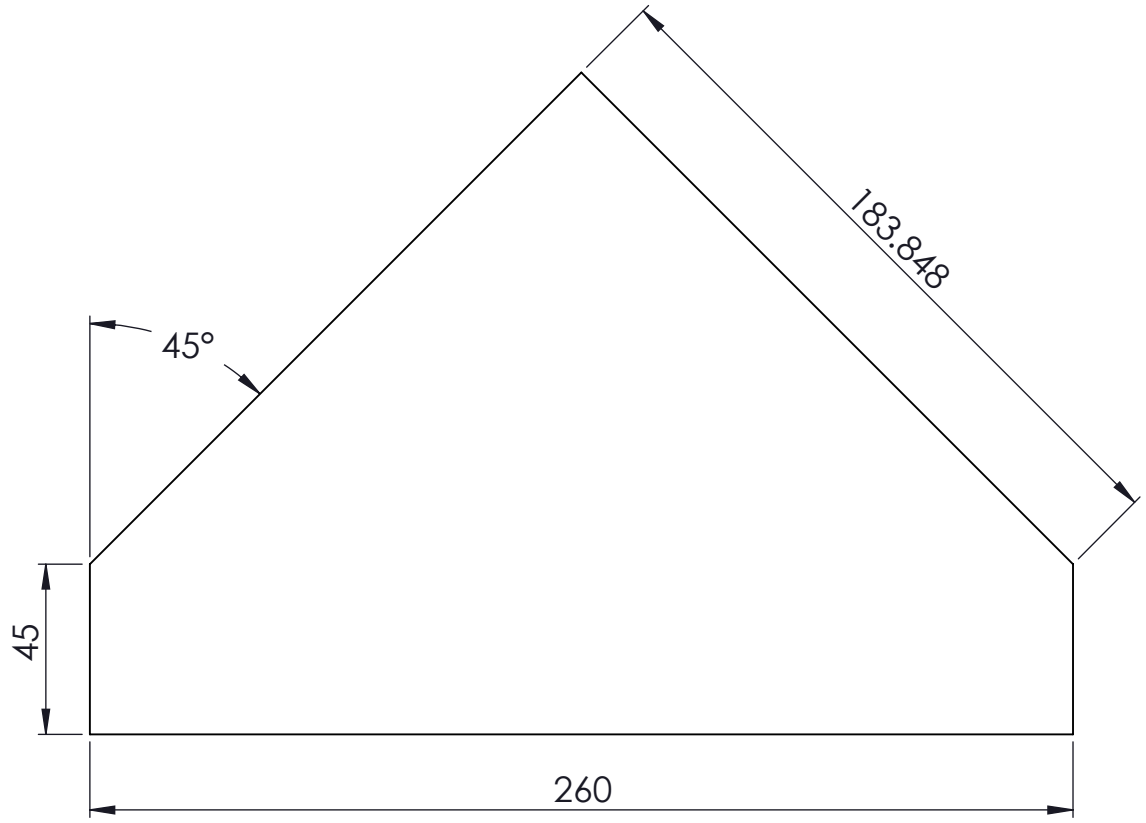

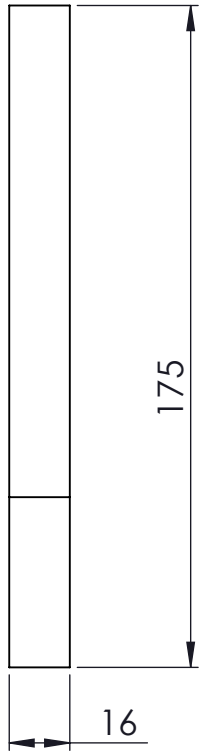

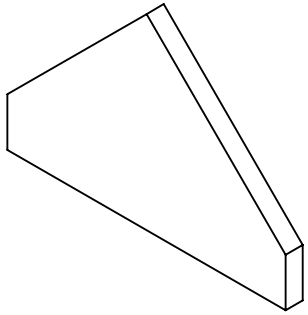

A4 Landscape	**University of Cape Town** Department of Mechanical Engineering			
	Title: Bridge_support			
Part Finish	Scale: 1:2	Date: 2014/04/18	Sheet 1	of 1
Material: Mild Steel	Drawn By: Vinay Shekhar		Drawing Number 90-04	

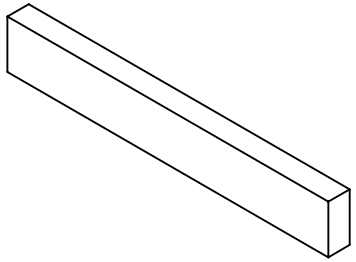

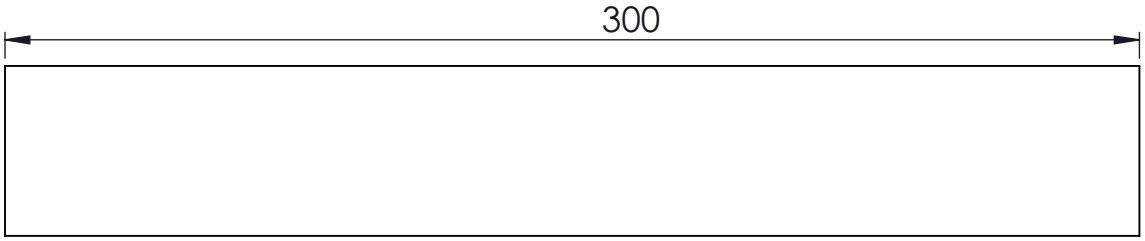

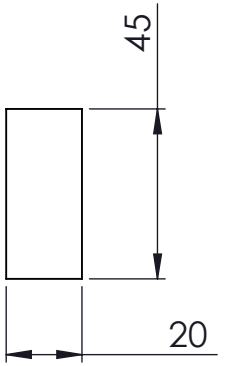

A4 Landscape	University of Cape Town Department of Mechanical Engineering			
	Title: Clamp_Region			
Part Finish	Scale: 1:2	Date: 2014/04/18	Sheet 1	of 1
Material: Mild Steel	Drawn By: Vinay Shekhar		Drawing Number 90-02	

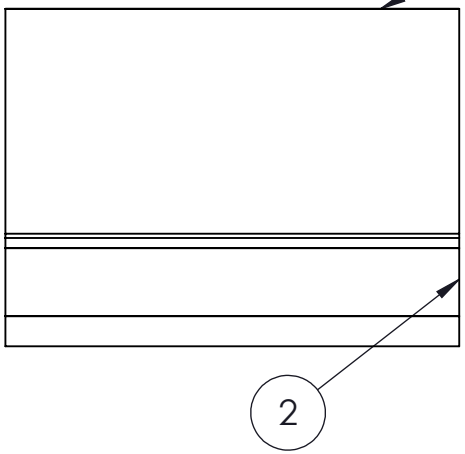

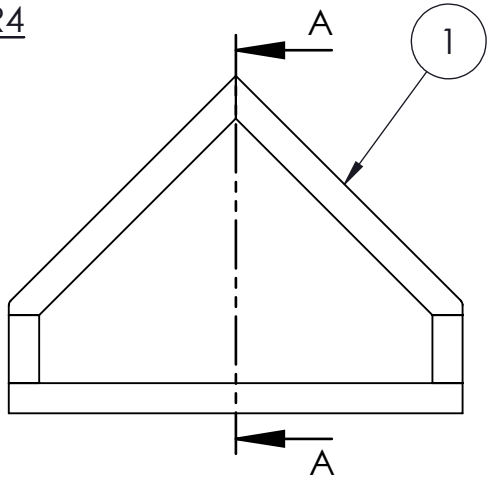

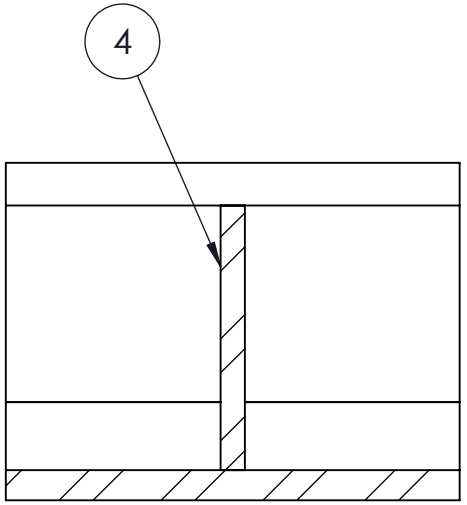

SECTION A-A

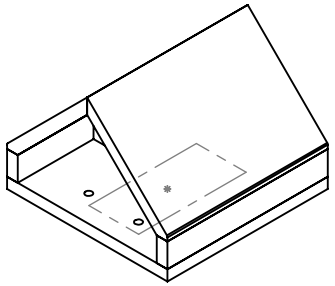

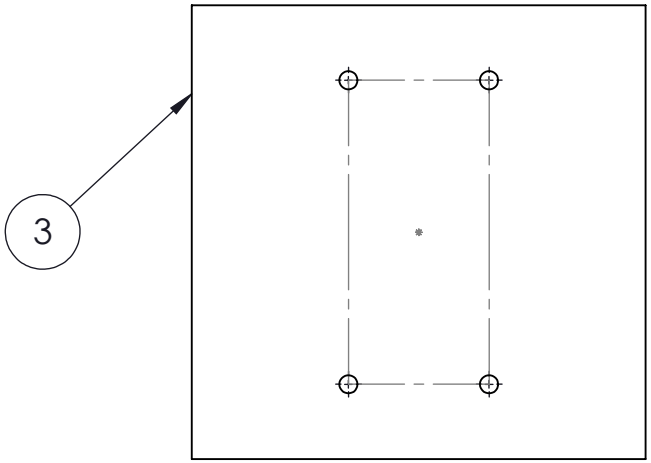

ITEM NO.	PART NUMBER	DESCRIPTION	QTY.
1	90_deg_V		2
2	Clamp_Region		2
3	Base_Section		1
4	Bridge_support		1

A4 Landscape	**University of Cape Town** **Department of Mechanical Engineering**			
	Title: **Rigid_90_deg_V**			
Assembly Drawing	**Scale:** **1:5**	**Date:** **2014/04/18**	Sheet 1	of 1
	Drawn By: Vinay Shekhar		**Drawing Number** 90-00	

Notes:

All joints to be welded

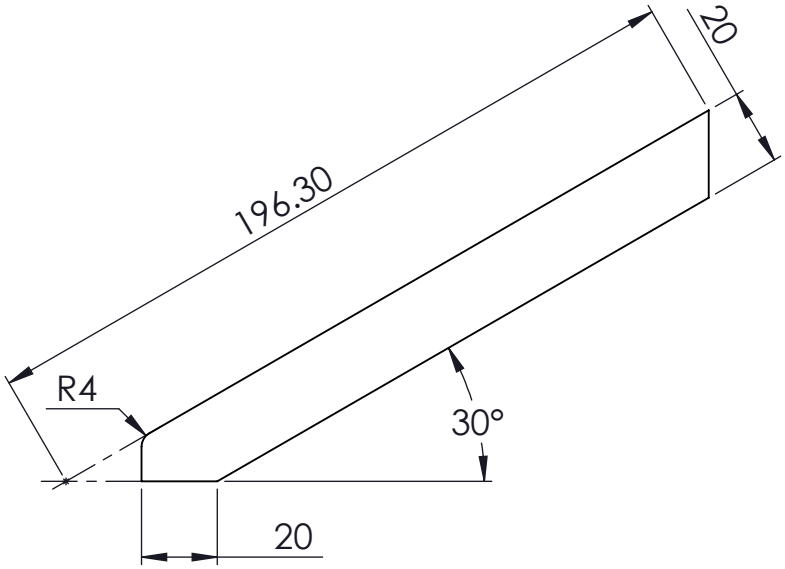

A4 Landscape	University of Cape Town Department of Mechanical Engineering			
	Title: 120_deg_V			
Part Finish	Scale: 1:2	Date: 2014/04/18	Sheet 1	of 1
Material: Mild Steel	Drawn By: Vinay Shekhar		Drawing Number 120-04	

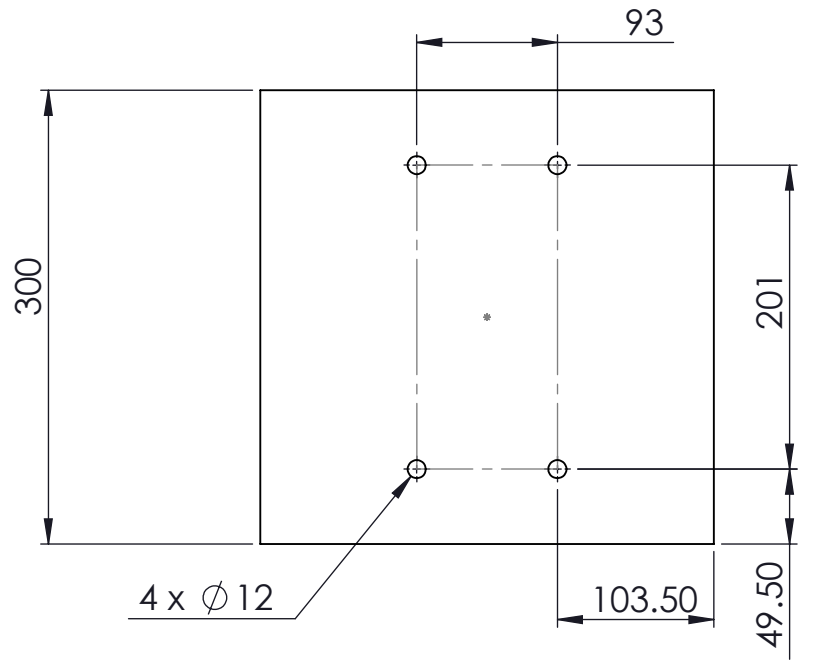

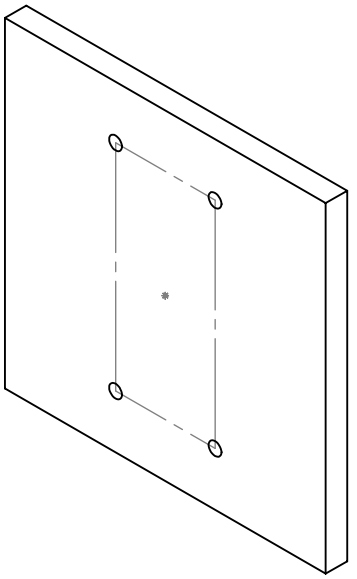

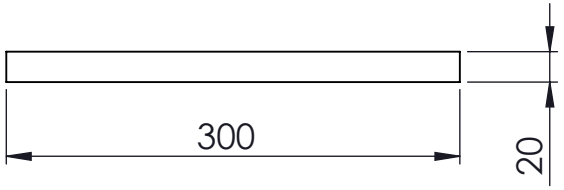

A4 Landscape	University of Cape Town Department of Mechanical Engineering			
	Title: Base_Section			
Part Finish	Scale: 1:5	Date: 2014/04/18	Sheet 1	of 1
Material: Mild Steel	Drawn By: Vinay Shekhar		Drawing Number 120-02	

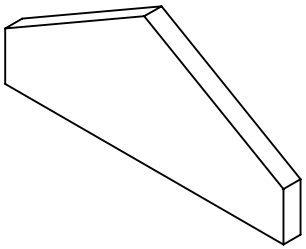

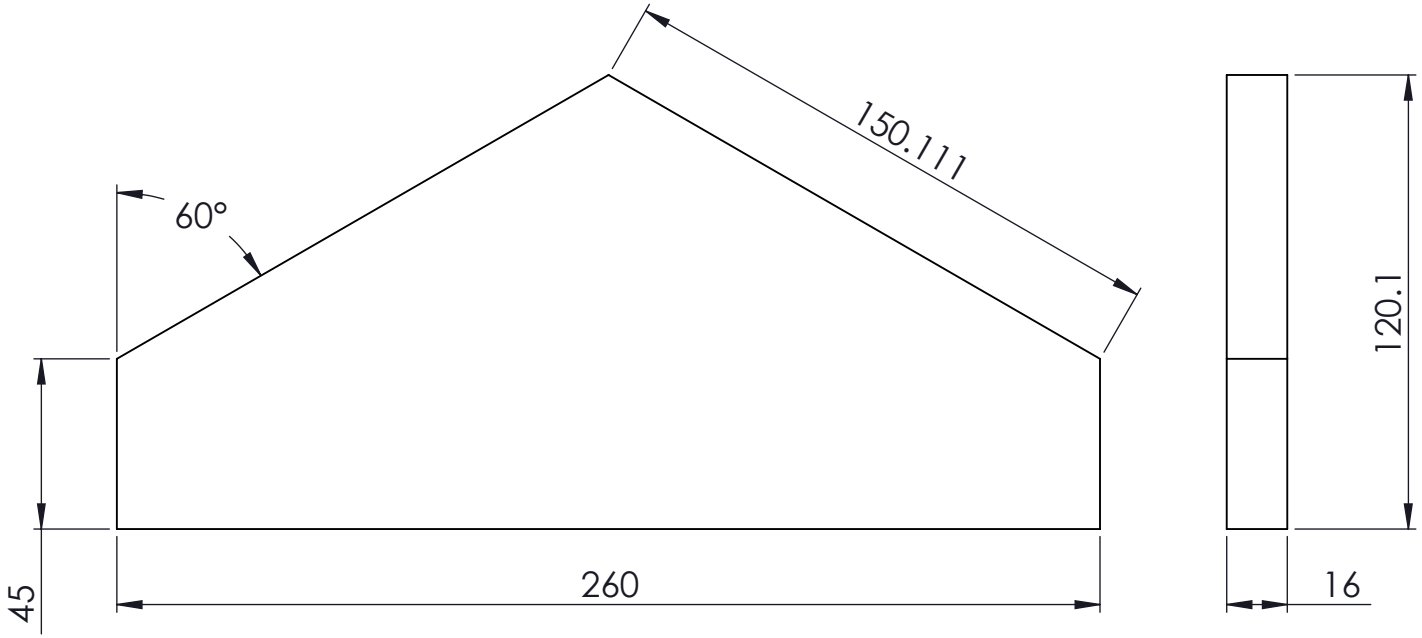

A4 Landscape	University of Cape Town Department of Mechanical Engineering			
	Title: Bridge_support			
Part Finish	Scale: 1:2	Date: 2014/04/18	Sheet 1	of 1
Material: Mild Steel	Drawn By: Vinay Shekhar		Drawing Number 120-03	

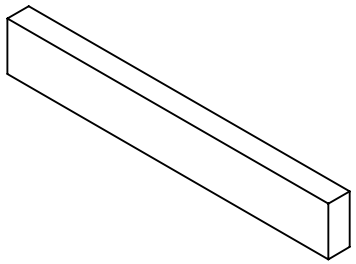

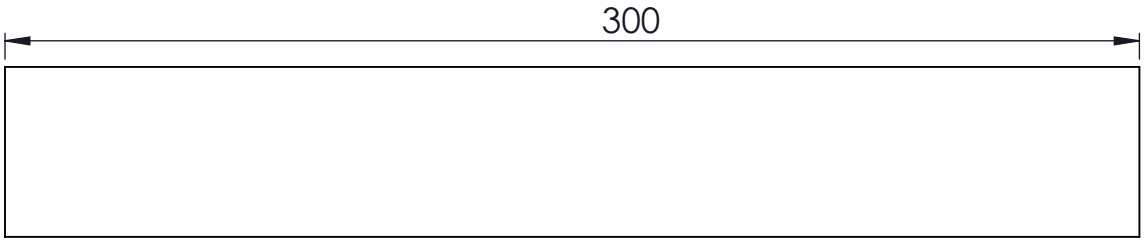

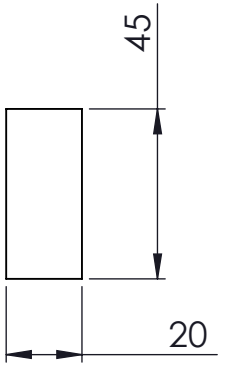

A4 Landscape	University of Cape Town Department of Mechanical Engineering			
	Title: Clamp_Region			
Part Finish	Scale: 1:2	Date: 2014/04/18	Sheet 1	of 1
Material: Mild Steel	Drawn By: Vinay Shekhar		Drawing Number 120-01	

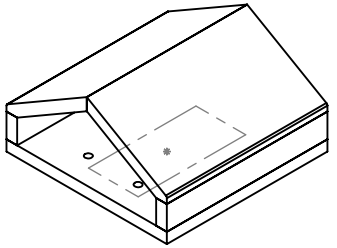

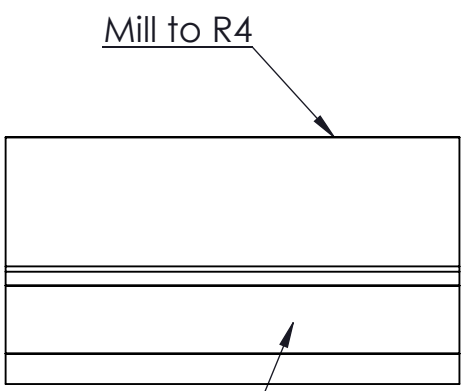

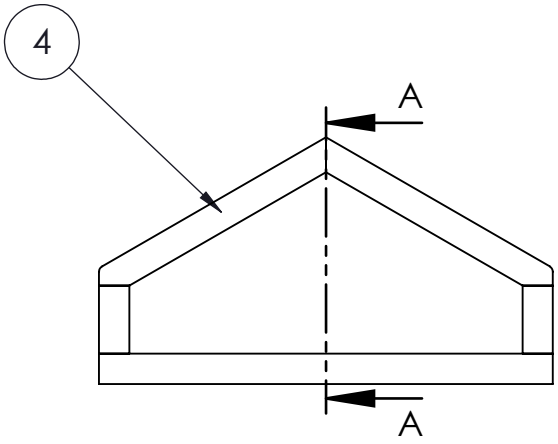

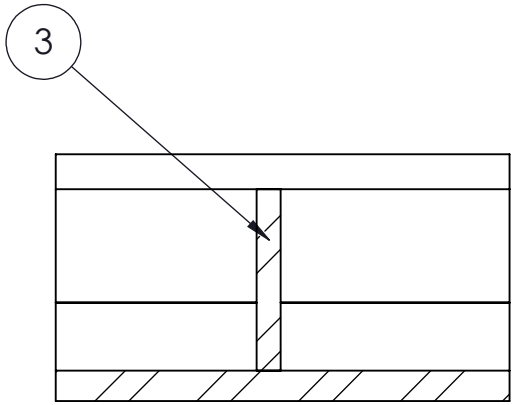

SECTION A-A

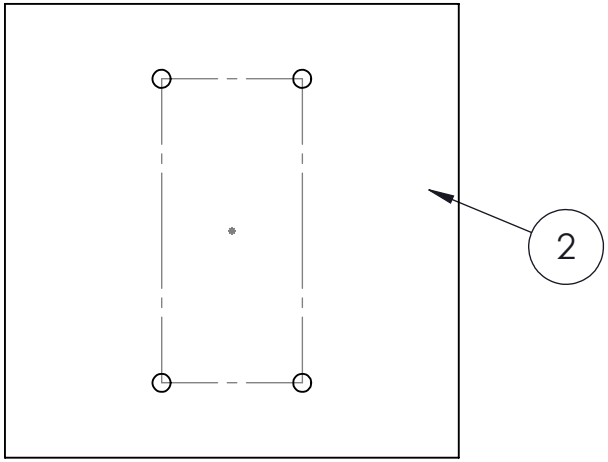

ITEM NO.	PART NUMBER	QTY.
1	Clamp_Region	2
2	Base_Section	1
3	Bridge_support	1
4	120_deg_V	2

A4 Landscape	**University of Cape Town** Department of Mechanical Engineering			
	Title: Rigid_120_deg_V			
Assembly Drawing	Scale: 1:5	Date: 2014/04/18	Sheet 1	of 1
	Drawn By: Vinay Shekhar		Drawing Number 120-00	

Notes:

All joints to be welded